GROWTH MODE AND CONDUCTION CHARACTERISTICS OF MOLECULAR SEMICONDUCTOR FILMS

By

Arvind Kumar

PHYS01200804026

BHABHA ATOMIC RESEARCH CENTRE, MUMBAI

A thesis submitted to the

Board of Studies in Physical Sciences

In partial fulfillment of requirements

For the degree of

DOCTOR OF PHILOSOPHY

of

HOMI BHABHA NATIONAL INSTITUTE

July, 2012

STATEMENT BY AUTHOR

This dissertation has been submitted in partial fulfillment of requirements for an advanced degree at Homi Bhabha National Institute (HBNI) and is deposited in the library to be made available to borrowers under rules of the HBNI.

Brief quotations from this dissertation are allowable without any special permission, provided that accurate acknowledgement of source is made. Requests for permission for extended quotation from or reproduction of this manuscript in whole or in part may be granted by the competent authority of HBNI when in his or her judgment the proposed use of the material is in the interests of the scholarship. In all other instances, however, permission must be obtained from the author.

(Arvind Kumar)

DECLARATION

I, hereby declare that the investigation presented in the thesis has been carried out by me. The work is original and has not been submitted earlier as a whole or in part for a degree/ diploma at this or any other Institution / University.

(Arvind Kumar)

Dedicated

to my

parents

Acknowledgements

At the end of my thesis I would like to thanks many people without the help of them it would have not been possible.

First and foremost, I would like to thanks my guide **Dr. D.K. Aswal**, for accepting me as his student to participate in this interesting work and for their constant encouragement during this work. Without his supervision as a great mentor, this work would not have been possible within time. I am greatly indebted to **Dr. S.K. Gupta, Head Technical Physics Division** for his support and guidance during the thesis work.

I feel great pleasure to express my sincere thanks to **Dr. A. K. Debnath** for helping me in the thin film depositions by molecular beam epitaxy and **Dr. Ajay Singh** for the analysis of the charge conduction characteristics.

I wish to express my deep sense of gratitude to the members of my doctoral committee **Prof. M. Senthil Kumar, IIT Mumbai** and **Dr. N.K. Sahoo, Head Applied Spectroscopy Division**, for their questions and suggestions, which have improved my research work.

I would like to thanks **Ms. N. Padma, Dr. A.K. Chauhan, Dr. S.P. Koiry, Dr. Vibha Saxsena, Soumen Samanta** and **Shri P. Jha** for their continuous support during the work.

I am also greatly indebted to **Shri K.P. Muthe, Dr. Manmeet Kaur, Shri R. Prasad, Dr. Niranjan Ramgir, Dr. Ranu Bhatt, Mrs. Ranita Basu, Ms. Niyanta Dutta, Mrs K Ganapati, Shri K.N. Meshram, Shri P. Veerender** and **Shri Vishal Balouria** for extending support and help at various stages of the thesis work.

I owe my thanks to all my HBNI friends specially **Debes, C. Vijay, Pankaj, Rohit, Naveen, Nazir**, **Anuvab** and **Lokesh** for their affectionate support and good wishes.

Life is just not professional; it has its root under the roof of loved ones. I am overwhelmed when it comes to express my gratitude towards my family members. I thank my parents, brother and sister for their supreme moral support and boundless love they have showered upon me. My special thanks to my Father who instilled in me the undying spirit to fight and never give up. I thank my mother for her blessings.

(Arvind Kumar)

CONTENTS

SYNOPSIS

There are two major classes of organic semiconductors: molecular (made of small molecules) and polymeric (made of long conjugated chains). While polymeric semiconductors often form disordered phases, molecular semiconductors frequently show ordered and crystalline structures. Molecular semiconductors have been attracting much attention due to their interesting optical and electrical properties, and therefore, are being used in many organic devices, such as, organic field effect transistor (OFET), organic light emitting diode (OLED), solar cell, gas sensors etc. [1-3]. Simplicity in manufacturing and lower costs makes feasibility of organic electronic devices for their commercialization. Most of the organic electronic devices require high quality thin films and it has observed that performance of these devices is greatly affected by the morphology and structure (ordered or disordered) of thin films. In the early years of device developments, the deposition of organic semiconductor thin films mainly imitated the methods of inorganic thin films, such as heteroepitaxy, in which an inorganic single crystal is usually used as a substrate. However epitaxial growth of molecular semiconductor on inorganic substrate is very difficult. This is because of two reasons: (i) molecular semiconductors have a particular geometrical shape with an inherent anisotropy that differs from the intrinsic isotropy of inorganic atoms. For example metal phthalocyanines (MPc's) have disk like geometry and pentacene has one dimension rod like geometry and also a lattice mismatch between films and substrate. (ii) Weak van der Waals interactions rather than strong covalent bonds exist between molecules or between molecules and substrates. Hence, the fabrication of high quality organic semiconductor thin films is more difficult than that of inorganic thin films. Another important issue in molecular semiconductor films is the charge conduction. Therefore, to achieve better performance of organic devices, proper understandings of (i) film growth mechanism(s) and (ii) electrical conduction mechanism in molecular semiconductor films are essential. In literature, a considerable amount of efforts have been devoted to study the charge transport mechanism in molecular semiconductor thin films, particularly at low temperatures. Due to the weak van der Waals interaction, molecular semiconductors have poor crystalline nature, which results in very low mobility (μ) usually in the range 0.01 to 10cm^2/Vs. A literature survey shows that it is difficult to measure the electrical conductivity at temperature below 120K, because of poor mobility, no measurable current is obtained. Undoubtedly, in order to investigate the low-temperature electrical conduction mechanism in molecular semiconductor films, the major issue is how to improve the mobility of charge carrier in the films.

Thin films of organic semiconductor films have been deposited by two methods: vacuum deposition and solution processing. In the case of vapor deposition, the organic semiconductor is vaporized under a vacuum and allowed to condense onto a substrate to form a film. For solution deposition, the molecular semiconductor is dissolved in an organic solvent. The solution is then coated onto the substrate by either drop-casting, spin-coating, dip-coating, or printing. Vacuum deposition is commonly used to fabricate organic semiconductor thin films in organic electronic devices. It has the advantages of providing control of the layer thickness, and the cleaning of the environment and substrate. Solution processing is a relatively fast and low-priced method of fabricating thin molecular films. Vacuum sublimed organic thin films have better structure ordering, smooth morphology and the intrinsic material properties.

In addition, the combination of different type of organic molecules is required in some devices such as organic solar cell or organic light emitting diodes, where the interface of two organic molecular layers (organic-organic heterojunction) plays an important role. Therefore, a complete learning of organic-organic interface is highly desired for effectiveness of these devices. Because entirely diverse nature of organic molecular semiconductor than inorganic ones, the energy level alignment and electrical conduction properties must have different mechanism in these organic heterojunction interfaces.

This thesis deals with the growth and characterization of mononuclear CoPc and FePc films as well as binuclear (Fe-Co)Pc films on various substrates *viz.* (001) $SrTiO_3$, (0001) sapphire, (100) $LaAlO_3$, ITO coated glass and quartz, using molecular beam epitaxy (MBE). In addition, heterojuntions comprising of n-type $F_{16}CuPc$ and p-type CoPc were deposited. Thin films of water soluble phthalocyanine (CuPcTs) were also prepared using solution process techniques. Structure and morphology of the MPc films were found to depend on chemical nature of substrate and various other growth parameters. The growth mode of large planar molecules is governed by a competition between “molecule-molecule” and “molecule-substrate” interactions. If the molecule-substrate interaction is dominant then molecules arrange in the *face-on* stacking mode, otherwise the stacking mode will be *edge-on.* We have found that the mobility of binuclear (Co-Fe)Pc films is 110 cm^2/Vs, which is higher by nearly two orders of magnitude as compared to the individual CoPc or FePc films. The charge transport studies carried on CoPc films grown on (001) $SrTiO_3$ revealed a unique temperature dependent metal-to-insulator like transition. The solution processed Pc films as well as binuclear (Co-Fe)Pc films were investigated for their gas sensing applications.

This thesis is planned in the following six chapters.

Chapter 1: Introduction

This chapter gives an overview of the molecular semiconductor and compares their electronic structure and properties with inorganic semiconductor. A review on molecular semiconductor growth is summarized. The electronic structure and optical properties together with its advantage over other molecular semiconductor are discussed. Finally, the scope of this thesis is presented.

Chapter 2: Experimental techniques

A general outline of different experimental techniques and instrumentations used in the present thesis work has been elaborated in this Chapter. The details of the MBE system (RIBER system model no EVA 32), used for the deposition of the phthalocyanine films and heterojunctions, is described. Brief descriptions of various characterization techniques, such as scanning electron microscope (SEM), atomic force microscopy (AFM), X-ray photoelectron spectroscopy (XPS), Fourier transformation infrared spectroscopy (FTIR), UV-visible spectroscopy (UV-vis), grazing angle X-ray spectroscopy (GIXRD), low temperature transport measurement system etc. are discussed. A detailed description of the Kelvin Probe method and gas sensing set up used in the present work are also described.

Chapter 3: Growth and conduction mechanism in mononuclear and binuclear phthalocyanine films

In this chapter, we discuss the growth of mononuclear CoPc, FePc and binuclear (Co-Fe)Pc films by MBE. Binuclear (Co-Fe)Pc films were found to grown only on sapphire substrates at 200°C if deposited using the CoPc/FePc mixture in 1:1 (w/w) ratio. Formation of binuclear was confirmed by MALDI (Multi Assisted Laser Desorption and Ionization) mass spectroscopy. Binuclear films have better *face-on* and edge-on overlapping compare to individual CoPc and FePc films. Better face-on stacking was also supported by GIXRD. The in binuclear (Co-Fe)Pc films exhibited μ ~110 cm^2/Vs. Furthermore temperature dependence of resistivity showed that binuclear films are in metallic regime, while CoPc and FePc films are in the critical regime of metal–insulator transition. These films exhibited trap-free space charge limited conduction (SCLC) in the temperature range 300K to 25K; while Copc and FePc films showed SCLC with exponential distribution of traps at low temperature.

Charge conduction in FePc films under high electrical field (i.e. upto 20MV/m) has been investigated. A bias dependent transition from ohmic to space-charge limited conduction to space charge limited conduction with field enhanced mobility is observed. At temperatures <100 K, by analyzing the low bias (< 100 V) data, which is governed by Schottky – barrier limited conduction. However at higher bias multistep tunnelling was observed in the FePc films.

A novel feature i.e. temperature dependent metal to insulator like transition, has been observed in ultrathin CoPc films deposited on (001) $SrTiO_3$ substrates. In-plane compressive strains induced by structural phase transition of $SrTiO_3$ substrate reduce the intermolecular distance, and as a result, metallic behavior is observed. In the low temperature metallic phase the charge transport occurs via field assisted tunnelling process.

Chapter 4: Phthalocyanine based heterojunctions

In this chapter we discuss growth of phthalocyanine based heterojunction comprising of *p*-type CoPc and *n*-type $F_{16}CuPc$ using MBE. The *J-V* characteristic of heterojunction shows ohmic conductance with two order of magnitude higher conductivity as compare to individual CoPc and $F_{16}CuPc$ films. The higher conductivity $F_{16}CuPc$/CoPc heterojunction is due to the charge carrier accumulation at interface, which is further confirmed by Kelvin probe study. The thickness of charge carrier accumulation is found to be 20 nm. This heterojunction showed reverse rectification behavior. No band-bending and charge carrier accumulation were found in CoPc/FePc (*p-p* type) heterojunction.

Chapter 5: Gas sensing using mononuclear and binuclear phthalocyanine films

In this chapter, we describe gas sensing behavior of water soluble copper phthalocyanine (CuPcTs) films prepared by solution process. These films exhibited room temperature sensitivity towards Cl_2 gas. Selectivity, repeatability, stability and linearity (sensitivity vs concentration) in the range 5ppb to 2000ppb are investigated. The chemical adsorption process of Cl_2 on CuPcTs has been analyzed using Elovich equation, which provides an alternative way of qualifying Cl_2 concentration from response rate of sensor. A comparison study of the gas sensing characteristics CoPc, FePc and binuclear (Co-Fe)Pc films has been studied. It has been found that binuclear films are better for gas sensing because of their high mobility.

Chapter 6: Summary and conclusions

The summary of the thesis work and main conclusions along with the future perspectives have been presented in this chapter. The main results obtain in the course of this thesis work are as follows.

- Morphology of metal phthalocyanine (CoPc and F_{16}CuPc) thin films grown by MBE strongly depends on substrate. However, in solution process technique the morphology is independent of substrate as they usually have amorphous character.

- A huge improvement of mobility (110 cm^2/Vs) in binuclear films, deposited on single crystal sapphire substrate has been demonstrated, which is attributed to the improved *face-on* as well as *edge-on* stacking of the binuclear (Co-Fe)Pc molecules.
- Charge transport studies in FePc films under high electrical fields in the temperature range 300-100 K revealed a bias dependent transition from "ohmic" to "shallow-trap mediated SCLC" to "SCLC with field enhanced mobility". Below 100K the transport is found to be dominated by contact limited process.
- CoPc films prepared deposited on $SrTiO_3$ substrates exhibited a temperature dependent metal-to-insulator transition, which was attributed to the compressive strains induced by cubic to tetragonal structural phase transition of $SrTiO_3$ substrate.
- In $F_{16}CuPc$/CoPc heterostructure ohmic conduction was observed due to very high free carrier density ($\sim 10^{17}/cm^3$) in the temperature range 300-30K. Accumulation layer width was found to be 20 nm using Kelvin Probe method. The temperature dependence of resistivity shows these films are in metallic side of critical regime.
- Room temperature ppb level Cl_2 gas sensing of CuPcTs thin film has been demonstrated. It has been shown that the sensors exhibit linear variation of sensitivity with concentration in the range 5 ppb to 2000 ppb. High mobility binuclear (Co-Fe)Pc films exhibited higher sensitivity as compared to the individual FePc or CoPc films.

List of Publications

In Journals

1. Enhanced Cl_2 sensitivity of ultrathin bi-nuclear cobalt-phthalocyanine/iron-phthalocyanine films,

   Arvind Kumar, A. K. Debnath, S. Samanta, A. Singh, R. Prasad, S. Singh, S. Basu, D. K. Aswal, S. K. Gupta,

   Sensors and Actuators B 171, 423 (2012).

2. Fluorinated copper-phthalocyanine / cobalt-phthalocyaine organic heterojunctions: Charge transport and Kelvin Probe study,

   A. K. Debnath, **Arvind Kumar**, S. Samanta, R. Prasad, A. Singh, S. Singh, S. Basu, D. K. Aswal, S. K. Gupta**,**

   Appl. Phys. Lett. **100, 142104 (2012).**

3. Metal – semiconductor transition in ultrathin cobalt-phthalocyanine films grown on $SrTiO_3$ single crystal substrates,

   S. Samanta, **Arvind Kumar**, A. Singh, A. K. Debnath, S. Basu, R. Prasad, D. K. Aswal, S. K. Gupta and J.V. Yakmi,

   Appl. Phys. Lett. **100**, **162101 (2012).**

4. Metallic-like conduction in Co-phthalocyanine/Fe-phthalocyanine composite films grown on sapphire substrates,

   Arvind Kumar, Ajay Singh, S. Samanta, A. K. Debnath, D. K. Aswal, and S. K. Gupta,

   Appl. Phys. Lett**. 99, 112102 (2011).**

5. Charge transport in ultrathin iron-phthalocyanine thin films under high electric fields, **Arvind Kumar**, Ajay Singh, Soumen Samanta, K. Vasundhara, A. K. Debnath, D. K. Aswal, S. K. Gupta and J. V. Yakhmi,

   J. Phys.: Condens. Matter, **23, 355801 (2011).**

6. Room temperature ppb level Cl_2 sensing using sulphonated copper phthalocyanine films **Arvind Kumar**, Ajay Singh, A.K. Debnath, Soumen Samanta, D.K. Aswal, S.K. Gupta, J.V. Yakhmi,

   Talanta, **82, 1485 (2010).**

7. Role of central metal atom and chemisorbed oxygen in gas sensing mechanism for cobalt-phthalocyanine thin films

   Arvind Kumar, Ajay Singh, A.K. Debnath, Soumen Samanta, D.K. Aswal, S.K. Gupta,

   Asian Journal of Physics**, 19, 207 (2010).**

In Conference/Symposia

1. Charge transport and Kelvin probe study of organic semiconductor heterojunction,

   Arvind Kumar, S. Samanta, A. Singh, A. K. Debnath, D. K. Aswal and S.K. Gupta,

   AIP Conference Proceedings of TFST(Thin Film: Science and technology), 2011 (to be published).

2. Trap free space charge limited conduction and high mobility in cobalt phthalocyanine - iron phthalocyanine composite thin films,

   Arvind Kumar, S. Samanta, Ajay Singh, A. K. Debnath, D. K. Aswal and S.K. Gupta,

   Advances of material sciences and technology-2012 Gujarat University, (to be published in Solid State Phenomena).

3. Reverse rectification behavior in NiPc/F$_{16}$CuPc heterojucntion,

   Arvind Kumar, Soumen Samanta, Ajay Singh, A. K. Debnath, D. K. Aswal and S.K. Gupta,

   AIP Conference Proceedings 56th DAE solid state physics symposium-2011, SRM university Chennai, 1447, 755 (2012).

4. Mechanism of charge transport in cobalt and iron phthalocyanine thin films grown by molecular beam epitaxy,

   Arvind Kumar, Soumen Samanta, Ajay Singh, A. K. Debnath, D. K. Aswal and S.K. Gupta,

   AIP Conference Proceedings of International Conference on Advances in Condensed and Nano Materials-2011-Chandigarh,1393, 15 (2011).

5. Temperature dependent current-voltage characteristics of iron-phthalocyainthine films, A. K. Debnath,

   A. Kumar, S. Samanta, A. Singh, D. K. Aswal, S. K. Gupta, J. V. Yakhmi,

   AIP Conference Proceedings of 55th DAE solid state physics symposium 1349 1047-1048 (2010).

6. Electrical and positron study of the interface of organic semiconductor heterojunction, Adrica Kyndiah, **Arvind Kumar**, S. Samanta, Ajay Singh, A. K. Debnath, J. V. Yakhmi, Priya Maheshwari, and P. K. Pujari,

   AIP Conference Proceedings of International Conference on Physics of Emerging Functional Materials (PEFM-2010) 1313, 409-411 (2010).

LIST OF FIGURES

Figure 3.50 Log-log plots showing *J*-*V* characteristics of CoPc films in the temperature range 80- 40 K. Inset shows the plot of conductivity as a function of inverse of the square-root of electric field at different temperatures.

Figure 3.51 Log-log plots showing *J*-*V* characteristics of 20 nm F_{16}CuPc films in the temperature range 300 - 160 K.

Figure 3.52 Log-log plots showing *J*-*V* characteristics of CuPcTs films on quartz substrate in the temperature range 300 - 260 K.

Figure 3.53 (a) The temperature dependence of resistivity (b) Plots of reduced activation energy W for CoPc, (c) Linear fit of conductivity versus $T^{3/2}$ data for)Co-Fe)Pc films.

Figure 3.54 Log-log plots showing *J*-*V* characteristics of 20 nm (Co-Fe)Pc films on in the temperature range 300 - 25 K.

Figure 3.55 J versus $V^{1/2}$ data (at 25K at low bias, with estimated barrier height of 0.052 eV) indicates Schottky-barrier limited conduction.

Figure 3.56 Work function images (size 5mm x 5 mm) of CoPc, FePc and binuclear (Co-Fe)Pc films.

Figure 3.57 (a) Temperature dependence of mobility (μ) and (b) Linear fit of μ Vs $T^{3/2}$ for binuclear (Co-Fe)Pc films.

Figure 3.58 *J*-*V* characteristics of 20 nm CoPc films on SiO_2, MgO and $LaGdO_3$ substrate.

Figure 4.1 Different types of organic semiconductor heterojunction (a) depletion heterojunction (b) accumulation heterojunction (c) electron accumulation/depletion heterojunction (d) hole accumulated/depletion heterojunction.

Figure 4.2 100nm×100 nm AFM images (a) 20 nm F_{16}CuPc film on $LaAlO_3$ substrate and (b) top surface of F_{16}CuPc(20nm)/CoPc(20nm) heterojunction films.

Figure 5.10 (a) Comparison of the response for FePc, CoPc and binuclear (Co-Fe)Pc films at 500 ppb for Cl_2 exposure (b) Comparison of Sensitivity for all films at 500 ppb of Cl_2 gas exposure. Inset bar chart showing the sensitivity of the binuclear (Co-Fe)Pc films for various oxidizing gases.

Figure 5.11 (a) Demonstration of the reproducibility (at 5ppb of Cl_2) and base conductance drift for binuclear (Co-Fe)Pc films. (b) Work function imaging of the fresh and Cl_2 exposed binuclear (Co-Fe)Pc films and (c) Shift in Fermi level after the exposure of Cl_2 gas.

LIST OF TABLES

CHAPTER-1

INTRODUCTION

1.1 Organic molecular semiconductors

Organic semiconductors are organic materials that exhibit semiconductor properties. Generally almost all organic solids are insulators. However, when their constituent molecules have π-conjugate systems and they are appropriately doped, charge carriers (electrons or holes) can move via π-electron cloud overlaps, especially by hopping, tunnelling and related mechanisms. Organic semiconductors can be classified into two major classes: (i) molecular semiconductors e.g. single molecules (polycyclic aromatic compounds, such as, pentacene, rubrene, anthracene, porphyrine, phthalocyanines etc) and oligomers (short chain i.e. having few monomers) and (ii) conjugated polymers: which consist of many monomers bonded together in a long chain e.g. poly(3-alkylthiophene), poly(p-phenylene vinylene), polyfluorene etc. Typical examples of both types of organic semiconductors are given in Fig. 1.1. In polymers, the number of repetition unit is indeterminate, thus they can have a variable molecular mass. On the other hand, molecular semiconductors have a well defined molecular weight. However, π-conjugation i.e. the arrangement of carbon atoms in a series of alternating single and double bonds is the common characteristic of both the classes. While polymers form disordered phases, small molecules frequently show ordered, crystalline structures. These materials exhibit a strong anisotropy in their optical and transport properties perpendicular and parallel to the molecular plane. Molecular semiconductors in general have high vapour pressures and are poorly soluble in different solvents. Therefore, the films of molecular semiconductors are usually deposited from the gas phase by sublimation or evaporation. On the other hand, conducting polymer being soluble, their films can be easily formed using cost effect solution process techniques such as spin-coating or printing techniques. However, the major advantage of molecular films with respect to the polymer films is that they can be grown with very high purity and crystalline order, which are the two major requirements for obtaining high charge carrier mobility.

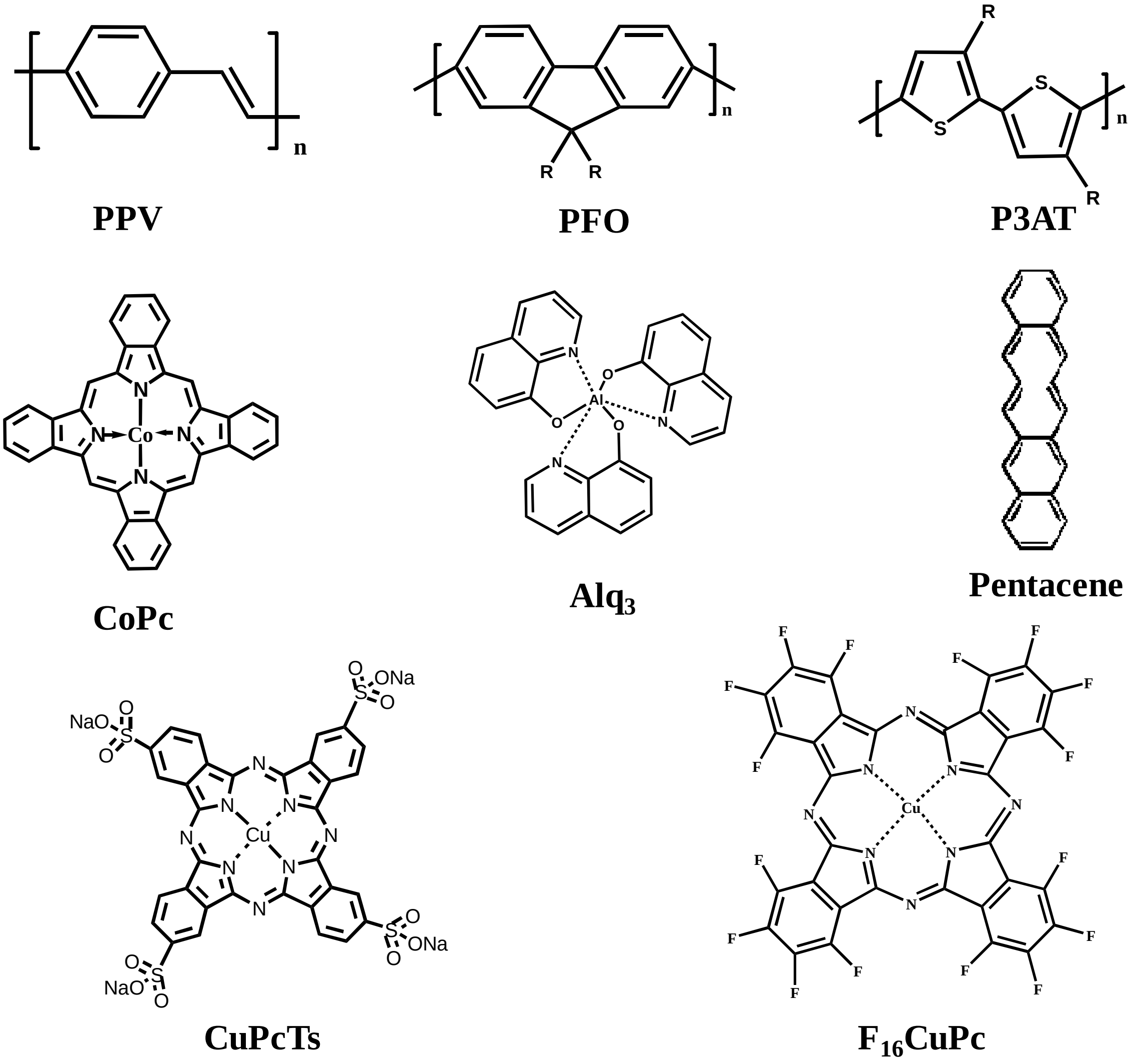

Figure 1.1 Molecular structures of conducting polymers: PPV: poly(p-phenylenevinylene), PFO: polyfluorene, P3AT: poly(3-alkylthiophene), Alq_3: tris(8-hydroxyquinoline)aluminium, CoPc: Co-phthalocyanine, pentacene, CuPcTs: copper phthalocyanine tetrasulfonate and F_{16}CuPc: Copper hexadecafluorophthalocyanine.

Characteristics of molecular semiconductors are the intramolecular bonds. The alternation of single (σ) and double (π) bonds, referred to as conjugation, is responsible for semiconductor nature of organic molecular. In a conjugated system, the carbon atoms involved in the conjugation are sp^2 hybridized (the 2*s* orbital is mixed with only two of the three available 2*p* orbitals) which means the three hybrid sp^2 orbitals form the σ bonds, with the σ-electrons being highly localized, leaving the p_z orbital unaltered. The mutual overlap between remaining non hybridized p_z orbitals of adjacent carbons leads to the formation of π bonds. The electrons of overlapping p_z orbitals form a delocalized electronic orbital over the whole conjugation length. These π electrons are delocalized over the whole molecule and are more loosely bound compared to the σ electrons These delocalized electrons responsible for semiconducting properties of this class of materials. As an example this is illustrated in Fig. 1.2 for benzene molecule.

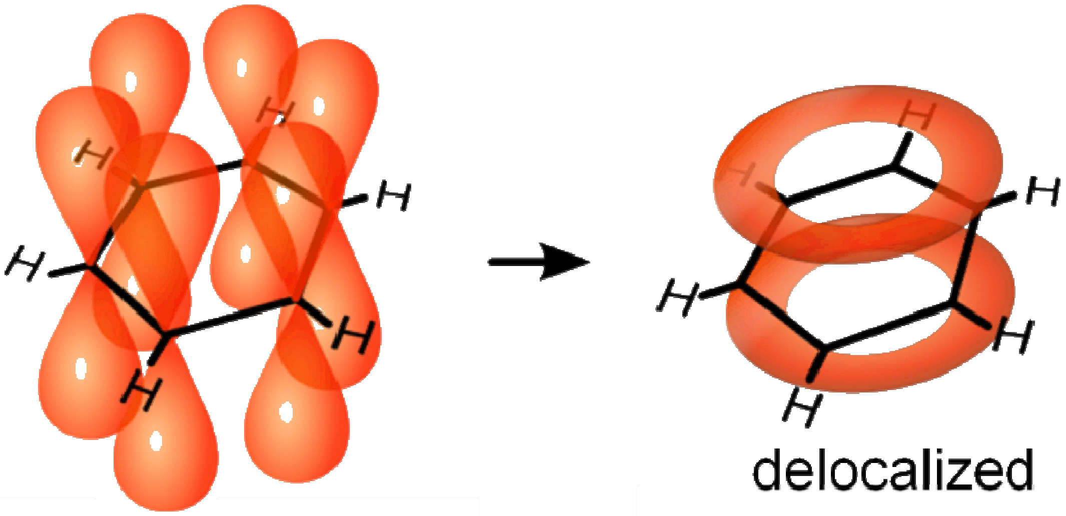

Figure 1.2 Schematics representation of π-orbitals in benzene (C_6H_6) molecule, responsible of its semiconducting nature. In the solid the overlap between π -orbitals of adjacent molecule will allow the charge transport through the solid.

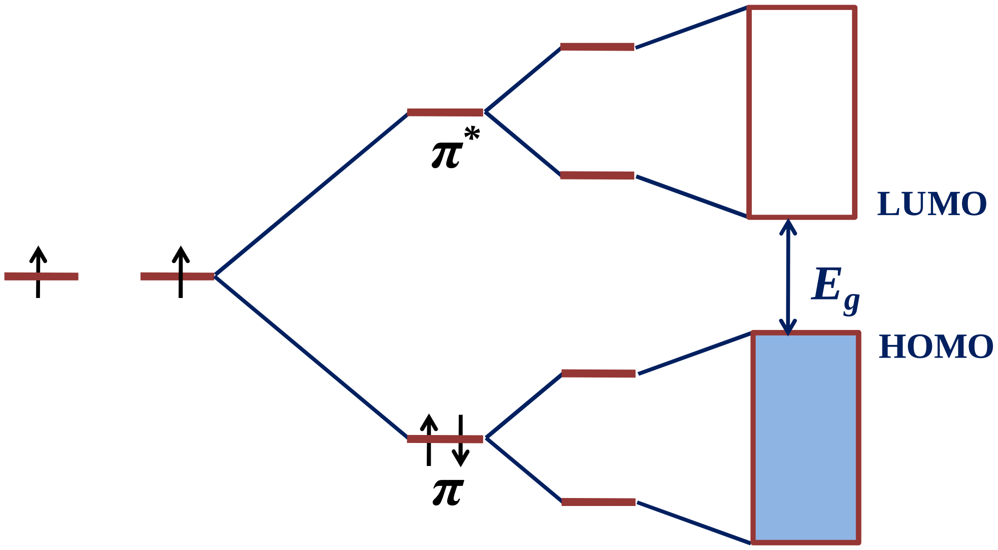

Figure 1.3 Schematic representation of the splitting of the energy levels of a molecules due to the interactions in the π-orbitals of a molecules leads to the formation of highest occupied molecular orbital (HOMO) and lowest unoccupied molecular orbital (LUMO) energy bands. Molecular interaction in the solid leads to the further splitting of molecular orbitals.

Due to the interactions of π electrons, the π molecular orbital splits into a bonding (π) and anti-bonding (π^*) molecular orbital, according to the Pauli exclusion principle as depicted in Fig. 1.3. The two electrons occupy the highest occupied molecular orbital (HOMO), while the letter remains empty and called lowest unoccupied molecular orbital (LUMO). The extended series of overlapping of *p* orbitals and the delocalization of electrons over the entire molecule leads to the further splitting of HOMO and LUMO resulting formation of band which is shown in Fig. 1.3. Intermolecular interactions in the solid lead also additional splitting. The HOMO and LUMO for organic semiconductors are analogous to the valence and conduction bands of the conventional inorganic semiconductor. Optical and thermal excitation can promote an electron to an unoccupied level. Thus the energy band gap for organic semiconductor corresponds to the gap between HOMO and LUMO of the molecule. The HOMO-LUMO separation in these conjugated molecules depends strongly on the overlapping of neighbouring *p* orbitals, which is in turn related to the planarity of the molecule and to side groups. In many cases, the HOMO-LUMO energy gap is relatively small (~ 1 to 3 eV) and the molecules can be doped to assume *n*- or *p*-type character. Thus, the π-conjugated molecules can act as semiconducting channels in organic molecular devices. However the band formation is not sufficient for organic molecular material to behave as semiconductor, there must be a mechanism of charge carrier transport between molecules. This is achieved due to the overlap of the *π-orbitals* from one molecule to those of its neighbouring molecule. Therefore a close packing of molecule and a crystalline structure of free of defects is essential to maximize the *π-orbital* overlap and thus improve the conduction properties of the material. The low molecular symmetry leads to highly anisotropic conduction parameters since the effective path for charge carrier transport is perpendicular to molecular plane, direction of maximum π-overlap [1]. Thus, parameters like the charge carrier mobility must be described by a mobility tensor μ_{ij} [2, 3]. In general, all physical properties of these materials may present anisotropic behaviour due to low symmetry of molecular constituents and the low-symmetry crystalline structure they form.

During past few decades, organic semiconductors have attracted significant and increasing interest due to their interesting electrical and optical properties. Their applications in flexible and low cost, and tuning possibilities in the manufacturing electronic devices make them suitable candidates for future electronic devices [4-7]. Moreover, organic molecules are potential candidate for pushing the existing scaling limits of the existing silicon based microelectronics to nanoscale [8-10]. The advantages offered by the organic molecules to be used in the nanoscale devices are: (i) small size (typically 0.5 to 2.5 nm), (ii) easy tuning of electronic properties by changing chemical structure of the molecule, and (iii) possibility of forming self–assembled monolayer on various substrates (e. g. thiols on Au, silanes on Si) . In recent years, various nanoelectronics molecular devices, such as, rectifiers, memory, resonant tunnel diodes and transistors have been demonstrated using two-dimensional ordered molecular monolayers and multilayers [11-13]. The interest in electrical properties of organic monolayers has developed enormous academic interest in this field [14-18]. Similarly, thin and thick films of various organic semiconductors are actively being investigated from the view point of understanding the physics underlying the charge transport as well as their applicability in new electronic applications e.g. flexible and low cost large area electronics, which is difficult to achieve using inorganic semiconductors. This research field is growing very fast. At present researchers are able to manage the material properties at the molecular level [19]. Moreover, many efforts are being made in the industrial development of the organic electronic devices. Many applications of organic semiconductors have been already demonstrated and some of them are commercially available in market. These include: mobile phones display based on organic field effect transistor (OFET) by Philips and Polymer Vision, automobile stereo display from Pioneer, organic light emitting devices (OLEDs) from Philips and full color displays Kodak digital cameras. On the development of organic electronics, Forest has commented: "*If the field continues to progress at its current, rapid pace, electronics based on organic thin-films materials will soon become a mainstay of our technological existence*" [20]. However, despite of these developments, organic devices have limitation in terms of their low charge carrier mobility (0.001-10 cm^2 /Vs) [16, 21, 22], which is several orders of magnitude lower than traditional inorganic semiconductor (e.g. Silicon 1400 cm^2 /Vs). In order to improve the performance of organics devices, it is necessary that their mobility need to be increased.

1.2 Phthalocyanines

The word Phthalocyanine is derived from the Greek term 'naphtha' (rock oil) and 'cyanine' (dark blue). The first phthalocyanine was produced accidentally in 1907 by Braun and Tcherniac as a minor product in the synthesis of o-cyanobenzamide from phthalamide and acetic anhydride [23]. C. E. Dent et al. reported the structure of the planar phthalocyanine molecule for the first time [24]. Phthalocyanines are an intensely blue-green coloured macrocyclic compound and traditionally have been used as dyes or pigments. Phthalocyanines form coordination complexes with most elements of the periodic table and exhibit semiconducting properties. Therefore they are currently being explored for their possible applications in the organic electronics. Majority of the research has been carried out on the mononuclear phthalocyanines i.e. molecule containing only one metal atom. However, phthalocyanines can form dimmers, in which two mononuclear phtahlocyanine (with similar or different metal atoms) units are covalently linked. Here we briefly overview the structural properties of mononuclear as well as binuclear phthalocyanines.

1.2.1 Mononuclear phthalocyanine

The metal-free phthalocyanine (H_2Pc) has the general formula $C_{32}H_{18}N_8$. It is chemically designated as 5, 10, 15**,** 20 tetraazatetrabenzporphyrin or tetrabenzporphyrazin

[25]. The molecule is planar consisting of four isoindole molecules linked together at the corners of the pyrrole ring by four nitrogen atoms as shown in Fig. 1.4.

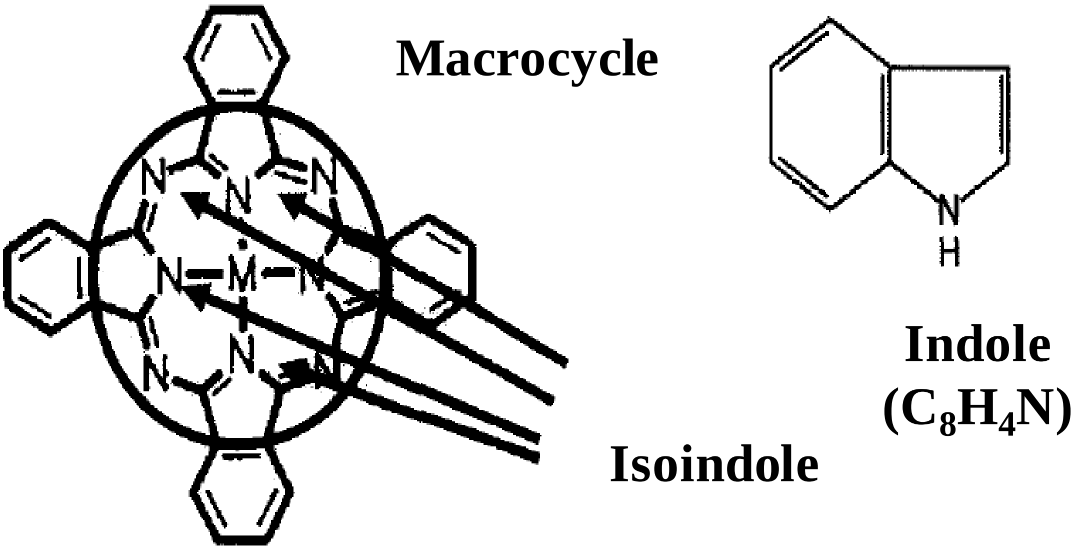

Figure 1.4 Molecular structure of metal phthalocyanine (MPc).

The space within the four central nitrogen atoms is occupied either by hydrogen atoms in the case of H_2Pc or by a metal atom in metal substituted phthalocyanines (MPc). In the simple metal phthalocyanines, such as CoPc, the two central hydrogen atoms are replaced by a single metal atom. MPc offer many interesting properties, including:

(i) Pc's are easily sublimed and can be crystallized with very high purity (10^{14} -10^{15} traps cm^{-3}) exceptional in organic chemistry.

(ii) Pc's show an exceptional thermal and chemical stability. In air MPc's undergo no noticeable degradation up to temperature 400 - 500°C and in vacuum most of them do not decompose below 900°C. They are not also affected by strong acids or bases [25, 26].

(iii) Pc's is highly conjugated molecule and contains 18 π electrons in the macrocyclic ring which leads to very intense absorption bands at around 400 nm and 700 nm.

(iv) Pc's are a very versatile system as there are possibilities of tuning its electronic properties by playing with different side group and central metal atoms. There are more than thousand different Pc's have been synthesized by changing either central metal atom or side groups. The replacement of central metal atom and side group modifies its electronic properties, while its molecular structure, in most of the cases, remains unchanged [25, 26]. For example CuPc is a *p*-type molecular semiconductor but the replacement of 16 hydrogen by fluorine makes the molecule ($F_{16}CuPc$) *n*-type. In fact, $F_{16}CuPc$ is one of the most stable *n*-type organic semiconductor known at present, and it has been used to fabricate the first *n*-channel organic transistor [27], and in complementary logic circuits [28, 29].

Due to the above properties, metal phthalocyanines have been intensely investigated for various organic devices, such as solar cells, OLEDs, OFETs and gas sensors [30-35].

Phthalocyanines appear in various crystalline forms due to different growth conditions or methods; this is called polymorphism which is purely a consequence of different pickings in the unit cells. The most common polymorphs of phthalocyanines are the α and β phases, as shown in Fig. 1.5. These two phases differ in the tilt angle of the molecular stack from the b-axis, which is 26.11° for α-phase and 44.81° for β-phase [36-38] . The growth of α-form is obtained in thin films when the substrate temperature is maintained below a phase transition temperature during growth [39]. As shown in Fig.1.6, the α and β phases are formed by quasi-orthorhombic [40] and monoclinic [36] unit cells, respectively.

The unit cell parameters of different phthalocyanines are listed in Table 1.1. Besides the α and β phases, γ ,δ, and χ phases were also observed on rare occasions [37].

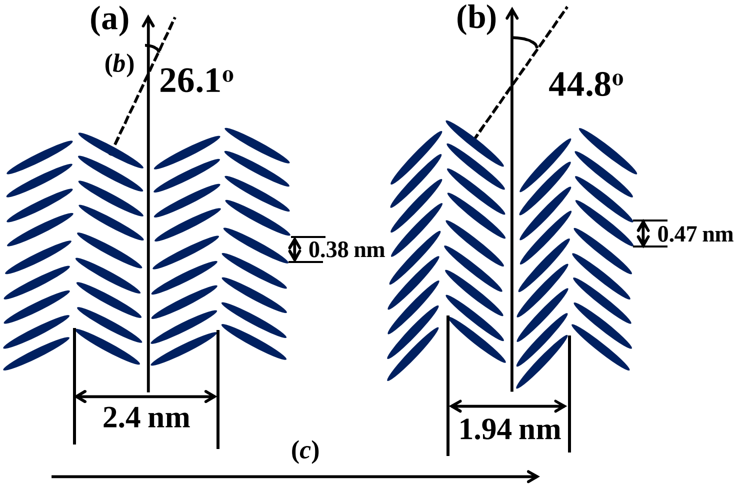

Figure 1.5 Schematics of crystalline (a) α-FePc (b) and β-FePc.

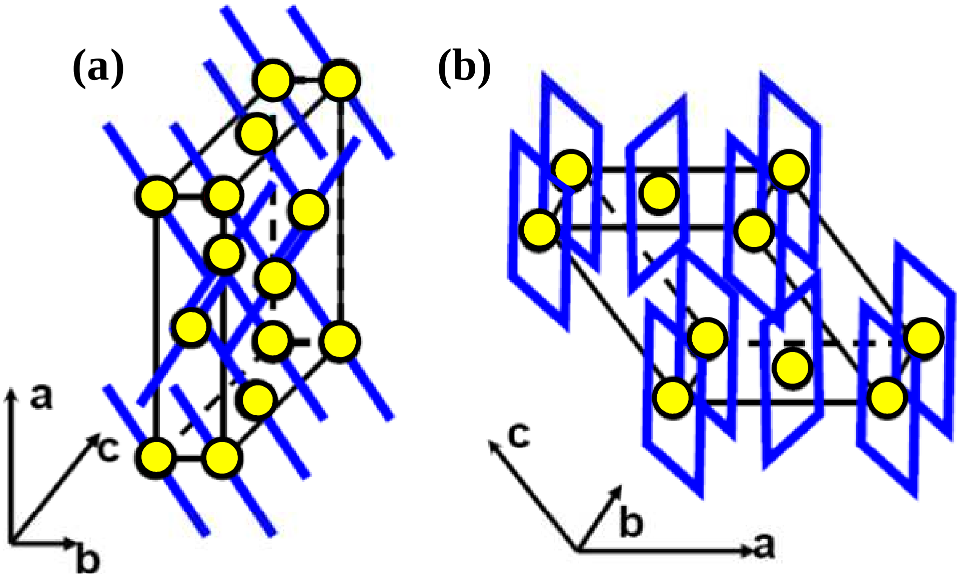

Figure 1.6 The schematic representation of a metal-phthalocyanine unit cell structure for (a) the *α-phase* and (b) the *β-phase*. The yellow circles show the centre atoms and the blue lines or blue planes are phthalocyanine rings.

Table 1.1

Unit cell parameters for various phthalocyanines

	H_2Pc [41]	**β-CuPc** [36]	**$F_{16}CuPc$** [42]	**α-FePc** [43]	**β-FePc** [25]	**α-CoPc** [43]	**β-CoPc** [44]
M	514.55	575.67	863.9	568.38	568.38	571.47	571.47
a(Å)	19.85	19.407	20.018	25.5	19.39	25.88	19.35
b(Å)	4.72	4.79	5.106	3.79	4.79	3.75	4.77
c(Å)	14.8	14.628	15.326	25.2	14.6	24.08	14.54
β	120.25°	120.56°	111.83°	90.4°	120.85°	90.2°	120.82°
Z	2	2	2	2	2	2	2

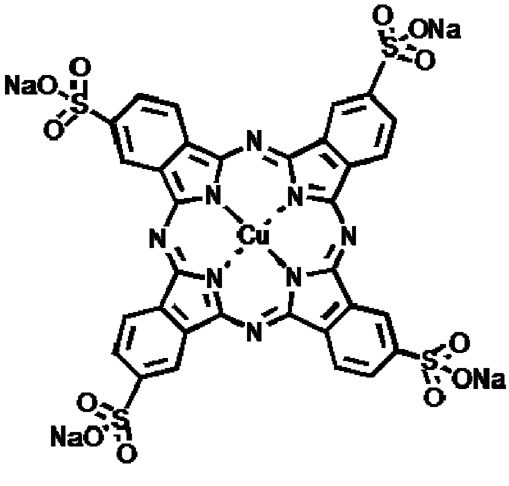

Figure 1.7 Molecular structure of water soluble CuPcTs.

Phthalocyanines are usually difficult to dissolve in common solvent (de-ionized water, ethanol, methanol etc.). For large scale device applications mainly in the form of micro electromachined devices (MEMs) or electronic nose as well as cost effective disposable sensors, it is necessary to manufacture the sensors by simpler technique such as solution spinning, printing, micro-drop coating, etc. Water soluble phthalocyanine can also be synthesized from non-substituted phthalocyanines by attaching sulfonate groups [45]. A typical example of water-soluble phthalocyanines is copper (II) phthalocyanine tetrasulfonic acid, tetrasodium salt (CuPcTs), and its structure is shown in Fig. 1.7. The structure of CuPcTs is very similar to CuPc except that polar SO_3Na attached to the corners of benzene rings and makes this compound water soluble [45]. These water soluble phthalocyanines have been used as FET and gas sensors [46, 47].

1.2.2 Binuclear phthalocyanine

Binuclear phthalocyanine, in which two mononuclear phtahlocyanine units are covalently linked, have been chemically synthesized [48]. The two phtalocyanine units of binuclear molecules can be either coplanar or co-facial, as shown in Fig. 1.8. From the view point of electronic applications, the coplanar molecules are useful, as they have extended conjugation. Large π electron conjugation can enhance the π- π stacking, and therefore, one can achieve improved molecular ordering, high charge carrier mobility and better device characteristics. Chemically, the synthesis of binuclear phthalocyanine is usually carried out from two phthalogens of different structures, however the yield of reactions are usually very low [48, 49]. Due to this limitation, investigation and practical applications of binuclear pthalocyanines have been very limited [50, 51]. In co-planar binuclear phthalocyanine, the linkage of pthalocyanine rings depends on the nature of chemical reaction e.g. they can share a common benzene ring, as shown in Fig. 1.8 (a), two rings can form direct covalent bonds or additional moieties can be used to join two rings. In Fig. 1.8 (a), the binuclear molecule lacks a benzene ring this is referred to as the (-1) linked binuclear phthalocyanine [52]. This type of binuclear phthalocyanine has been used for electrochemical sensors [53]. There are some reports where the monolayer/multilayers of binuclear phthalocyanine have been prepared using Langmuir-Blodgett (LB) technique or by drop casting method [50, 51]. In these studies, first the synthesis of precursor binuclear phthalocyanine was carried out and then films were prepared by LB technique. However there are no reports on the growth of binuclear phthalocyanine films using physical vapor deposition.

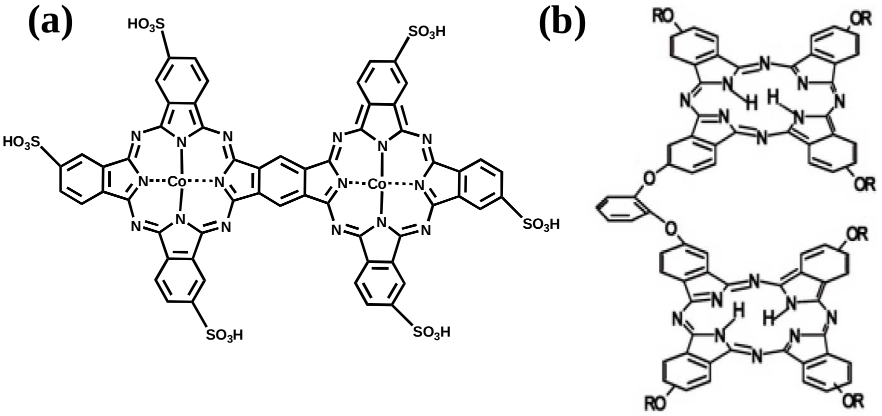

Figure 1.8 Chemical structure of (a) coplanar and (b) co-facial binuclear phthalocyanine molecules.

1.3 Growth modes of molecular semiconductor thin films

Thin films of molecular semiconductors are essential for the investigation of their charge transport properties as well as fabrication of electronic devices. It is therefore important to understand the modes by which molecular films grown on different substrates. In the case of metal and inorganic-semiconductors film growth mechanisms are well-established. However, there is hardly any understanding on the growth mechanisms of organic films. In general, metal and inorganic-semiconductors films grow on different substrates by three different modes, which depends on the relative surface energy between substrate and films as well as on the lattice mismatch [i.e. (a_s - a_f)/a_f, where a_s and a_f are, respectively, lattice parameter of the substrate and the film]:

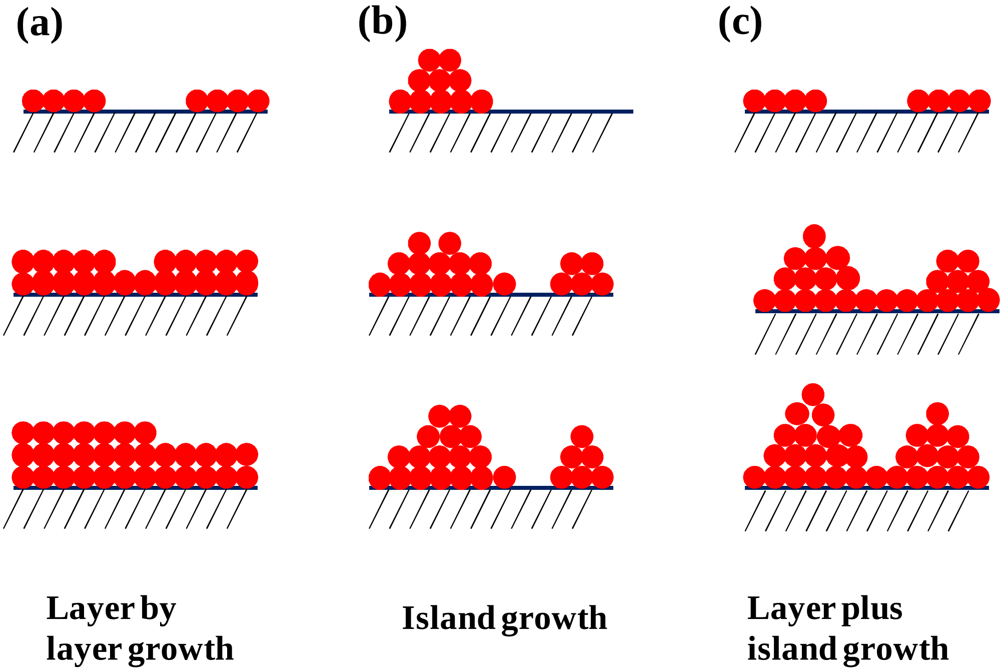

Figure 1.9 Schematic representations of three different growth modes of thin films (a) Frank-van der Merwe mode, (b) Volmer–Weber mode (c) Stranski– Krastanov mode.

(i) *Frank-van der Merwe mode:* In this mode layer-by-layer growth occurs if the interaction between the substrate and film atoms is stronger than that between neighboring films atoms the lattice mismatch is zero, as shown in Fig. 1.9 (a). Each new layer starts to grow only when the last one has been completed.

(ii) *Volmer–Weber mode:* In this mode the film grows in the form of separate 3D islands to minimize the overall surface energy, if the interaction between the neighboring films atoms stronger than the over layer substrate interaction, as shown in Fig. 1.9 (b).

(iii) *Stranski– Krastanov mode:* This layer-plus-island growth mode is an interesting intermediate case. In this mode one or sometimes several complete monolayers form first, followed by individual. This mixed growth mode occurs due to large lattice mismatch although interaction between the substrate and film atoms is stronger than that between neighboring films atoms, as shown in Fig. 1.9 (c).

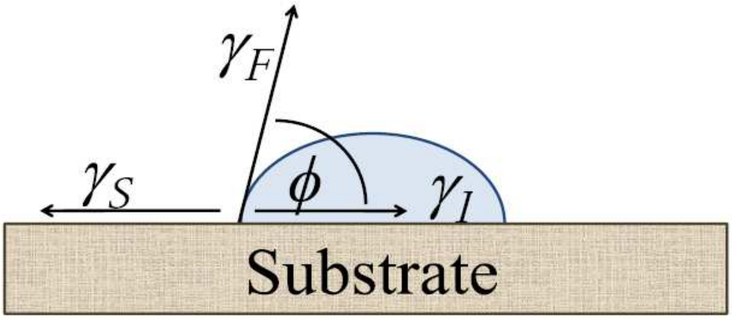

Figure 1.10 A simplified picture of an island formation: γ_S is the surface free energy of substrate, γ_F is the free energy of the film material and γ_I is the interface energy of the film-substrate

The above mentioned growth modes can be described using Young's equation that takes surface energies and interface energy into account, as schematically shown in Fig. 1.10. According to Young's equation, wetting angle of a liquid nucleus on substrate can be expressed as:

$$\gamma_S = \gamma_I + \gamma_F \cos \varphi$$

where γ_S is the surface free energy of substrate, γ_F is the free energy of the film material and γ_I is the interface energy of the film-substrate. Using the Young's equation the two limiting growth modes, layer by layer and island can be distinguished by the angle φ,

(i) layer growth : $\varphi = 0$, $\gamma_S > \gamma_I + \gamma_F$

(ii) island growth: $\varphi > 0$, $\gamma_S < \gamma_I + \gamma_F$

The layer-plus-island growth can easily be explained by assuming a lattice mismatch between deposited film and substrate. The lattice of the films tries to adjust to substrate lattice, but at the expense of elastic deformation energy. The transition from layer to island growth occurs when the spatial extent of the elastic strain field exceeds the range of adhesion forces within the deposited material.

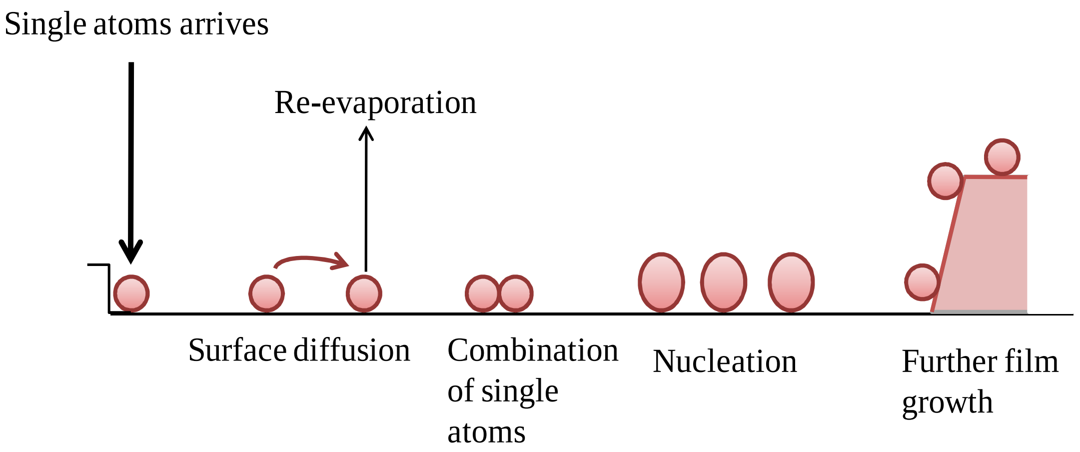

Figure 1.11 Schematics representation of initial stages of thin film formation by physical vapor deposition method.

In physical vapor deposition method, material is created in the gas phase (atomic or molecular form) by thermal, electron beam, sputtering, or laser ablation, which are then allowed to deposit on the surface of the substrate. The individual atomic processes occurring during the formation of a film on the surface of substrate that determine growth mode are illustrated in Fig. 1.11. The surface of the substrate is covered with large number of absorption sites and a molecule becomes bound to one of these with characteristics energy. The absorbed atoms do not remain stationary but may re-evaporate; requiring energy equal to adsorption energy, or it may diffuse or hop to adjacent sites. In all these process, characteristics activation energies have to be overcome. Other processes are collision and recombination. Each group of atoms eventually reaches a size that is more likely to grow than decay. The formation of such island of material is known as nucleation. The next stage of thin film formation is coalescence, in which individual island continue to grow by addition of more atoms, until they touch one another to form continuous network.

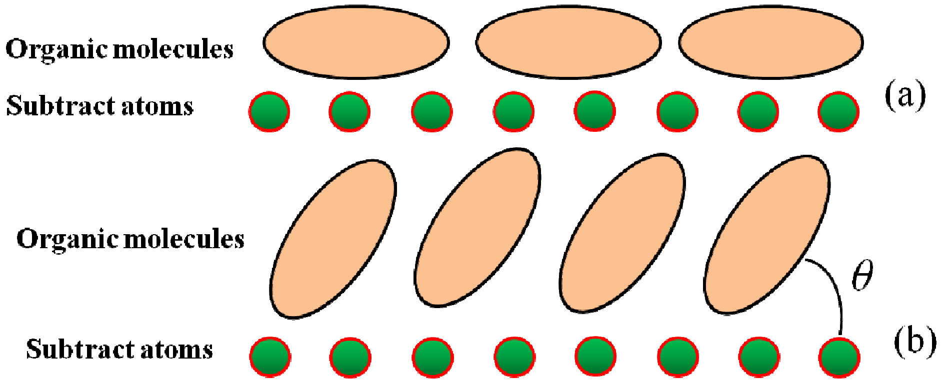

Figure 1.12 (a) Size effect of molecule or associated unit cell on inorganic substrate (lattice mismatch) (b) effect of orientational degree of freedom leads to additional source of disorder during the growth.

In case of organic semiconductors, thin film formation mechanism is more complex. Organic molecules have a particular geometrical shape with an inherent anisotropy that differs from the intrinsic isotropy of inorganic atoms. Molecules are composed of covalent bonds between neighboring atoms and molecule-molecule interactions are usually weak van der Waals forces [54]. In addition, the chemical interaction between molecule and substrate can strongly influence the growth mode. Therefore, growth modes of molecular films are quite complicated. Typical relationship between organic molecules and inorganic substrates are shown in Fig. 1.12, and some key issues that can lead to uniquely different growth modes in comparison to inorganic counterparts are as follows.

(i) Organic molecules are ‘extended objects’ and thus have internal degrees of freedom. This is probably the most fundamental difference between growth of atomic and growth of organic molecular systems. The orientational degrees of freedom which are not included in conventional growth models can give rise to qualitatively new phenomena, such as the change of the molecular orientation during film growth, as shown in Fig. 1.12 (b). Also, even without considering a transition during the growth, the distinction of ‘lying-down’ and ‘standing-up’ films is important and obviously only possible for molecular systems. The vibrational degrees of freedom can have an impact on the interaction with the surface as well as the thermalization upon adsorption and the diffusion behavior [55]**.**

(ii) In contrast to the inorganic semiconductor where each ad-molecule is a single atoms with spherical symmetry, for organic molecule like phthalocyanine each ad-molecule involve more than 50 covalently bounded atoms, forming a unit with low symmetry. The size of molecule and associated unit cell are in nanometer scale, and thus, deposition on inorganic substrate presents lattice mismatches of one order of magnitude, as shown in Fig. 2.12 (a) [56].

(iii) The interactions between molecules as well as between molecules and substrate are often dominated by weak van der Waals forces. It is important to emphasize that when integrated over all atoms within a molecule, the weak interaction energies add up and lead to substantial molecular binding energies in the eV range. Nevertheless the weaker interactions per atom lead to 'softer' materials and, for example, strain can be accommodated more easily. Due to the weaker interactions the thermal expansion coefficients (typically in the 10^{-4} K^{-1} range) are large when compared to inorganic materials, which possibly leads to higher thermally induced strain at film–substrate interfaces.

(iv) Since we are concerned with closed-shell molecules and van der Waals type crystals, there are no dangling bonds at the organic surface, and thus the surface energies are usually weaker than for inorganic substrates.

Generally, most of the above points directly or indirectly impact the interactions and thus also the barriers experienced during diffusion. Thus, not only the static structure, but also the growth dynamics exhibit differences compared to inorganic systems.

1.4 Thin film deposition methods

In principle, all the techniques used for making inorganic thin films (e.g. thermal, electron beam, sputtering, molecular beam epitaxy, laser ablation, solution methods etc) can be used for the deposition of the molecular semiconductor thin films. However, depending upon the solubility of the molecular semiconductors, organic films are deposited by following two major techniques:

(i) Physical vapor deposition

(ii) Solution processing

In the physical vapor deposition, the molecular semiconductor is vaporized or sublimated and, molecules get deposited onto a substrate to form a film. For solution deposition, the molecular semiconductor is completely dissolved in an organic solvent. The solution is then coated onto the substrate by either drop-casting, spin-coating, dip-coating, or printing. Vapor deposition normally yields more uniform films that can be controlled using various growth parameters, such as, deposition rate, substrate temperature etc. and therefore, is commonly used for fabricating organic electronic devices. It has also the advantages of providing a clean environment during film deposition. One of the most used methods is organic molecular beam epitaxy (OMBE), which imitates the molecular beam epitaxy (MBE) of inorganic thin films. OMBE provides a fine control over the deposition rate e.g. a rate of 1 monolayer/min can be easily be achieved by controlling the effusion cell temperature. Solution processing, on the other hand, is a relatively fast and low-priced method of fabricating thin molecular films. However, in this method film uniformity, control of crystallinity etc. are usually difficult to control. In the following we present an overview the literature on the organic film deposition by OMBE and solution process methods.

1.4.1 Molecular beam epitaxy

In 1989 Hera et al. reported first study on the growth of organic molecule CuPc on cleaved face of MoS_2 using MBE [57]. MBE provides the path for best possible control of growth conditions in clean environmental [56] and this has triggered growth of several organic films using MBE [56, 58-61]. Despite of several studies, the growth behavior of organic films deposited using MBE is not fully understood. As discussed earlier, the unit cell of molecular semiconductors are much larger than those of inorganic substrates. Thus the lattice matching condition does not occur, which makes the epitaxial growth of molecular semiconductors very difficult. Recently, van der Waals epitaxy (vdE) term has been coined to refer an epitaxial growth of molecular film on weakly interacting substrate [58]. A mismatch between the substrate and film lattices results in "strained van der Waals epitaxy", although for highly strained growth, epitaxial structures tend to relax at a critical thickness, thus generating defects [56]. Following van der Walls epitaxy a number of studies have been reported on MBE growth of organic molecular thin films. The most extensive studies of epitaxial growth of organic molecular films have been concentrated on phthalocyanines films on ionic substrate such as alkali halide substrate, metals and on passivated substrate of Si(111) and GaAs(111) [56, 58, 59]. Recently a new method called weak epitaxy growth (WEG) has been developed for the deposition of high-quality organic semiconductor thin films. "Weak" means to decrease the interaction between the molecules and the substrate by way of introducing a buffer layer [62, 63] . Using WEG method layer-by-layer growth of *n*-type F_{16}CuPc on the monolayer *p*-sexiphenyl (*p*-6P) on SiO_2 substrate with roughness less than 1 nm has been reported [63]. Highly orientated crystalline films of *p*-type phthalocyanine were also fabricated by WEG method [64, 65].

Recently Soumen has investigated in detail the growth of phthalocyanine films using OMBE on different substrates. He has demonstrated that (i) due to high vapor pressures of pthalocyanines, the growth temperatures are $< 200^\circ$C, which are much lower than used in inorganic films deposition, (ii) The molecule-substrate interaction plays a dominant role in the growth mode of growth of phthalocyanine films e.g. if the molecule-substrate interaction is strong e.g. in case of (0001) sapphire then the molecule stack in *face-on* configuration, whereas for weakly interacting substrates e.g. glass or quartz, the molecules stack in the edge-on configuration. (iii) The controlled defects e.g. twin boundaries in (100) $LaAlO_3$ substrates or grain boundary of a bicrystal (100) substrate act as a template for the growth of highly ordered phthalocyanine films [3, 66, 67].

1.4.2 Solution method

If the molecules are thermal unstable and has a finite solubility in certain solvents then solution process is useful technique for deposition of the molecular films. In this method, molecules are dissolved in an appropriate solvents and the solution is coated on substrates using different methods, such as, spin coating, drop casting, doctor balding or ink-jet printing. In spin coating techniques, a drop of solution is applied to the substrate which is placed on a rotating substrate with high speed around 2000 rpm. The solution spreads on the substrates and dries rapidly as it rotates leaving a solid film. In doctor balding technique, a solution containing the soluble molecule is spread with uniform thickness by means of "doctor blade". Although by solution process techniques it is expected to produce a films in which individual molecule are relatively disordered, but this is not always true. There are many reports on organized layer of organic molecule deposited by solution process [7, 68]. Furthermore by spin coating high-quality continuous films of uniform thickness of same crystalline order similar to that of Langmuir-Blodgett (LB) films of analogous compounds can be produced. The requirement is that the materials are significantly soluble in volatile solvents without the necessity for surface activity. The main advantages of solution process techniques are easy and low cost, and large area deposition can be easily made.

1.5 Outline of thesis

This thesis is focused on the deposition of phthalocyanine films using both molecular beam epitaxy as well as solution process techniques and to investigate their charge transport properties as a function of applied electric field and temperature. The main objectives are:

(i) Growth of mononuclear phthalocyanine *p*-type FePc, CoPc and *n*-type F_{16}CuPc films using MBE.

(ii) Growth of binuclear (Co-Fe)Pc films by MBE using CoPc and FePc as the source materials.

(iii) Deposition of mononuclear phthalocyanine CuPcTs films by solution process.

(iv) Investigation of the charge transport in mononuclear *p*-type CoPc, FePc, binuclear (Co-Fe)Pc, and *n*-type F_{16}CuPc films as a function of bias and temperature.

(v) Growth and characterization of *p*-type/*n*-type bilayer heterostructure by MBE and their charge transport studies.

(vi) Studies on the gas sensing characteristics of various pthalocyanine films.

The thesis comprising of various experimental technique used during the thesis work, and various results obtained on the studies mentioned above is organized as follows.

In Chapter 2 the various experimental techniques are discussed. The details of MBE system used for the deposition of phthalocyanine films and heterostructures are described. A brief description of the characterization techniques, such as Scanning electron microscopy (SEM), Atomic force microscopy (AFM), X-ray photoelectron spectroscopy (XPS), Fourier transform infrared (FTIR) spectroscopy, UV-Visible spectroscopy, Kelvin probe microscopy are presented. The set up used for the measurements of charge transport and gas sensing characteristics are presented.

In Chapter 3, details of the growth of mononuclear CoPc, FePc and binuclear (Co-Fe)Pc films by MBE are presented. Charge conduction in FePc films under high electrical field are presented. A bias dependent transition from ohmic to space-charge limited conduction to space charge limited conduction with field enhanced mobility is observed. At temperatures <100 K, by analyzing the low bias (< 100 V) data, which is governed by Schottky – barrier limited conduction. However at higher bias multistep tunnelling was observed in the FePc films.A novel feature i.e. temperature dependent metal to insulator like transition, has been observed in ultrathin CoPc films deposited on (001) $SrTiO_3$ substrates. In-plane compressive strains induced by structural phase transition of $SrTiO_3$ substrate reduce the intermolecular distance, and as a result, metallic behavior is observed. Binuclear (Co-Fe)Pc films were found to grown only on sapphire substrates at 200°C if deposited using the CoPc/FePc mixture in 1:1 (w/w) ratio. Formation of binuclear was confirmed by Multi Assisted Laser Desorption and Ionization (MALDI) mass spectroscopy. The binuclear (Co-Fe)Pc films exhibited charge carrier mobility of ~110 cm^2/Vs, which is around two order of magnitude higher than CoPc and FePc films.

In Chapter 4, the deposition and characterization of p-type CoPc/ n-type $F_{16}CuPc$ heterojunction are presented. The results on the charge transport Kelvin Probe studies on these heterostructures are presented.

In Chapter 5, the gas sensing behavior of water soluble copper phthalocyanine (CuPcTs) films prepared by solution process is presented. These films exhibited room temperature sensitivity towards Cl_2 gas. Selectivity, repeatability, stability and linearity (sensitivity vs concentration) in the range 5ppb to 2000ppb are investigated. The chemical adsorption process of Cl_2 on CuPcTs has been analyzed using Elovich equation, which provides an alternative way of qualifying Cl_2 concentration from response rate of sensor. A comparison study of the gas sensing characteristics CoPc, FePc and binuclear (Co-Fe)Pc films has been studied. It has been found that binuclear films are better for gas sensing because of their high mobility.

Chapter 6 summarizes the main results obtained during the course of thesis and directions for the future research associated with this thesis are outlined.

CHAPTER-2

EXPERIMENTAL TECHNIQUES

2.1 Introduction

In this chapter we discuss different techniques utilized to prepare and characterize the phthalocyanine films and heterostructures. Thin films are deposited using organic molecular beam epitaxy as well as by drop cast method. Films are characterized by a host of techniques, such as, atomic force microscopy, scanning electron microscopy, X-ray photoelectron spectroscopy, Fourier transforms spectroscopy and UV-Vis spectroscopy, X-ray diffraction, Kelvin probe method etc. We present the details of the electrical characterization of the films.

2.2 Deposition of phthalocyanine films

In this section we present the details of the phthalocyanine films preparation using MBE as well as solution process.

2.2.1 Molecular beam epitaxy

Conceptually organic molecular beam epitaxy is technologically an improved version of the conventional thermal evaporation technique. MBE offers additional advantages to the other deposition techniques, particularly in terms of ultra high vacuum (UHV) environment that allows growth of epitaxial layer with extremely high purity. Other unique characteristics of MBE are:

(i) *The beam nature of the mass flow from source to substrate*: The molecules evaporated from a source in a vacuum chamber assume the features of a beam when the mean free path (λ) of the molecules is much larger than the source-to-substrate distance. The occurrence of beam nature, therefore, depends on λ of evaporating molecules and concentration of residual gas molecules in the evaporation chamber. Both these conditions are associated with vacuum conditions of the growth chamber. The λ is related with pressure (*p*) as

$$\lambda = 3.11 \times 10^{-24} \frac{T}{pd^2} \tag{2.1}$$

where *d* is the diameter of the molecules [69]. The growth chamber is maintained at better than 10^{-8} torr vacuum level during growth and at this pressure mean free path (λ) for the phthalocyanine molecule is 4×10^{4} m as calculated using eq. 2.1. The value of λ is clearly greater than the typical source to substrate distance (40 cm) and thus ensuring the beam nature of the molecule. Apart from the pressure during growth the residual gas pressure is also pumped down to better than 10^{-9} torr which ensure the low concentration of residual gas molecules which affect the beam nature of the molecule. This low residual gas pressure also confirms that no monolayer of residual gas formed during deposition even when the film is deposited at very slow growth rate.

(ii) *High degree of control over growth parameters*: The molecular beams are usually produced by effusion cells, where constituent materials are evaporated under a fine temperature control [69]. The beam flux and hence, the deposition rate, is monitored by a gauge located near to the substrate. The beam flux can be precisely controlled by temperature of source, with a stability of better than 1%. The precise control over the molecular beams enables to keep the growth rate of the film as low as 1 monolayer per second. The continuous rotation of the substarte and thus confirming excellent uniformity in film thickness as well as in composition on a large area substrate and high reproducibility of film preparation.

Molecular beam can be individually blocked by beam shutter and therefore complex heterostructure with sharp interface can be produced.

(iii) *In-situ growth characterization of the films*: MBE is usually equipped with characterizations tool such as reflection high-energy electron diffraction (RHEED**)**, X-ray photoelectron spectroscopy (XPS), ultraviolet photoemission spectroscopy (UPS) etc. which enables an *in-situ* analysis of the films.

2.2.1.1 Configuration details of RIBER-32 EVA MBE system

The photograph of the MBE system (RIBER EVA 32 E) used for thin film deposition in the present study is shown in Fig. 2.1. It consists of three chambers namely, Introduction Chamber, Analysis Chamber and Growth Chamber. All of them are UHV chambers and are made of stainless steel. All seals are made of OFHC copper gaskets. This construction allows high temperature baking (~200°C) of the entire system to reduce out gassing from the walls. Analysis and Growth chambers are situated in a line, whereas, the Introduction Chamber is situated at 37° off the line joining Analysis and Growth Chambers. Introduction chamber is connected with Analysis chamber and similarly Analysis chamber with Growth chamber are connected through gate valves. There are two magnetically coupled sample transfer mechanisms. One is used to transfer the sample from Introduction to Analysis Chamber and the second is used to transfer sample from Analysis to Growth Chamber. Therefore, substrate cleaning and characterization, film deposition and characterization are performed in-situ under UHV conditions. The details of the three chambers are presented below.

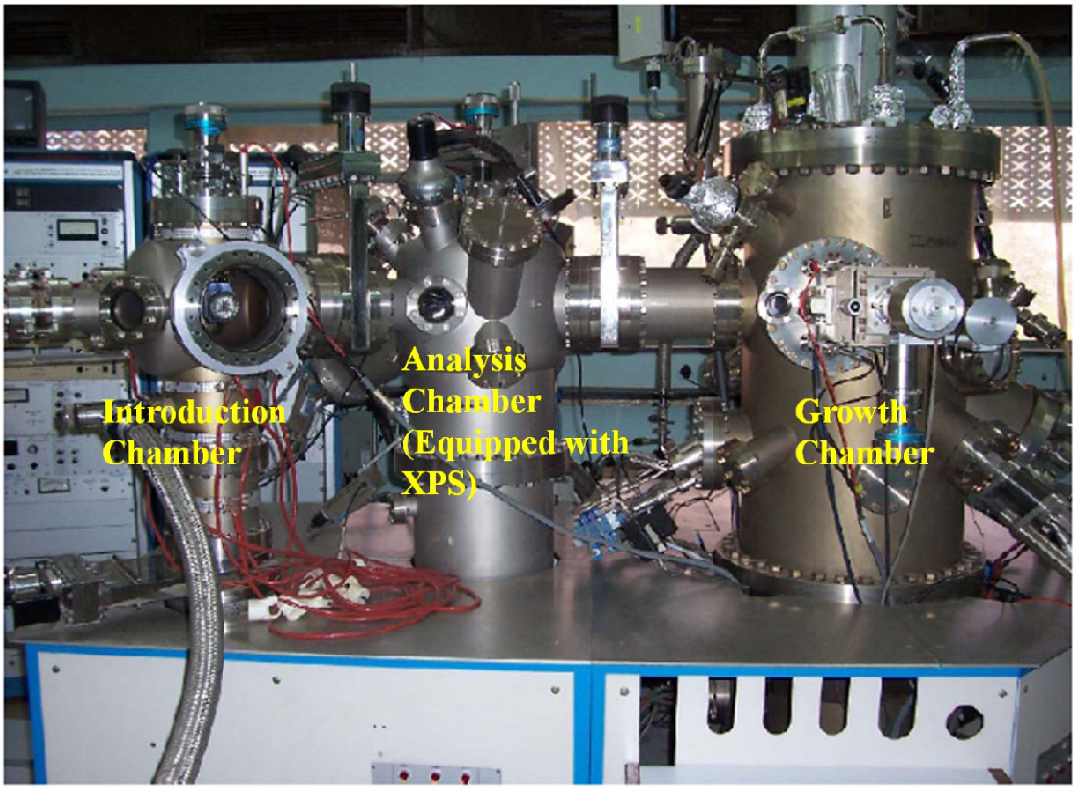

Figure 2.1 Photograph of the MBE deposition system used for the deposition of MPc films.

(i) *Introduction chamber:* In this chamber, shown in Fig. 2.1, the substrates are loaded through the front opening flange. The substrates are fixed on a heater assembly using silver paste, and the substrates can be cleaned by degassing the substrate up to a temperature of 800°C. After loading the sample it is rapidly pumped down from atmospheric pressure to ~10^{-9} Torr with sorption and ion pumps. The heater assembly having the substrate is transferred to the Analysis and/or Growth Chambers using the transfer rods.

(ii) *Analysis chamber:* This chamber serves the following two purposes i.e. cleaning of the substrates by ion etching and (ii) surface characterization of substrates and grown films using X-ray photoelectron spectroscopy. This chamber is equipped with a substrate heater which can be heated upto 800°C. In order to determine the level of cleanliness of the substrate and, chemical state and composition of the substrate and grown films the chamber is equipped with X-ray photoelectron spectroscopy (XPS) techniques.

(iii) *Growth chamber:* The growth chamber is the most important part of the MBE system. In this chamber all the controlling elements, such as, beam sources with their individual shutters, a main shutter, and manipulator with substrate heater and rotation, pressure control system etc. are located.

The Growth chamber can be evacuated to better than 10^{-9} torr by using a combination of turbomolecular pump and ion pump with a fully cryoshrouded titanium sublimation pump. A helium closed-loop cryopump is also mounted for supplementary pumping.

Effusion cells are the key components of an MBE system, because they must provide excellent flux stability and uniformity, and material purity [69]. The chamber contains three effusion cells. In the present study, we have used them for CoPc (99.99%), FePc (99.99%) and F_{16}CuPc (99.98%). Each effusion cell includes an oven (filament + thermocouple) and fully degassed thick PBN crucible, surrounded by adequate tantalum shielding for use in proximity of a cryoshroud. PBN crucibles are designed to provide a very stable flux during charge depletion. The heating filament is made of high purity tantalum foil. The contact thermocouple is located at the bottom of the crucible. Electrical insulators are made of PBN. The cell can be operated upto the 1400°C, and its temperature can be controlled with an accuracy of 1°C. The source mounting flange houses power and thermocouple feedthroughs. Power supply and temperature control are implemented by the use of microprocessor-based controllers**.**

The manipulator consists of a gauge head and a substrate heater which can be heated upto 800°C. The manipulator allows the azimuthal rotation of the substrate during growth. The substrates are positioned to maximize growth uniformity for a substrate of size 1 inch diameter.

Quartz crystals monitor are mounted near the substrate to monitor the deposition rate. Alternatively deposition rate are also monitor by the flux gauge**.**

2.2.1.2 Deposition procedure

Following two steps are involved in the deposition of phthalocyanine films.

(i) *Substrate preparation*: Substrate preparation is very important step before growth studies. In the present studies we have used indium tin oxide (ITO) coated glass, twinned (001) $LaAlO_3$, (0001) Al_2O_3 and (100) $SrTiO_3$ substrates. Prior to the introduction in the in the MBE chamber the substrates are thoroughly cleaned in different organic solvents. In the first step the substrates were ultrasonicated in trichloroethylene bath for 10 minutes to remove oil, grease etc. Thereafter the substrates were sonicated in acetone and methanol separately to remove polar and non-polar organic, inorganic impurities and dust particles. To remove the solvent, the substrates were dried under the jet flow of dry high purity Ar gas. Finally films are loaded in the introduction chamber of MBE system.

(ii) *Loading into MBE system and deposition:* In the second step, pre-cleaned substrates were loaded into the introduction chamber, which was subsequently evacuated to 10^{-7} torr. The substrates were heated to 500ºC to remove the residual solvent particle and other impurities. The substrates were then transferred to analysis chamber, where XPS studies were carried out to examine their cleanliness. If the substrates are found to be clean, they were transferred in-situ to the growth chamber for deposition. Otherwise, they were taken back to introduction chamber for further heat treatment to remove the impurities. Prior to the deposition the, source materials (FePc, CoPc or F_{16}CuPc) were degassed at 200 ºC for 2 to 3 times for the removal of volatile impurities. During deposition the pressure of the growth chamber was maintained better than 10^{-9} torr. The films were deposited at various substrate temperatures (25ºC to 250ºC) and the substrate heater can be controlled within ±1ºC accuracy of temperature. The deposition rate of the film is monitored by the flux gauge and the deposition rate was varied between 0.02 and 0.5 nm/s by controlling the effusion cell temperature. In order to achieve excellent uniformity in composition and thickness, the source-to-substrate distance was kept comparatively large (40 cm) and the substrates were rotated during the deposition. After the deposition, the films were transferred to the analysis chamber again and films were characterized by XPS. Finally the films were taken out through the introduction chamber for further ex-situ characterization and charge transport measurements.

2.2.2 Solution process

Deposition of organic films requires solubility of the organic molecules in an appropriate solvent. Unfortunately, the solubility of FePc, CoPc and F_{16}CuPc in majority of organic solvents as well as in water is very poor, therefore their films cannot be prepared by solution process. (CuPcTs) is soluble in water, and therefore we have chosen this material for making thin films by drop casting method. First, the substrates (quartz and sapphire) were carried out by sonicating them in try-chloro-ethylene, acetone and methanol for 10 min each, respectively. Substrates were then dried using argon gas jet stream. In the second step, the solution, prepared by dissolving 5 mg. of CuPcTs in 0.1 ml of de-ionised water and 0.4 ml of methanol and sonicated for 10 min, was spread on substrate. Deposited films were dried for few hours under ambient conditions and finally vacuum annealed at 250°C for 15 min.

2.3 Characterization techniques

2.3.1 Atomic force microscopy (AFM)

AFM measures the interatomic forces acting between a fine tip and a sample surface, as schematically depicted in Fig. 2.2. The tip is attached to the free end of a cantilever or tuning fork and is brought very close to a surface. Attractive or repulsive forces resulting from interactions between the tip and the surface will cause a positive or negative bending of the cantilever. AFM operates in three different modes: contact mode, non-contact mode and tapping mode. At relatively large distance from the sample surface, the force of attraction between the tip and the sample surface dominants, whereas repulsive force is most significant at very small distance (less than few angstroms).

In non-contact mode or dynamic mode, the tip is held order of tens to hundreds of angstroms from the sample surface, and the interatomic force between the tip and sample is attractive (largely a result of the long-range van der Waals interactions). In contact mode or static, the tip is brought in to close contact with sample surface less than a few angstroms, so that force between tip and sample becomes repulsive. The resulting deflection by cantilever is monitored and measured by different detection techniques. For organic material, the major problem with this mode of operation is that, surfaces can be easily scratch or damaged due to the direct contact with the tip. These drawbacks are overcome by tapping mode. Though, since the force of attraction is much weaker than the repulsion, the resolution is usually lower than the contact mode of operation.

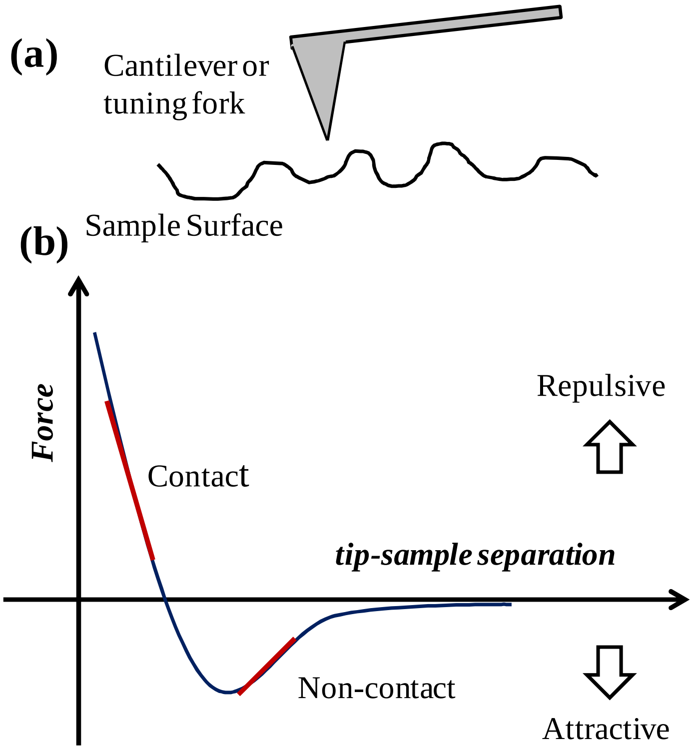

Figure 2.2 (a) Interaction of the AFM tip with sample surface. (b) Force versus separation between AFM tip and the sample surface.

The tapping mode combines the advantages of contact and non-contact mode. In tapping mode-AFM the cantilever is oscillating close to its resonance frequency (100-500 kHz) with amplitude of approximately 20 nm so that the tip just touching (tapping) the surface. An electronic feedback loop ensures that the oscillation amplitude remains constant, such that a constant tip-sample interaction is maintained during scanning. The resolution of this tapping mode is almost the same as that of contact mode, but it is faster and much less damaging.

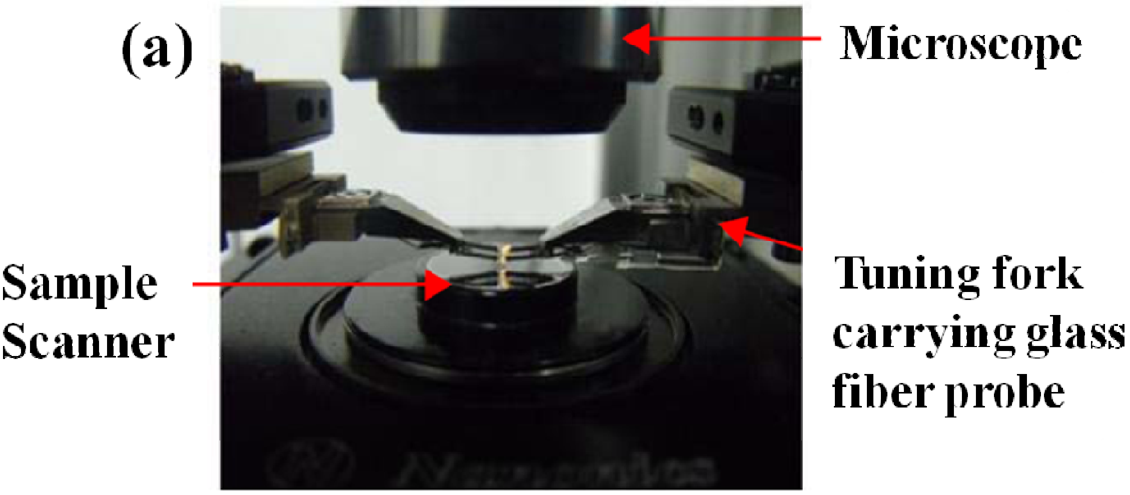

Nanonics 4000SPM/AFM

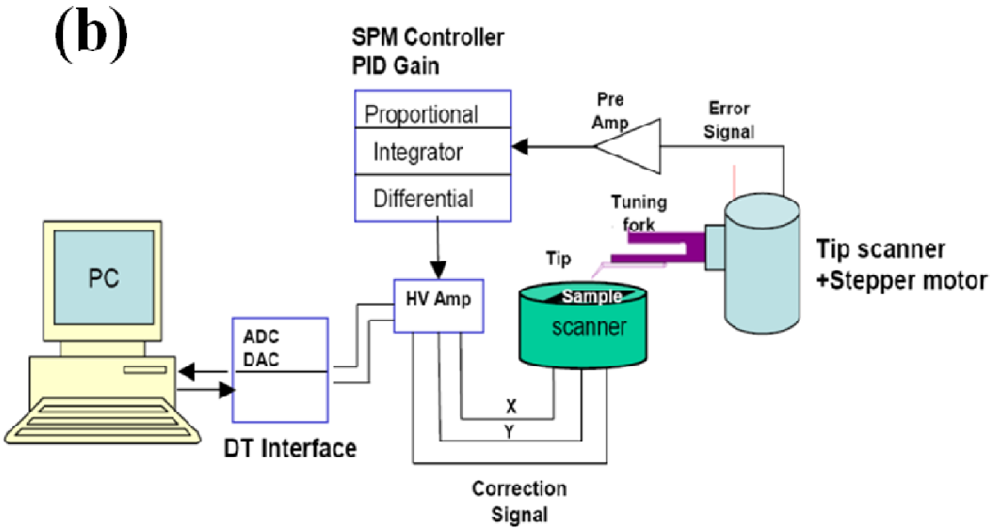

Figure 2.3 (a) Photograph showing the AFM tip and sample stage. (b) Block diagram of AFM.

The atomic force microscope used in the present studies was Nanonics 4000SPM/AFM system, as shown in Fig. 2.3 (a). In this case, the probe is made of the glass fiber tip (diameter 10nm) which is attached to tuning fork with pizocrystal [70]. The images are recorded in the tapping mode by oscillating the tip at resonance frequency (20-50 kHz depending on the tips). The probe was scanned in phase mode. During scan, phase changes due to tip surface interaction. The difference in signal called an error signal; this signal is sent to proportional, integrator and differentiator (PID) controller. PID sends the feedback via high voltage pizo driver to make constant phase by moving pizodriver in z direction at that x, y point. This way an image is generated. A schematic diagram of signal processing is shown in the Fig. 2.3 (b). The image so generated was processed (like smoothing, flattening etc) by NWS software [71]. This software was also used to study surface roughness by extracting line profile from the image.

2.3.2 Scanning electron microscopy (SEM)

SEM provides information relating to topographical features, morphology and phase distribution [72, 73]. The operation of SEM is described in Fig 2.4. The scanned electron beam is produced in an electron microscope column. Electrons are emitted from heated cathode and arranged through electric and magnetic fields in a proper direction to achieve the required incident beam at sample surface. The principal elements of electron column are electron gun, the condenser lens, and the scanning and deflecting coils. Electrons in the SEM are accelerated at voltages in the range 2-40 kV.

Two types of interactions occur in SEM between the electrons beam and the sample structure. These interactions may be either elastic, if the electron beam strikes the sample and there is a change in its direction without changing its energy (backscattered electrons), or an inelastic interaction, which occurs when the beam of electron strike an orbiting shell electron of the sample, causing ejection of new electrons (secondary electrons), If the vacancy due to the creation of a secondary electron is filled from a higher level orbital, an X-Ray characteristic of that energy transition is produced. In addition, Auger electrons, and cathodoluminescence are produced, as shown in Fig. 2.5. These interactions reveal the important information about the sample to find out the surface characteristics and the chemical nature of the sample.

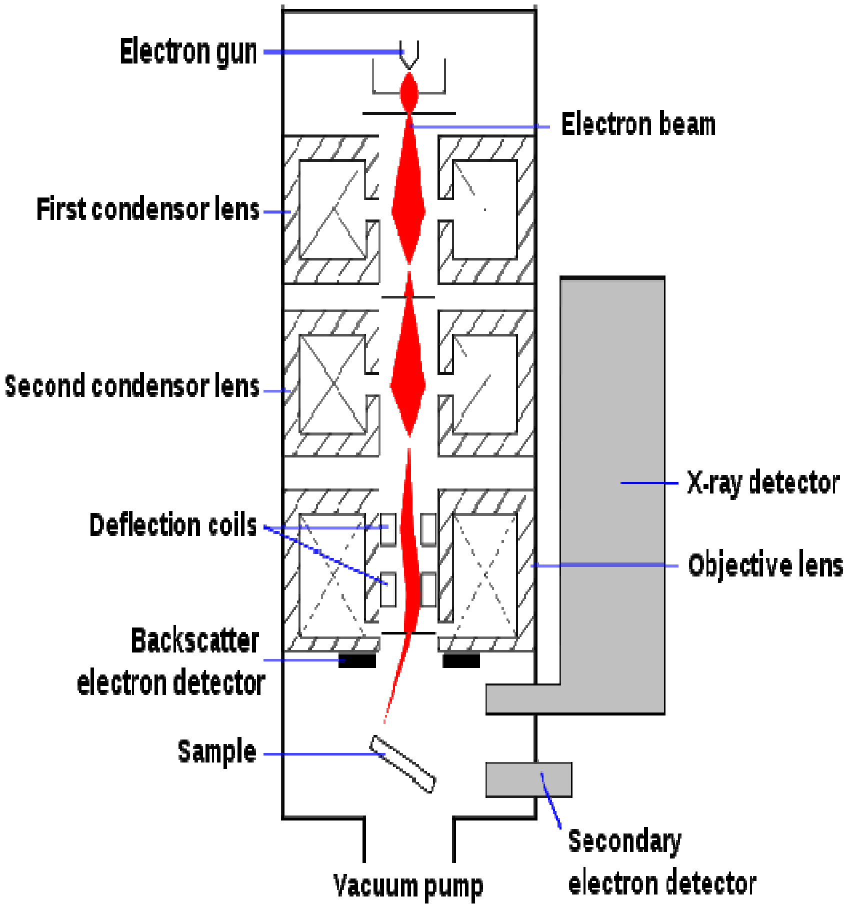

Figure 2.4 Block diagram of a typical SEM setup.

The most widely utilized signal is the secondary electron signal. Nearly all of secondary electrons come from a region very closer to the sample surface. Secondary electrons are characterized from other electrons by having energy of less than 50 eV. The secondary electron is emitted from an outer shell of the specimen atom upon impact of the incident beam. It is the most useful signal for examining surface structure and gives the best resolution image of 10 nm or better. Since the secondary electron intensity is a function of the surface orientation with respect to the beam and the secondary electron detector and thus, produces an image of the specimen morphology. The secondary electron intensity is also influenced by the chemical bonding, charging effects and back scattered electron intensity, since the back scattered electron generated secondary electrons are significant part of the secondary electric signal.

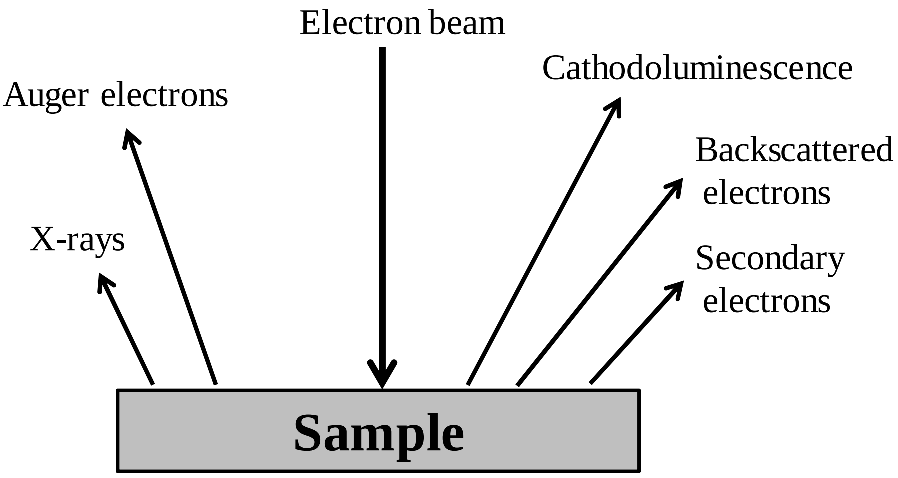

Figure 2.5 Interaction of the electron beam with sample.

The detector is Everhart-Thornley detector composed of a scintillator, collector, light pipe, and photo multiplier tube. First electrons striking the positively biased scintillator and converted to a burst of photons, that travel through the light pipe to a photomultiplier tube which converts the photons of light into a voltage. The strength of this voltage depends on the number of secondary electrons that are striking the detector. Thus the secondary electrons produced from a small area of the specimen give rise to a voltage signal of a particular strength. The voltage is led out of the microscope column to an electric console, where it is processed and amplified to generate a point of brightness on the cathode ray tube screen. Contrast in the SEM image is the difference in intensity, or brightness of the pixels that make up the image. The difference in intensity represents difference in signal from corresponding picture elements on the sample. A photograph of SEM, (Tescan make VEGA MV2300T/40 system) used in the present study is shown in Fig. 2.6.

Backscattered electrons consist of high-energy electrons (greater than 50 eV) originating in the electron beam, that are reflected or back-scattered out of the specimen interaction volume. The intensity of their signals increases with increase the atomic number. Backscattered electron signal is often used to show atomic number contrast, in which areas of higher average atomic number produce more back scattered electrons, and thus appear brighter than lower atomic number regions. The contrast in this image is not due to colour differences but is produced by different intensities of electrons back scattering from the layers with different average atomic number.

The characteristics X-rays signal depends exclusively on the atoms that produced it, hence can be used for chemical identification analysis. The EDS X-ray detector (also called EDS or EDX) measures the number of emitted x-rays versus their energy. The energy of the X-ray is characteristic of the element from which the X-ray was emitted.

Cathodoluminescence (CL) is the emission of photons of characteristic wavelengths from a material that is under high-energy electron bombardment is used to study the internal structure of the material.

Figure 2.6 The photograph of the SEM (model: Tescan VEGA MV2300T/40).

2.3.3 X-ray photoelectron spectroscopy (XPS)

XPS was developed as a surface analysis technique in the mid-1960s by Siegbahn and his coworkers [74]. Core level electrons have the binding energies matching to the energies of the photons that lie in X-ray region [74, 75]. XPS are based on the photoelectric effect, through which an atom absorbs a photon with energy ($h\nu$) in excess of binding energy (E_b) of an electron; a photoelectron is emitted with kinetic energy

$K.E. = h\nu - E_b$

In XPS a soft X-ray source (Al-K_α and Mg-K_α) is used to ionize electrons (by knocking out the core-level electron) from the surface of a solid sample (top few atomic layers). The binding energies of these electrons are measured, which are characteristics of the elements. Binding energies of core electrons are not only element-specific but also contain chemical information, because the energy levels of core electrons depend slightly on the chemical state of the atom. Such shift in the energies of core level electrons arising due to chemical state of electrons is known as chemical shift. The advantages of XPS technique are (*i*) quantitative analysis of elements and chemical states of all elements except hydrogen and helium, (*ii*) typical element detection limits are 0.1 atomic percentage from the top few nm, and (*iii*) samples can be conductors, semiconductors or insulators [76-78].

The XPS system which we have used is mounted in the analysis chamber of the MBE system, and thus the in-situ (i.e. without breaking vacuum) and ex-situ (i.e. exposing to ambient) study of the deposited films were carried out. The XPS system (RIBER system model: FCX 700) consists of Al-K_α(1486.6eV) and Mg-K_α (1253.6eV) X-ray sources and MAC-2 electron analyzer. The binding energy scale was calibrated to Au-$4f_{7/2}$ line of 83.95eV. For charge referencing adventitious C-1s peak set at 285eV was used. Each data set was first corrected for the non-linear emission background. The data was then fitted with Gaussian function to find the peak positions.

2.3.4 Fourier transform infrared spectroscopy (FTIR)

The frequencies and intensities of the vibrational modes observed in FTIR provide detailed information about the nature of the bonding in the molecule [79]. FTIR spectra were recorded using Bruker system (vertex 80V). The necessary condition for the infrared absorbance is the presence of permanent dipole moment or change in dipole moment of the chemical bond (between two atoms) when it interacts with IR. The absorption of IR leads to change in vibration level. So IR absorption helps to identify the characteristic vibrational frequencies of organic functional group. Most of the organic molecules have vibrational frequencies in the mid infrared range of 4000 to 400 cm^{-1}. FTIR works on the principle of interferometer that gives an interferogram, a plot of light intensity versus optical path difference. The ray diagram of formation of interferogram is shown in the Fig. 2.7. This interferogram is finally Fourier transformed to give a spectrum of infrared radiation intensity versus wave number.

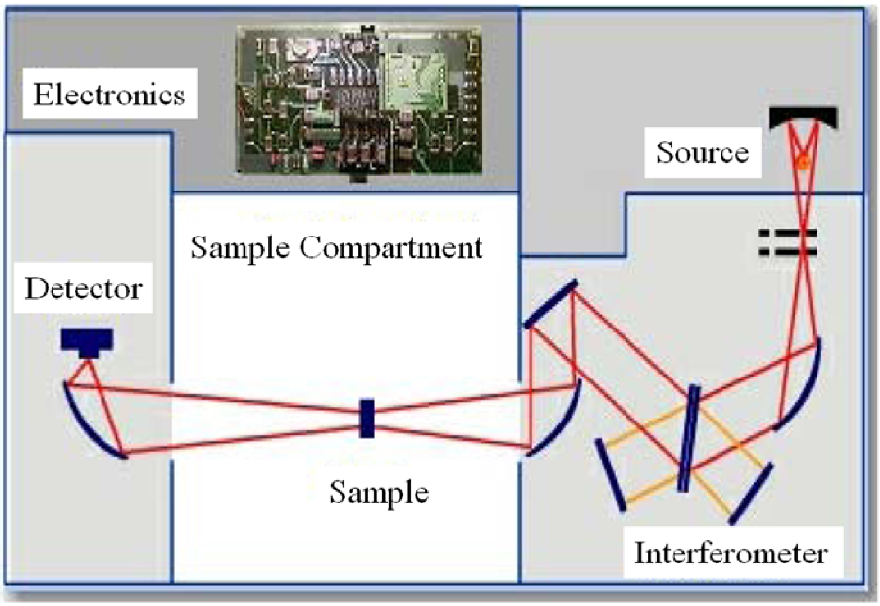

Figure 2.7 Ray diagram of recording FTIR spectra along with electronic circuit of system vertex 80V.

For our experimental purpose, FTIR spectra were recorded in two different spectroscopy modes: attenuated total reflection (ATR) and diffuse reflectance mode. In the ATR mode, an infrared beam is directed onto an optically dense crystal with a high refractive index at a certain angle. This internal reflectance creates an evanescent wave (see Fig. 2.8) that extends beyond the surface of the crystal into the sample held in contact with the crystal. This evanescent wave protrudes only a few microns (0.5 - 5 μm) beyond the crystal surface and into the sample. Consequently, there must be good contact between the sample and the crystal surface. In regions of the infrared spectrum where the sample absorbs energy, the evanescent wave will be attenuated or altered. The attenuated energy from each evanescent wave is passed back to the IR beam, which then exits the opposite end of the crystal and is passed to the detector in the IR spectrometer. The system then generates an infrared spectrum. This mode is very good technique to measure FTIR spectra of the film.

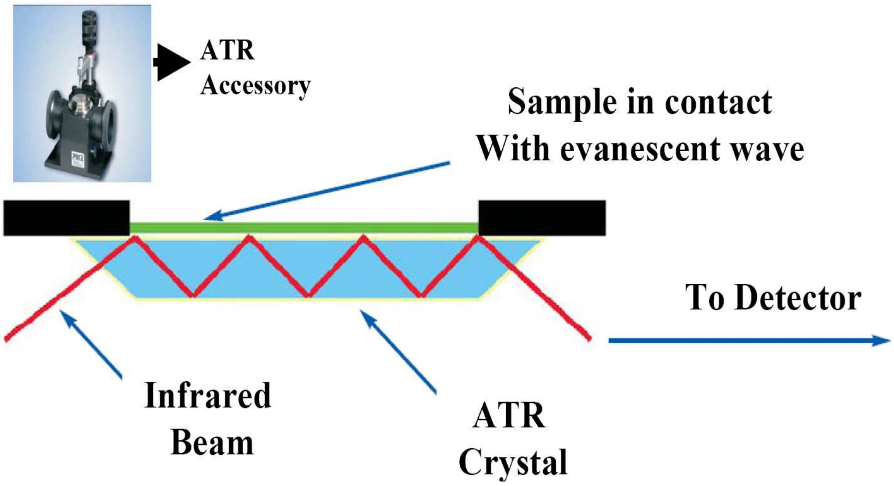

Figure 2.8 Ray diagram of recording FTIR spectra in ATR mode. The accessory used for ATR spectra is also shown in the inset of the diagram.

2.3.5 UV-Visible spectroscopy

Absorption of the ultraviolet or visible light by molecules containing π-electrons, σ-electrons or even non-bonding electrons (n-electrons) leads to electronic excitation among various energy levels within the molecule; as a consequence, the wavelength of absorption peaks can be correlated with the type of bonds in the spices [80]. A diagram showing the various kinds of electronic excitation that may occur in organic molecules is shown in Fig. 2.9. The transition between bonding and antibonding are two types:

(i) *$\sigma - \sigma^*$ transition,* requires large energies corresponding to absorption, most of the transitions occurs below 200nm.

(ii) *$\pi - \pi^*$ transition,* occurs with molecules containing conventional double bond or triple bond.

Similarly the transitions between non-bonding and antibonding orbitals are $n - \pi^*$ and $n - \sigma^*$. The absorption may sometime occur due to the *d* and *f* electron and also due to charge transfer electrons. So this absorption study is very important tool to indentify the molecule or functional group in the molecule.

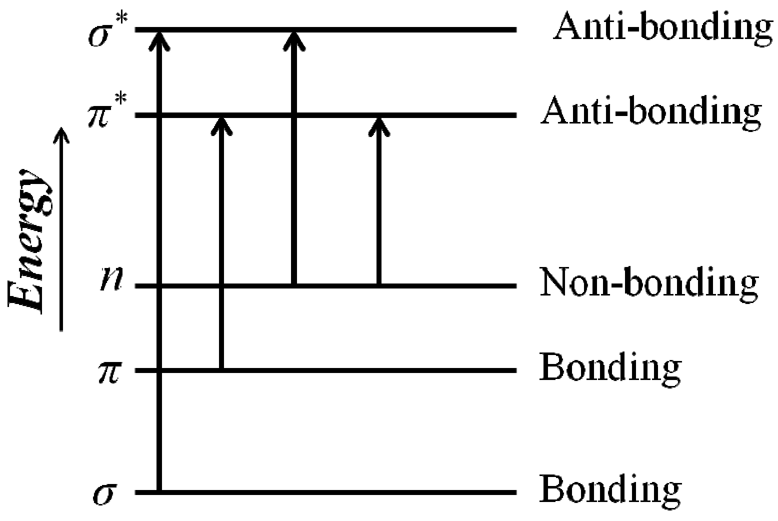

Figure 2.9 Electronic energy levels and possible electronic transitions of π, σ, and n electrons.

For our experiment we have used JASCO B430 spectrometer. The schematic of the double beam single monochromator spectrometer is shown in Fig 2.10. In this spectrometer the intensity (I) of the beam passing through the sample is compared with a reference beam (I_0) and in output we get absorbance ($A = log_{10}I/I_0$) vs wavelength. Absorbance is directly proportional to the numbers of absorbing molecules (concentration) in the light-path and path length. This is called Beer-Lambert law, can be expressed as

$$A = \varepsilon lc \qquad (2.2)$$

where ε is the molar extinction coefficient, c concentration of absorbing species and l is path length.

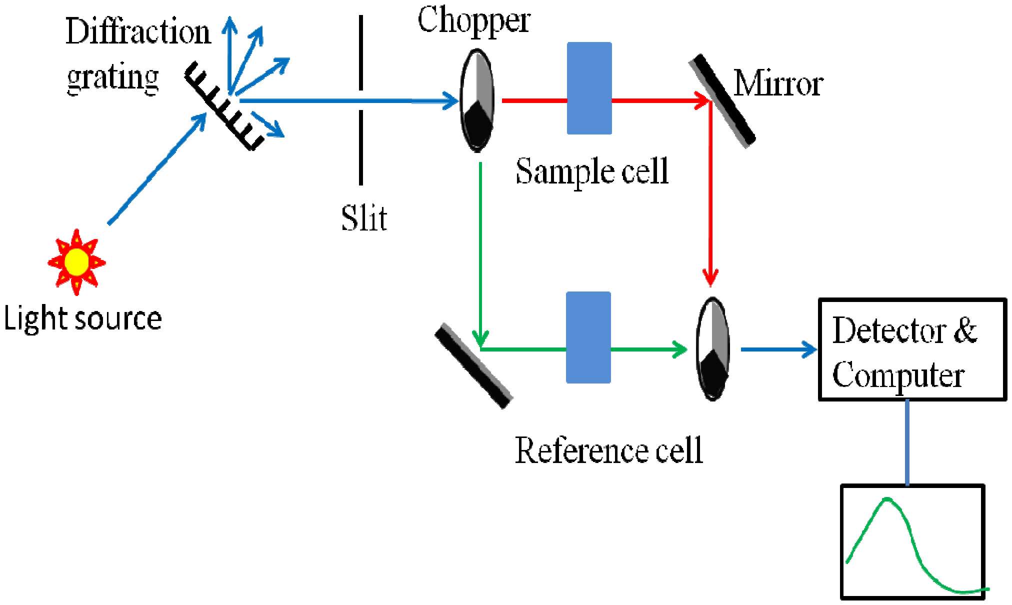

Figure 2.10 Block diagram of a typical double beam single monochromator UV-spectrometer.

2.3.6 Raman spectroscopy

The Raman effect arises when a photon is incident on a molecule and interacts with the electric dipole of the molecule. It is a form of electronic (more accurately, vibronic) spectroscopy, although the spectrum contains vibrational frequencies. In classical terms, the interaction can be viewed as a perturbation of the molecules electric field. In quantum mechanics the scattering is described as an excitation to a virtual state lower in energy than a real electronic transition with nearly coincident de-excitation and a change in vibrational energy. Thus, by analyzing the scattered photons information on the vibrational motions of atoms in molecules is obtained. These motions are a function of molecular conformation, of the distribution of electrons in the chemical bonds, and of the molecular environment. Thus, interpretation of the Raman spectrum provides information on all these factors [81, 82].

Raman spectra were recorded using LABRAM–1 micro/macro Raman spectrometer (Horiba Jobin Yvon, Bensheim, Germany). The 488-nm line of an Ar^+ laser was used for excitation and the scattered Raman signals were analyzed in a back-scattering geometry using a single monochromator spectrometer equipped with a Peltier-cooled CCD detector for multichannel detection.

2.3.7 Kelvin Probe method

The Kelvin Probe is a non-contact, non-destructive vibrating capacitor device used to measure the work function difference, or for non-metals, the surface potential, between a conducting specimen and a vibrating tip. The Kelvin method was first postulated by the renowned Scottish scientist W. Thomson, later Lord Kelvin, in 1861[83, 84]. He described the movement caused by coulomb repulsion within a gold leaf electroscope when zinc and copper plates brought into close proximity while the plates were electrically connected as shown in Fig . 2.11. In 1932, this technique is modified by Zisman as a vibrating capacitor [85].

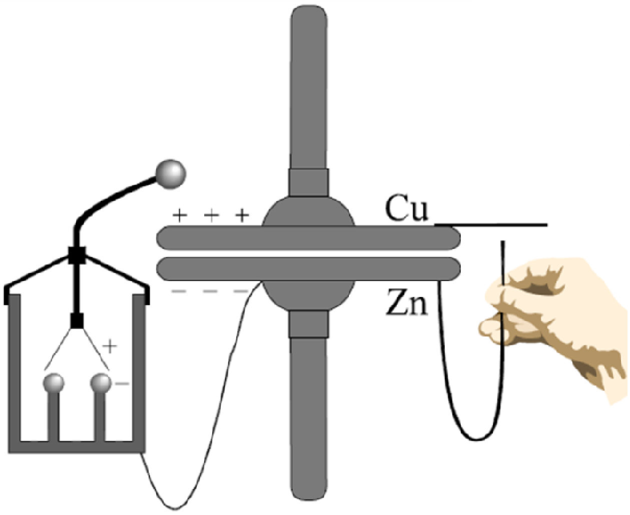

Figure 2.11 The original apparatus used by Lord Kelvin.

The Work Function is usually described as being the *'least amount of energy required to remove an electron from a surface atom to infinity or equivalently the vacuum level'*. The Kelvin probe measures the work function indirectly, i.e. via equilibrium not via extracting electrons [84]. The Kelvin probe (KP) technique measures the contact potential difference (CPD) between surface of sample and KP tip in close proximity. The principle of the KP techniques is shown in Fig 2.12. The electronic energy level diagram for two conducting but isolated materials (sample and tip) of different work functions is shown in Fig 2.12 (a). ϕ_{tip} and ϕ_{sample} represent the work functions of the tip and sample respectively, with $\phi_{sample} < \phi_{tip}$. If an external electrical contact is made between them, electrons flow from the sample with the smaller work function to the tip with the larger work function. This causes the tip to charge positively while the sample charges negatively to equalize their Fermi level. This creates an electric potential between them, shifting their electronic states relative to each other as shown in Fig. 2.12 (b). This electric potential called contact potential difference (V_{CPD}) and is exactly equals to the sample and tip work function difference. If ϕ_{tip} is known then ϕ_{sample} can be calculated by measuring V_{CPD}. The V_{CPD} is calculated by applying a variable "backing potential" V_b in the external circuit. At the unique point where $V_b = -V_{CPD}$ the electric potential between the plates vanishes and a null output signals obtained as shown in Fig. 2.12 (c).

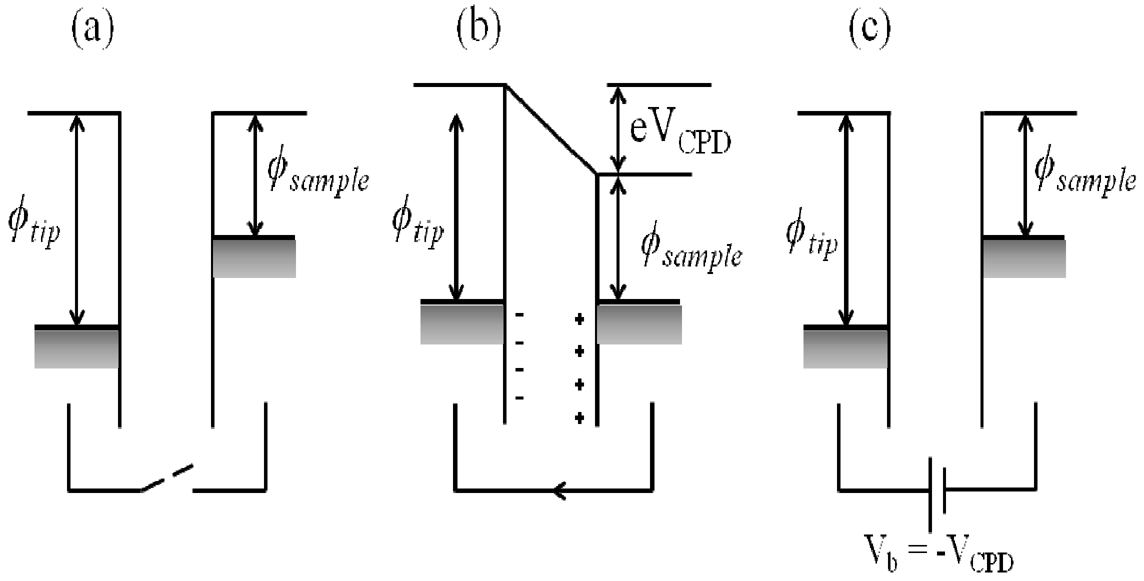

Figure 2.12 Principle of Kelvin probe measurement.

Traditionally, the V_{CPD} was determined by vibrating the reference electrode (KP tip) above the sample and adjusting V_b until a zero or null output resulted. This method of detection is extremely sensitive to noise since the Kelvin Probe signal is diminishing with respect to the noise background. In addition, KP measurements can only detect the CPD, real work function measurements are only possible through calibration i.e. the KP needs to be calibrated against a surface with known work function.

For our measurement, we have used Scanning Kelvin Probe system SKP5050 manufactured by KP technology as shown in Fig. 2.13 (a). The Kelvin probe tip (made of gold) and sample mounting stage is shown in Fig 2.13 (b). In this system V_{CPD} is measured by off-null detection method or 'Baikie Method' where the signal is measured at high signal levels far from balance is correspondingly much less sensitive to noise than traditional systems, with work function resolution 3-5 meV. In our measurements, standard gold/aluminum sample manufactured by KP technology was used for calibration purpose.

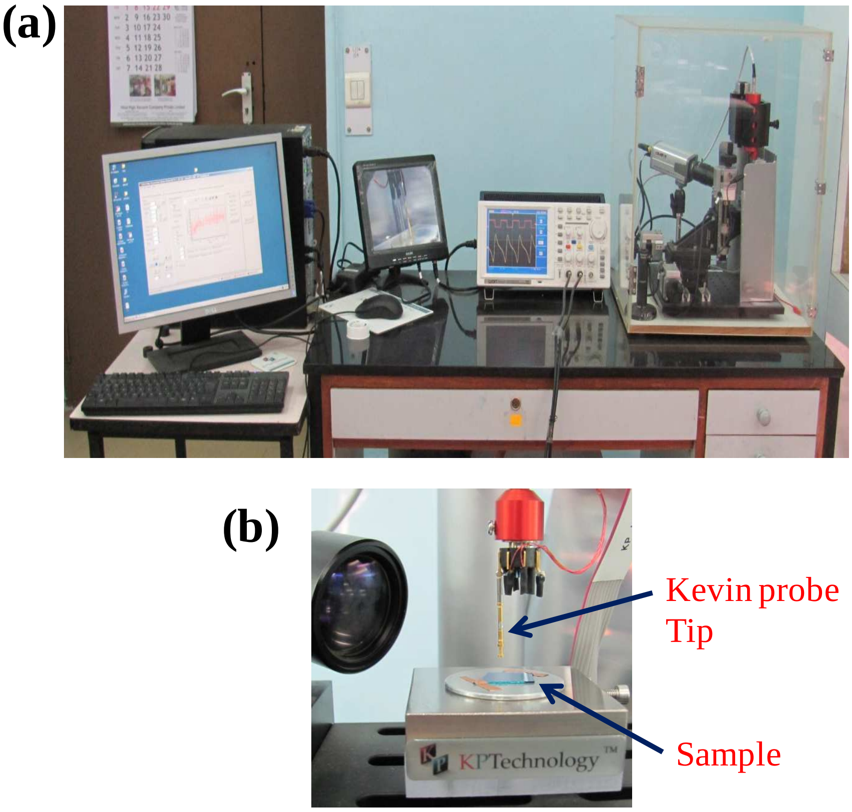

Figure 2.13 A photograph of (a) Scanning Kelvin probe system SKP5050 manufactured by KP technology and (b) Kelvin probe tip and sample stage.

2.3.8 X-ray diffraction (XRD)

For the determination of the structure of the deposited films, X-ray diffraction in different configurations are carried out. These are discussed as follows.

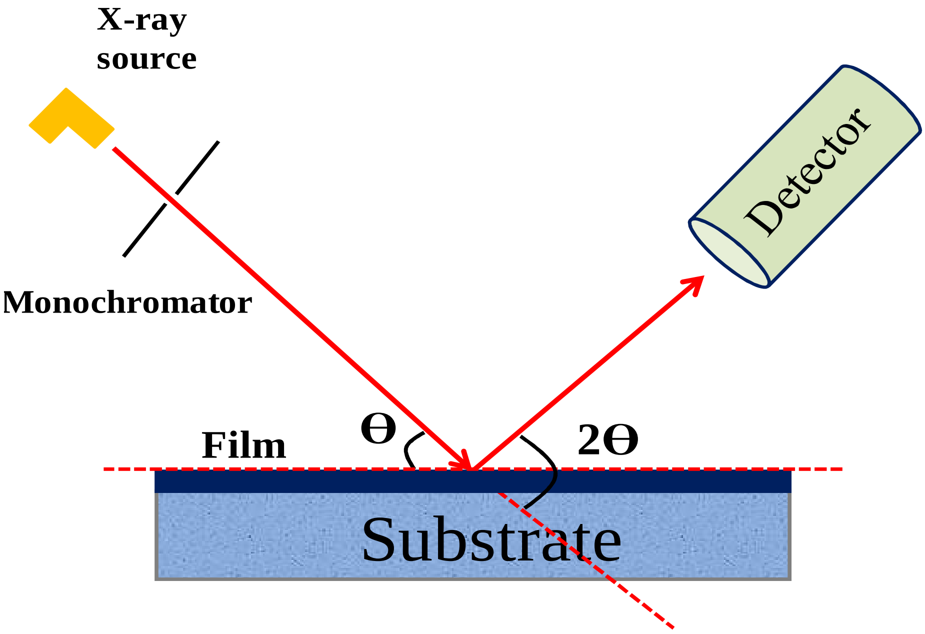

Figure 2.14 Schematic diagram of powder X-Ray diffractometer

2.3.8.1 Powder XRD

We have used powder X-ray diffractometer (Seifert XRD 3003TT) in θ-2θ scan mode to characterize the orientation and structure of the grown Pc thin films. Fig. 2.14 shows the schematic diagram of the diffractometer, which consists of an X-ray source, and a goniometer for mounting sample and X-ray detector. The X-ray source used was Cu K_α having wavelength of 1.54056Å, which has been selected using a Graphite monochromator. For mounting thin films, a specially designed Perspex holder (having a groove of dimension 10 mm×10 mm×1mm) was employed. The films were mounted on this groove using red wax in such a way that X-rays fall on the film plane. Since the wavelength (λ) of X-rays coincides with the atomic spacing (d) in the solids, it diffracts in those orientations of 2θ, where the Bragg condition of diffraction [86] i.e. $2d \sin\theta = n\lambda$ (θ being the angle which incident beam makes with the plane of sample) is satisfied. While recording the diffraction pattern with detector, the sample is synchronously rotated along with the detector, such that the incident X-ray incident beam makes an angle θ with the plane of sample whereas detector is at angle 2θ with respect to incident beam. This is commonly known as θ-2θ scan of X-ray diffraction. The recorded diffraction pattern is compared with standard pattern to get information about the phase of the samples. The lattice parameters are obtained by fitting the recorded diffraction peaks using least-square fitting software.

2.3.8.2 Grazing angle XRD

In powder or normal geometry contribution from the substrate to diffraction can sometimes overshadow the contribution from the thin films. Therefore the structures of the very thin films (typically less than 20 nm) were investigated by Grazing angle X-ray diffractometer. The schematic of this diffraction configuration is shown in the Fig. 2.15. In this configuration, incident X-ray falls at a very small angle (e.g. 0.1°) which is fixed with the sample surface and detector does 2θ scan. The sampling depth (D) is related with angle of incidence (φ) by the formula,

$$D_{(\varphi)} = \frac{\lambda}{4\pi q}$$

where λ is the x-ray wave length (1.541Å), and

$$q = \left[\sqrt{\left(\varphi^2 - \varphi_c^2\right) + 4(\delta_i)^2} + \varphi_c^2 - \varphi\right]^{1/2} \left(\sqrt{2}\right)^{-1}$$

$\delta_i = \lambda(\frac{\mu}{4\pi})$, φ_c is the critical angle of incidence and μ is the linear absorption coefficient [87] . In the present studies, we have employed φ = 0.1°, which leads to a sampling depth of ~ 10 nm; and thus this technique becomes ideal for analyzing the structure of very thin films without having interference from the substrates.

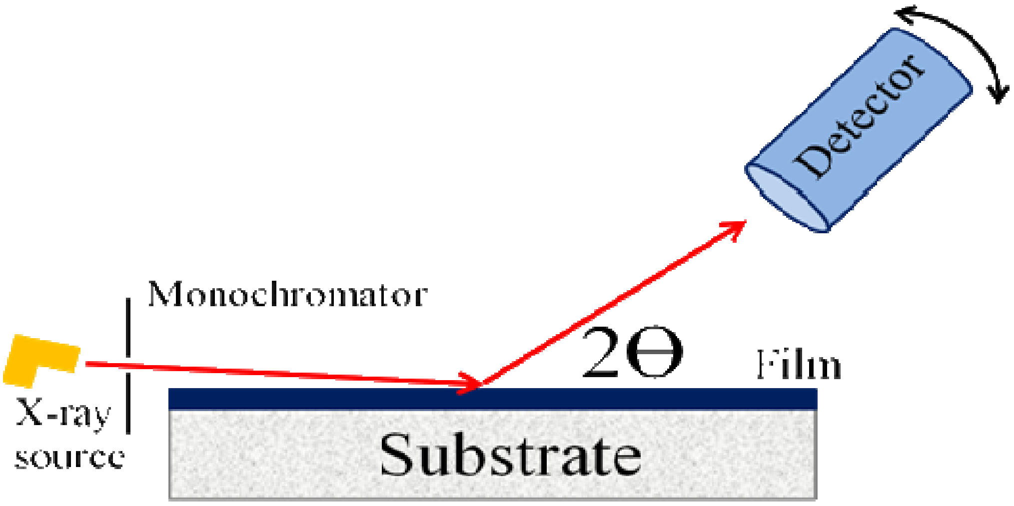

Figure 2.15 Schematic diagram of the grazing angle X-ray diffraction.

2.3.9 X-ray reflectivity

When X-ray beam falls on a surface it under goes total external reflection below certain critical angle (θ_c). Above the θ_c, the X-ray starts penetrating inside the layer and the reflectivity of the sample falls off with a slope depending on the incidence angle and the roughness of the interface. The oscillation on the reflectivity spectrum above θ_c (generally known as the Kiessig oscillations) is due to the finite thickness of the layer. In general, the thickness of the film can be obtained from the frequency of oscillation, while the slope of the curve gives the roughness of the interface [88]. Grazing incidence X-ray reflectivity (GIXRR) for Pc thin films was carried out using CuK$_\alpha$ radiation (1.54 Å) on a computer-controlled reflectometer (Kristalloflex 710 D X-ray generator (SIMENS) and D5000 diffractometer) and the obtain reflectivity data fitted theoretically to extract thickness and interface roughness.

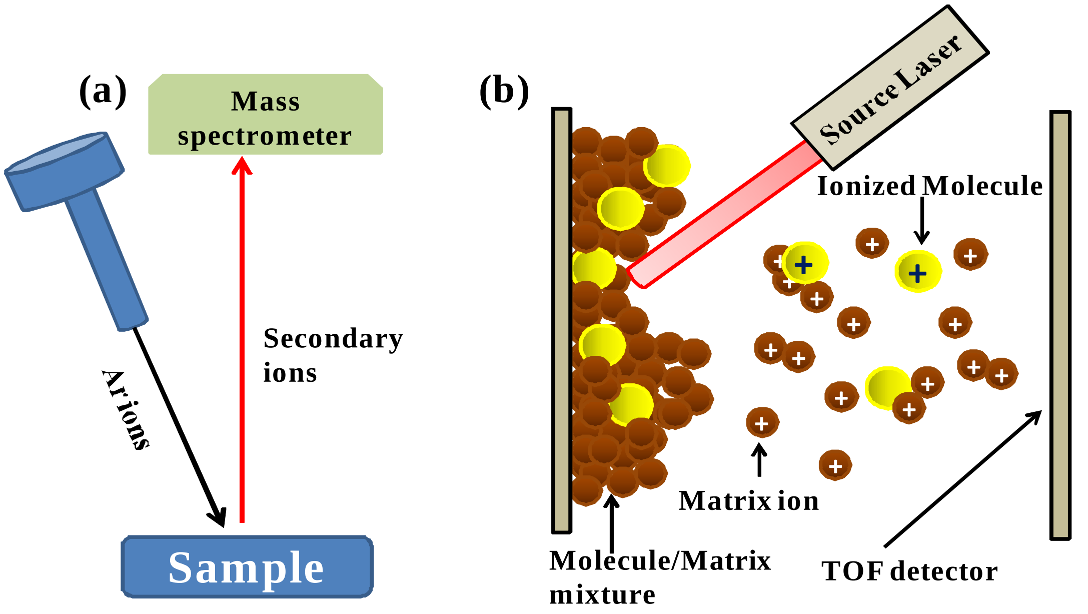

Figure 2.16 Schematics diagrams of (a) SIMS and (b) MALDI techniques.

2.3.10 Secondary Ion Mass Spectrometry (SIMS) and Matrix-assisted laser desorption/ionization (MALDI)

Both techniques (SIMS and MALDI) give information about the molecular mass. In SIMS technique, sample is bombarded with high energy Ar ion (~ 5-40 keV), which sputter the films in the forms of ionized molecules / their fragmented parts. The resulting of ionized molecules / their fragmented are accelerated into a mass spectrometer, where they are mass analyzed by measuring their time-of-flight (TOF) from the sample surface to the detector as schematically shown in Fig. 2.16 (a).

In case of MALDI, a sample is mixed or coated with an energy absorbing matrix and subsequently a laser beams (N_2 laser, wavelength ~ 300 nm, energy density ~ 20 $\mu J/cm^2$) falls on the films as schematically shown in Fig. 2.16 (b). This process assist in emission of molecular ion, which later analyzed using TOF mass spectrometer, ions are separated and recorded based on their mass (molecular mass) to charge ratio (*m/z*). The desorption process in MALDI is soft with very low fragmentation of analyte molecules [89].

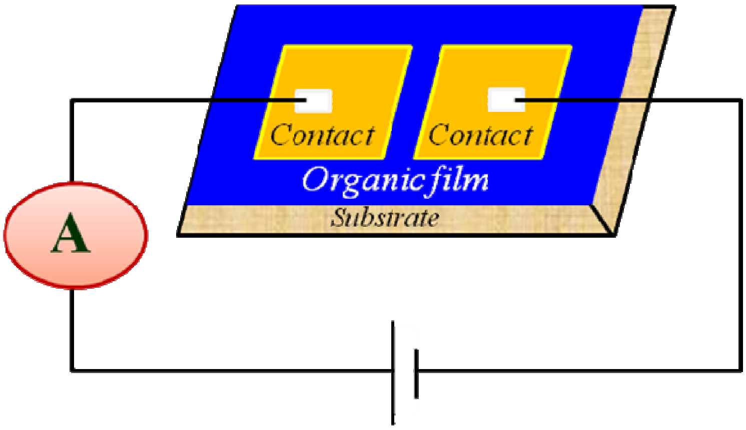

Figure 2.17 A schematic of in plane charge transport measurement geometry.

2.4 Charge transport measurement

For electrical and gas sensing measurement gold electrode were deposited by thermal evaporation method. Gold pads (size: 2 mm ×3 mm) were deposited through a metal mask with different electrode spacing (12 µm). The films are loaded in vacuum chamber which is connected to a TMP based vacuum pumping system. To deposit gold electrodes, 99.99% pure gold wire is loaded on a tungsten filament, which was resistively heated by external power supply. To prevent diffusion of gold atoms into the Pc films, electrodes are deposited with very slow rate (0.5 Å/s). The deposition rate and thickness of the deposited electrodes is monitored through a quartz crystal monitor.

The charge transport measurements were carried out using in planar geometry. The in-plane geometry, as shown in Fig. 2.17, has following distinct advantages over the out-of-plane geometry in which films is sandwiched between two electrodes.

(i) In the out-of-plane geometry, metal atoms from the electrode can get incorporated in the films, which can act as charge trapping centers, and hence, can give rise to hysteresis in *J-V* characteristics [109]. This makes it difficult to isolate the intrinsic hysteretic effect. This problem will not arise in the in-plane geometry, as the electrodes are far apart (12 μm).

(ii) Large electrode spacing also indicates that the contribution of contact resistance is very small compared to the film resistance.

Therefore in our studies we measured *J-V* characteristics using two-probe in-plane geometry. To measure *J-V* characteristics a silver wire is attached to the previously deposited electrode by conducting silver paint. Keithley 6487 picoammeter/voltage source and computer based data acquisition system were used to record the *J-V* characteristics. All measurements were carried out in dark to avoid the problem of photoconductivity. In order to rule out the effect of film inhomogeneities, *J–V* characteristics were measured on at least three pairs of electrodes deposited on a film at different positions. For measuring the temperature dependence of the resistivity and temperature dependent *J–V* characteristics, the samples were mounted in a closed cycle cryostat. The cryostat (CCR APD Cryogenics make) consists of a compressor, which compresses the Helium gas and expands it in the vicinity of the sample chamber. Because of Joule Thomson expansion of Helium gas, its temperature falls and it cools the region surrounding it. Platinum resistance sensors (Pt-100) are used to monitor the temperature. Lakeshore temperature controller (Lakeshore 330 auto tuning temperature controller) controls temperature of the sample chamber. A small manganin heater was used to heat the sample for measurements of transport properties at different temperatures.

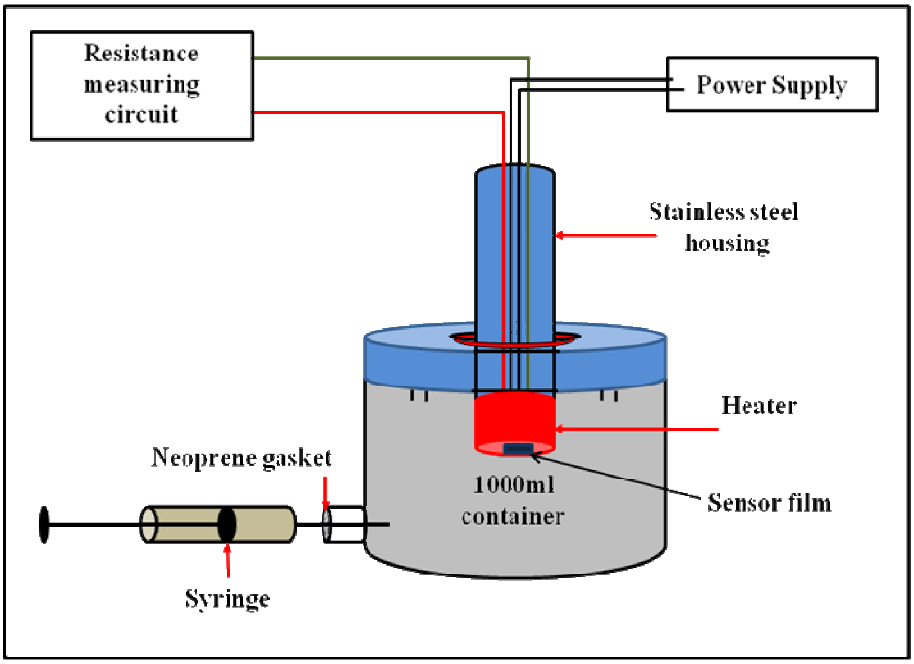

Figure 2.18 Schematic representation of gas sensing measurement setup.

2.5 Chemiresistive gas sensing measurement

The gas sensitivity of the films was measured using a home-made gas sensitivity measurement setup, as shown in Fig 2.18. The sensor films are mounted on a heater surface. The temperature of the heater was controlled by an external power supply and temperature controller. The sensor assembly was mounted in a leak tight 1000 ml stainless steel container, and the known amount of gas (to be sensed) was injected into the chamber using a micro-syringe. To measure the response of the sensor films for a particular gas, current at a particular bias as a function of time was measured by Keithley make 6487 picoammeter/voltage source and computer based data acquisition system. For the recovery of the sensor, the chamber was exposed to the ambient atmosphere. A photograph of gas sensing setup, used in the present study is shown in Fig. 2.19 (a). The sample was mounted on a heater in a leak tight stainless steel chamber (net volume: 1000 cm^3) as shown in Fig. 2.19 (b).

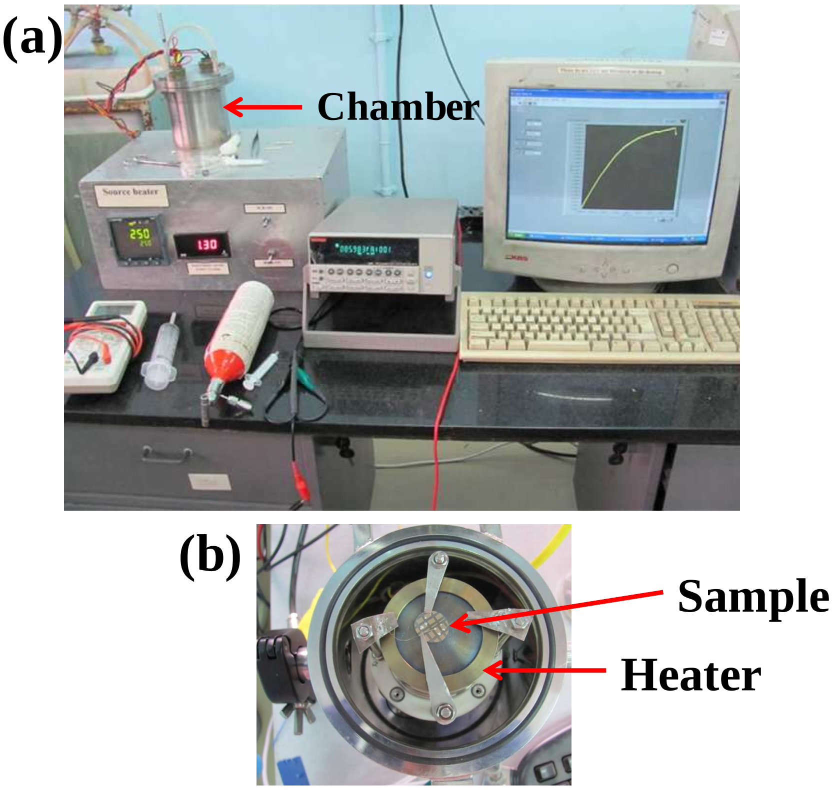

Figure 2.19 A photograph of (a) gas sensing setup and (b) top view of stainless steel chamber.

CHAPTER-3

GROWTH AND CONDUCTION MECHANISM OF MONONUCLEAR AND BINUCLEAR PHTHALOCYANINE FILMS

3.1 Growth of mononuclear phthalocyanine films

In this section we discuss the results on the growth and characterization of phthalocyanine films deposited by MBE as well as solution processing.

3.1.1 Phthalocyanine films by MBE

Thin films of *p*-type FePc, CoPc as well as *n*-type F_{16}CuPc films were deposited by MBE on various substrates (0001) Al_2O_3, twinned (001) $LaAlO_3$, and (100) $SrTiO_3$ substrates. We have optimized all the deposition parameters, such as, film thickness, deposition rate, and substrate temperature. The optimized values of these parameters are respectively, 20 nm, 0.2 nm/s and 200°C. All the results in this thesis work are presented using films grown under these optimized parameters until unless specifically mentioned.

3.1.1.1 FePc films

Here we describe the results on FePc films deposited on (0001) Al_2O_3 substrate. Al_2O_3 crystalline substrate in its pure form is also known as *sapphire* or *corundum*. The (0001) orientation of Al_2O_3 substrate is shown in Fig. 3.1 (a) and is described by in terms of hexagonal four-dimensional Miller-Bravais indices [90]. The unit cell parameters are a = 4.757 Å, b = 4.757 Å, c = 12.9877 Å and $\alpha = 90°$, $\beta = 90°$, $\gamma = 120°$ [91]. The structure of Al_2O_3 is consists of a hexagonal closed packed structure consists of 12 Al^{3+} and 18O^{2-}. The oxygen stacking sequence runs along the c-axis, and a unit cell consists of six oxygen layers, giving six formula units per unit cell. The normal termination for the clean (0001) α-Al_2O_3 is one Al ion per three O ions with Al terminal ion slightly above the plane of closely packed oxygen [92]. The Al terminated surface or some time hydroxylated Al terminated surface become very reactive to the phthalocyanine molecules [93]. The AFM image shown of the (0001) Al_2O_3 sapphire substrate is shown in Fig. 3.1 (b) that has a roughness of < 0.25 nm.

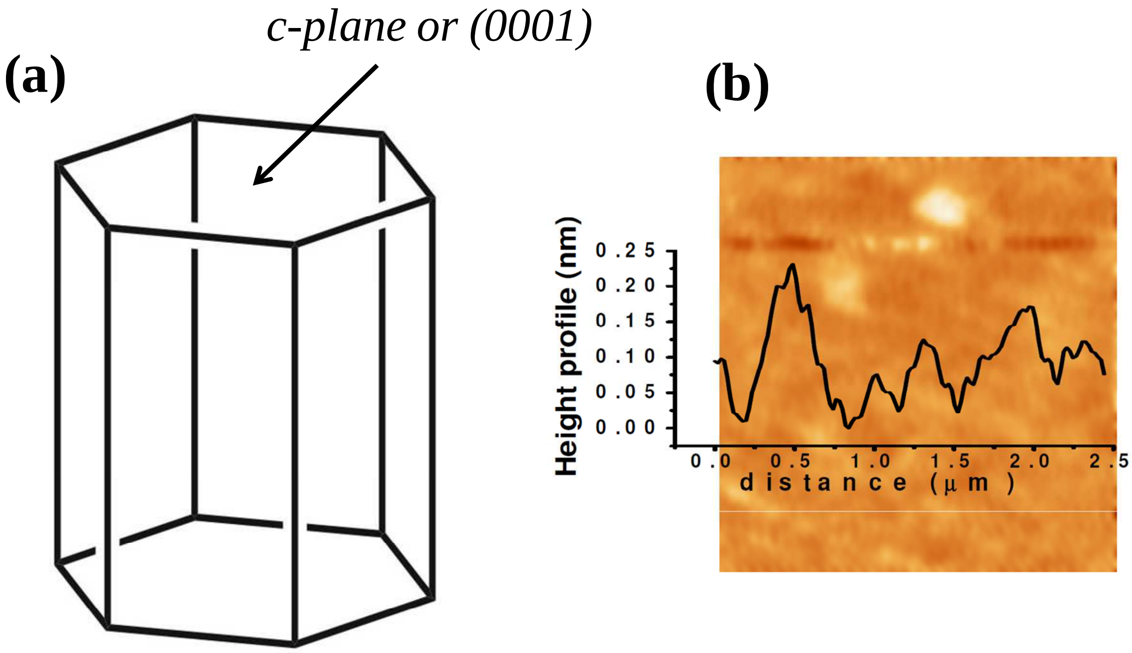

Figure 3.1 (a) Representation of (0001) orientation of hexagonal Al_2O_3 substrate. (b) AFM image of (0001) Al_2O_3 substrate.

Typical GIXRD spectrum of the FePc film deposited on (0001) Al_2O_3 is shown in Fig. 3.2 (a). Presence of a single intense Bragg peak at an angle of 25.90º (FWHM ~ 0.16º), indicates that film is highly crystalline in nature. From this data the estimated inter-planer distance was found to be 0.34 nm. It indicates that the FePc molecules are lying flat on the substrate and are stacked *face-to-face* with *b*-axis parallel to the surface normal as shown in Fig 3.2 (b) [94]. A possible reason for the *face-on* stacking could be the interaction between metal atoms of FePc molecules and (0001) Al_2O_3 surface. It has been reported in literature that (0001) Al_2O_3 surfaces are highly reactive and metal films deposited in these substrates grow in a layer by layer (i.e. Frank van der Merwe mode) growth mode [93, 95] . However, the effect of substrate no longer remains as the thickness is increase e.g. films having thickness ~ 100 nm exhibited a polycrystalline nature [96].

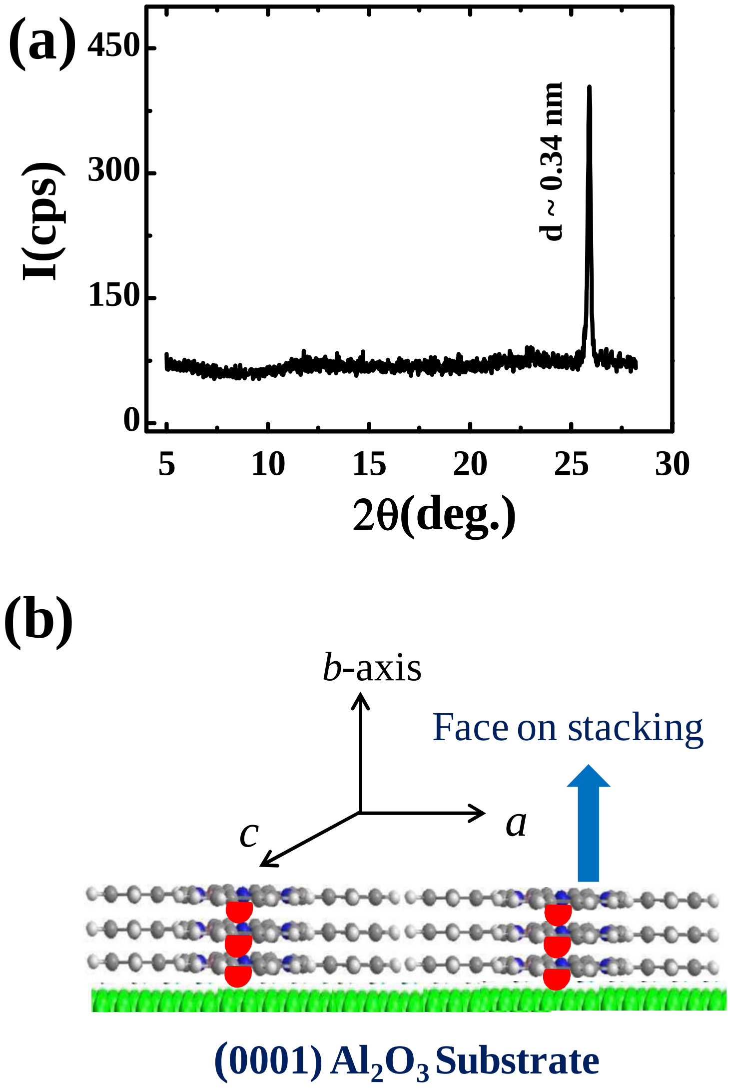

Figure 3.2 (a) GIXRD pattern of FePc films on (0001) Al_2O_3 substrate (b) Schematic depicting the molecular stacking of FePc molecules in *face-on* configuration.

Fig. 3.3 (a) shows typical 5 µm x 5 µm AFM image of FePc film grown on (0001) Al_2O_3 substrate. It apparent that the morphology of films consists of dense packed grains. Fig. 3.3(b) shows the roughness profile along the line drawn in Fig. 3.3 (a). It is observed that most of the grains coalesce and few of them have excess growth perpendicular to the substrate plane. The average surface roughness of the film was found to be ~3 nm.

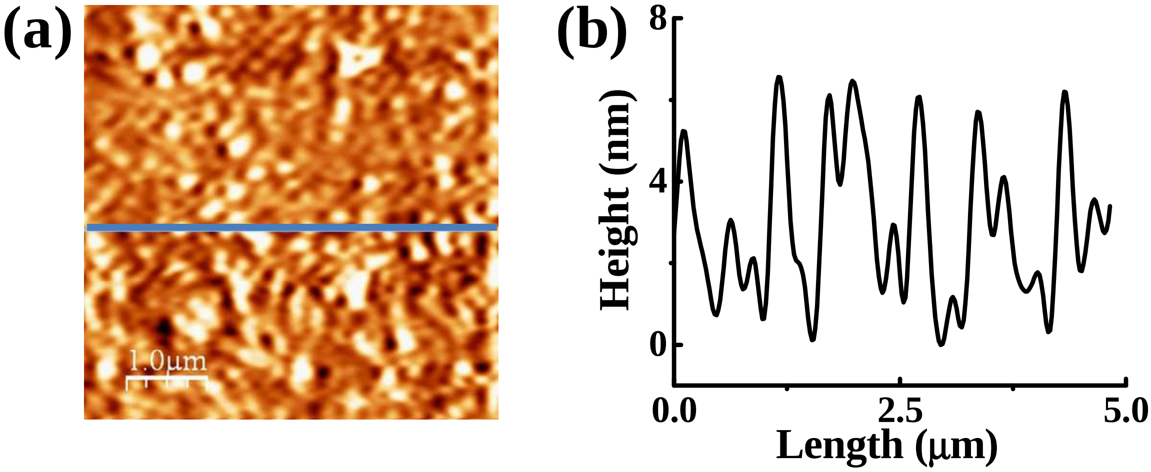

Figure 3.3 (a) AFM images (size: 5 µm x 5 µm) of the FePc films on (0001) Al_2O_3 substrate. (b) Height profile is given along the line drawn on the image.

Typical UV-Visible spectrum recorded for FePc films is shown in Fig. 3.4. In the near UV region the B-band or Soret band representing the π-π^* transition appears at peak position 326 nm. The Q- band near the visible region, which originates from π-π^* transition in the porphyrin ring appears at 561 and 619 nm [97]. For the FePc powder dissolved in chloroform solution, the Q- band appears at 588 nm and 705 nm (shown inset of Fig 3.4). The blue shift of the UV-visible spectrum for the films as compared to FePc powder dissolved in chloroform solution confirms the *face-on* stacking (H- aggregation) of the molecules [98].

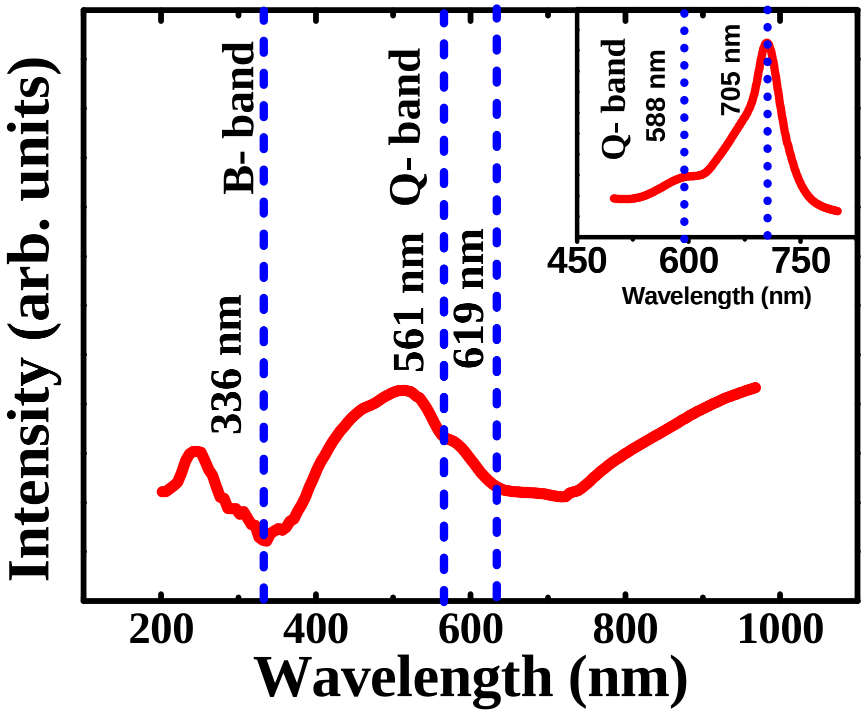

Figure 3.4 UV-Vis spectrum for FePc films (the inset shows UV-Vis spectra for FePc powder dissolved in chloroform solution).

3.1.1.2 CoPc films

Here we present the results on the CoPc films deposited on (0001) Al_2O_3 and (100) $SrTiO_3$ substrates.

(a) CoPc films on (0001) Al_2O_3 substrate

The GIXRD pattern of the CoPc films grown on (0001) Al_2O_3 substrate is shown in Fig. 3.5. Presence of a single intense Bragg peak at 25.88° (equivalent to intermolecular plane distance of 3.45 Å), corresponds to the *face-on* stacking of the molecules. It indicates that the CoPc molecule lying is highly crystalline with *b*-axis normal to the substrate, which is identical to that of FePc films.

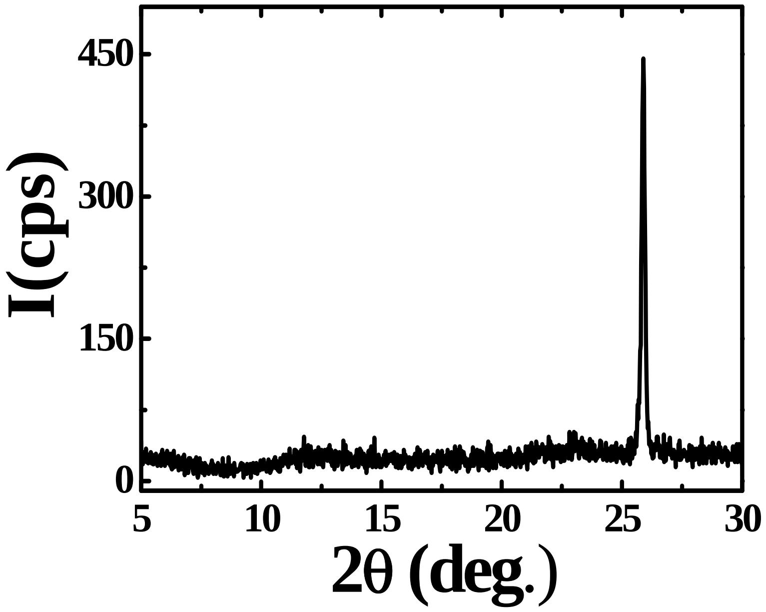

Figure 3.5 GIXRD pattern of CoPc films grown on (0001) Al_2O_3 substrate.

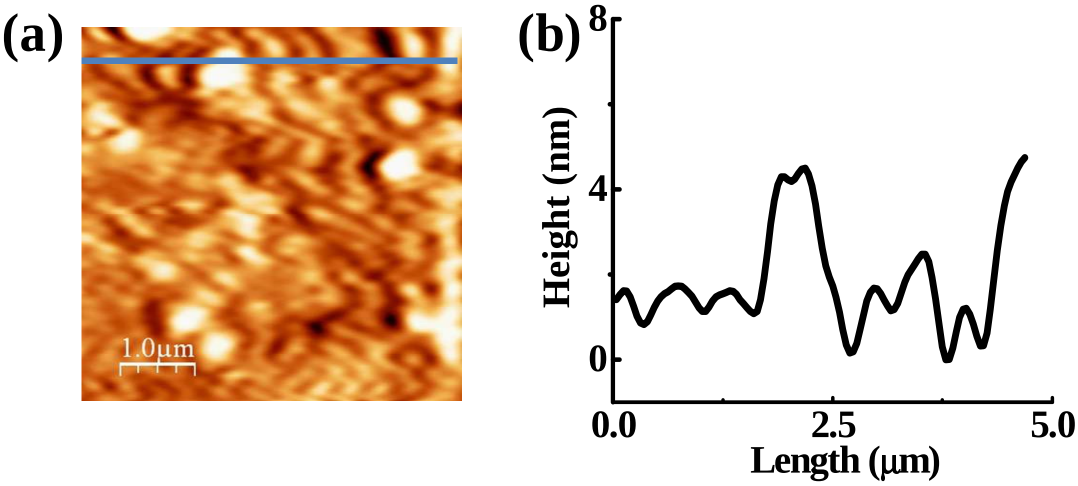

Figure 3.6 (a) AFM image (size: 5 μm x 5 μm) of the CoPc films on (0001) Al_2O_3 substrate. (b) Height profile is given along the line drawn on the image.

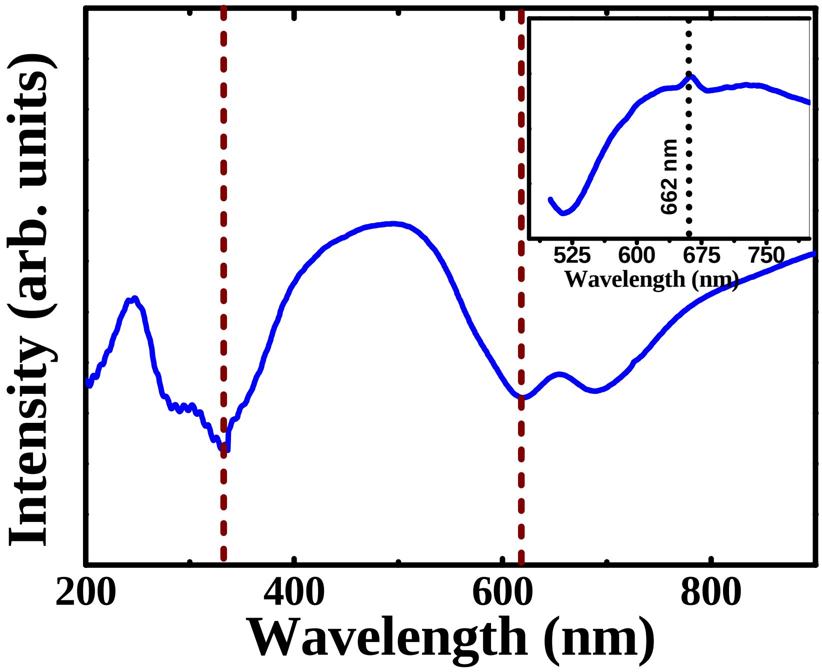

Figure 3.7 UV-Vis spectrum for FePc films (the inset shows UV-Vis spectra for CoPc powder dissolved in chloroform solution.).

Fig. 3.6 (a) shows typical AFM image of CoPc films grown on (0001) Al_2O_3 substrate. It reveals that film consists of highly dense grains. Fig. 3.6 (b) shows the roughness profile along the line drawn in Fig. 3.6 (a), which reveals an average roughness of 2.5 nm.

In UV-Visible spectrum recorded CoPc films (shown in Fig. 3.7) a sharp B-band or Soret band representing the π-π^* transition appearing at 326 nm. The Q- band appears at around 620 nm. For the CoPc powder dissolved in chloroform solution, the Q- band appears at 662 nm. The blue shift of the UV-visible spectrum for the films as compared to powder of these molecules dissolved in chloroform solution confirms the *face-on* stacking (H-aggregation) of the CoPc molecules.

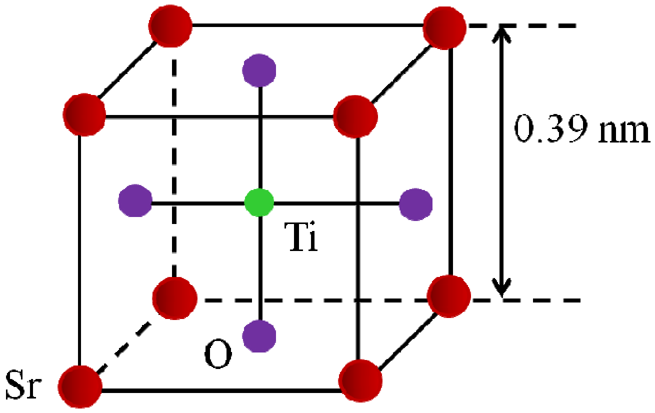

Figure 3.8 $SrTiO_3$ unit cell at room temperature which shows a cubic structure.

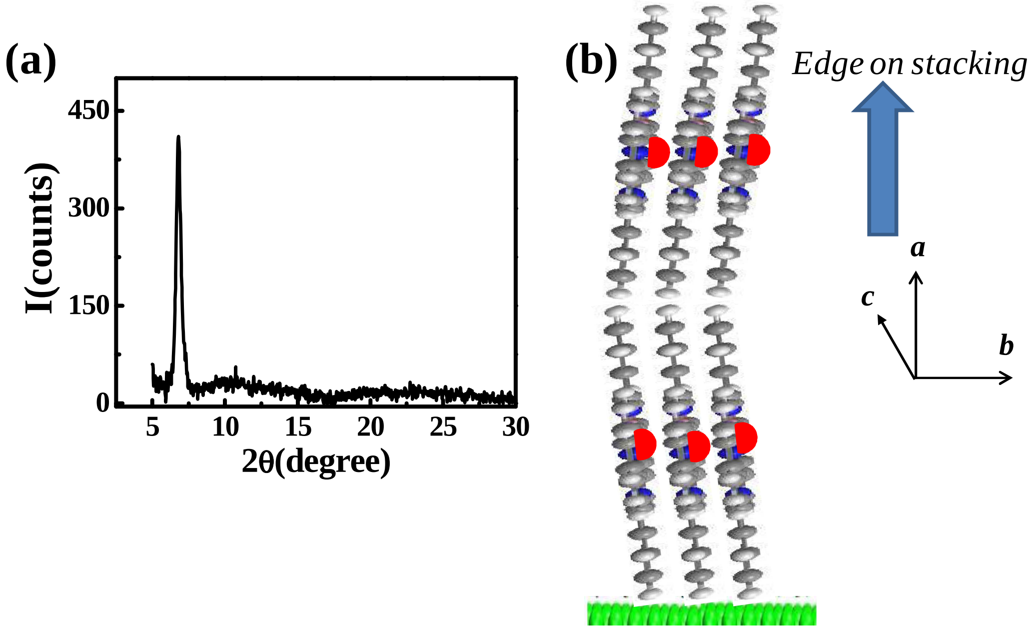

Figure 3.9 (a) GIXRD data for CoPc films grown on (100) $SrTiO_3$ (b) Schematic representation of the stacking of CoPc molecules with *a*-axis perpendicular to the substrate plane.

(b) CoPc films on (100) $SrTiO_3$ substrate

The (100) $SrTiO_3$ (also abbreviated as STO) has cubic structure, as shown in Fig. 3.8 with lattice parameter *a* = 3.9 Å at room temperature. It goes a structural phase transition from cubic to tetragonal at 105K [99].

A GIXRD spectrum for CoPc films grown on (100) $SrTiO_3$ is shown in Fig. 3.9 (a). In GIXRD, presence of a Bragg peak at 6.7°, corresponding to the (002) peak of α-CoPc phase, indicates that films are crystalline with *a*-axis normal to the surface and molecules are stacked edge to edge [66]. In this molecular orientation *b*-axis (*π*-*π* staking direction) is parallel to the substrate plane as shown in Fig. 3.9 (b).

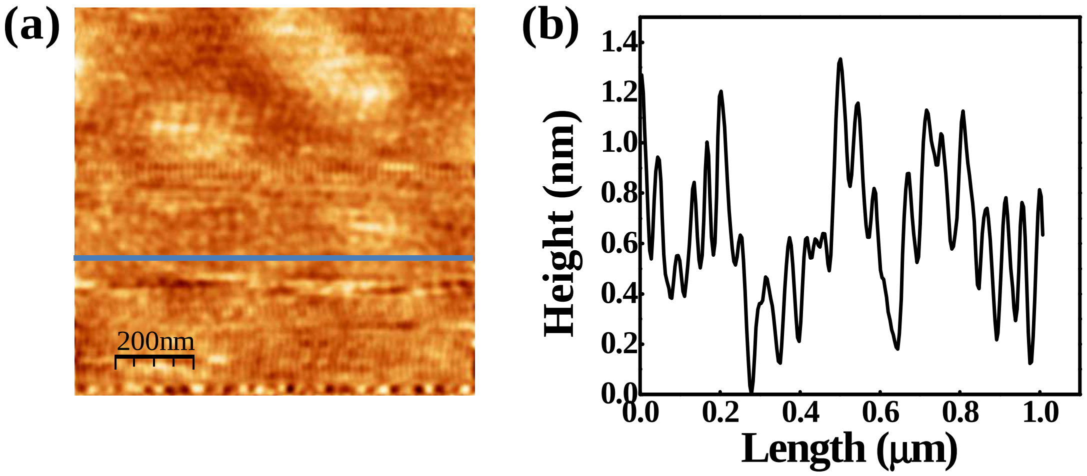

Figure 3.10 AFM image of CoPc films on (100) $SrTiO_3$ substrate.

The AFM image of CoPc films on (100) $SrTiO_3$ along with height profile is shown in Fig. 3.10 (a). Fig. 3.10 (b) shows the roughness profile along the line draw in Fig 3.10 (a). It reveals that films consists of highly dense CoPc grains and very smooth in nature with average roughness 0.6 nm.

3.1.1.3 F_{16}CuPc films

F_{16}CuPc films were deposited on twined (001) $LaAlO_3$ substrate. The high temperature phase of $LaAlO_3$ is cubic whereas the room temperature structure is rhombohedral. The lattice parameters of rhombohedral $LaAlO_3$ at room temperature are *a* = 5.357 Å, α = 60°6', which corresponds to *a* = 3.79 Å, α = 90°5' based on a pseudo-cubic cell [100]. Since α is larger than 90°, $LaAlO_3$ is associated with a spontaneous strain along the cubic <111> directions during the cubic to rhombohedral transition. To compensate this spontaneous strain the twinning arises.

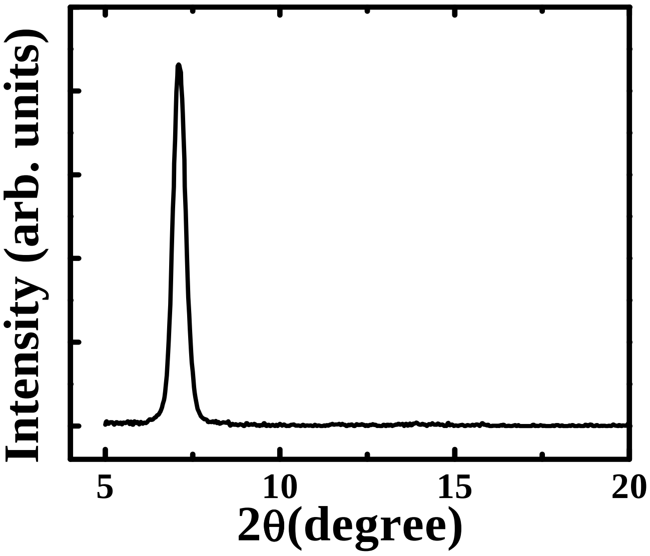

Figure 3.11 GIXRD data for F_{16}CuPc film grown on (001) $LaAlO_3$ substrate.

The GIXRD data of F_{16}CuPc films on $LaAlO_3$ substrate is shown in Fig. 3.11. The GIXRD peaks appears at the 7.17°, indicating that F_{16}CuPc molecules are stacked edge to edge with *a*-axis normal to the surface which is identical to the CoPc molecule stacking on (100) $SrTiO_3$ substrate.

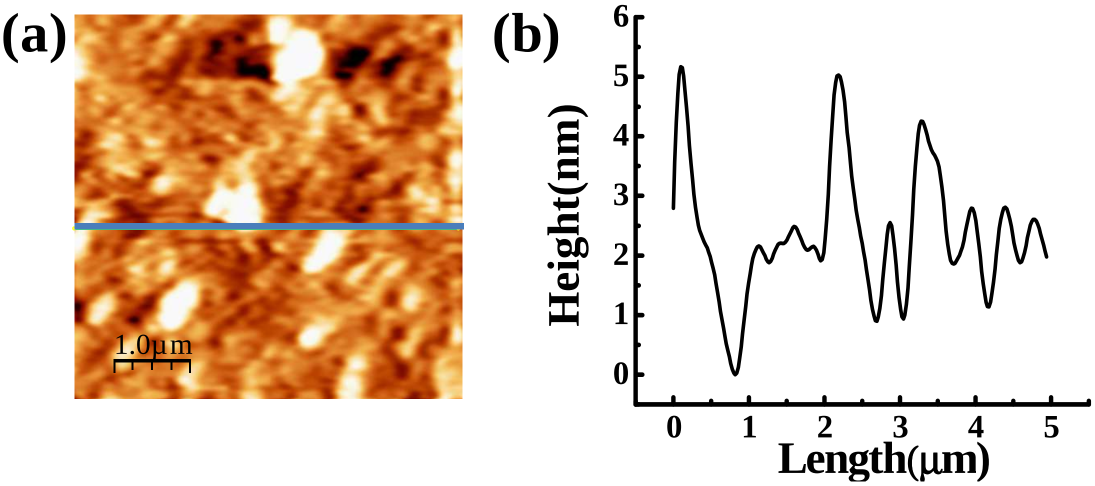

Figure 3.12 (a) AFM image (size: 5 µm x 5 µm) of F_{16}CuPc films on (001) $LaAlO_3$ substrate. (b) Height profile is given along the line drawn on the image.

Fig. 3.12 (a) shows typical AFM image of F_{16}CuPc films grown on $LaAlO_3$ substrate. It reveals that film consists of highly dense grains. Fig. 3.12 (b) shows the roughness profile along the line drawn in Fig. 3.12 (a), and it shows that films have an average roughness of 1.2 nm.

3.1.2 Sulfonated phthalocyanine films by solution process

Thin films of CuPcTs of nominal thickness ~ 1µm were prepared by drop cast method on pre-cleaned quartz and (0001) Al_2O_3 substrate and finally vacuum annealed at 250°C for 15 min. The detail of the deposition is discussed in Chapter 2.

Typical SEM images and GIXRD pattern of CuPcTs films on quartz and (0001) Al_2O_3 substrates are shown in Fig. 3.13 (a) and (b) respectively. It is clear that the morphology of CuPcTs films is identical deposited on quartz and (0001) Al_2O_3. Absence of the any peak in the XRD data shows that these films are amorphous in nature. In case of drop cast method role of substrate (i.e roughness and chemical reactivity) is not as important as in MBE deposition. A photograph of drop cast films is shown in Fig. 3.13 (c), which indicates the non-uniformity of the films, in particularly at the edges of the substrate. This is expected due to the evaporation of the solution drop.

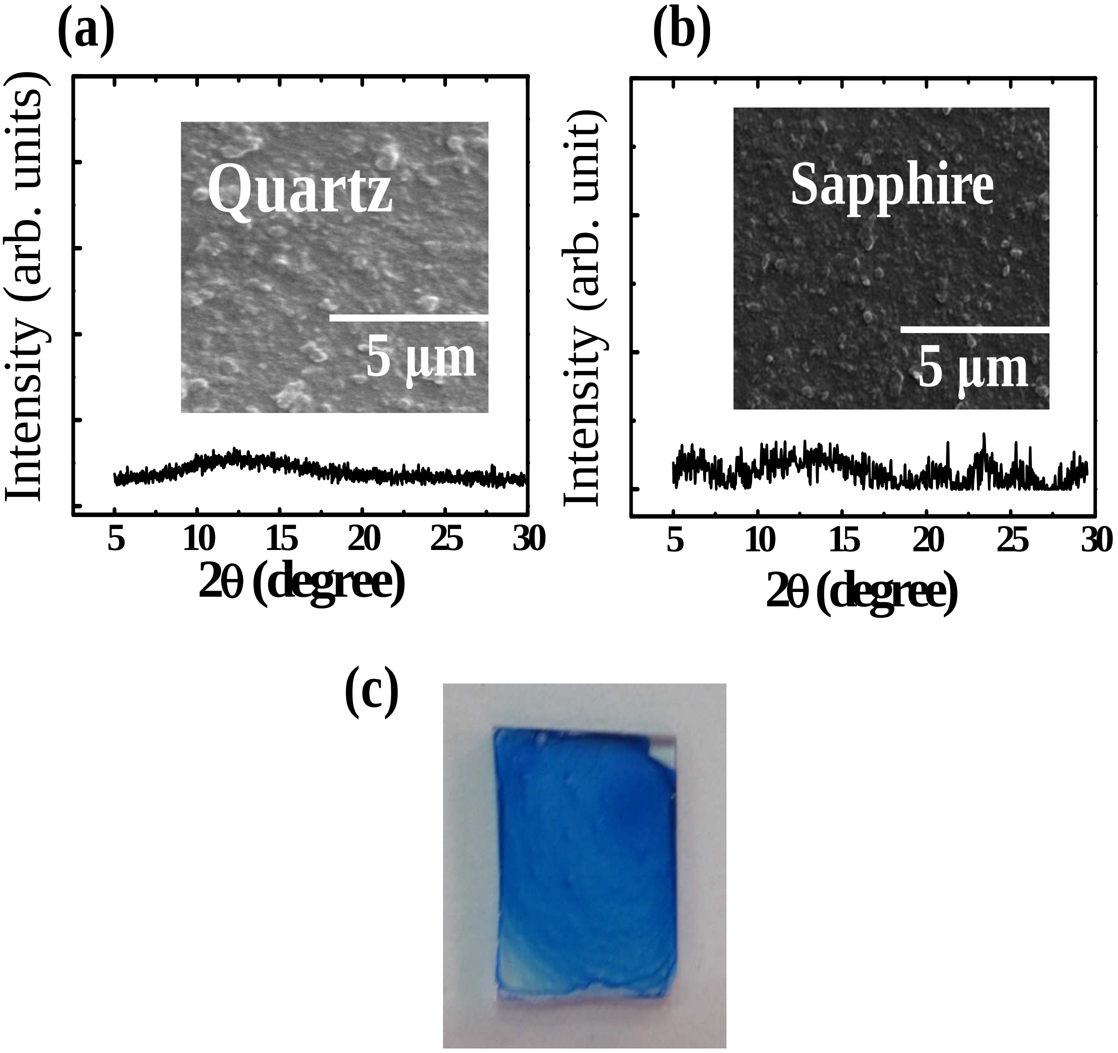

Figure 3.13 GIXRD patterns and SEM images of drop casted CuPcTs films (a) on quartz substrate (b) (0001) Al_2O_3 substrate (c) A photograph of drop casted CuPcTs film on quartz substrate.

3.2 Growth of binuclear (Co-Fe)Pc films by MBE

In this section we present the growth of binuclear (Co-Fe)Pc films on (0001) Al_2O_3 substrates. For preparing binuclear films two methodologies were adopted: (i) co-evaporation from independent CoPc and FePc sources with deposition rates independently controlled by source temperatures and (ii) using evaporation of a homogenous mixture of CoPc and FePc in equal weight ratio prepared by grinding for 30 min. Both routes yielded similar results. The second approach is relatively easier to control and hence all the samples reported in the present study were prepared using this approach. The characterization of binuclear (Co-Fe)Pc films is presents below.

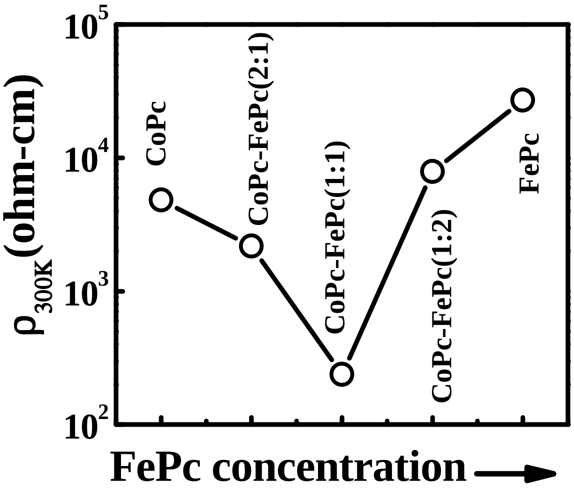

Figure 3.14 Room temperature resistivity (ρ_{300K}) of composite CoPc-FePc films as a function of FePc concentration.

3.2.1 Room temperature resistivity

Fig. 3.14 shows the variation of room temperature resistivity (ρ_{300K}) measured at 50 V as a function of FePc concentration in the composite CoPc-FePc films. The resistivity is found to be for concentration of 1:1 due the formation of minimum binuclear (Co-Fe)Pc (as discussed later) and is significantly higher for individual films. The results indicate best transport characteristics for binuclear (Co-Fe)Pc films and therefore these binuclear (Co-Fe)Pc films have been further studied.

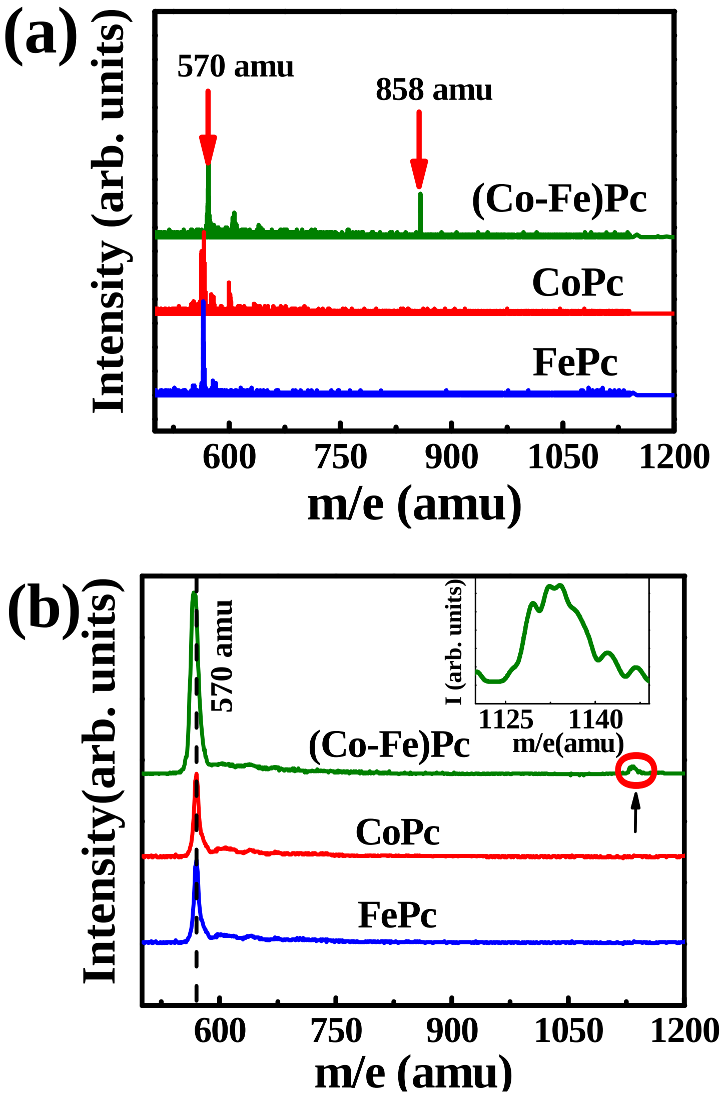

Figure 3.15 (a) Secondary ion time of flight mass spectrometry (SIMS) data. (b) Matrix assisted laser desorption ionization time of flight mass spectrometry (MALDI) data for FePc, CoPc and binuclear (Co-Fe)Pc films.

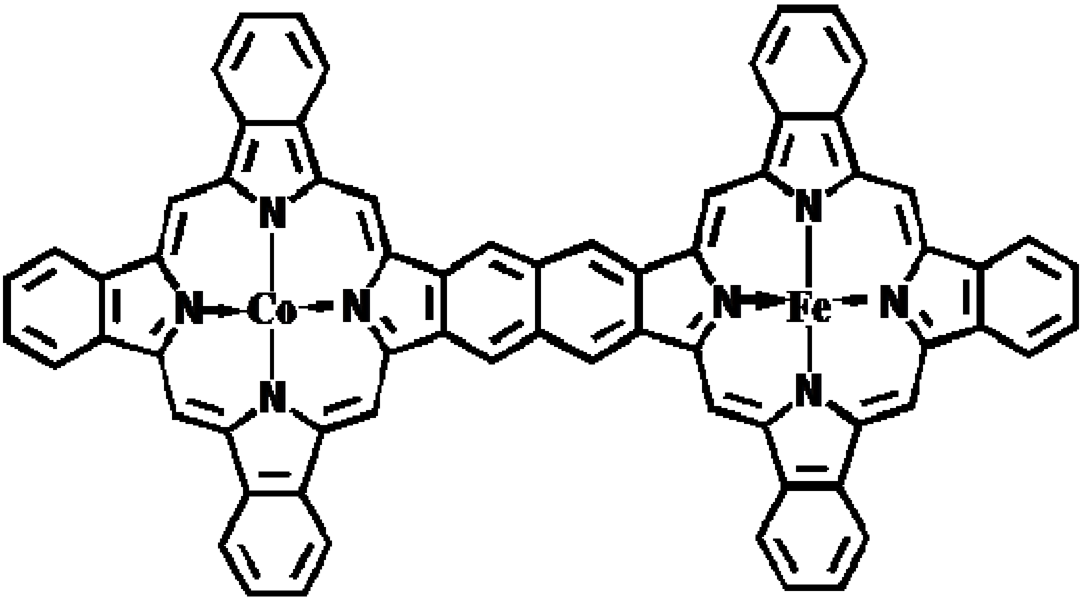

Figure 3.16 Schematic showing the chemical structure of binuclear (Co-Fe)Pc molecule.

3.2.2 Mass spectrometry study

The binuclear (Co-Fe)Pc films along with mononuclear FePc and CoPc films were characterized by (Secondary Ion Mass Spectroscopy) SIMS and (Matrix Assisted Lasers Desorption Ionization) MALDI time of flight mass spectrometry. The results obtained from SIMS and MALDI techniques are shown in Fig. 3.15 (a) and (b) respectively. In the SIMS spectra for all films monomer peak is present at ~ 570 amu, however for binuclear films there is an additional peaks at 858 amu, which suggest that in binuclear films there are molecules having higher molecular mass than individual FePc or CoPc. This indicates that the binuclear molecules undergo fragmentation. This picture is clearer in the MALDI spectrum shown in Fig. 3.15 (b). Here in addition to monomer peak present for all films, additional peak at higher molecular mass (1136 amu), which is almost double as compared to the monomer mass, confirming the formation of binuclear (Co-Fe)Pc molecules. The proposed molecular structure of a binuclear (Co-Fe)Pc molecules is shown in Fig. 3.16. In this scheme CoPc and FePc are covalently joined through the corner benzene ring.

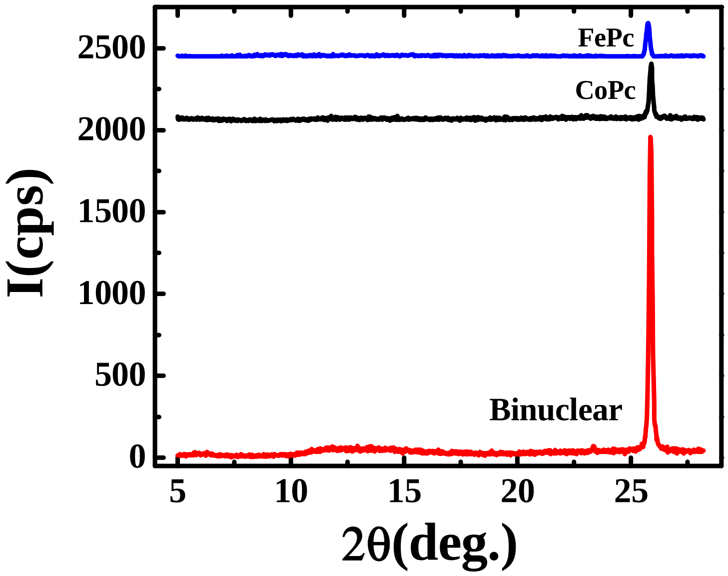

Figure 3.17 GIXRD spectra of binuclear (Co-Fe)Pc films along with CoPc and FePc films.

3.2.3 Structure and morphological characterization

The GIXRD spectra of binuclear (Co-Fe)Pc films along with mononuclear CoPc and FePc films are shown in Fig. 3.17. A single peak at an angles 25.88° (FWHM~ 0.14°) were observed for binuclear films and estimated inter-planer distance was found to be 3.43Å for binuclear films. It indicates that binuclear molecules are lying nearly flat on the substrate and are stacked *face-to-face*, with the short *b*-axis parallel to the surface normal similar to mononuclear molecules, which we have already discussed. As the spectra of binuclear films has been measured under similar conditions along with individual films of same thickness, high intensity, and smallest full width half maximum (FWHM) of binuclear films indicates the better *face-on* stacking of the molecules compared to mononuclear films.

The AFM image shows dense and smooth morphology of binuclear (Co-Fe)Pc films indicating the films grow in 2-dimensional growth mode as shown in Fig. 3.18 (a). Fig. 3.18 (b) shows the roughness profile along the line draw in Fig. 3.18 (a) and it shows that average roughness of (Co-Fe)Pc films is 1 nm. It indicates (Co-Fe)Pc films are smoother than mononuclear CoPc and FePc films.

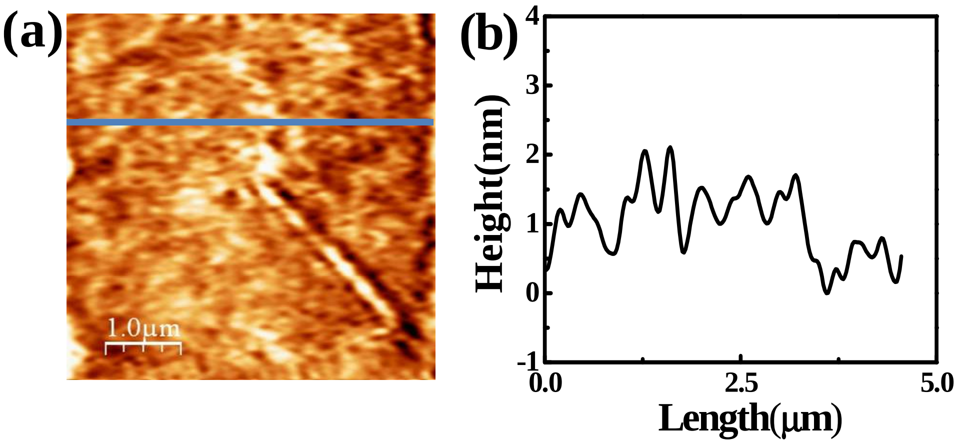

Figure 3.18 (a) AFM image of binuclear (Co-Fe)Pc film. (b) Height profile is given along the line drawn on the AFM image.

3.2.4 X-ray photoelectron spectroscopy study

The X-ray photoelectron spectroscopy (XPS) data's for the FePc, CoPc and binuclear (Co-Fe)Pc films are shown in Fig. 3.19. It can be seen that for binuclear (Co-Fe)Pc phthalocyanine Co-2p$_{3/2}$, Fe-2p$_{3/2}$, N-1s and C-1s peaks shifts to higher binding energy values. An increase in binding energy of core electrons of any element indicates that valence electrons of the atoms are participating in the bonding. Therefore for binuclear (Co-Fe)Pc films it can be concluded that effective valence electron cloud of pyrrole rings and central metal (cobalt / iron) has shifted towards benzene rings of the molecules and takes part in molecular bonding. The feature of this bonding between two molecules can be seen in the C-1s spectra, where a new peak at binding energy of ~ 288 eV has evolved for binuclear films. Our XPS results are in contrast with the results of the Zhang et. al , where their XPS results show that the two different metal phalocyanines in their binuclear films are electronically non-interacting, however a new phase with improved ordering of molecules is formed [101].

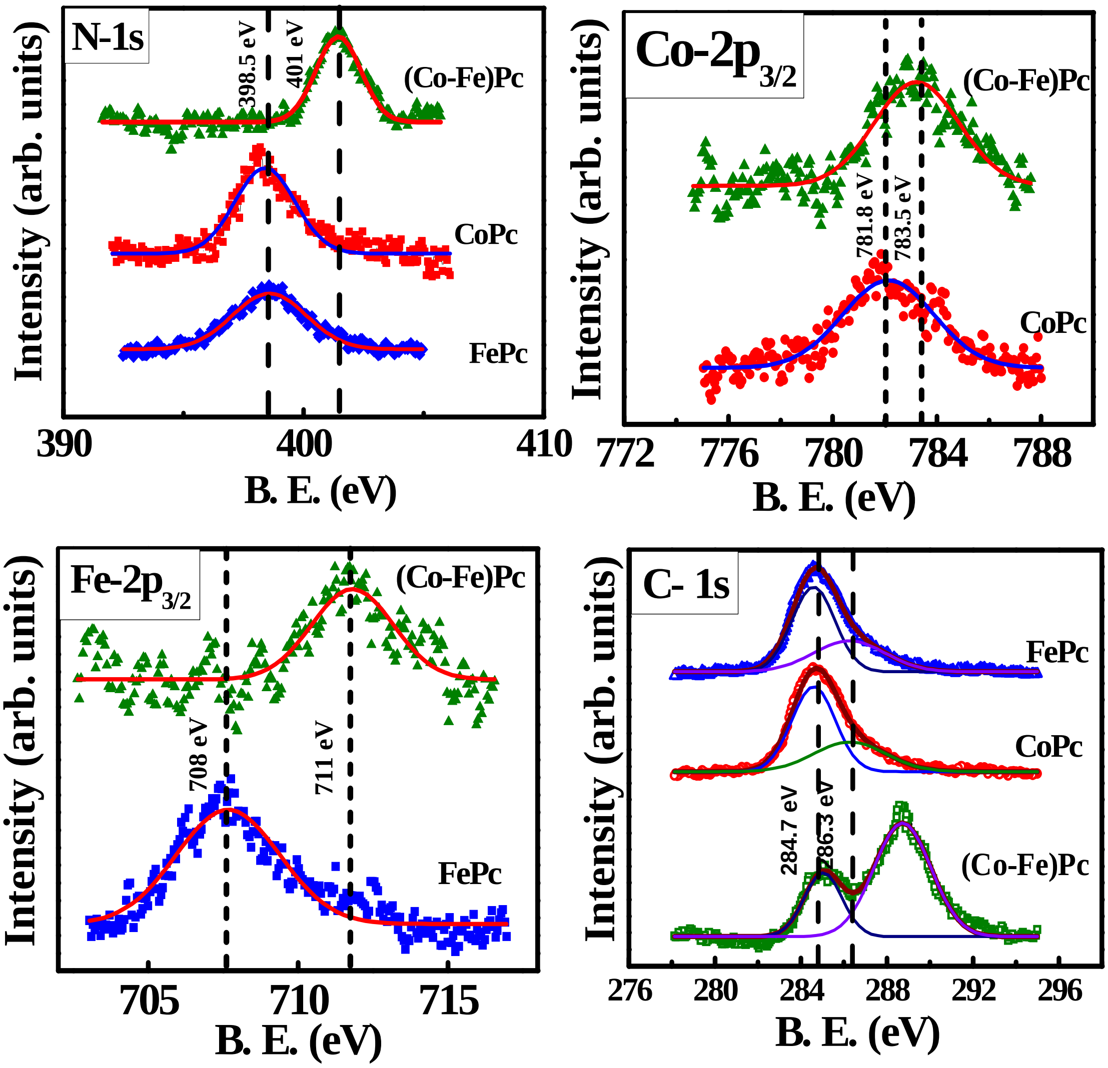

Figure 3.19 Co-2p$_{3/2}$, Fe-2p$_{3/2}$, N-1s and C-1s XPS spectrum for the CoPc, FePc and binuclear (Co-Fe)Pc films.

3.2.5 Raman spectroscopy

Fig. 3.20 shows Raman spectra of all films in the wave number region 1230 - 1560 cm^{-1} .The most intense peaks in this region are at ~1541 cm^{-1} and 1340cm^{-1}. The peak at 1541cm^{-1} has been attributed to the B_1 Raman mode due to large tangential C-N-C bridging bond displacements and the peak at 1340cm^{-1} is attributed to the M (Co or Fe)-N symmetric stretching mode in phthalocyanine rings [102]. The intense Raman peak of C-N-C bridge bond is normally used as marker for change in metal ion environment [103]. For the bi-nuclear (Co-Fe)Pc films, pronounced blue shift of C-N-C peaks is clearly evident (the enlarged spectral region around 1541 cm^{-1} is shown in the inset of Fig. 3.20). It indicates that electronic environment around Co / Fe atoms is significantly different in the binuclear (Co-Fe)Pc films as compared to mononuclear CoPc and FePc films.

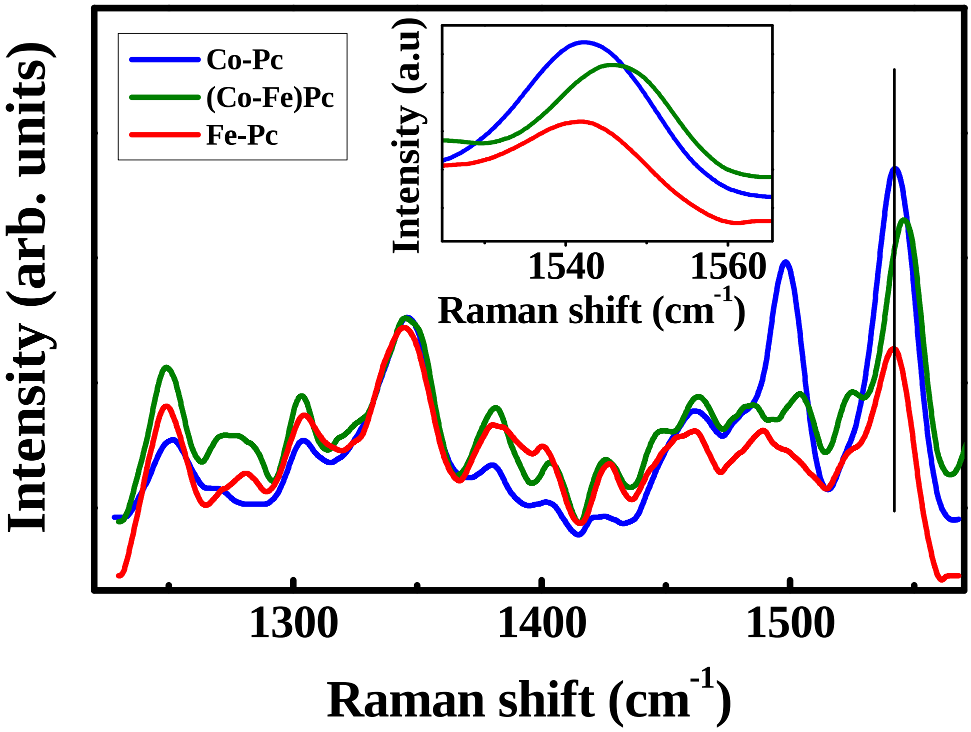

Figure 3.20 Raman spectra for the FePc, CoPc and binuclear (Co-Fe)Pc films.

3.2.6 UV-visible spectroscopy

UV-Vis absorption spectra of FePc, CoPc and binuclear (Co-Fe)Pc films are shown in Fig. 3.21. For CoPc and FePc films a sharp B-band appearing at ~ 336 nm, and a broad Q-band absorption in the region of 600-750 nm for phthalocyanines films as we have discussed earlier. A clear blue shift of B and Q bands is seen for binuclear (Co-Fe)Pc films as compared to CoPc and FePc films, indicating the energy levels has been changed in binuclear (Co-Fe)Pc films as compared to CoPc and FePc films. As we have discussed for phthalocyanine films, in general the blue or red shift of the UV-visible spectrum is observed if there is H (i.e. *face-on* overlap) or J aggregation (i.e sidewise overlap) of the molecules [104]. Since in this case a clear blue shift of the spectra for binuclear (Co-Fe)Pc films as compare to mononuclear CoPc and FePc films confirms the presence of binuclear (Co-Fe)Pc molecule as suggested by MALDI technique [105].

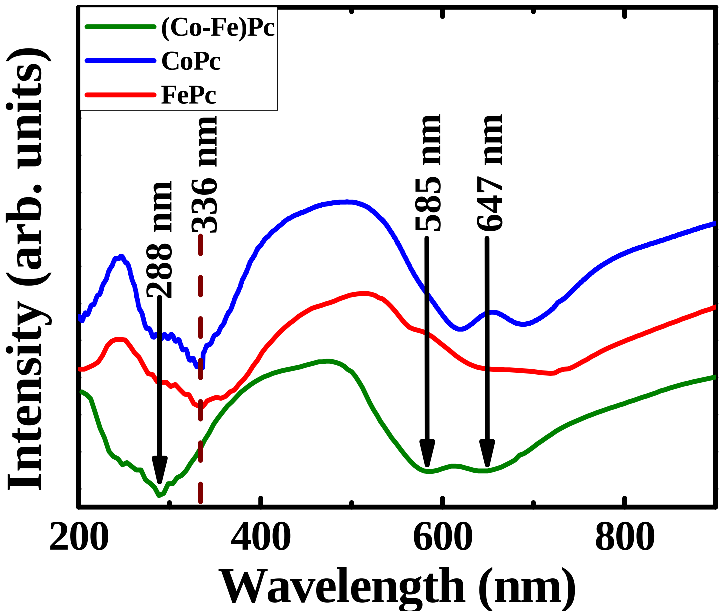

Figure 3.21 UV-Vis spectrum for the FePc, CoPc and binuclear (Co-Fe)Pc films.

3.2.7 Growth mechanism of binuclear films

The results of SIMS, MALDI, GIXRD, AFM and UV-Vis clearly indicates the formation of binuclear (Co-Fe)Pc films. It may be noted here that the binuclear films were found to form on only (0001) Al_2O_3 substrates. Such binuclear molecules were not found to form on other substrates, such as, $LaAlO_3$, $SrTiO_3$ etc. The mechanism of the binuclear formation on (0001) Al_2O_3 could be attributed to the *face-on* stacking of the molecules as well as the catalytic effect of the Al^{+3} terminated surface.

To explain the better structure ordering and smooth morphology of binuclear films compare to the mononuclear films we have purposed a model on the basis of this binuclear formation. In the case of binuclear phthalocyanine molecule (as shown in Fig. 3.16), there is a pile up of electron density (required for bonding) at the bridging sites between FePc and CoPc molecules and the remaining part of the molecule will be electron deficient hence positive. Confirmation of this comes from XPS data as we have discussed above. In binuclear (Co-Fe)Pc films effective valence electron cloud of pyrrole rings and central metal has shifted towards benzene rings of the molecules and takes part in molecular bonding with other molecules. Due to higher dipole moment of binuclear phthalocyanine molecules the van der Waals interaction between molecules will be stronger as compare to mononuclear FePc and CoPc molecule, which results in a very good molecular arrangement. In the in-plane direction there is an edge overlap between molecules while in out of plane the stacking of molecules will be *face- to- face*. Such a stacking of molecules in binuclear phthalocyanine is shown by schematic diagrams in Fig. 3.22 (a). In case of mononuclear CoPc or FePc films, in the out of plane direction molecules will be stacked in *face-to-face* manner, and in the in plane molecules are stacked in edge-on manner as shown in Fig. 3.22 (b). Initially, CoPc and

FePc molecule lying flat, but after a certain thickness molecule- molecule interaction dominates and CoPc and FePc molecules films starts to grow randomly. That's why roughness of mononuclear CoPc and FePc films is more compare than binuclear (Co-Fe)Pc films.

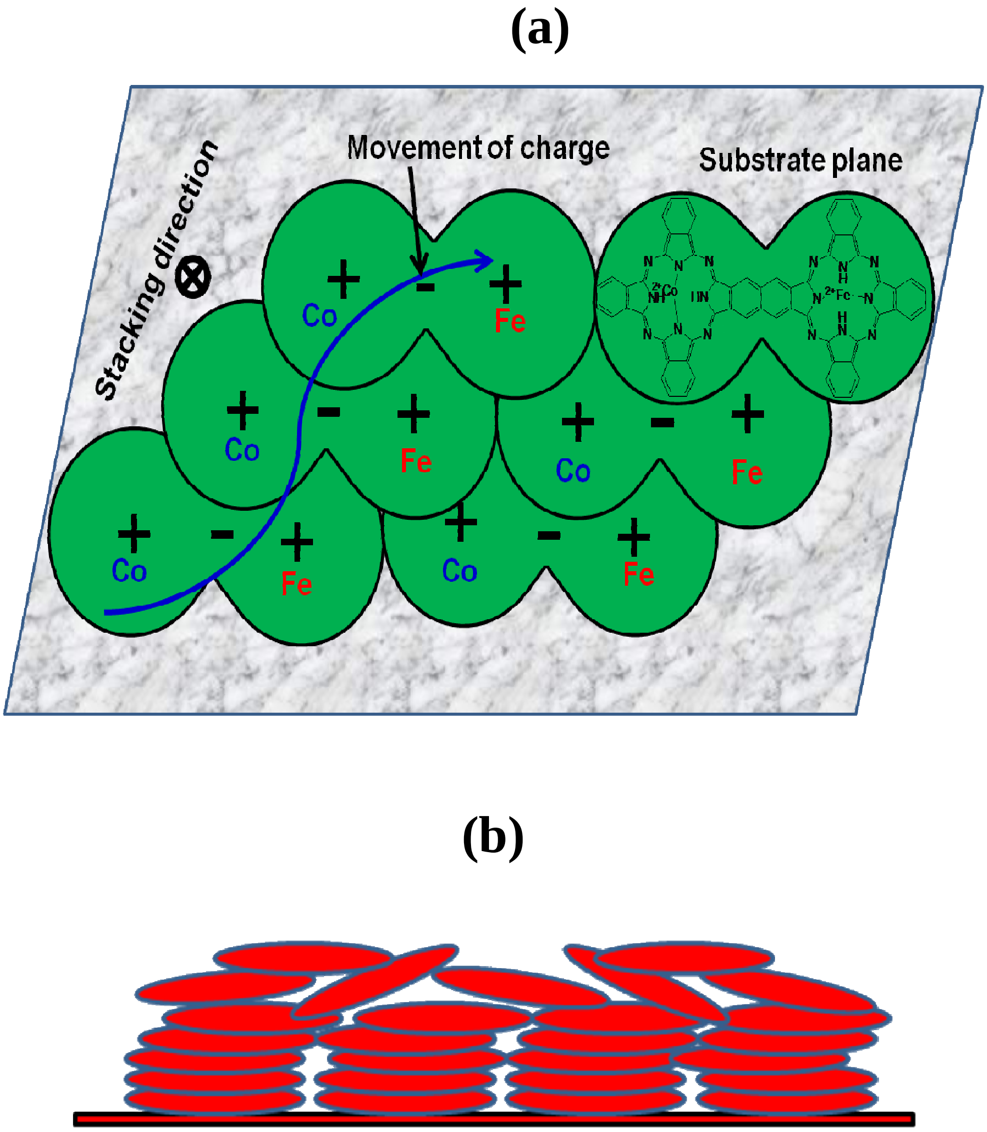

Figure 3.22 Molecular stacking schematic (perpendicular to the substrate plane) shown for (a) binuclear (Co-Fe)Pc and (b) mononuclear CoPc and FePc.

3.3 Theoretical models for charge conduction

The charge conduction in organic semiconductor can be divided in two categories: (i) bulk limited conduction and (ii) electrode limited conduction. In any charge conduction study there will always be a charge injecting electrode and a collecting electrode and the active layer between them as shown in Fig. 3.23. The dominant process between these two will be decided by the relative position of Fermi level of metal and semiconductor and the potential barrier existing between metal electrode and semiconductor. Both conduction processes in detail are described below:

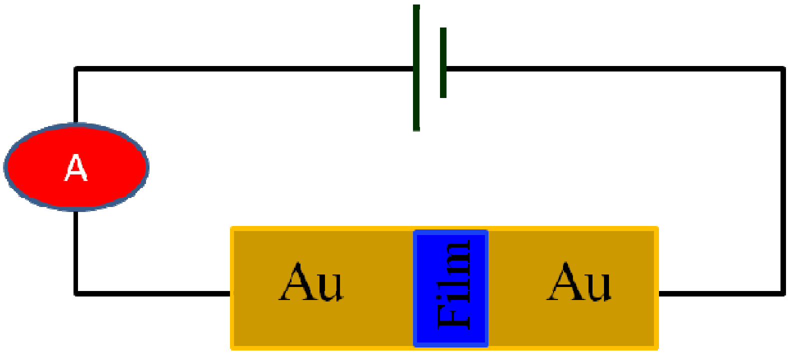

Figure 3.23 The schematic of charge transport measurement showing an active organic semiconducting layer sandwich between charge injecting and collecting electrodes.

3.3.1 Bulk limited conduction

If the contact between the electrode and the molecular semiconductor is Ohmic, with resistance of the bulk material is much higher than the contact resistance, then the current will be easily injected into the semiconductor material and the charge conduction will be dominated by the bulk [96]. By Ohmic contact we means that the density of the free charge carriers at the region of contact is much higher than the density of free charge carriers in the bulk of the semiconductor. An Ohmic contact thus provides a sufficient reservoir of charge carriers and is capable of supplying carriers to the material as required by the bias conditions [37]. The term “Ohmic contact” does not essentially mean that the current follows Ohm’s law, i.e. that the current I depends linearly on the voltage V. The various type of bulk limited conductions observed in molecular semiconductor are described below.

3.3.1.1 Ohmic conduction

Ohmic conduction occurs when the bias is so low that injected charge carriers are negligible compared to the thermally generated charge carriers in bulk. Therefore charge carriers will drift from one electrode to another due to the application of electric field. Under these conditions, the current density is linearly proportional to the applied bias, which is given by Ohm’s law

$$J = n_0 e \mu \frac{V}{d} \tag{3.1}$$

where n_0 is the free carrier density and μ is the charge carrier mobility.

3.3.1.2 Space charge limited conduction (SCLC)

At higher bias, the carriers injected from the Ohmic contacts exceed that of the thermally generated carriers and these carriers start piling up in the vicinity of injecting electrode. However the injected charge carrier density decays very fast in moving away from the injecting electrode. The injected carrier profile creates its own a strong electric field. The conduction that flows in the semiconductor is control by this space charge field and is known as the space charge limited conduction. In space charge condition, the J-V characteristics depend on the applied bias, temperature and the nature and density of traps in the semiconductor. Here we describe the details of space charge limited conduction (a) trap free space charge limited conduction (b) space charge limited conduction with trap.

(a) Trap free space charge limited conduction

We first consider the perfect intrinsic semiconductor, free of traps. Current-voltage relation in the space-charge limited currents regime can be obtained using following equation:

Continuity equation: $$\frac{dJ}{dx} = 0 \tag{3.2}$$

Current density: $$J = e\mu n_{(x)} F_{(x)} \tag{3.3}$$

Poisson equation: $$\frac{dF_{(x)}}{dx} = -\frac{e}{\varepsilon_0 \varepsilon_r} n_{(x)} \tag{3.4}$$

where μ is the mobility defined as the constant of proportionality in the relationship between the applied electric field, F, and the drift velocity of the charge carriers, ν, given by $\nu = \mu F$, e is the charge of the electron, $n_{(x)}$ is the local charge carrier density, $\varepsilon_0 \varepsilon_r$ is the permittivity of the semiconductor material.

From eq. (3.3) and (3.4)

$$J = -\mu \varepsilon_0 \varepsilon_r \frac{dF_{(x)}}{dx} F_{(x)} \tag{3.5}$$

$$Jx = \mu \varepsilon_0 \varepsilon_r \frac{F_{(x)}^2 - F_{(0)}^2}{2} \tag{3.6}$$

Using $F_{(0)} = 0$ (because for Ohmic contacts, the electric field at the interface ($x = 0$) must be zero), we get

$$F_{(x)} = \sqrt{\left(\frac{2jx}{\mu\varepsilon_0\varepsilon_r}\right)} \tag{3.7}$$

Finally the current voltage relationship can be obtained by integration of the electric field using the boundary condition $F_{(0)} = 0$,

$$V = \int_0^d F_{(x)}dx \tag{3.8}$$

We get,

$$J = \frac{9}{8}\varepsilon_0\varepsilon_r\mu\frac{V^2}{d^3} \tag{3.9}$$

This is nothing but Mott- Gurney law describing current-voltage relation in a trap free insulator [106]. It is evident from the eq. (3.9) that current density varies with square of voltage and by knowing the value of permittivity, mobility can be found out from the J-V^2 plot.

Thus the crossover voltage at which the transition Ohm's law (eq. 3.1) to trap-free square law (eq. 3.9) occurs can be derived as:

$$V_t = \frac{8en_0d^2}{9\varepsilon_0\varepsilon_r} \tag{3.10}$$

(b) Space charge limited current in presence of trap

In the actual samples, impurities, dislocations and rough grain boundaries are commonly observed, creating local energy states (trap) below the transport energy level reduce the current at lower injection level as they capture and immobilize most of the injected charge carrier. The presence of these unfavourable trap states can influence the transport of charge within the bulk, resulting in non-ideal current-voltage characteristics. The trap can either be shallow or deep depending on their energy level. On the basis of their energy levels, the traps can be classified as shallow or deep. The so-called *shallow traps* refer to traps whose energy levels (E_{tn}) are located above the quasi-Fermi (E_{Fn}) level for electron traps, and to traps whose energy levels (E_{tp}) are located below the quasi–Fermi level (E_{tp}) for hole traps. Conversely, deep traps refer to traps whose energy levels are located below the quasi-Fermi level for electron traps, and to traps whose energy levels are located above the quasi–Fermi level for hole traps as shown in Fig. 3.24**.** If the trap depth is large or temperature is low, most of the injected carriers are trapped. A given applied voltage can carry only a fixed quantity of total charge in the semiconductor. Hence the injected free carrier density is significantly reduced in the presence of traps. Both the trapped and the free charge carriers determine the space charge. The Poisson eq. (3.4) changes to,

$$\frac{dF}{dx} = -\frac{e}{\varepsilon_0 \varepsilon_r}(n_{(x)} + n_{(t)}) \tag{3.11}$$

where $n_{t(x)}$ is the trapped carrier density. The transport equation (3.3) remains unchanged. Eq. (3.3) and (3.11) are now solved to get *J*–*V* relation for the molecular semiconducting sample. To solve these equations we need to identify the trap depth E_t. We will consider that the traps distribution is uniform in space but may have a non-uniform distribution in the energy space. Three different distributions in the energy space have been considered in detail in the literature [107, 108]. (1) all traps at a single energy level, (2) a Gaussian distribution of traps in the energy space, (3) exponentially distributed traps in the energy space.

- *Single energy level traps the distribution can be written as*

$$h(E) = N_{(t)}\delta(E - E_{(t)}) \tag{3.12}$$

- *An exponential distribution*

$$h(E) = \frac{N_{(t)}}{kT_C} \exp\left(-\frac{E}{kT_C}\right) \tag{3.13}$$

- *A Gaussian distribution peaking at* E_t

$$h(E) = \frac{N_t}{\sigma\sqrt{2\pi}} \exp\left(-\frac{(E-E_t)^2}{2\sigma^2}\right) \tag{3.14}$$

Here, N_t is the total density of traps, T_c and σ are distribution parameters of local states for the exponential and Gaussian distribution of traps.

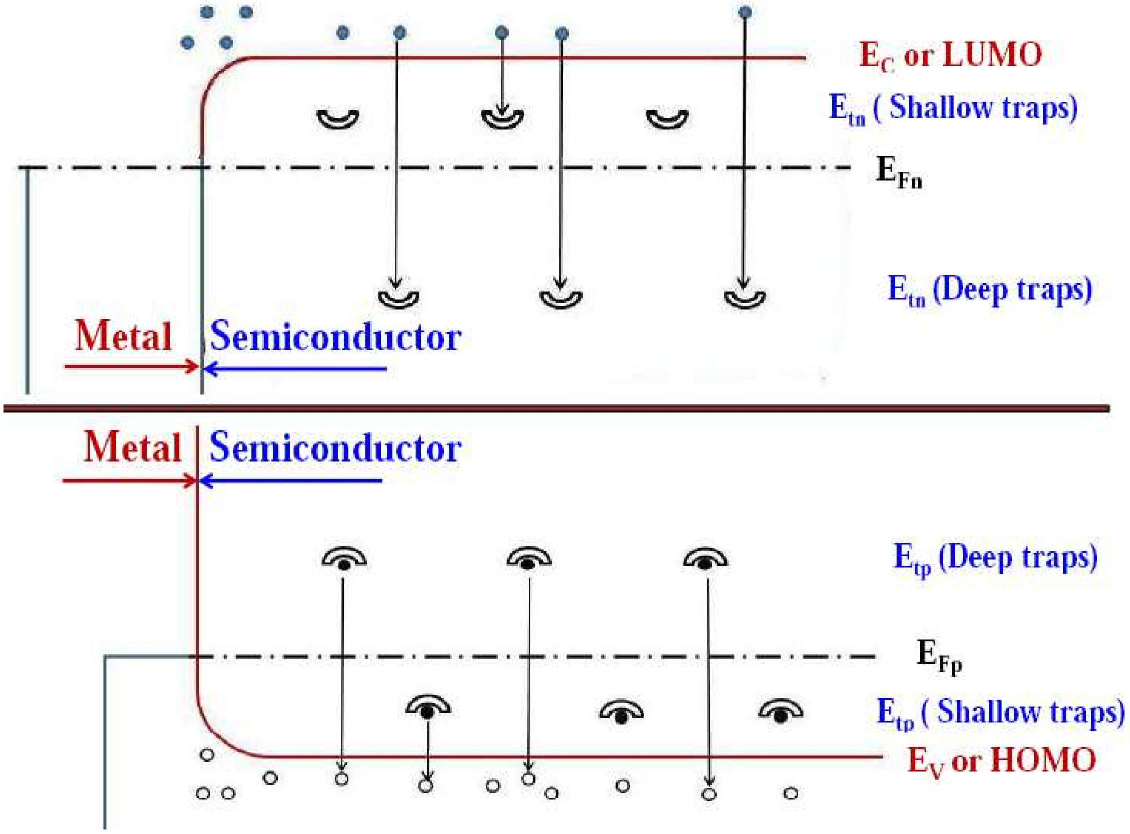

Figure 3.24 Schematic of shallow and deep traps for electrons and holes.

We first consider the single level shallow traps lying between the Fermi level and the valence band edge (we are considering conduction by holes). The concentration of the traps carrier (holes) is given by [107],

$$n_{t(x)} = \int_{E_l}^{E_u} N_t \delta(E - E_t) \frac{1}{\left(1 + \exp\left(\frac{E_F - E}{kT}\right)\right)}$$

Energies E_l and E_u are the lower and upper limits of the trapping level. On integrating this equation give [107, 109, 110]

$$n_{t(x)} = \frac{N_{(t)}}{1 + \frac{N_{(t)}\theta_{(t)}}{n_{(x)}}} \tag{3.15}$$

where,

$$\theta_{(t)} = \frac{N_v}{N_{(t)}} \exp\left(-\frac{E_t}{kT}\right) \tag{3.16}$$

and N_v is the effective density of states in the valence band. Using eq. (3.15) for $n_{(t)}$ and the boundary condition eq. (3.8), the solution of the Poisson and transport equations gives,

$$J = \frac{9}{8}\theta_{(t)}\varepsilon_0\varepsilon_r\mu\frac{V^2}{d^3} \tag{3.17}$$

It can be easily shown that

$$\theta_{(t)} = \frac{n}{n + n_{(t)}} \tag{3.18}$$

Thus $\theta_{(t)}$ represents ratio of free to total charge carriers. If there are no traps, $n_{(t)} = 0$, then $\theta_{(t)} = 1$and eq. (3.17) reduced to eq. (3.9). If $n_{(t)} >> n$, under this condition $\theta_{(t)}$ becomes the ratio of free to trapped carriers.

The crossover voltage at which the conduction from Ohmic to SCLC begins to dominate is given by

$$V_{tr} = \frac{8en_0 d^2}{9\theta_{(t)}\varepsilon_0\varepsilon_r} \tag{3.19}$$

In the case semiconductor contains deep traps, an analytical expression for J for cannot be obtained, but numerical solutions can easily be obtained [107].

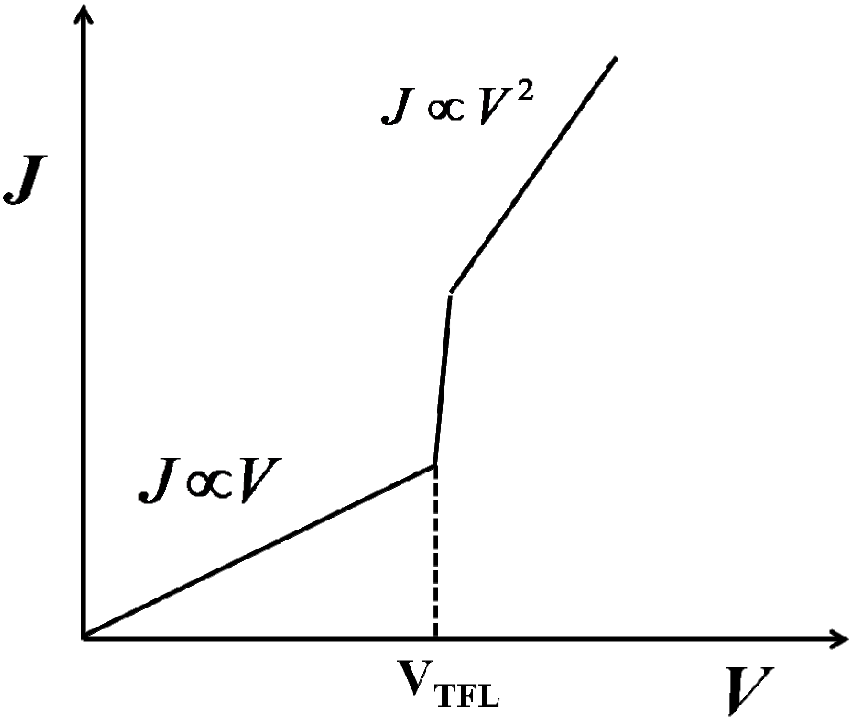

Figure 3.25 Space charge limited current versus voltage characteristic for semiconductor containing trap. V_{TFL} is the trap filled limit.

Now we will consider the case of exponentially distribution of traps. The concentration of traps in this case is give by

$$h(E)=\frac{N_{(t)}}{kT_C}\exp\left(-\frac{E}{kT_C}\right)$$

Trap characteristics distribution, the concentration of trapped carrier (holes) is given by

$$n_{(t)}=\int_{E_{FP}}^{\infty}\frac{N_{(t)}}{kT_C}\exp\left(-\frac{E}{kT_C}\right)\frac{1}{1+\exp\left[{(E_{FP}-E)}/{kT}\right]}dE \qquad (3.20)$$

Denoting $l=\frac{T_C}{T}$, the above equation becomes to

$$n_{(t)}=\alpha N_{(t)}\left(\frac{n}{N_v}\right)^{1/l}$$

This gives the relation between free to trapped carrier concentration. In this expression the factor $\alpha={\left({\pi}/{l}\right)}/{\sin\left({\pi}/{l}\right)}$ arises because 0 K approximation (step function) for the Fermi occupancy function have not used here. This factor can be taken unity. By the boundary condition eq. (3.8), the following analytical expression for *J* is obtained [107],

$$J=\mu e^{1-l}N_V\left(\frac{\varepsilon_0\varepsilon_r}{\alpha N_t}\right)^l\left(\frac{l}{l+1}\right)^l\left(\frac{2l+1}{l+1}\right)^{(l+1)}\frac{V^{(l+1)}}{d^{(2d+1)}} \qquad (3.21)$$

From above expression it is clear that presence of trap not only limits the magnitude of the *J* but also distort the V^2 behavior. Thus if semiconductor contains the trap, most of injected charge carrier remains trapped and current by injection remains small until all the traps are filled. At sufficient high voltage, the trap became saturated and it behaves as trap free V^2 law given by eq. (3.9). The voltage at which filling of all trap is achieved is called trap filled-limit voltage" (V_{TFL}) shown in Fig. 3.25 and expression for it is given by [108, 111]

$$V_{TFL} = \frac{eN_{(t)}d^2}{2\varepsilon_0\varepsilon_r} \tag{3.22}$$

In the case of Gaussian distribution of trap (eq. (3.10)) the situation is more complex since exponent at the applied voltage ($l+1$) and thickness of the sample ($2l+1$) are not constant but they are the function of applied voltage. The details studies of this situation are given in Refs. [112, 113].

3.3.1.3 Hopping conduction

In inorganic semiconductors, atoms are strongly bounded together by covalent bond with well long range ordered configurations. The energy band in this case extends continuously in the bulk and charge conduction occurs through free wave-like propagation of carriers in well-known conduction or valance bands, with occasional scattering of carriers with phonon, impurity sites, or grain boundaries. Therefore in these materials, mobilities can reach large values more than 1000 $cm^2/V.s$. However, in molecular semiconductors, the constituting molecules are only weakly bound together through van der Waals forces and the conventional view of band formation is not very true. In these materials, band widths are typically smaller than k_BT and charge are intrinsically localized due to the weak wave function overlap between two adjacent molecules [1, 114]. The freely wave-like propagation of charge carriers as commonly seen in inorganic semiconductor no longer exists in molecular semiconductor. In molecular semiconductors, the mobilities are found to be very low (≤ 10 $cm^2/V.s$). If a rough calculation of a mean-free path distance for the scattering of the charge carriers were made, it would be smaller than the intermolecular spacing. Therefore, the charge conduction mechanism in molecular semiconductor cannot be the same as that observed in crystalline inorganic semiconductor. In fact, it must be a rate-limiting process where in each step, charge carriers have to overcome an activated energy barrier, and the mobility can be given by Arrhenius relation

$$\mu \propto \exp\left(-\frac{\Delta E}{kT}\right) \tag{3.23}$$

where ΔE is the activation energy.

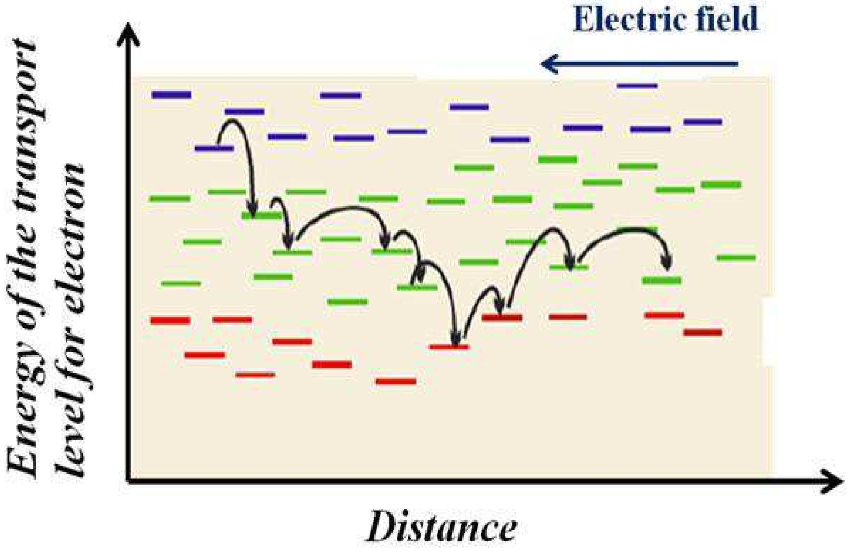

Figure 3.26 Schematic representation of hopping transport in the molecular semiconductor.

In this simple picture, upon application of electric field the charge carrier will hop from one localized state *i* to another localized state *j*. This process is shown in Fig. 3.26. This thermally activated process is dominant transport mechanism in molecular semiconductor. Therefore, unlike the inorganic semiconductor the mobility and hence the conductivity of (disordered) molecular semiconductor increase exponentially with temperature. This hopping process involves thermionic emission (phonon-assisted hopping) or direct tunnelling of carriers between localized states. Phonon assisted hopping takes place when carriers trapped in localized states absorb a phonon and classically jump to the next localized site, whereas tunnelling can take occur between two localized states if the electronic wave functions of the two localized states effectively overlap. Most of the hopping models for molecular semiconductors are based on the Miller-Abrahams formalism that was originally used to explain the hopping process in deep traps in inorganic semiconductors [115]. The photon assisted hopping rate between two localized sites is:

$$W_{ij}(r_{ij}, E_i, E_j) = v_0 \exp\left(-\frac{2r_{ij}}{\alpha}\right) \times \exp\left(-\frac{E_j - E_i}{kT}\right) \qquad E_i > E_j \qquad (3.24)$$

$$= v_0 \exp\left(-\frac{2r_{ij}}{\alpha}\right) \qquad E_j < E_i$$

where v_0 is the attempt to jump frequency, α is the inverse localization length, r_{ij} is the distance between two localized states i and j and E_i and E_j site. The first exponential in eq. (3.24) describes the tunnelling probability from a localized site i to another localized site j separated by a distance r_{ij}. The second represents the probability of absorbing a phonon for hops between two sites. For an energetically upward hop, $E_j > E_i$, the hopping rate follows an exponential function. For an energetically downward hop, $E_j < E_i$, the hopping rate is equal to 1, that is independent of the energy difference of the hopping sites and the temperature.

3.3.1.4 Poole-Frankel effect

Hooping model described the temperature dependent mobility, but it failed to explain the electrical dependent mobility. This field dependent and temperature mobility is explained by W. Gill for poly (N-vinyl carbazole) using the Poole- Frenkel effect [116]. He suggested following empirical relation for field dependent mobility,

$$\mu = \mu_0 \exp(\gamma\sqrt{F}) \tag{3.25}$$

where

$$\gamma = B\left(\frac{1}{kT} - \frac{1}{kT_0}\right) \tag{3.26}$$

In these expressions μ_0 denotes the zero field mobility; B and T_0 are parameters of the system.

In Fig. 3.27, the idea behind the Poole-Frenkel effect is illustrated, which describes the reduction the barrier of a charge carrier in a columbic potential by applied electric field. When in the bulk a charge carrier is trapped in an impurity level it is unable to contribute to the conductivity until it overcomes the potential barrier and is promoted to the transport level. If an electron trap is regarded as a positively charged centre at a fixed position in the bulk semiconductor, the potential energy of the electron is

$$V_{(x)} = -\frac{e^2}{4\pi\varepsilon_0\varepsilon_r x} - eFx \tag{3.27}$$

In the absence of the externally applied field, the maximum value of the coulombic barrier is $E_0 = -\frac{e^2}{4\pi\varepsilon_0\varepsilon_r x}$. When the field is applied, barrier E_0 is reduced on one side of the trap, as shown in Fig. 3.27. $V_{(x)}$ now has a maximum on the x-axis through the trap centre at a distance through the trap centre at a distance

$$x_m = \left(\frac{e}{4\pi\varepsilon_0\varepsilon_r}\right)^{1/2} \tag{3.28}$$

from the trap the value of the potential at this point

$$\Delta\phi_{PF} = \left(\frac{e^3}{\pi\varepsilon_0\varepsilon_r}\right)^{1/2} F^{1/2} = \beta_{PF} F^{1/2} \tag{3.29}$$

where $\beta_{PF} = \left(\frac{e^3}{\pi\varepsilon_0\varepsilon_r}\right)$ is the Poole-Frenkel field lowering coefficient.

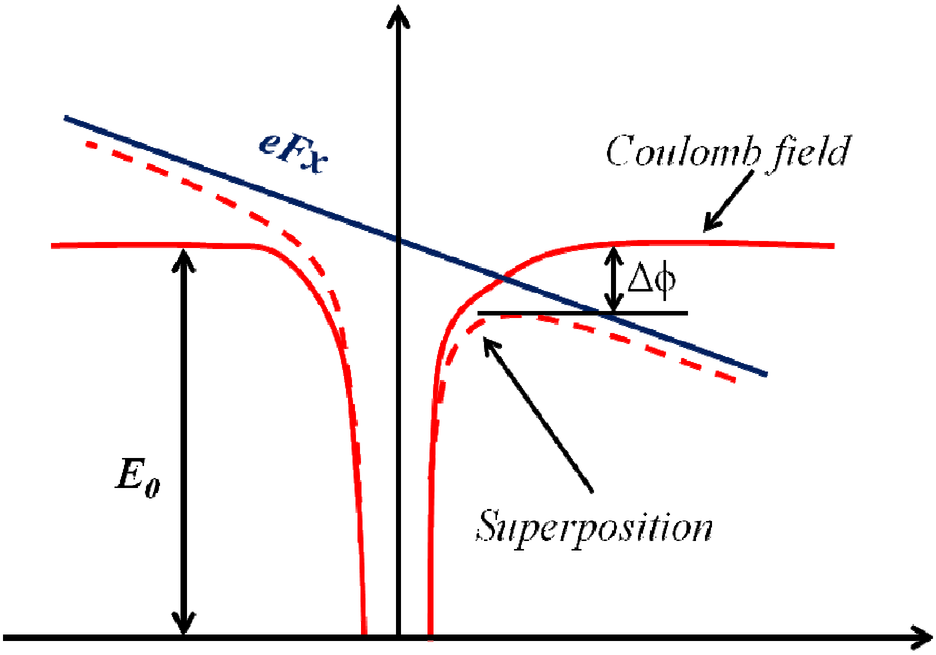

Figure 3.27 Poole-Frenkel effect at a trap in the bulk of the semiconductor.

The effective barrier height is considered to be reduced by $\Delta\phi_{PF}$, and consequently the proportion of carriers which are free is increased. The current density is given by [117]

$$J = J_0 \exp\left(\frac{\beta_{PF} F^{1/2}}{kT}\right) \tag{3.30}$$

where $J_0 = \sigma_0 F$ is the low field current density. Thus a linear plot of *logJ* against $V^{1/2}$ should be obtained, from which a value of the field-lowering coefficient can be obtained and compared with the predicted theoretical value.

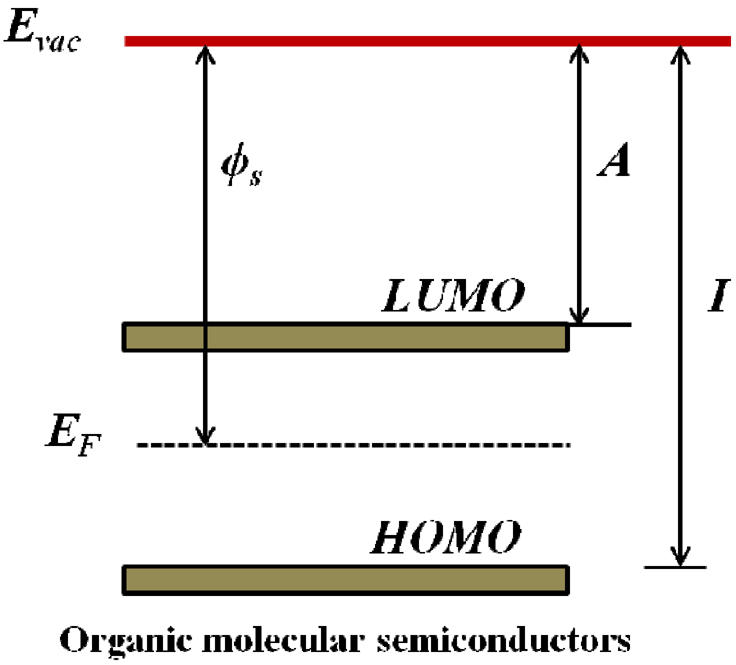

Figure 3.28 Schematics of energy diagram of organic molecular semiconductor.

3.3.2 Electrode limited conduction

The injection process is dominated by the charge injection barrier at the interfaces between the active molecular layer and the metal electrodes, which is defined as the energy difference between Fermi-level E_F of the electrode and HOMO (or LUMO) of the organic molecular semiconductor. Therefore, it is necessary to consider electronic properties and band alignment of the metal/organic molecular semiconductor (M/OMs) interfaces. The energy band diagram of a typical molecular solid is shown in Fig 3.28. The upper most horizontal line is the vacuum level (E_{vac}). E_{vac} is defined as the minimum energy level for an electron to escape from the solid. The energy separation between the HOMO and E_{vac} is the ionization potential (I). The separation between the LUMO and E_{vac} is the electron affinity

(*A*). Difference between Fermi level E_F and Vacuum level is called work function ϕ_s of materials.

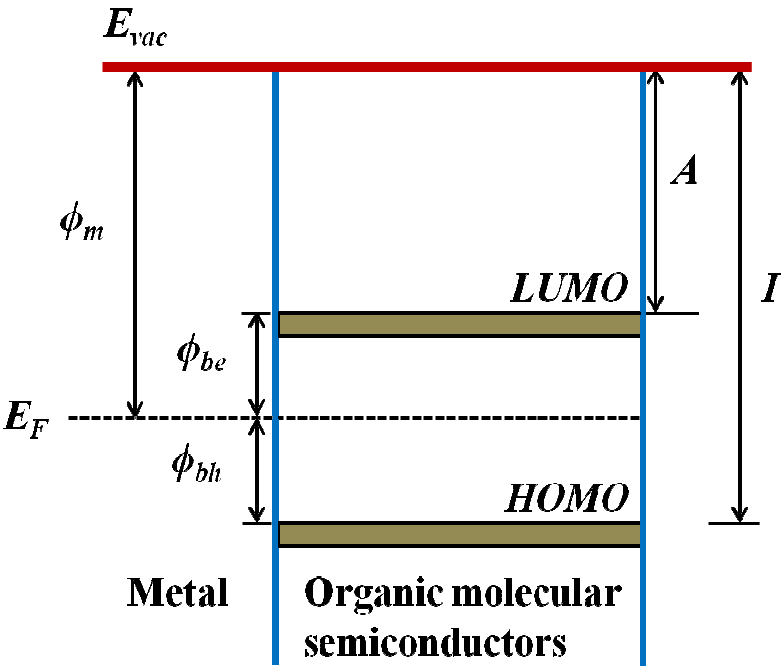

Figure 3.29 Schematics of energy level alignment at M/OMs interface assuming vacuum level alignment at the interface and no interfacial dipole (Mott-Schottky model).

Unlike inorganic semiconductor, the surface of molecular solid has no dangling bonds. Therefore, the molecular energy level alignment at M/OMs interfaces ideally should follow the classic Mott–Schottky model, in which no interaction occurs at the interfaces region [118, 119]. So, vacuum level alignment at the interface region is used. Fig. 3.29 illustrates the energy diagram according to the ideal Mott–Schottky rule of M/OMs interface when a metal and an organic solid are brought into contact. The interface barrier heights for hole (ϕ_{bh}) and electron (ϕ_{bn}) can be expressed as

$$\phi_{bh} = I - \phi_m \tag{3.31}$$

$$\phi_{bn} = \phi_m - A \tag{3.32}$$

where ϕ_m is the metal work function, I is the ionization potential and A is the electron affinity.

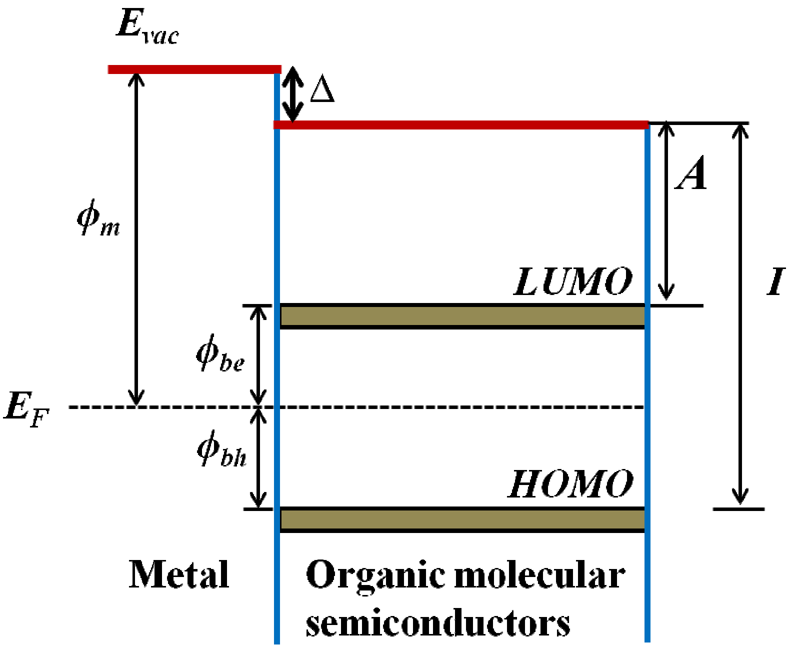

Figure 3.30 Schematics of energy level alignment at M/OMs interface assuming vacuum level shift at interface and with interfacial dipole (Δ).

However, in the real M/OMs interface, a common vacuum level alignment does not occur because of the formation of interface dipole inducing vacuum level shift (Δ). As a consequence, the vacuum level becomes discontinuous at the M/OMs interface. This abrupt change (Δ) in the vacuum level between metal and organic molecular semiconductor has been observed experimentally [120, 121]. As shown in Fig. 3.30, the existence of Δ demonstrates the interface barriers have to be modified by the amount Δ:

$$\phi_{bh} = I - \phi_m + \Delta \tag{3.33}$$

$$\phi_{bn} = \phi_m - A - \Delta \tag{3.34}$$

The origin of the interface dipole remains controversial. A variety of possible explanations like, (1) charge transfer between the metal and the OMs layer, (2) formation of chemical bond (3) image effect or push back effect, (4) existence of interfacial states, and (5) permanent dipole moment can lead to the large interface dipole formation [121-123]

Depending upon the applied electric bias, temperature and active layer thickness, different charge injection mechanism may occur at the metal/semiconductor interface. These mechanisms are discussed below.

3.2.2.1 Tunnelling mechanism

Tunnelling is a quantum-mechanical effect in which the wave function of the carrier is attenuated only moderately by the thin barrier, so that the carrier has a finite probability of existence on the opposite side of the barrier. Simmons [124] has reviewed the tunnelling process in some detail under a wide variety of conditions of applied voltage and work function values. Tunnelling is normally applicable only for very thin film thickness less than about 10 nm when subjected to a high electric field. In particular, it has been proposed [125] that a modified Fowler-Nordheim expression may be applicable for tunnelling through an interfacial region of thickness d_t, where the electric field at the barrier is sufficiently high to reduced it width to 5 nm [37]. Under this condition expression for current density is

$$J = \frac{e^3V^2}{8\pi h\phi d_t^2}\exp\left(-\frac{8\pi(2m)^{1/2}\phi^{3/2}d_t}{3ehV}\right) \tag{3.35}$$

Where *h* is the Planck's constant, *Φ* is the barrier height and effective thickness respectively of the tunnelling barrier and m is the mass of free electron.

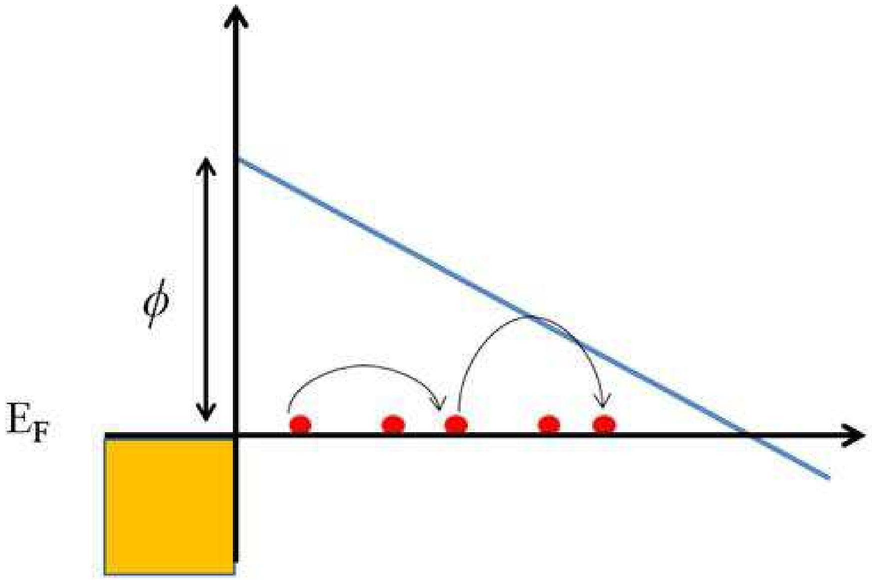

Figure 3.31 Schematic of sequential tunnelling of electron form metal electrode to the conduction band of insulator/semiconductor via localized states.

3.3.2.2 Multistep tunnelling (MUST) mechanism

Apart from the direct tunnelling which requires a higher voltage, there is a possibility of sequential tunnelling of charge carrier from the metal electrode to the conduction or valence band of the semiconductor. The physical process is schematically shown in the Fig.3.31. The interface between metal and semiconductor always contains some localized states, these localizes states helps the charge carrier to tunnel sequentially from the electrode to bulk. In this model conductivity can be derived as [126-128]

$$\sigma = \sigma_0 \exp\left(-\sqrt{\frac{F_0}{F}}\right) \tag{3.36}$$

$$\text{with } F_0 = \frac{16\sqrt{2m}\alpha\phi^{3/2}}{3e\hbar} \tag{3.37}$$

F_0 is related to the material through the potential barrier (Δ) and material parameter α that depends weakly on the temperature. Here $\alpha = ln(p^{-1})$, where p^N is the probability of forming a N-step tunnelling path of the MUST. The important feature of the eq. (3.36) is its rather weak sensitivity to the concentration of the localized states in the gap, which is generally difficult to know.

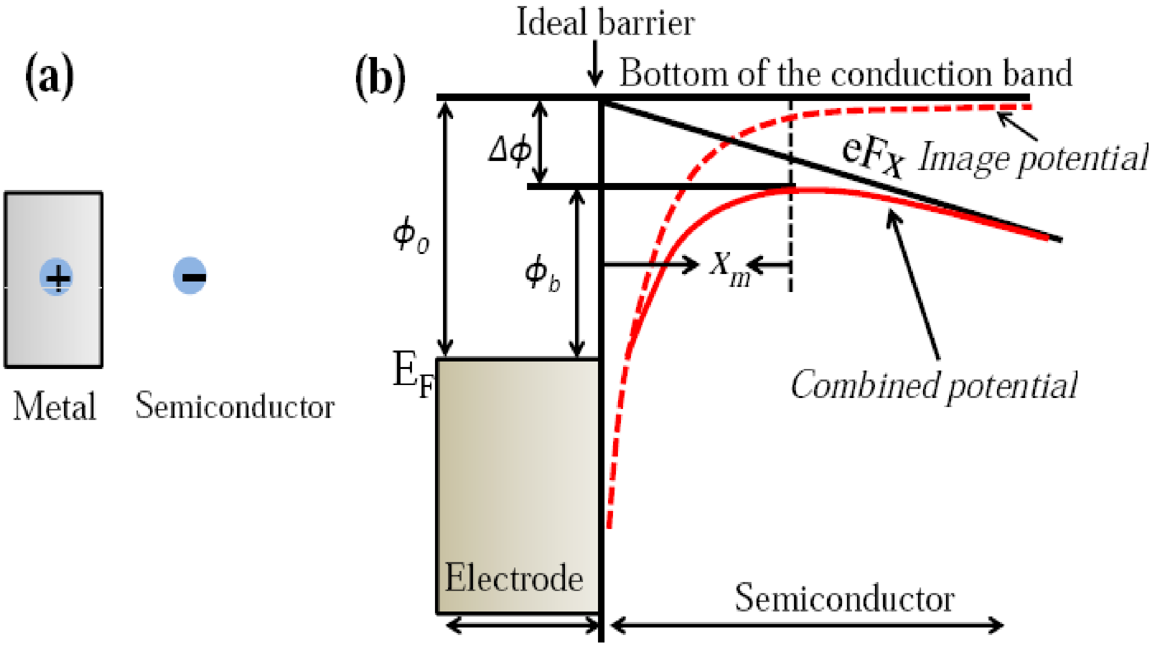

Figure 3.32 (a) Representation of image force problem when an electron is very close to the metal surface. (b) Energy barrier lowering, $\Delta\phi$ due to image force and applied field. x_m is a measure of the width of the barrier.

3.3.2.3 Schottky mechanism

When the barrier is too thick to tunnel from one electrode to other, the current flowing through the semiconductor is limited mainly by the rate at which electrons are thermally excited over the interfacial potential barrier into the semiconductor transport level. In this case current is given by the Richardson thermionic emission [129]:

$$J = \frac{4\pi mek^2T^2}{h^3}\exp\left(-\frac{\phi}{kT}\right) = AT^2\exp\left(-\frac{\phi}{kT}\right) \tag{3.38}$$

where A (1.2 × 10^6 $\mathrm{Am^{-2}}$) is the Richardson constant and ϕ is potential barrier independent of applied voltage. To determine the height of the barrier in an applied electric field $F \neq 0$, we must take into account the so-called Schottky effect (as shown in Fig. 3.32): an injected electron at a distance x from the metal surface produces a positive image charge in the metal through influence, whose field gives rise to what is termed the image force

$$F_{image} = -\frac{e^2}{4\pi\varepsilon_0\varepsilon_r(2x)^2} \tag{3.39}$$

Its potential which is called image potential is obtained by integrating this force from $x = 0$ to $x = \infty$, which gives

$$\phi_{image} = -\frac{e^2}{16\pi\varepsilon_0\varepsilon_r x} \tag{3.40}$$

So due to the presence of image potential and uniform electric field the shape of the original step potential barrier changes as shown in the Fig. 3.32 (b). In view of modified potential the potential energy of an electron at a distance x from the interface is given by

$$\phi_{image} = \phi_0 - \frac{e^2}{16\pi\varepsilon_0\varepsilon_r x} - eFx \tag{3.41}$$

The potential has a maximum at $x_m = \sqrt{\frac{e}{16\pi\varepsilon_0\varepsilon_r F}}$. Therefore the superposition of image force and electric field lowers the potential barrier ϕ_0 by an amount

$$\Delta\phi = \left(\frac{e^3}{4\pi\varepsilon_0\varepsilon_r}\right)^{1/2} F^{1/2} \equiv \beta_S F^{1/2} \tag{3.42}$$

to the effective height of the barrier $\phi_b = \phi_0 - \Delta\phi$. $\beta_S = 0.5\beta_{PF}$ is Schottky field lowering coefficient. The maximum of the superposed potential lies at a distance x_m from the surface of the metal

$$x_m = \sqrt{\frac{e}{16\pi\varepsilon_0\varepsilon_r F}} \tag{3.43}$$

In this modified barrier height the current density is given by Richardson-Schottky equation [130]

$$J = AT^2 \exp\left(-\frac{\phi_0}{kT}\right)\exp\left(\frac{\beta_S F^{1/2}}{kT}\right) \tag{3.44}$$

3.4 Charge conduction in mononuclear phthalocyanine films

In this section, we present a brief overview of literature on the on the charge transport studies in mononuclear Pc thin films, in literature. The Schottky effect in Al/CuPc/Ag structure was observed by Barkhalov and Vidadi [131] for the reverse bias. Similar effect have been studied by other groups in Al/M(Cu, Zn)Pc/Au structure [132, 133]. It was proposed that a layer of aluminium oxide grew at the interface of Pc and Al electrode, by the diffusion oxygen through the organic material. The barrier height was determined to be 1.27eV for ZnPc and Al electrode interface [132].

Moreover, Poole Frankel effect, which is bulk analogous of Schottky effect, was also reported for the Pc films. This effect was originally observed by Gill [116]. Poole-Frankel conductivity in a structure incorporating CuPc was first reported by Hassan and Gould [134]. Latter Poole-Frankel effect was also observed in several other structures, including Al/CuPc/Au [135], Au/PbPc/Al [136, 137]. In some cases field lowering co-efficient is slightly higher than the theoretical value, which was attributed to the non-uniform internal electric field distribution.

SCLC mechanism is generally used to explain charge transport in OLEDs and OFETs where phthalocyanine films were used as active layer [138, 139]. SCLC conduction in Au/CuPc/Au structure is first extensively studied by Sussman and concluded that SCLC, dominated by exponential distribution of traps, was responsible for the conduction in temperature range 210-430K [140]. Space charge limited conduction, dominated by both discrete trap levels and exponential trap distributions has been identified in many Pc thin films [134, 135, 141-143]. From all these reports it is easily concluded that the total trap concentration for exponential distributions span a wide range from 10^{20} to 10^{26} m^{-3}. However this variation is believed to be due to purity of material, preparation condition and oxygen contents. Furthermore, the mobility for various Pc films calculated by various methods is rather poor and varies in the range 10^{-6}-10^{-2} cm^2/Vs [140, 143, 144]. The low mobility values in Pc thin films mainly arises due to the weak van der Waals forces among molecules, leading to a poor overlap of the wave-function of π-electrons between adjacent molecules. This is further weakened due to presence of both energetic (diagonal and non-diagonal) and positional disorders. These disorders depend on the nature of molecular stacking (face-on or edge-on), adsorbed oxygen species and presence of impurities [145]. Even in single crystals that are defect free, the π-electron wave-function overlapping of adjacent Pc molecules is not highest due to inherent edge-to-face on molecular packing. A major consequence of the low mobility in Pc films is that their charge transport properties have been investigated only in the temperature range 473-175 K. The low temperature charge transport studies of Pc films below 175 K have never been investigated. The major reason for this is that due to poor mobility, the current at low temperatures goes below the measurable limits i.e. below pA. Thus in order to investigate the low temperature charge transport in Pc films, it essential that their mobility need to be improved. In the next section we will discuss our results on the charge transport properties of FePc, CoPc and F_{16}CuPc films grown by MBE.

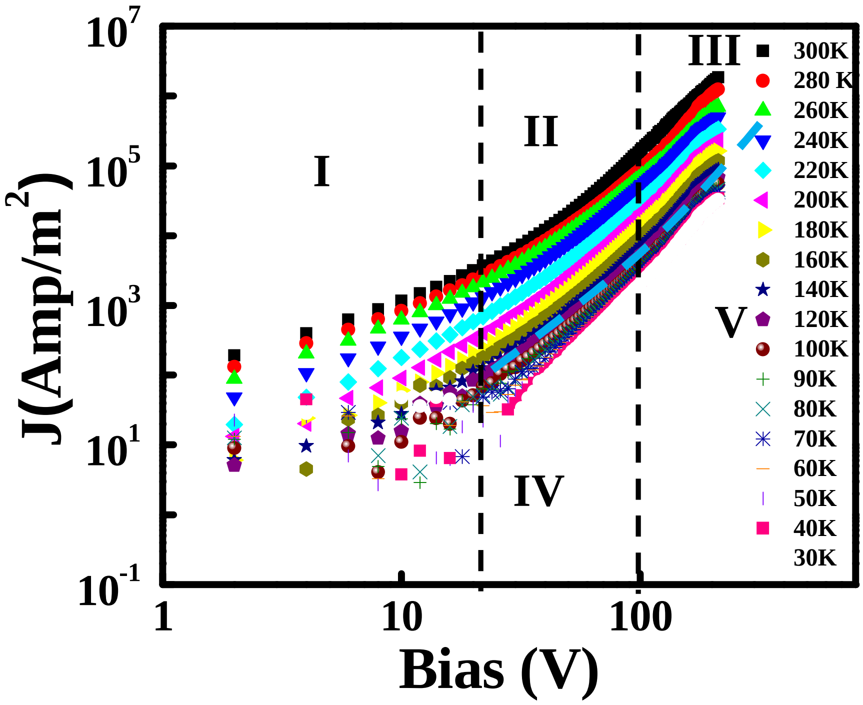

Figure 3.33 Log-log plots showing current-voltage (*J*-*V*) characteristics of 20 nm FePc films in the temperature range 300-30 K. Based upon dependence of current on applied bias and/or temperature, five regions I to V have been identified (marked by thick dashed lines).

3.4.1 Charge conduction in FePc films

3.4.1.1 Temperature dependent J-V characteristics

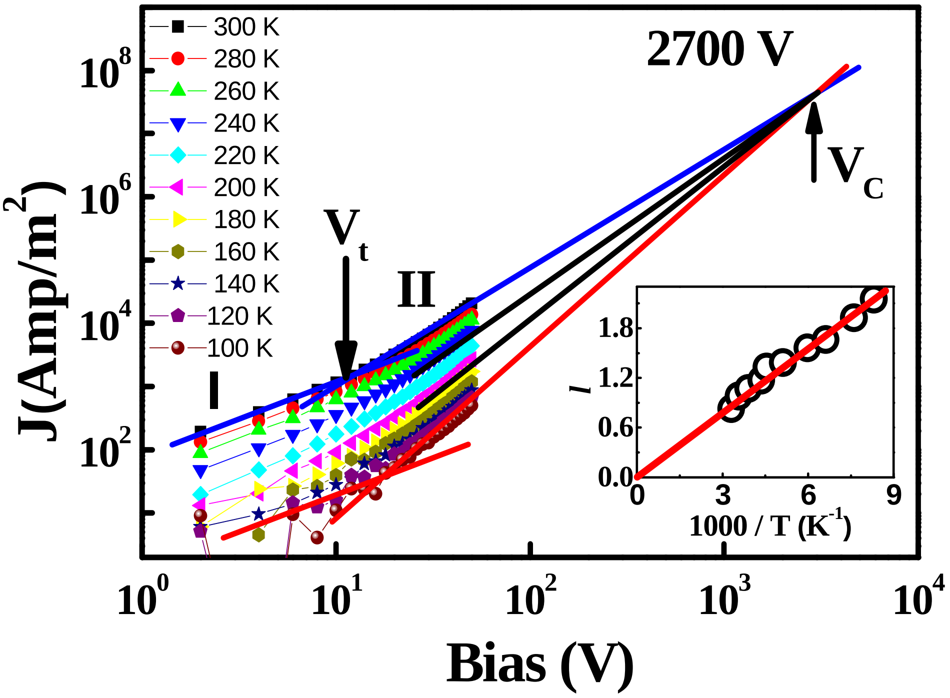

Figure 3.34 Log-log plots of *J-V* characteristics in the temperature range 300-100K, showing a transition from ohmic (region I) to shallow trap mediated space charge limited conduction (region II), the crossover voltage is denoted by V_t. The extension of *J-V* data's in the voltage range of 30-90V meet at cross over voltage V_c = 2700 V.

In order to investigate the charge conduction in FePc films on (0001) Al_2O_3 substrate, we have measured temperature dependent current-voltage (*J-V)* characteristics which are shown in the Fig. 3.33. Since the *J-V* characteristics are symmetrical for positive and negative bias therefore data is shown for positive bias only. Unlike disordered films, no hysteresis is observed in the present case [146]. The *J-V* characteristics were analyzed in low and high electric field region. Based on the nature of J dependence on V and T, five distinct regions (marked as I to V) have been identified. Broadly, regions I, II and IV belong to the low bias (< 100 V), whereas regions III and V lie in the high bias region (> 100V). The analyses of these regions are described below.

Regions I and II

As shown in Fig. 3.34, a transition from region I to region II takes place as a function of applied bias. In the region I, at low voltages (< 20 V at 300 K) the slope of the linear fit to data is ~1, indicating an ohmic conduction. As we have discussed in molecular semiconductors, an ohmic conduction normally occurs if the thermally generated carriers exceed that of injected carriers through the electrode, and the J in this case is given by eq. (3.1) $J = n_0 e \mu V / d$, where n_0 is the thermally generated hole concentration, e is electronic charge, μ is the hole mobility and d is the electrode separation. However, the slope value in region II is ~2, indicating that the charge transport is via shallow trap mediated space-charge limited conduction (SCLC). SCLC occurs if the injected carrier density is higher than the thermally generated carrier density and the J depends on applied bias using the eq. (3.9) $J = \frac{9}{8}\theta_{(t)}\varepsilon_0\varepsilon_r\mu\frac{V^2}{d^3}$ where $\varepsilon_0\varepsilon_r$ is permittivity of the film and $\theta_{(t)}$ is the fraction of free charge carriers . Using data of Fig. 3.34, we have calculated the values of n_o and μ (assuming $\theta_{(t)}$ ~1 which we will justify later) at room temperature in the following manner. The value of μ at room temperature was estimated from the slope of J versus V^2 data [37, 96], and found to be 1.9 cm^2/ Vs. This μ value is higher by two order of magnitude as compared to that reported for metal phthalocyanine [37]. The values of n_0 is determined from the crossover voltage (V_t) between ohmic and SCLC region (as shown in Fig. 3.34) using the eq. (3.10)

$V_t = 8n_0ed^2/9\varepsilon_0\varepsilon_r$ [67]. The estimated value of n_0 at 300 K is 6×10^{18} m^{-3}, which is in agreement with reported literature [96].

It can be clearly seen from Fig. 3.34, with the lowering of temperature the slope of *J-V* characteristics increases (>2) in region II. It indicates the possibility of SCLC in presence of exponentially trap distribution, and in this case *J* is expressed by: $J = e\mu N_V\left(\frac{\varepsilon}{eP_0kT_t}\right)^l \frac{V^{l+1}}{d^{2l+1}}$, where N_V is the effective density of states at the valence band edge, P_0 is the trap density per unit energy range at valence band edge, and $l = T_t/T$ (T_t is the temperature characterizing the trap distribution) [96]. In the region II, it is seen that *J-V* characteristics at different temperatures converge to V_c = 2700 V, indicating that current is temperature independent (for $V = V_c$) and the activation energy is zero. The voltage V_c is related to trap density N_t by equation: $V_c = qN_td^2/2\varepsilon_0\varepsilon_r$ [96]. Using this equation, we obtain $N_t = 5.7 \times 10^{21}/m^3$. The trap characteristic temperature T_t can be determined using exponent of *J-V* characteristics ($\alpha = l+1$) determined at different temperatures from data. A plot of l versus $1/T$ is shown in the inset of Fig. 3.34. The slope of the curve gives the value of T_t (~242 K). A transition from trap free SCLC regime at room temperature to exponentially distributed trap controlled SCLC at low temperature can occur due to free carrier density at room temperature being higher than the trapped carrier density. However, as the temperature is reduced the free carrier density is reduced and the trapped carrier density increases, resulting in exponentially distributed trap controlled SCLC characteristics. Similar bulk limited transport has been reported in various other phthalocyanine films using space-charge-limited conduction (SCLC) model [147, 148].

To justify that $\theta_{(t)} \sim 1$, we first estimated the value of Fermi energy E_F (at room temperature) using $n_0 = N_v\exp[-(E_v-E_F)/kT$ from free carrier density (n_0) and literature value of effective density of states in valence band (i.e. highest occupied molecular level HOMO level in case of organic semiconductor as) $N_v = 10^{27}$ m^{-3} [96] . Now to find out the trap distribution $N_1(E) = P_0 \exp\left(\frac{E_v - E}{kT_1}\right)$ above HOMO edge, we first estimated P_0 using relation $N_t = P_0 kT_t$, here N_t is the total trap density. By knowing P_0 (as 2.73 x 10^{23} eV^{-1}m^{-3}), we estimated $N_1(E)$ i.e density of trap state above HOMO level and plot is shown in Fig. 3.35. As seen from the plot most of the traps are on the average at E ~ 0.1 eV from E_v (i.e. from the HOMO level edge). Density of trapped carriers (n_{t0}) can be estimated from $n_{t0} = N_t.\exp\{(E-E_F)/kT\}$ to be ~ 1.1 x10^{15} m^{-3}. A very small concentration of trapped carriers compared to n_0 (6 x 10^{18} m^{-3}) justifies use of $\theta = 1$ in our analysis.

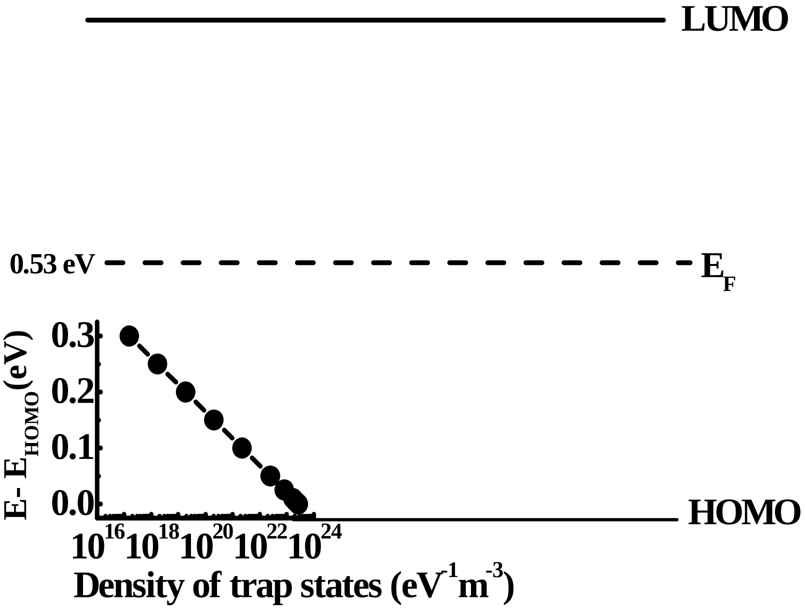

Figure 3.35 Fermi energy levels (E_F) position is shown with respect to the HOMO and LUMO level for FePc films. In the left side show the plot of density of traps states as a function of energy.

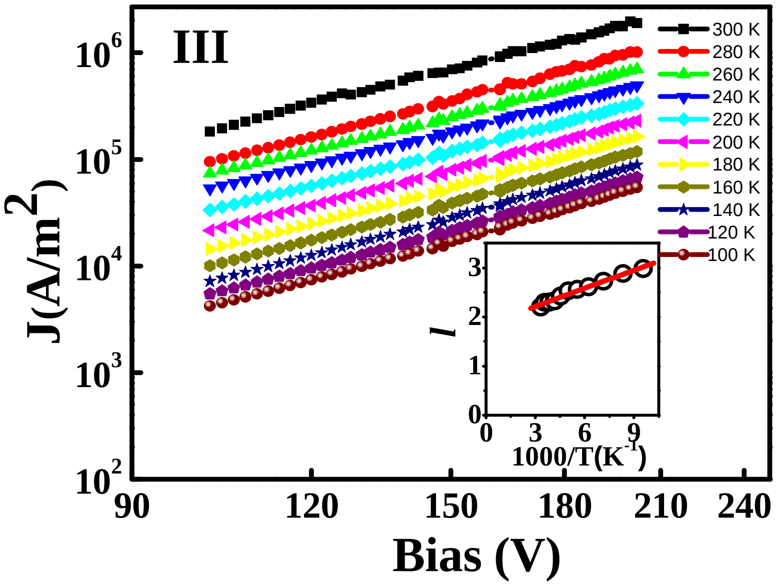

Figure 3.36 *J-V* data of region III is plotted in log-log scale. The inset shows the *l* versus 1/T plot.

Region III

In the region III (i.e. high voltage region of data, > 100 V) of the *J-V* characteristics (shown in Fig 3.36), the slope of *J-V* characteristics is higher than 2 and it increases with lowering of temperature. At higher field values there are following two possibilities which can gives rise to slope > 2: (i) SCLC in the presence of traps which are exponentially distributed in energy above the valence band edge as discussed earlier and (ii) SCLC along with the field dependence of the mobility. To test which model best describes the charge transport, we first plotted the *l* vs 1/*T* as shown in the inset of Fig. 3.36, the straight line fit of data does not pass through origin. Hence we rule out the possibility of the SCLC in presence of exponential trap distribution. To explain such non-linear *J-V* characteristic, the field dependence mobility is invoked in the SCLC relation according to the eq. (3.25)

$\mu(E) = \mu\ (0)\exp(\gamma\sqrt{E})$ and eq. (3.26) $\gamma = B\left(\frac{1}{K_BT} - \frac{1}{K_BT_0}\right)$ [149]:

According to the SCLC with field enhanced mobility, the effect of high electric field is to reduce energy barrier between two hopping site and as result charge carriers transport takes easily. In other words the effect of high field suppresses the charge carrier trapping.

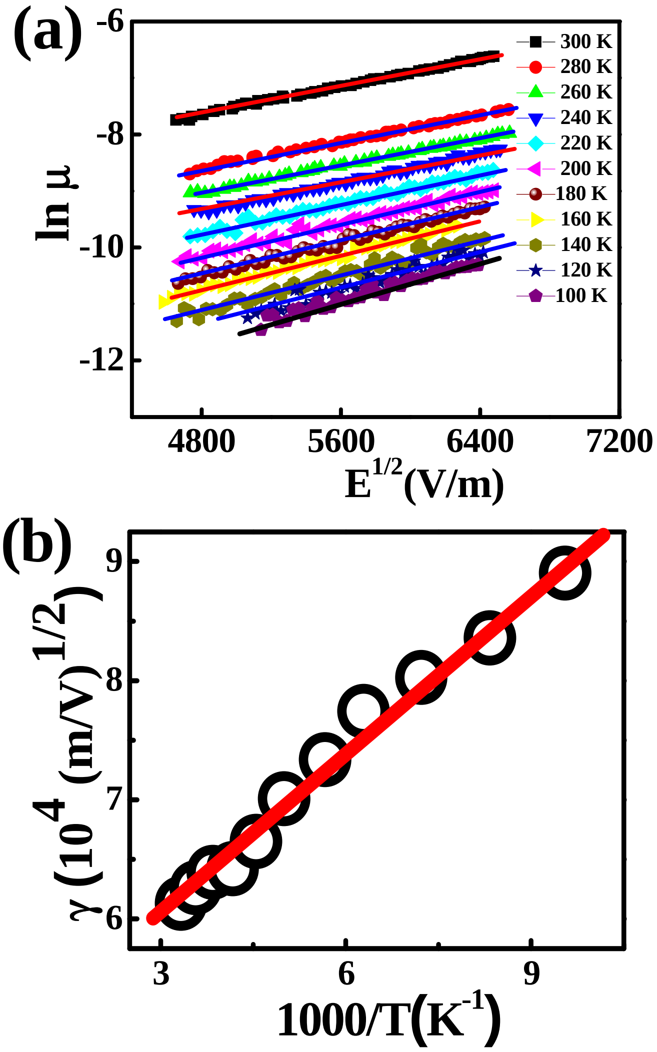

Figure 3.37 (a) Field dependence of the mobility obtained from data of region III. (b) Temperature dependence of field enhancement coefficient γ (which describe the field dependence of the mobility).

A simple approach of estimating field dependence of mobility is described by Wu et. al. in which μ is related with a function g through the relation: $\mu = \frac{1}{E}\frac{dg(E)}{dE}$, where $g(E) = \frac{dJ}{\varepsilon}$ and $E = \left(\frac{V}{d} + \frac{J}{d}\frac{dV}{dJ}\right)$ [96]. The estimated field dependence of μ at different temperature (300 K- 100 K) is shown in Fig. 3.37 (a). The straight line fit of the data $ln\ \mu$ versus $E^{1/2}$ data at each temperature shows the validity of SCLC with field dependence of mobility. From these fits we obtained the temperature dependence of γ. From the inverse temperature dependence of γ (as shown in the 3.37 (b)) the fitted parameters values was found to be: T_0 = 98 K, and B = 3.94 x10^{-4} eV(m/V)$^{1/2}$. The values of derived parameter and their temperature dependence are according to the reported literature for organic materials [150].

Regions IV and V

As shown in Fig. 3.33, for temperatures < 100K, the *J-V* characteristics show very different behaviors in regions IV and V. In region IV i.e. at low bias, *J* drops sharply with lowering *T*; whereas in region V i.e. at very high bias, the *J* shows a very weak *T* dependence and the slope of *J-V* data is constant at all temperatures. These data, as analyzed below, indicate that the electrode-limited processes govern the charge transport at low temperatures. In region IV, a linear fit of J *vs* $V^{1/2}$ data, as plotted in Fig. 3.38 (a) in a semi-log scale, indicates that charge transport is governed by Schottky model: $J = AT^2\exp(-\phi/kT)\exp(\frac{\beta_s}{kTd^{1/2}}V^{1/2})$, where *A* is Richardson constant (1.2×10^6 Am^{-2}), ϕ is barrier height at the Au/FePc interface and β_S $\{=(e^3/4\pi\varepsilon_0\varepsilon_r)^{1/2}\}$ is the field lowering coefficient. The obtained values of β_S and ϕ are 1.94×10^{-5} eVm$^{1/2}$/V$^{1/2}$ and ~0.17 eV respectively. The experimentally determined value of β_S is close to its theoretical value (2×10^{-5} eVm$^{1/2}$/V$^{1/2}$), which supports Schottky-barrier limited conduction mechanism in region IV. The value of ϕ also matches with literature reported value [67, 96].

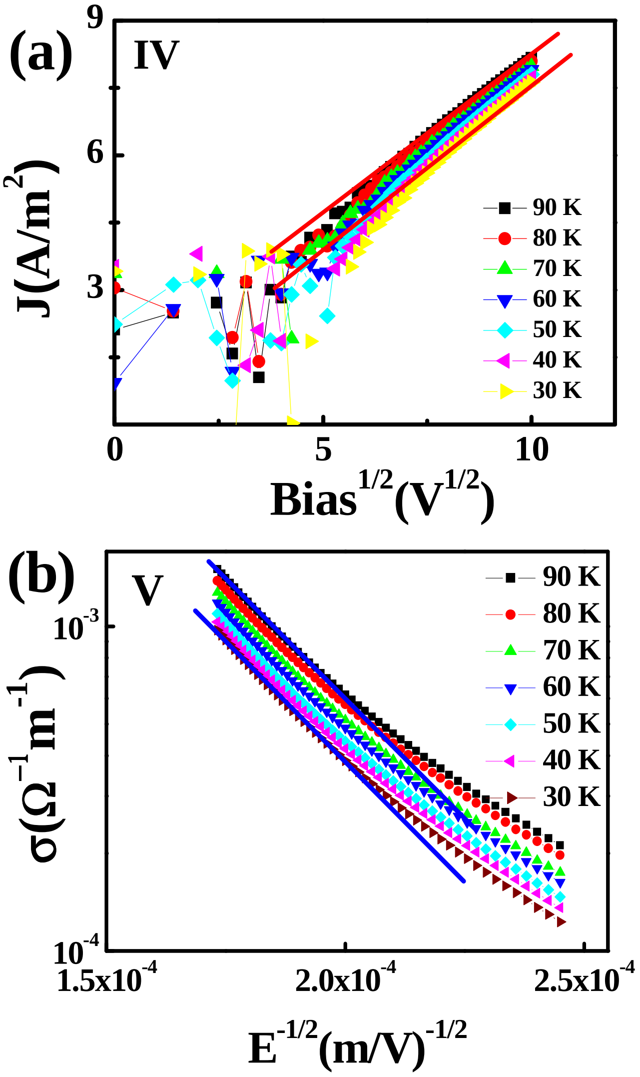

Figure 3.38 (a) Data of region-IV plotted as *ln J vs* $V^{1/2}$. Linear fits to data indicate Schottky-barrier limited conduction. (b) Data of region-V plotted as conductivity as a function of inverse of the square-root of electric field.

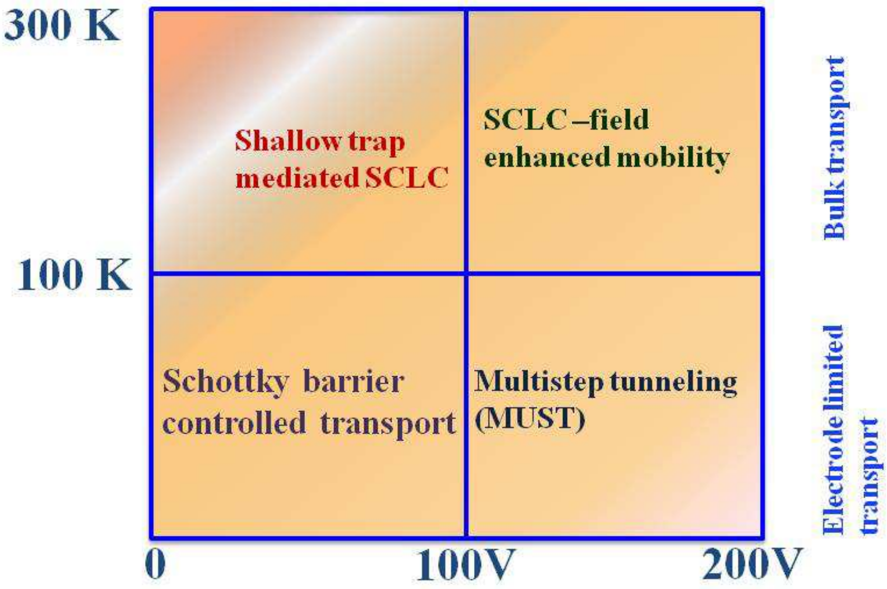

Figure 3.39 Schematic of temperature-bias (*T*-*V*) plane summarizing various conduction mechanisms in FePc films.

A weak *T* dependence of *J* in the region *V* indicates a possibility of tunnelling mechanism. It has been discussed that if localized states are present in the gap, then these states assist sequential tunnelling of charge carries (i.e. from the Fermi level of the electrode to the conduction level of the film) and this process is termed as multi-step tunnelling (MUST). It has been demonstrated that MUST is observed only in high μ devices and this mechanism leads to an inverse square-root field dependence of conductivity i.e. $\sigma \propto \exp\left(-\sqrt{\frac{E_0}{E}}\right)$, where $E_0 = \frac{16\sqrt{2m}\alpha\phi^{3/2}}{3e\hbar}$. E_0 is related to the material through the potential barrier (ϕ) and a parameter α given by $\alpha = \ln(p^{-1})$, where p^N is the probability of forming N-step tunnelling path. As shown in Fig. 3.38 (b), in region-V the conductivity varies as the inverse square-root of the field, confirming the MUST mechanism. By least square fitting of data at 30 K, the obtained value of E_0 is 2277 kV/cm. Using interface barrier ϕ = 0.17 eV (as determined earlier) and p = 0.84 (hence α is 0.17), the theoretically calculated value of E_0 is 2273 kV/cm, which is consistent with experimentally observed value. MUST mechanism have experimentally been reported in organic field effect transistors and organic light emitting diodes having high mobility. However, the experimentally observed E_0 value in these cases are very high (~6400 kV/cm) due to high contact barrier of 0.5 eV [126-128, 150]. One of the possible explanations for observation of MUST in high μ devices could be higher contact resistance compared to the sample resistance, as a result most of the applied bias drop across the contacts and makes MUST a favourable mechanism. The various charge transport mechanisms operating in the FePc films as a function of temperature and bias are summarized in the Fig. 3.39.

3.4.1.2 Temperature dependent resistivity

Temperature dependence of the resistivity (ρ) of FePc films is shown in Fig. 3.40 (a). An increase in ρ with decreasing temperature for all the films suggests their critical or insulating behaviour. These behaviors can be identified through Zabrodskii plots i.e. temperature dependence of the reduced activation energy (W), which is defined as [151]:

$$W = - dln[\rho(T)]/dlnT \qquad (3.42)$$

Positive, zero and negative slopes of W versus T corresponds to the metallic, critical and insulating regimes, respectively [151-153]. The variation of W with T for FePc films is shown in Fig. 3.40 (c). It is seen that for all films the value of W is nearly independent of the temperature i.e. slope is zero. It indicates that all films are in the critical regime. In the critical regime of metal to insulator transition, resistivity is expected to show power law dependence ($\rho \propto T^{-\beta}$) [3, 152]. A nearly linear dependence of log ρ on log T for FePc films shown in Fig. 3.40 (b), suggesting that these films are in critical regime.

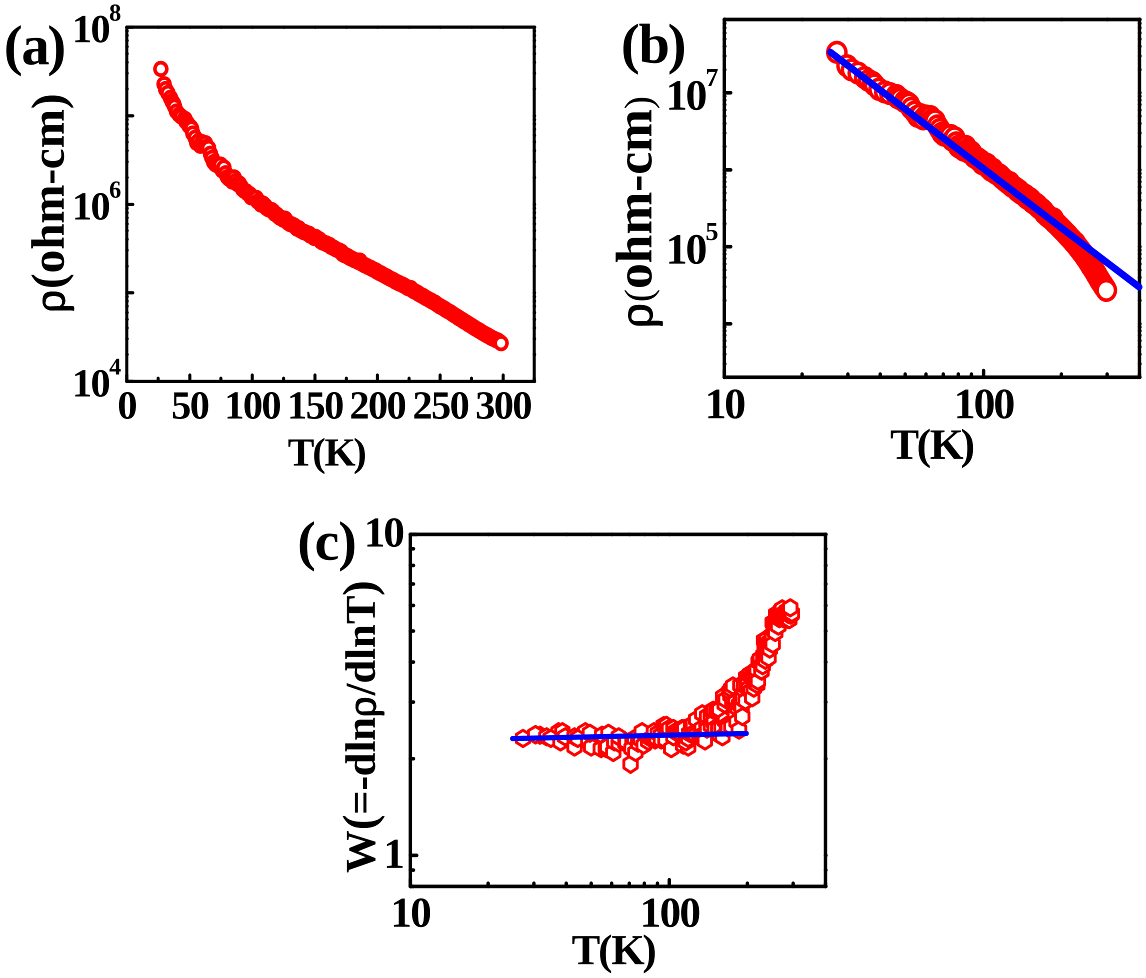

Figure 3.40 (a) The temperature dependence of resistivity ρ (b) Nearly linear dependence of *log* ρ versus *log T* plots (c) Plots of reduced activation energy W (= -dln[ρ(T)]/dlnT) for FePc films.

3.4.2 Charge conduction in CoPc films

In this section we present the charge conduction properties of CoPc films deposited on (0001) Al_2O_3 and (100) $SrTiO_3$ substrates.

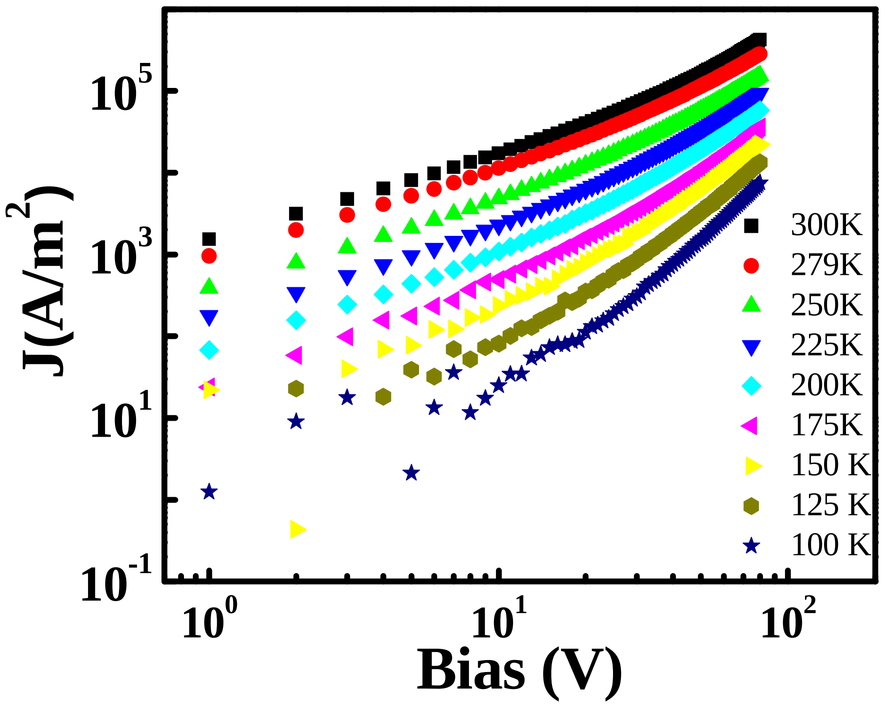

Figure 3.41 Log-log plots showing *J-V* characteristics of CoPc films in the temperature range 300-100 K.

3.4.2.1 CoPc films on (0001) Al_2O_3 substrate

The *J-V* characteristics of CoPc film on (0001) Al_2O_3 substrate, as shown in Fig. 3.41, have been analyzed for temperature range of 100-300 K and below 100 V. The characteristics at room temperature show ohmic and SCLC characteristics with $\alpha = 2$ while at low temperatures value of exponent (at high current) increases indicating SCLC mechanism with exponential distribution of traps. A transition from trap free SCLC regime at temperature to exponentially distributed traps controlled SCLC at low temperature can occur due to free carrier density at room temperature being higher than the trapped carrier density. In the estimation of mobility we have assumed $\theta_{(t)} = 1$, since the trapped charge carrier density is ~ 5 x 10^{10} cm^{-3} i.e. four order of magnitude lower than free carrier density (as we have justified for FePc films). For lower temperatures, dependence of exponent α on $1/T$ is shown Fig. 3.42 (b). Using $\alpha = l + 1 = T_t/T + 1$, the slope of the curve gives the value of T_t =236 K. To determine total trap density, *J-V* data obtained at different temperatures has been plotted in log-log scale in Fig. 3.42 (a). It is seen that characteristics at different temperatures converge to V_c = 1370 V, indicating that the current is temperature independent (for $V = V_c$) and the activation energy is zero. Using value of V_c, the trap density N_t is found to be 1.1 x $10^{16}/\text{cm}^3$ using equation: $V_c = qN_td^2/2\varepsilon_0\, \varepsilon_r$. It is seen that CoPc films have better mobility compared to that of FePc films.

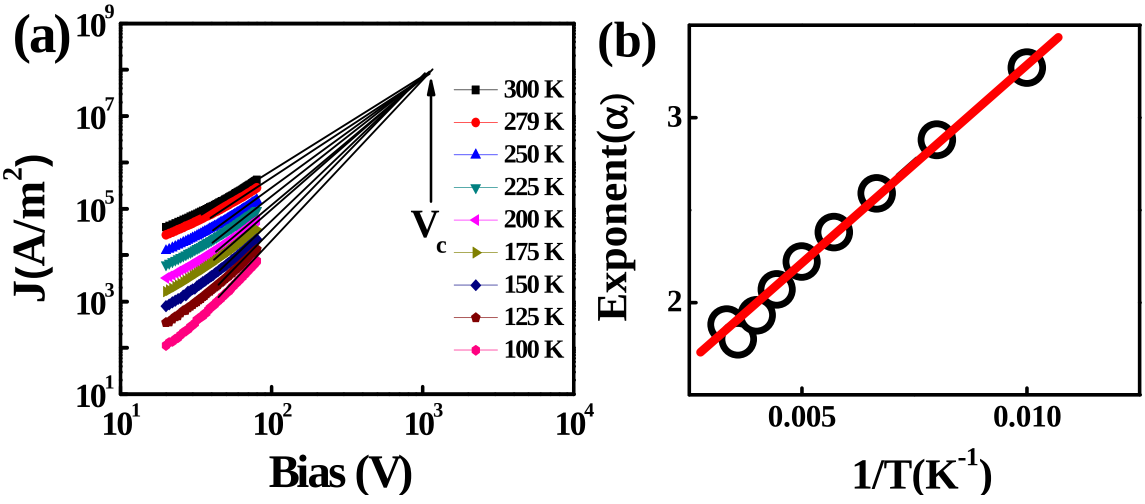

Figure 3.42 (a) Power law fit of *J-V* data's. The fits meet at cross over voltage V_c = 1368 V. (b) The temperature dependence of voltage exponent (α).

Temperature dependence of the resistivity (ρ) of CoPc films is shown in Fig. 3.43 (a). The variation of *W* with *T* for FePc films is shown in Fig.3.43 (c). It is seen that for CoPc films the value of *W* is nearly independent of the temperature i.e. slope is zero. It indicates that CoPc films are in the critical regime. A nearly linear dependence of log ρ on log T for CoPc films, as shown in Fig. 3.43 (b), suggesting that these films are in critical regime.

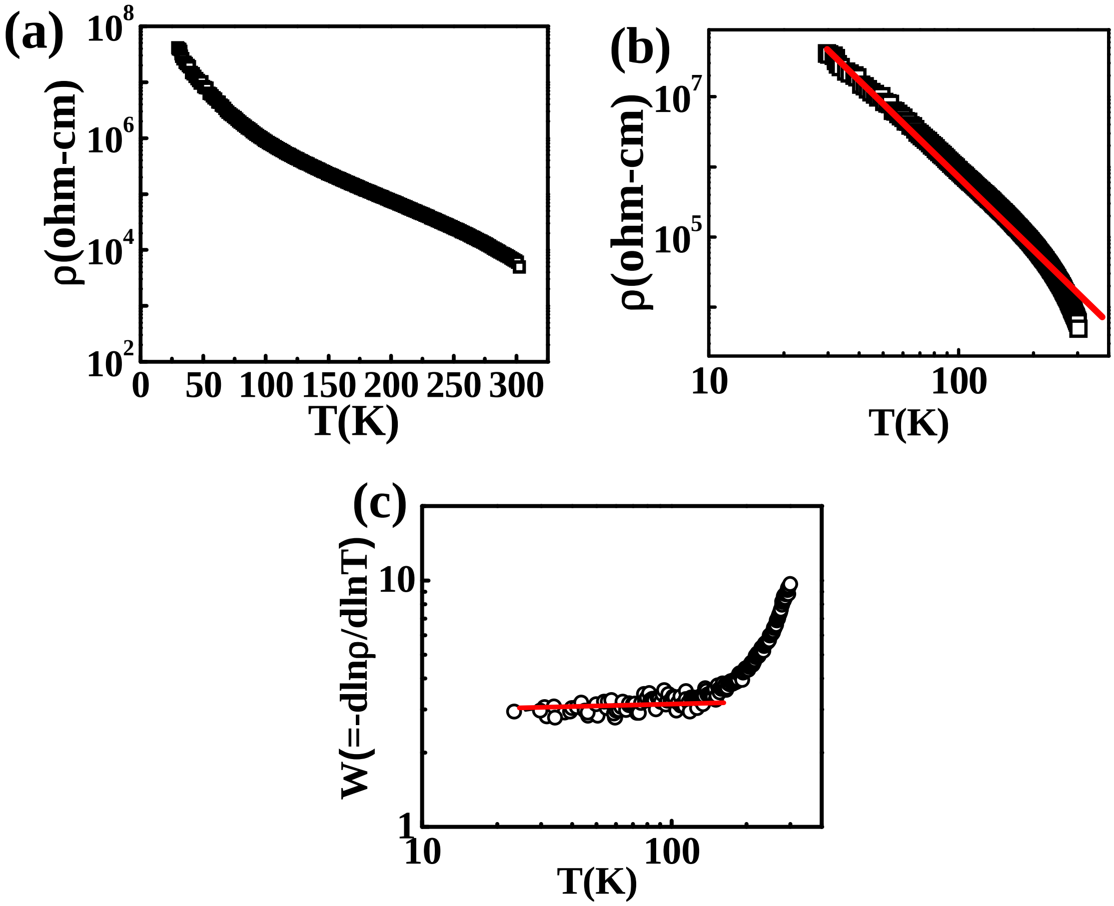

Figure 3.43 (a) The temperature dependence of resistivity ρ (b) Nearly linear dependence of *log* ρ versus *log T* plots (c) Plots of reduced activation energy W (= -dln[ρ(T)]/dlnT) for CoPc films.

3.4.2.2 CoPc films on (100) $SrTiO_3$ substrate

The temperature dependent ρ plots of CoPc films deposited on (100) $SrTiO_3$ along with (0001) Al_2O_3, (001) $LaAlO_3$ and bi-crystal $SrTiO_3$ are shown in Fig. 3.44 (a). It is evident that that films grown on (100) and bi-crystal $SrTiO_3$ substrate shows lowest room temperature resistivity value (0.5Ω-cm) as well as weak semiconductor-like temperature dependence. It was reported that twin boundaries of (001) $LaAlO_3$ and grain boundary of $SrTiO_3$ substrate acts as template for a higher degree of CoPc molecular ordering [3, 67]. From Fig. 3.44 (a), it can also be seen that films prepared on (100) $SrTiO_3$ and (0001) Al_2O_3 substrates show nearly similar value of the room temperature ρ (165 Ω-cm) in concomitant with similar semiconducting–like temperature dependence of ρ up to 110 K. It is interesting to note that below 110 K, films prepared on (100) $SrTiO_3$ exhibit a sharp drop in ρ with temperature (i.e. metal-like behavior). However, for temperatures < 80 K, the ρ becomes independent of temperature. In contrast films deposited on (0001) Al_2O_3 show semiconducting behavior in the entire measure temperature range. As seen from Fig. 3.44 (b), semiconductor–metal transition of CoPc films prepared on (100) $SrTiO_3$ is highly reversible with respect to temperature cycling.

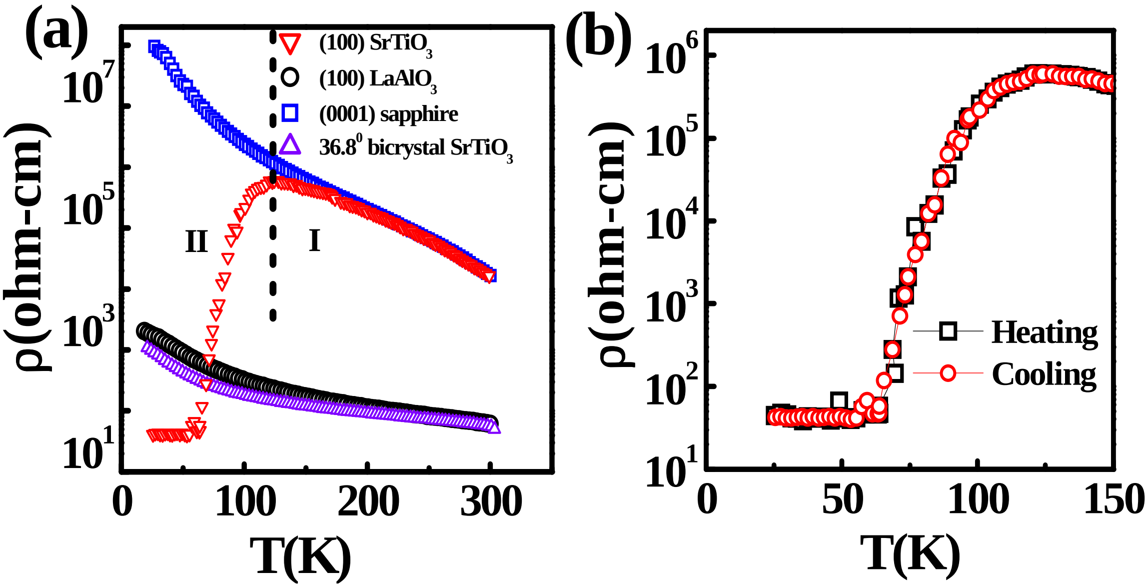

Figure 3.44 (a) The temperature dependence of resistivity ρ (b) Nearly linear dependence of *log* ρ versus *log T* plots

The metallic behavior of CoPc films on (100) $SrTiO_3$ in the temperature range 80-110 K is also identified through Zabrodskii plots, described by $W = -\,\mathrm{dln}[\rho(T)]/\mathrm{dln}T$. A positive slope, as shown in the inset of Fig. 3.45, suggests a metallic behavior. The lowest ρ in the metallic state of CoPc films prepared on (100) $SrTiO_3$ is nearly comparable to the room temperature ρ of highly ordered films prepared on (001) $LaAlO_3$ and bi-crystal $SrTO_3$ substrates. This suggests that molecular ordering has improved in the low temperature metallic state of CoPc films.

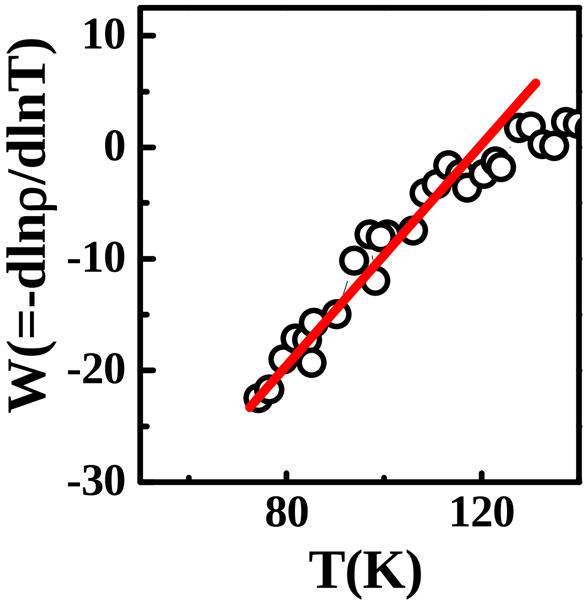

Figure 3.45 Plots of reduced activation energy W (= -dln[ρ(T)]/dlnT) for (Co-Fe)Pc films.

In order to investigate the change in molecular ordering at low temperatures, we have recorded temperature dependent GIXRD for CoPc films prepared on (100) $SrTO_3$ and the results are shown in Fig. 3.46 (a). As we have shown 300 K, presence of a Bragg peak at 6.78°, corresponding to the (200) peak of the α-CoPc phase, indicating that film is crystalline with a-axis normal to the substrate. The calculated value of a lattice parameter is found to be

26.12 Å. We have also recorded the XRD pattern for CoPc powder, which could be indexed to monoclinic structure with unit cell parameters of a = 26.12 Å, b = 3.79 Å, c = 25.2 Å, β = 90.4° and volume = 2494.61 Å^3. Same a-parameters of the film and powder indicate both have identical crystal structures. With lowering temperature, no change in the Bragg peak position of CoPc films was observed until 110 K. However, for temperatures <110 K, this peak shifts to lower angle i.e. 2θ = 6.51°, which corresponds to a lattice parameter equal to ~27.05 Å. An increased a lattice parameter (direction normal to the substrate plane) clearly indicates that lattice parameters b and c (both lie in the plane of the substrate) might also have changed. It is well established that at ~110 K, $SrTiO_3$ undergoes a cubic-to-tetragonal structural transition with reduction in volume and an increase in c/a ratio (from 1 to 1.00056) i.e. in-plane compression of the unit cell [154-156]. It is therefore natural to attribute the changes in the lattice parameters of CoPc films to the structural transition of the $SrTiO_3$. Since the b and c axes of CoPc lay in the plane of the substrate, therefore, in principle, in-plane compression should decrease both these lattice parameters. However, as shown in Fig. 3.47, along the b-axis (i.e. in the substrate plane) CoPc molecules are stacked in *face-to-face* configuration, which facilitates reduction of b-parameter due to strong π-π interactions under in-plane compression. On the other hand, along a- and c-axes (i.e. out of substrate plane), molecules are stacked in *face-to-edge* configuration, implying that if b-parameter decreases then both a- and c-parameters would increase, and this is exactly what we experimentally observed for the a-parameter. Since the charge transport properties strongly depend on the b-parameter (as discussed later), it is essential to estimate its value. Unfortunately, b-parameter cannot be experimentally measured as the films are highly oriented. We therefore estimated b-parameter by assuming both c-parameter and unit cell volume as constant, which is plotted in Fig. 3.46 (b). After the structural transition, the *b*-parameter decreases from 3.80 to 3.66 Å. Since *c*-parameter have two opposing effects i.e. reduction due to in-plane contraction of substrate and elongation due to *face-to-edge* stacking of molecules, therefore it is reasonable to assume its value as constant. Similarly, assuming constant unit cell volume would give a lower limit to decrease in *b*-parameter. Decrease in *b*-parameter leads to an improved to π-π interactions among molecules, and hence an improved charge conduction. Evidence that (100) $SrTiO_3$ substrate is responsible for the triggering of metallic behavior in CoPc films is also evident from the temperature dependence of ρ for films having thicknesses > 200nm, which exhibit semiconducting behavior in the entire temperature range owing to a weak film– substrate interaction as shown in Fig 3.48.

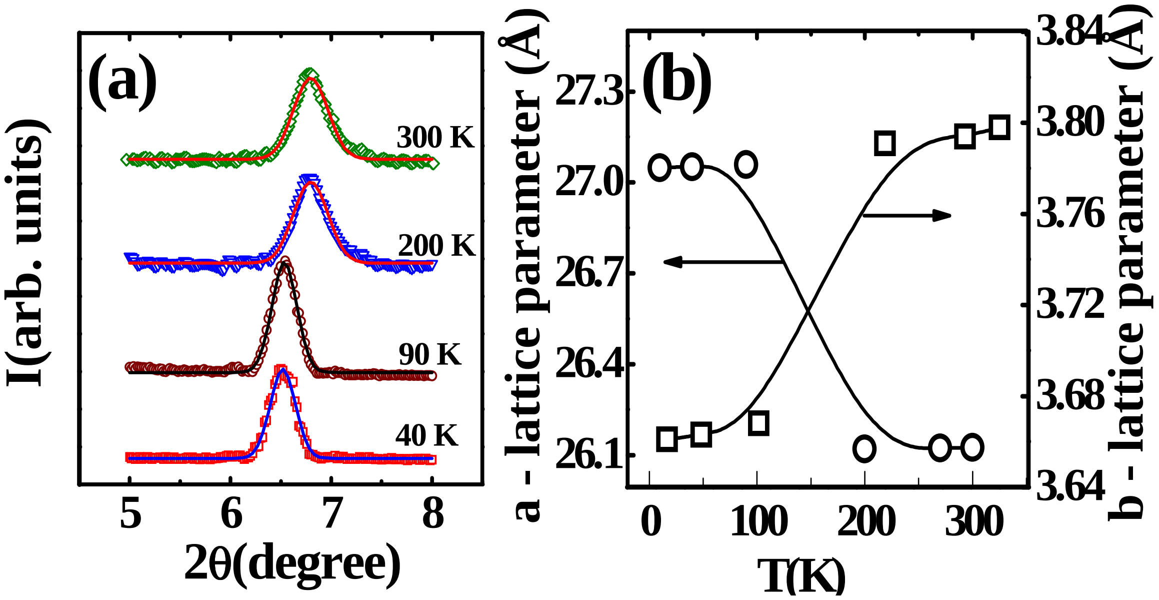

Figure 3.46 (a) Temperature dependent GIXRD data for CoPc film grown on (100) $SrTiO_3$. (b) Temperature dependence of *b* and *c* lattice parameters for CoPc films.

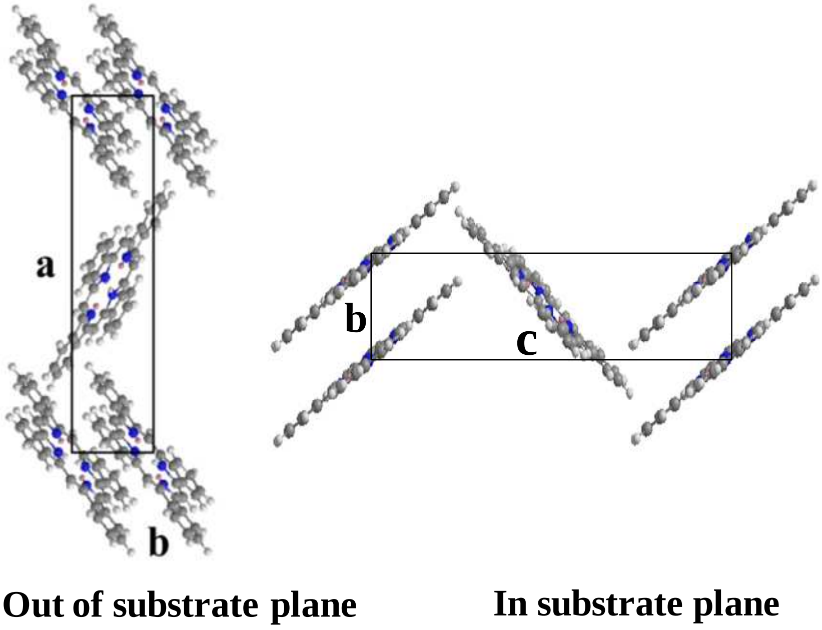

Figure 3.47 Schematic representation of the stacking of CoPc molecules in *a*-*b* (out of substrate plane) and *b*-*c* planes (in substrate plane).

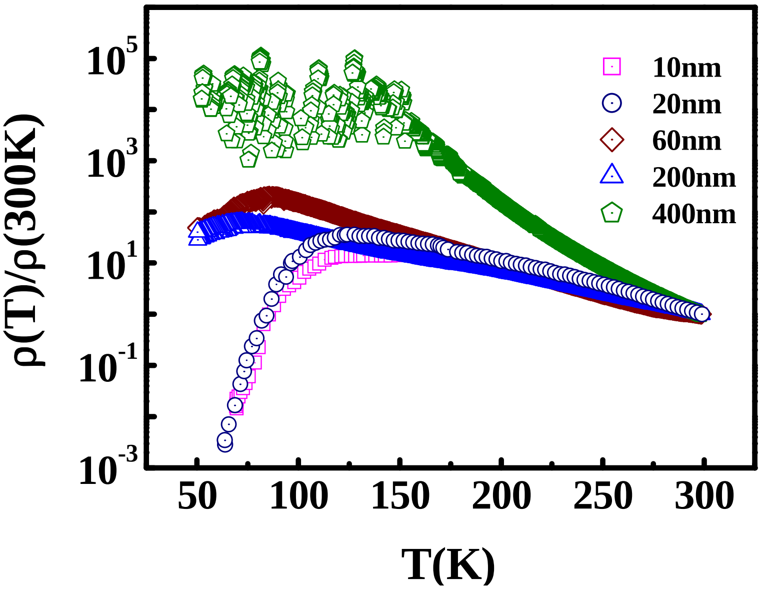

Figure 3.48 The temperature dependence of resistivity ρ for CoPc films of different thickness (100) $SrTiO_3$.

We further analyze the temperature dependence of ρ in the semiconducting and metallic regions marked by respectively I and II in Fig. 3.44 (a). In the semiconducting regime (300–110 K), transport occurs through variable range hopping (VRH) of charge carriers among the localized states and the ρ is given by: $\rho(T) = \rho(0)\exp(T_0 / T)^{\frac{1}{d+1}}$, where d is the dimensionality (D) of the hopping process and T_0 is the characteristics Mott temperature [151]. A linear fit of $\ln \rho$ vs $T^{-1/4}$, as shown in the inset of Fig. 3.49, indicates charge transport in region-I is governed by 3D VRH mechanism. In the metallic region (i.e. region II, $T \leq 110$ K), since the intermolecular distance (i.e. b-parameter) decreases therefore nearest neighbor hopping (NNH) mechanism is expected. In NNH, the conduction mechanism is governed by a parameter λ defined as: r/a_B, where r is hopping distance and a_B is the effective Bohr radius ($a_B = 4\pi\varepsilon\hbar^2 / m^* e^2$; ε is the permittivity of the material, $\hbar$ is the Planck's constant and m^* is the effective mass of electron). For λ >>1 a semiconducting behavior is expected, while metallic behavior occurs if $\lambda \rightarrow 1$ [157]. Assuming $\varepsilon_0\varepsilon_r = 2.43\times10^{-11}$ F/m and $m^* = 0.47\ m_e$ (as reported for organic semiconductor), the estimated value of a_B comes out to be 3.39 Å [158]. Taking hopping distance r equal to the intermolecular distance (3.66 Å), the value of λ comes out to be ~1, indicating metallic behavior due to the NNH conduction.

The temperature dependent J-V characteristics of the regions-I are shown in Fig. 3.49. Unlike disordered films, no hysteresis is observed in the present case. In region-I, the slope of the linear fit to J-V data is ~1, indicating an ohmic conduction that occurs as thermally generated carriers exceed to those injected through the electrode. However, the slope value in the higher bias (>20 V) is ~ 3, indicating that the charge transport is via exponentially distributed trap mediated space-charge limited conduction (SCLC) as given by eq. (3.21). From Fig. 3.49, it can be seen that with the lowering of T, slope of J-V characteristics increases at high bias and all these curves converge to V_c = 205 V. Taking this V_c value, trap density (N_t) is found to be 7.6×10^{14}/cm^3 using the relation: $V_c = qN_t d^2/2\varepsilon_0\varepsilon_r$. From eq. (3.21) and taking the value of trap density $N_t = P_0 kT_t$ the estimated value of room temperature μ ~ 4.3×10^{-7} cm^2/Vs. Such low value of μ indicates that inter-molecular connectivity is poor near room temperature.

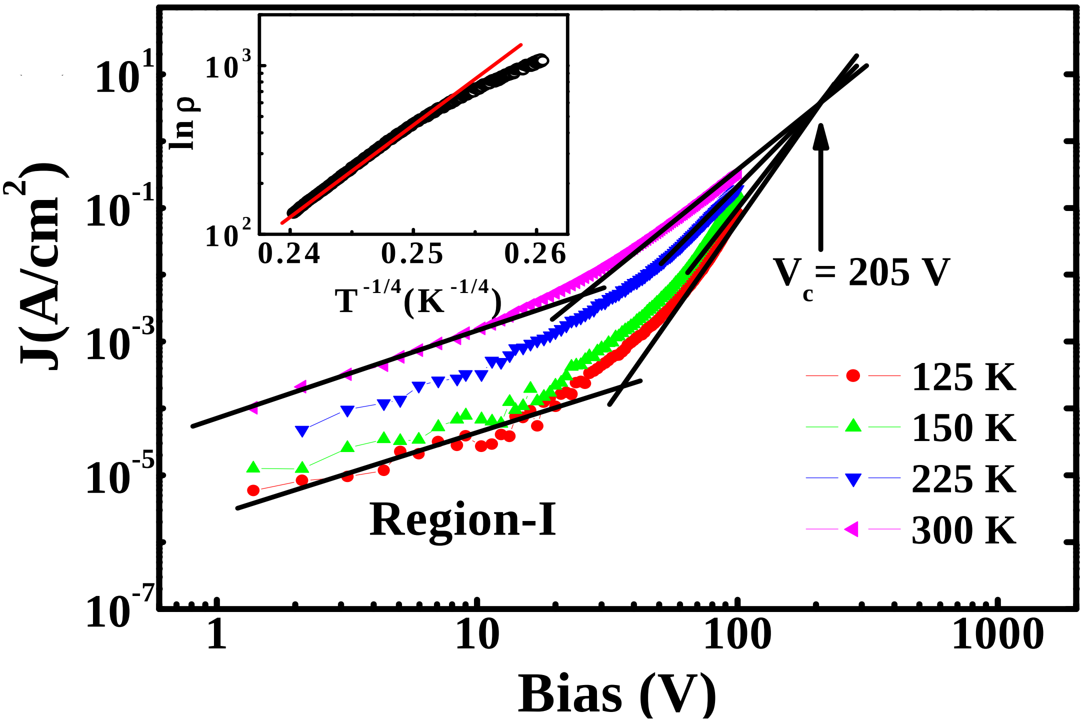

Figure 3.49 Log-log plots showing *J-V* characteristics of CoPc films in the temperature range 300 - 125 K. Inset shows the linear fit of lnρ vs $T^{-1/4}$ data, indicating 3D-VRH conduction.

In region-II, i.e. at temperature < 110 K, the *J-V* characteristics (as shown in Fig. 3.50) shows a peculiar behavior, In the bias range of 0–20 V, current is extremely low and for higher bias the current increases rapidly. The constant slope (~13) of *J-V* curves (at high bias > 20 V) with the variation of temperature indicates that field assisted tunnelling current dominates here. In this temperature range (particularly below 70 K) and at higher bias, J is nearly independent of temperature (also reflected as temperature independent ρ at $T < 90$ K in Fig. 3.44 (b)), which indicates tunnelling of charge carriers. In case of field assisted tunnelling, the energy gained by charge carriers from electric field is higher or comparable to the energy difference between the localized states involved in transitions and the conductivity has an inverse square-root dependence given in eq. (3.36). As shown in inset of Fig. 3.50, the conductivity indeed varies as the inverse square-root of the field, confirming the field assisted tunnelling of charge carriers. By least square fitting of data at 70 K, the estimated tunnelling barrier ϕ comes out to be ~12.78 meV. A rough estimate of field enhanced tunnelling probability of charge carriers between molecules can be done using simple tunnelling approximations. The energy gained by charge carrier over its localization length (w ~14 Å) in the external electric field is given by $\Delta\xi = eEw$. For a maximum field strength E = 83 KV/cm (corresponds to maximum voltage in the present case), the estimated value of $\Delta\xi$ is 11.62 meV. Transmission probability through the tunnel barrier in presence of high electric field is given by $p = \exp\left\{-2[(\phi - \Delta\xi)/\phi)]^{1/2}\right\}$. For Φ ~ 12.78 meV, and $\Delta\xi$ = 11.62 meV, the value of p comes out to be ~0.74. Such a high probability i.e. $p \rightarrow 1$ corresponds to the metallic behavior at high fields. In the present case typical field strength (~17 kV/cm) required to derive the system from semiconducting to metallic states and it matches well with the reported values for other organic semiconductors [126].

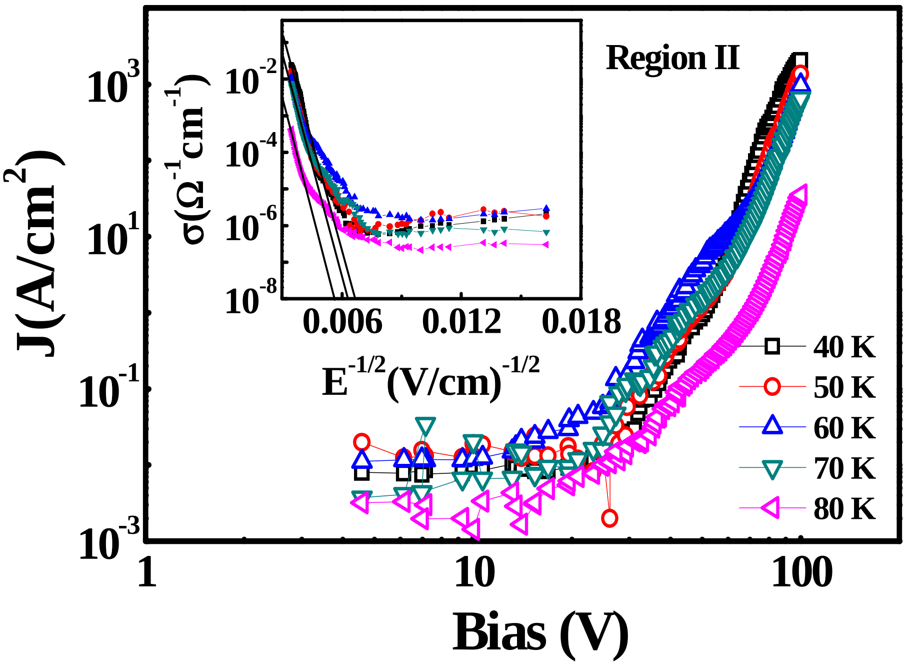

Figure 3.50 Log-log plots showing *J-V* characteristics of CoPc films in the temperature range 80-40 K. Inset shows the plot of conductivity as a function of inverse of the square-root of electric field at different temperatures.

3.4.3 Charge conduction in F_{16}CuPc films

The *J-V* characteristics of F_{16}CuPc films of 20 nm $LaAlO_3$ substrate is shown in Fig. 3.51. Two different power law behavior (J~V^{α}) is observed as a function of applied bias with varying exponent (α) values. At room temperature for low bias < 10 V, α ~ 1 indicates ohmic conduction. For the bias range > 20 V, α ~ 2 indicates space charge limited conduction (SCLC). The values of n_0 can be determined from the crossover voltage (V_t) as discussed earlier. The estimated value of n_0 for for F_{16}CuPc is ~10^{14} cm^{-3}, which is in agreement with reported literature [37, 67]. The μ values at room temperatures were. The room temperature μ for F_{16}CuPc films is found to be ~ 5 cm^2/Vs calculated using the slopes of J-V^2 plot of data of Fig. 3.51. This μ value is higher by two orders in magnitude as compared to that reported for metal phthalocyanine films [37]. The temperature dependence resistivity of $F_{16}CuPc$ films is discussed in Chapter 4.

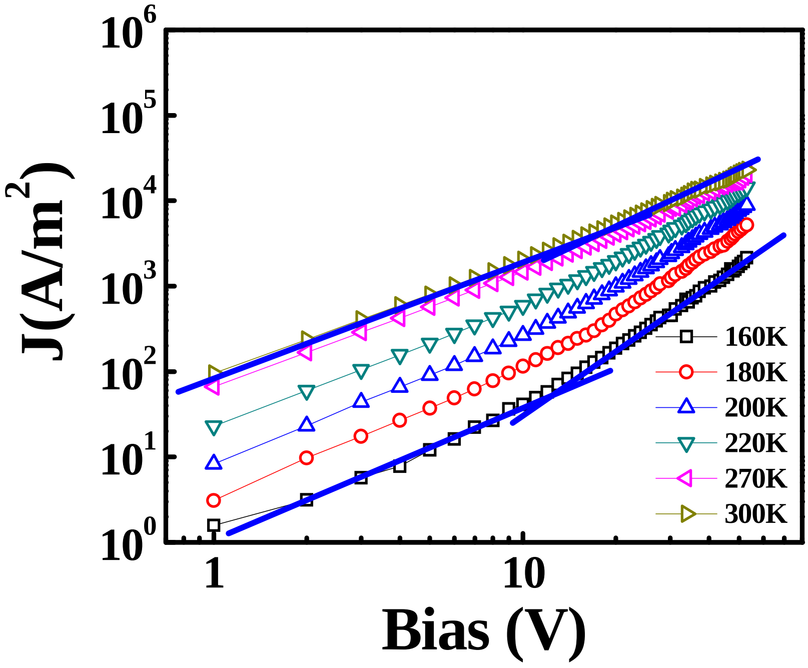

Figure 3.51 Log-log plots showing *J-V* characteristics of 20 nm $F_{16}CuPc$ films in the temperature range 300 - 160 K.

3.4.4 Charge conduction in drop casted CuPcTs films

J-V characteristic of CuPcTs films of thickness ~ 1 µm at room temperature are shown in Fig. 3.52. The magnitude of *J* is for CuPcTs films are three orders of magnitude lower as compared to CoPc and FePc films as we have discussed in previous section. Further for these films, the different power law behaviour ($J \sim V^{\alpha}$) is observed as a function of applied voltage with varying exponent α. At room temperature for low bias < 15 V, α ~ 1 indicates ohmic conduction. For the bias range > 20 V the value α of is ~ 4. This high value of indicates the SCLC with deep traps. Therefore, mobility of these films could not be calculated from *J-V* curve. As we have discussed earlier, the drop CuPcTs films are amorphous in nature as compare to other phthalocyanine (CoPc, FePc or F_{16}CuPc) films deposited by MBE. These films do not transport any measurable current low 280K. Therefore temperature dependent resistivity and *J-V* could not be measured below 280 K.

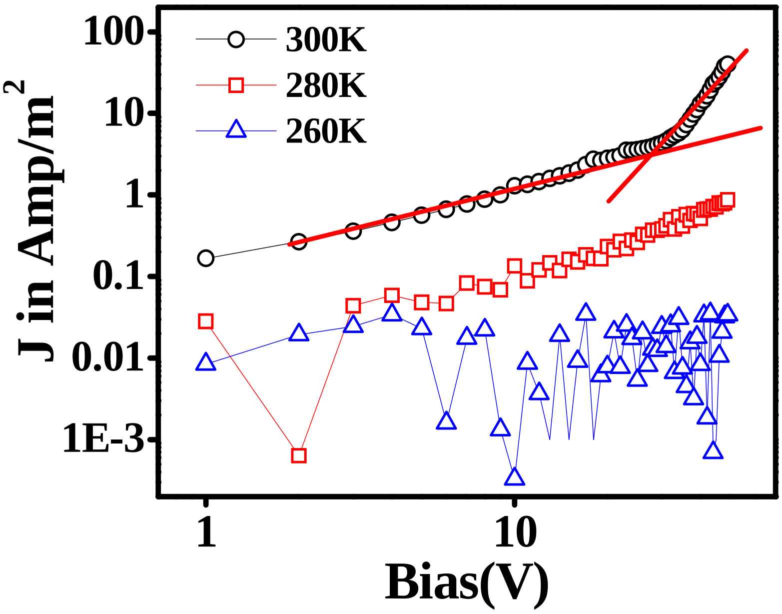

Figure 3.52 Log-log plots showing *J-V* characteristics of CuPcTs films on quartz substrate in the temperature range 300 - 260 K.

3.5 Charge conduction in binuclear (Co-Fe)Pc films

3.5.1 Temperature dependent resistivity

Plot of ρ and conductivity W parameter as function of temperature for (Co-Fe)Pc films is shown in Fig 3.53 (a) and (c). The positive, slope of W vs T indicates that (Co-Fe)Pc films are metallic regime in accordance with much lower resistivity of (Co-Fe)Pc films. In the metallic regime the temperature dependence of conductivity can be described as:

$$\sigma(T)=\sigma(0)+mT^{p/2} \tag{3.35}$$

where σ (0) is a constant, and for electron-phonon interaction p =2.5 – 3. This model has been widely used to describe the metallic behaviors of the conducting polymers films such as heavily doped polypyrrole films [152, 159]. As shown in Fig. 3.53 (b), $T^{3/2}$ dependence of conductivity shows validity of above equation indicating that electron-phonon scattering is the main mechanism for charge carrier scattering in the composite films.

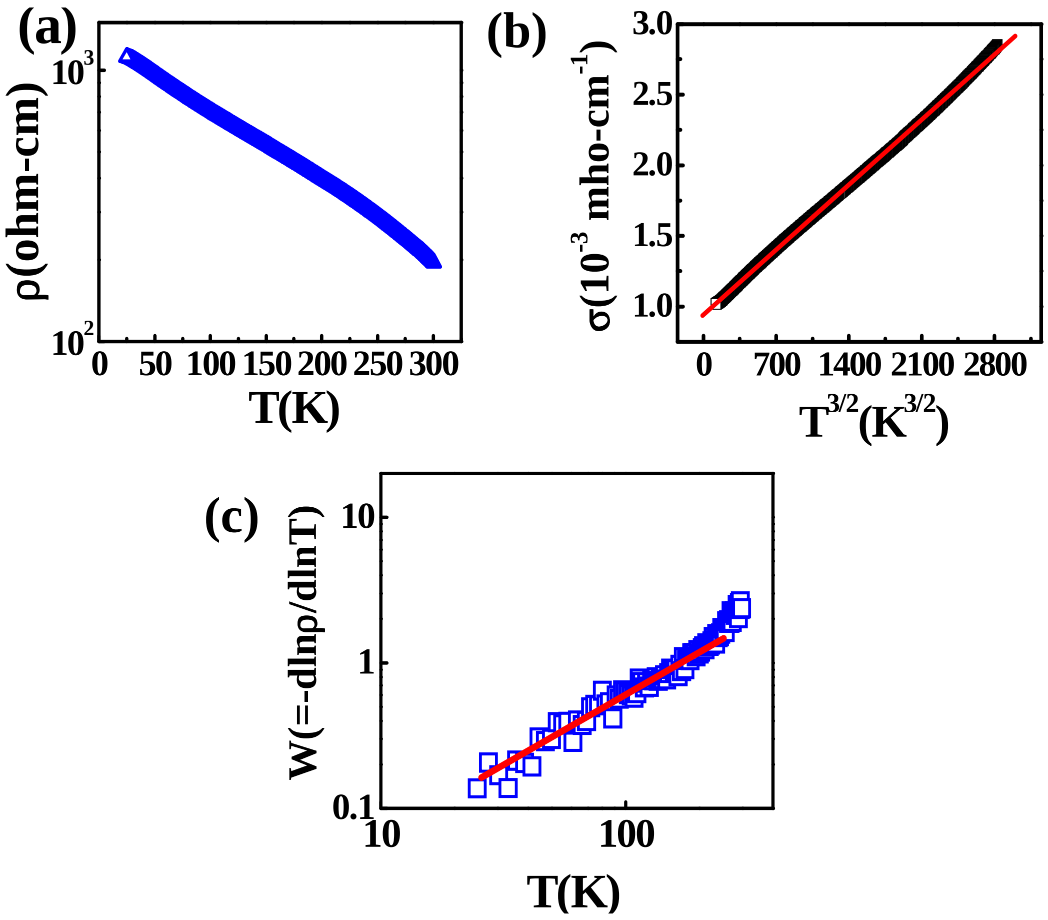

Figure 3.53 (a) The temperature dependence of resistivity (b) Plots of reduced activation energy *W* (c) Linear fit of conductivity versus $T^{3/2}$ (confirms the validity of electron phonon scattering) for binuclear (Co-Fe)Pc films .

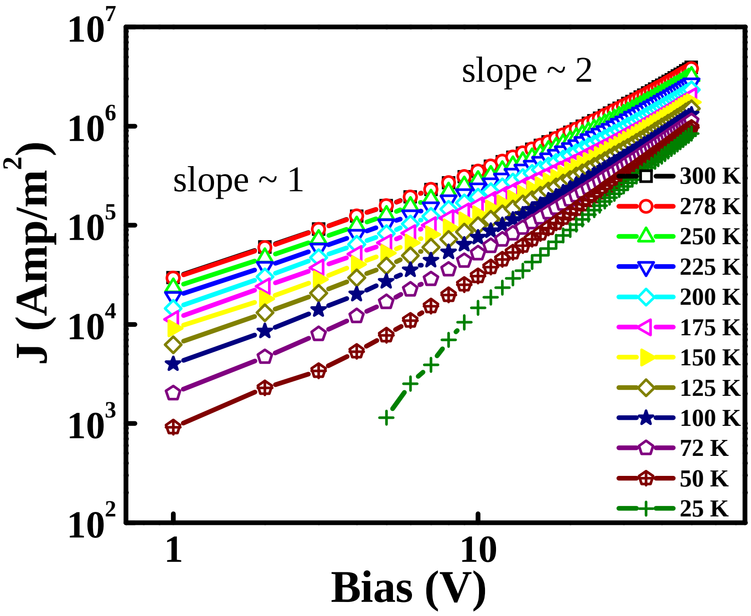

Figure 3.54 Log-log plots showing *J-V* characteristics of 20 nm (Co-Fe)Pc films on in the temperature range 300 - 25 K.

3.5.2 Temperature dependent *J-V* characteristics

J-V characteristics of binuclear (Co-Fe)Pc films measured at different temperatures are shown in Fig. 3.54. It is seen that the characteristics at temperatures between 50 and 300 K are linear at low voltages while those at 25 K are nonlinear indicating a different mechanism at 25 K. In what follows, we analyze data at higher temperatures in terms of ohmic behavior followed by SCLC mechanism and that at 25 K in terms of electrode limited process followed by SCLC. Characteristics at higher temperatures show power law behavior ($J \sim V^{\alpha}$), with a crossover in exponent (α) from 1 to 2 (with increase in the bias voltage). This indicates the charge transport is ohmic in the low bias and at higher bias the transport mechanism changes to shallow trap mediated SCLC mechanism described by eq. (3.9). The crossover voltage decreases with lowering of the temperature due to reduction in the numbers of thermally generated carriers. Using slope of J-V^2 plots and assuming literature value of $\varepsilon_0\varepsilon_r$ (2.43 x10^{-11} F/m), value of μ at room temperature was determined to be 1.1 x 10^2 cm^2/Vs. This is the highest value of the μ till date. Using this value of μ, and eq. (3.1) for characteristics at low voltages, we find thermally generated hole concentration (n_0) of 1.1 x 10^{20} m^{-3} (at 300 K). Here, in the estimation of mobility we assumed $\theta_{(t)} = 1$ i.e. a trap free condition as the characteristics do not indicate presence of trapping centres even at very low temperatures and the conductivity of these films is very high indicating low trap density if any. Values of different parameters such as mobility and carrier concentration of (Co-Fe)Pc films with CoPc and FePc films are summarized in Table -3.1. It is interesting to note that mobility and hole concentration are at least three order of magnitude higher compared to that normally reported for metal phthalocyanine films, indicating the high structural ordering of molecules in all films [37, 160]. Nearly similar value of free hole concentration (n_0) for all films is also supported by the similar value of the WF value (as given in the next section) , indicating that improvement of the conductivity of the (Co-Fe)Pc films is solely due to the better structural order rather than change in the free carrier density.

Table 3.1

Values of hole concentration (n_0), trap characteristics temperature (T_t), trap denisty (N_t) and mobility (μ), determined using J-V characteristics for CoPc films grown on (0001) Al_2O_3 substrate.

Films	**n_0 (cm^{-3})**	**T_t (K)**	**N_t (cm^{-3})**	**μ(cm^2/V-s)**
(Co-Fe)Pc	1.1x 10^{14}	236	1.1 x 10^{16}	110
CoPc	1.1x 10^{14}	190	1.4 x10^{16}	5.3
FePc	1.1x 10^{14}	-	-	1.1

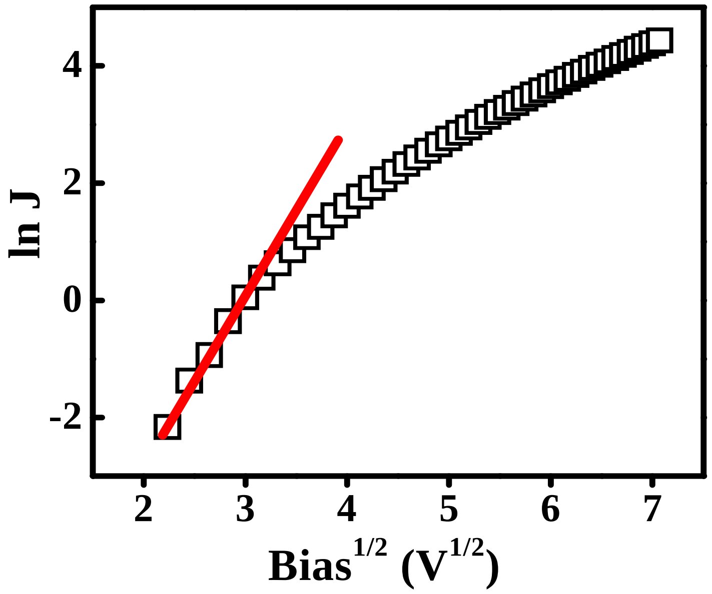

Figure 3.55 *J* versus $V^{1/2}$ data (at 25K at low bias, with estimated barrier height of 0.052 eV) indicate Schottky-barrier limited conduction

It may be noted that, *J-V* data at 25 K shows a different trend at voltages < 10 V, compared to high temperature data. At low voltages < 10 V, the slope is 3.6 and at high voltages the slope is nearly equal to 2. A very sharp increase in current at low voltages indicates electrode limited current. The *J-V* data for temperature of 25 K, plotted as ln *J* versus $V^{1/2}$ in Fig. 3.55, indicates current limited by PF mechanism (eq. (3.30)) or Schottky barrier present at the electrodes-films interface (eq. (3.44)). We observed a linear fit of the data at low voltages as per eq. (3.30) or eq. (3.44) and the field lowering coefficient (β_S) was found to be 2.03 x10^{-5} eVm$^{1/2}$/V$^{1/2}$ confirming the Schottky emission mechanism. The value of energy barrier ϕ_0 was found to be 0.052 eV. This value of ϕ_0 is very close to the estimated value of 0.105 eV (obtained from the work function data of gold and (Co-Fe)Pc films). For (Co-Fe)Pc films, contact effect becomes dominant at low temperature due to the high conductivity. The data at 25 K for voltages > 10 V is not limited by contacts and therefore analyzed using SCLC model.

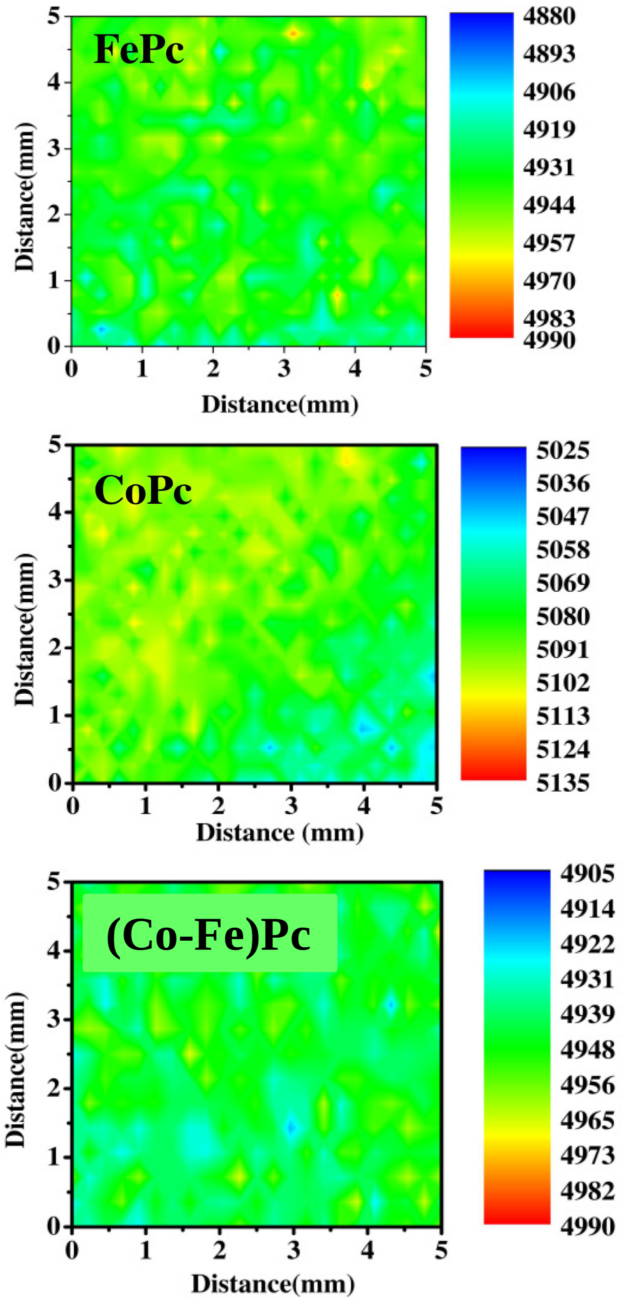

Figure 3.56 Work function images (size 5mm x 5 mm) of CoPc, FePc and binuclear (Co-Fe)Pc films.

3.5.3 Kelvin probe study

Fig. 3.56 shows the work function images (5 mm x5 mm) of the FePc, CoPc and binuclear (Co-Fe)Pc films, which indicate that all the films are very uniform. The estimated average values of work functions for FePc, CoPc and binuclear (Co-Fe)Pc films are 4.91, 5.08 and 4.96 eV respectively with a standard deviation of 18-24 meV. Nearly same work function for all films suggests that they have similar free carrier concentration. These values of work function are close to the work function of gold (5.1 eV) indicating that gold electrode can give ohmic contacts to these films [96].

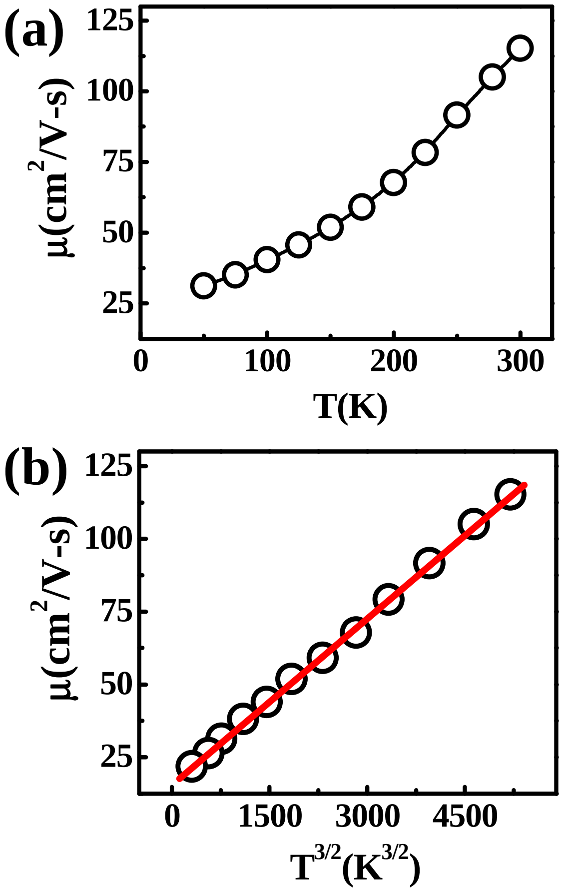

Figure 3.57 (a) Temperature dependence of mobility (μ) and (b) Linear fit of μ Vs $T^{3/2}$ for binuclear (Co-Fe)Pc films.

3.5.4 Temperature dependent mobility

Mobility was similarly determined at various temperatures and is found to increase with temperature from 29 cm^2/Vs at 25 K to 110 cm^2/Vs at 300K as shown in Fig. 3.57 (a). The linear fit μ Vs $T^{3/2}$ plot as shown in Fig. 3.57 (b) indicates the $\mu(T) \propto T^{3/2}$ dependence for binuclear (Co-Fe)Pc films. This dependence is valid for motion of charge carrier in an ionized medium where an interaction between charge carrier and ions takes place [161]. As we have described in Section (3.2.7) that in binuclear films since binuclear (Co-Fe)Pc molecule got enhanced dipole moment**,** therefore the charge carrier movement within the molecules will feel its presence, hence will exhibit $T^{3/2}$ dependence of μ.

3.5.5 Proposed model for high conductivity /mobility of the binuclear (Co-Fe)Pc films

As we have discussed in Section (3.2.7) that due to additional dipole moment of binuclear phthalocyanine molecules the van der Waals interaction between molecules is stronger, therefore in plane as well as out of plane molecular stacking will be much better compare to mononuclear CoPc and FePc films. This better structure quality along with larger π–electron cloud extent of the binuclear (Co-Fe)Pc molecules will results in high mobility and metallic nature of charge carrier as shown in Fig.3.22 (a). In case of mononuclear CoPc or FePc films, in the out of plane direction molecules will be stacked in *face-to-face* manner, and in the in plane molecules are stacked in edge on manner, as shown in Fig.3.22 (b). Such an arrangement of CoPc or FePc molecules results in poor intermolecular connectivity hence low mobility.

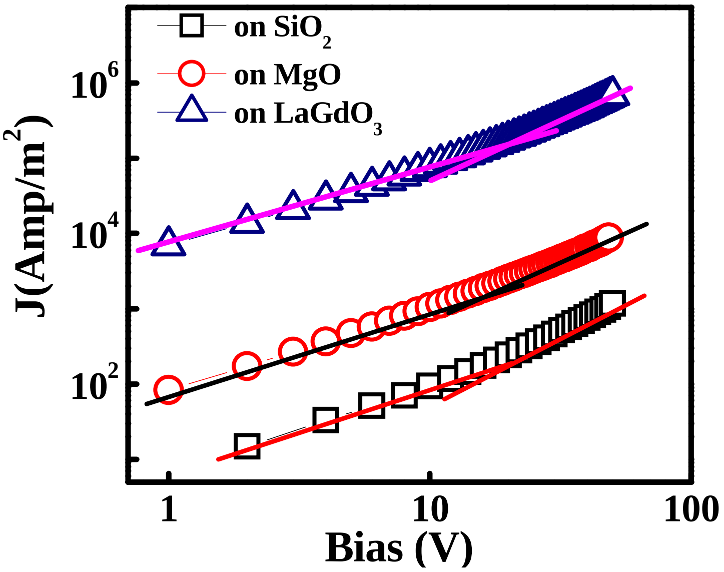

Figure 3.58 *J-V* characteristics of 20 nm CoPc films on SiO_2, MgO and $LaGdO_3$ substrate.

3.5.6 Role of films thickness and substrate on mobility of binuclear (Co-Fe)Pc films

As we found that $\mu > 100$ cm^2/Vs in binuclear films is about two to three orders of magnitude higher than earlier reports [96, 101]. According to the reported literature, various other combinations of metal phthalocyanines such as CuPc-NiPc and CuPc-CoPc combination exhibits the higher mobility compared to individual phthalocyanine, therefore it can be concluded that enhanced mobility is a generic effect for composite phthalocyanine [101]. In our case in addition to effect of binuclear molecule other possible reasons for improved mobility compared to literature could be (i) most of the studies reported in the literature, use silicon substrates for mobility measurements in field effect transistor geometry and as shown below, films on silicon have poorer mobility, [37, 50, 162, 163] (ii) for transport measurements and mobility measurements using SCLC, films are generally prepared in sandwich geometry where bottom contact (gold electrode) affects the substrate characteristics that are important for good quality films [37, 153] and (iii) the films are usually much thicker, and we find that only ultrathin films have planar well organized growth needed for high mobility [31]. To show the importance of substrate, binuclear films under similar conditions were also deposited on three different substrates namely; oxidized silicon, MgO, and $LaGdO_3$, Room temperature *J-V* characteristics of typical film on different substrates are shown in the Fig. 3.61. The analysis of the *J-V* data shows a transition from ohmic to space charge limited conduction and the value of mobility for binuclear films on different substrate is shown in Table-3.2. It may be noted that for binuclear (Co-Fe)Pc films prepared on oxidized silicon (i.e. substrate normally used for field effect transistor studies) mobility was found to be 3.9 $\times 10^{-2}$ cm^2/Vs, which is in good agreement with low mobility (~5 $\times 10^{-2}$ cm^2/Vs) reported for binuclear phthalocyanine films prepared on silicon for FET geometry [50].

Table 3.2

Values of room temperature μ, determined using *J-V* characteristics for binuclear (Co-Fe)Pc films grown on various substrate under identical condition.

Substrate	**μ (cm^2/Vs)**
On SiO_2	3.9×10^{-2}
MgO	2.2×10^{-1}
$LaGdO_3$	18.7

3.6 Conclusions

We have demonstrated that mononuclear FePc, CoPc and binuclear (Co-Fe)Pc films grow with molecules *face-on* stacking on (0001) Al_2O_3 substrate due to the interaction between molecule and of Al terminated surface. AFM and GIXRD studies revealed that (Co-Fe)Pc phthalocyanine films have better structural ordering and smooth morphology as compared to the FePc and CoPc films. This is attributed to the additional dipole moment of binuclear (Co-Fe)Pc molecules, which results better *face-on* stacking as compare to the CoPc and FePc molecules.

In CoPc and FePc films the value of μ was found to be 5.3 and 1.1cm^2/Vs, respectively. For binuclear (Co-Fe)Pc films exhibited μ ~110 cm^2/Vs which is two orders of magnitude higher than CoPc and FePc films. This is the highest value of the mobility till date. This high value mobility of binuclear (Co-Fe)Pc films is attributed to the better molecular ordering.

The temperature dependence of resistivity of binuclear (Co-Fe)Pc films exhibited metallic behavior in the temperature range 300K-25K which is the manifestation of the improved ordering also. The *J-V* characteristics of binuclear (Co-Fe)Pc films exhibited trap-free SCLC in the temperature range 300K to 25K. For CoPc and FePc films the temperature dependence resistivity showed that, these films are in the critical regime of metal–insulator transition. The *J-V* characteristics of mononuclear films exhibited SCLC with exponential distribution of traps at low temperature.

The temperature dependent *J-V* characteristics of FePc films have also been investigated at very high bias *i.e.* in the bias range of ± 200 V. In the temperature range of 300K–30K, the charge transport is governed by bulk-limited processes with a bias dependent crossover from ohmic ($J{\sim}V$) to exponentially distributed shallow trap mediated space-charge-limited conduction ($J{\sim}V^{\alpha}$, $\alpha \geq 2$) to space charge limited conduction with field enhanced mobility ($\ln \mu \sim E^{1/2}$). However, at temperatures < 100 K, the charge transport is governed by electrode-limited process, which undergo a bias dependent transition from Schottky ($ln\ J \sim V^{1/2}$) to multistep-tunnelling (MUST).

In the case of CoPc films grown on (100) $SrTiO_3$ substrate, it has been demonstrated that the molecule stack in *edge-on* configuration. The temperature dependence of resistivity exhibited semiconductor to like transition at ~110K. XRD measurement revealed that this transition is due to in-plane compressive strains induced by structural phase transition (from cubic to tetragonal ~ 110K) of $SrTiO_3$ substrate reduce the intermolecular distance.

The structure and morphology of water soluble CuPcTs films prepared by drop casting method were found to be independent of substrate, and have usually amorphous character and therefore these films do not transport any current below 280K.

CHAPTER-4

PHTHALOCYANINE BASED HETEROJUNCTION

4.1 Introduction

Organic/Organic (O/O) interfaces, sometimes also referred to as organic heterojunctions, have been attracting much attention in recent years. These O/O heterojunctions play important role in these organic based devices such as light emitting diodes, field effect transistor and photovoltaic devices [164-168]. The properties of O/O interfaces can be quite different from the individual organic part. Recent results show that the interfaces of crystalline molecular solids possess amazing electronic properties. For instance, metallic conduction was observed at O/O heterojunctions [169]. This is in contrast to the pure organic films, which exhibit semiconducting-like behaviour [37, 96]. Because entirely diverse nature of organic semiconductor than inorganic ones, the energy level alignment and electrical conduction properties must have different mechanism in these O/O heterojunctions. Thus studies of interfacial properties of highly crystalline O/O interfaces have become important for the understanding of the interaction mechanisms and devices based on organic heterojunctions. For example, in organic light emitting diodes, the application of a double-layer configuration may improve the efficiency of the device significantly. In such type of devices, a combination of two organic layers is chosen to get an efficient and balanced injection of (opposite) charges at either electrode. In addition, the recombination zone (opposite charges merge to form excitons), is moved from the metal–organic interface to the organic–organic interface, and this reduces the quenching of the luminescence at the metal electrode. The details of the electronic structure at the organic–organic interface determine whether an efficient confinement of charges and exciton formation take place in there combination zone.

The semiconductor heterojunction can be classified by the conductivity type (*p*-type or *n*-type) of two semiconductors forming the heterojunction. When both the semiconductors have the same type of conductivity, the heterojunction is called an isotype heterojunction; otherwise, it is called an anisotype heterojunction. Moreover, on the basis of difference in work functions (ϕ) difference, both isotype and anisotype heterojunctions can be further classified in to two categories. Hence, the heterojunctions can be divide in to four cases, which is shown in Fig. 4.1[170]. In the anisotype heterojunction, electron and holes can be simultaneously accumulated and depleted at both sides of the heterojunction due to difference of their Fermi level (work functions), as shown in Fig. 4.2 (a) and (b). In isotype heterojunction, an accumulation layer at one side of heterojunction interface and a depletion layer at the other side of heterojunction interface can be formed [170, 171]. All four cases are described below:

(a) Depletion heterojunction

If the Fermi level of *n*-type semiconductor is higher than *p*-type semiconductor ($\phi_\mathrm{n} < \phi_p$) the electrons and holes depletion layer is formed on the corresponding semiconductor layer near the heterojunction interface, and the space charge region is composed of immobile negative and positive ions as depicted in Fig. 4.1 (a). This heterojunction is called a depletion heterojunction.

(b) Accumulation heterojunction

If the Fermi level of *n*-type semiconductor is lower than *p*-type semiconductor ($\phi_\mathrm{n} > \phi_p$) the heterojunction with free charge carriers is thus formed on both sides of the space charge region. This heterojunction is called a accumulation heterojunction ions as depicted in Fig. 4.1(b).

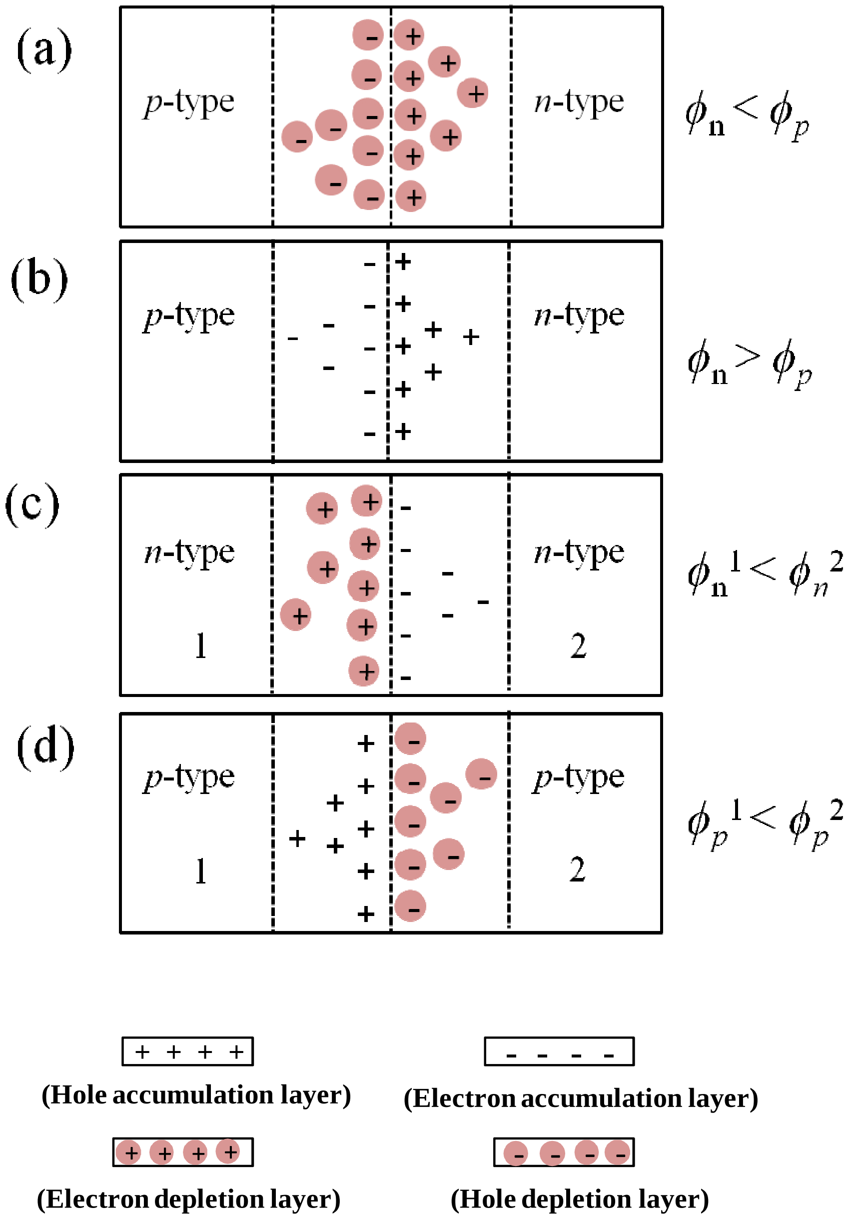

Figure 4.1 Different types of organic semiconductor heterojunction (a) depletion heterojunction (b) accumulation heterojunction (c) electron accumulation/depletion heterojunction (d) hole accumulated/depletion heterojunction.

(c) Electron accumulation/depletion heterojunction

The heterojunction is formed by two *n*-type semiconductors having different work functions (Fermi levels) assuming $\phi_n^1 < \phi_n^2$. The semiconductor layer of higher Fermi level ϕ_n^1 near the heterojunction interface is electron depletion region, and other semiconductor with work function ϕ_n^2 is electron accumulated region. The heterojunction is called electron accumulated /depletion heterojunction, as depicted in Fig 4.1(c).

(c) Hole accumulation/depletion heterojunction

The heterojunction is formed by two *p*-type semiconductors with different Fermi levels assuming $\phi_p^1 < \phi_p^2$. In this case holes are accumulated at the side of semiconductor with high Fermi levels (low work function ϕ_p^1) and are depleted at the side of the semiconductor with low Fermi level (high work function ϕ_p^2). This type heterojunction is called holes accumulated /depletion heterojunction as depicted in Fig 4.1(c).

4.2 Organic/Organic interface: band bending and interfacial dipole

As we have discussed in Chapter 3, at metal/OMs interfaces an interface dipole Δ of about 0.5–1 eV is usually observed and vacuum level alignment at interface is not valid [121]**.** It was found that, with few exceptions most of the O/O interfaces are also characterized by the vacuum level discontinuity, where Δ is less than 0.2 eV [172]. The low value of Δ is because of the relatively weak van der Waals interactions between organic materials. Moreover in case of O/O heterojunction the valve of Δ was found to be highly sensitive to molecular orientation of the molecule [173-175]. Band bending and space charge region at both sides of O/O interfaces have also been observed [170].

Lau *et al* observed the band bending and interface dipole (Δ = 0.19 eV) an F_{16}CuPc/CoPc interfaces by ultraviolet photoelectron spectroscopy. Further due to the charge transfer free holes and free electrons are accumulated in the space charge layer with a width 15 nm. and free carrier density 10^{18} cm^{-3} [172]. This accumulation results were further confirmed by conductivity measurement. The current in bi-layer CuPc/F_{16}CuPc was one order magnitude higher than the single layer of CuPc and F_{16}CuPc [170, 176]. Similar, type of accumulated and high conductivity region were observed at BP2T/F_{16}CuPc heterojunction interfaces with electron accumulation thickness in F_{16}CuPc about 10 nm and holes accumulation thickness in BP2T also 10 nm [170]. In ZnPc/C_{60} heterojunction electrons and holes depletion layers were observed. The high conductivity characteristics were not found in the ZnPc/C_{60} heterojunction and this heterojunction is similar to the inorganic *p*-*n* junction as depicted in Fig 4.1 (b) [170].

4.3 CoPc (*p*-type)/F_{16}CuPc (*n*-type) heterojunction

Heterojunction films comprising of *n*-type F_{16}CuPc and *p*-type CoPc (each layer having a thickness of 20nm) were deposited on $LaAlO_3$ substrates using molecular-beam epitaxy (MBE). The growth temperature and deposition rate were, respectively, 200°C and 3Å /s. The results are discussed below.

4.3.1 Structure and morphological studies

Typical AFM images of F_{16}CuPc (20 nm) and F_{16}CuPc(20 nm)/CoPc(20 nm) deposited on $LaAlO_3$ substrates are shown in Fig 4.2 (a) and (b) respectively. F_{16}CuPc film consists of highly dense grains with rms roughness of ~1.3 nm. However, CoPc layer grown on top of F_{16}CuPc exhibits much smoother morphology (rms roughness ~ 0.8 nm).

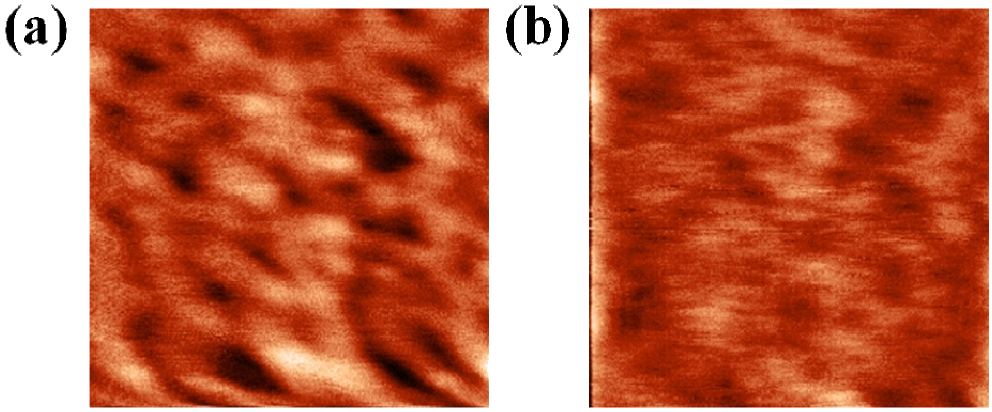

Figure 4.2 100nm×100 nm AFM images (a) 20 nm F_{16}CuPc film on $LaAlO_3$ substrate and (b) top surface of F_{16}CuPc (20nm)/CoPc (20nm) heterojunction films.

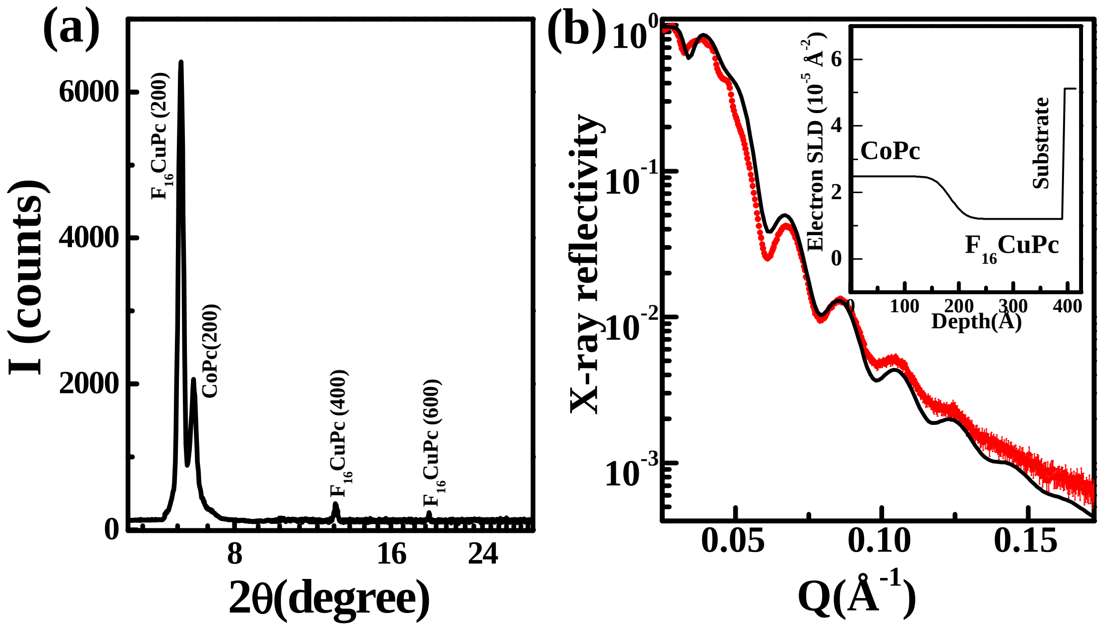

Figure 4.3 (a) GIXRD data for F_{16}CuPc(20nm)/CoPc(20nm) heterojunction films (b) X-ray reflectivity spectrum for F_{16}CuPc(20nm)/CoPc(20nm) heterojunction films. Solid line is theoretical fit of data. Inset show the depth profile of electron scattering length density (SLD).

The GIXRD pattern recorded for F_{16}CuPc(20 nm)/CoPc(20 nm) heterojunction films, as shown in Fig. 4.3 (a), reveals intense sharp diffraction peaks at $2\theta = 6.3^o$ and 6.7^o, which corresponds to F_{16}CuPc and CoPc layers, respectively. The a lattice parameter estimated from GIXRD data are 14.21 Å and 13.10 Å for F_{16}CuPc and CoPc respectively and it matches very well with the reported values [67, 177]. Intense (200) and higher order diffraction peaks indicate that both CoPc and F_{16}CuPc layers are highly ordered with molecules stacked in the *edge-on* standing configuration on the substrate surface. The *edge-on* standing configuration implies that the π-π stacking direction of the molecules is parallel to the substrate plane, which is ideal for the in-plane transport measurements [178].

GIXRR spectrum, i.e., specular reflectivity as a function of wave vector transfer Q [$Q = \left(4\pi/\lambda\right)\sin\theta$, where θ is the incident angle and λ is the wavelength of the probe] for the heterojunction films is shown in Fig. 4.3 (b). The reflectivity data has been fitted using a depth dependent scattering length density (SLD) profile, that is, $\rho(z) = \rho_{chem}(z) = \sum_i N_i(z) b_i$; where N is the in-plane average of the number density, z is the film depth averaged over in plane features, and b is the electron scattering length. The estimated values of films thickness, surface roughness, and density obtained from best-fit theoretical simulation of the data (shown by solid line in Fig. 4.3 (b)) are given in Table 4.1. The estimated thickness of each layer is close to the nominal thickness of 20 nm (obtained from quartz thickness monitor during deposition).

Table 4.1

Various parameters of heterojunction films and substrate as obtained from the fitting of X-ray reflectivity data.

Layer	Thickness (Å)	Density(gm/cc)	Roughness (Å)
CoPc	190±10	2.6±0.2	1±0.5
$F_{16}CuPc$	180±10	1.5±0.15	20±2
Substrate ($LaAlO_3$)	-	6.5±0.3	1±0.5

4.3.2 Conduction characteristics

The temperature dependence of resistivity (ρ) for heterojunction films (20 nm thick $F_{16}CuPc$/20 nm thick CoPc) as well as for individual films (each films 20 nm thick) is shown in Fig. 4.4 (a). It be seen that heterojunction films shows the lowest room temperature ρ (~30 ohm-cm) i.e. nearly three order of magnitude lower compared to individual films. The ρ of our heterojunction films is one order of magnitude lower than single crystal like phthalocyanine heterojunction prepared using weak-epitaxy-growth method [179]. It indicates the high structural quality of our samples. It may be noted that although individual CoPc and $F_{16}CuPc$ shows nearly similar value of room temperature ρ ~ (5 x10^4 ohm-cm) but the rapid increase of ρ with the lowering of T for $F_{16}CuPc$ is possibly due to the chemisorbed oxygen induced charge trapping [96]. An increase in ρ with decreasing temperature for all films suggests their critical or insulating behavior. These behaviors can be identified through W plot. The variation of W with T for $F_{16}CuPc$, CoPc and heterojunction films is plotted in Fig. 4.4 (b). It is seen that for all films the value of W is nearly independent of the temperature i.e. slope is zero. It indicates that all films are in the critical regime. In the critical regime of metal to insulator transition, resistivity is expected to show power law dependence ($\rho \propto T^{-\beta}$) on temperature with β = W [152, 153]. A nearly linear dependence of log ρ on log T for all films shown in Fig. 4.4 (b), suggesting that these films are in critical regime. The lowest value of β (~1/3) for heterojunction films suggests they are more metallic in nature [152, 153].

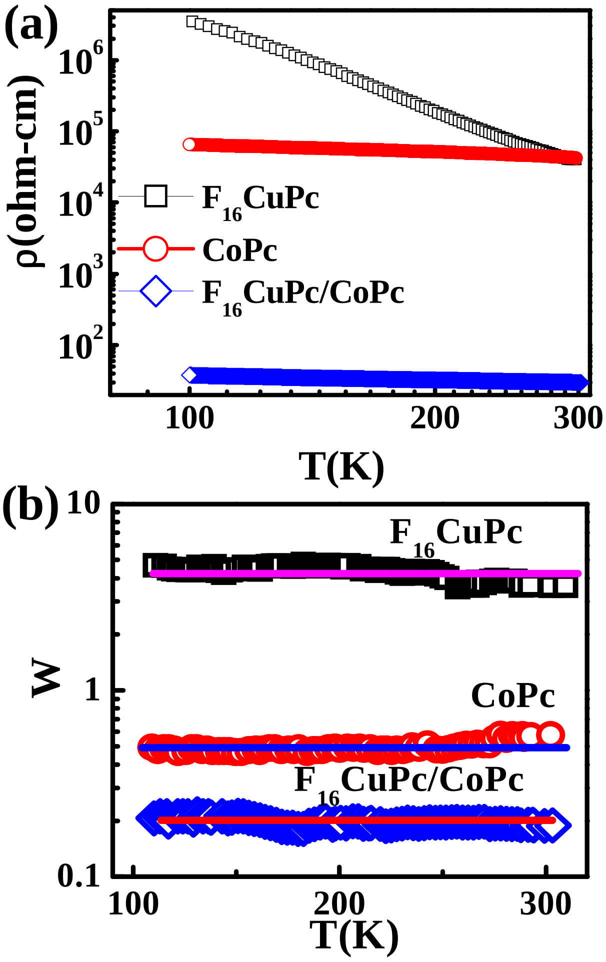

Figure 4.4 (a) Temperature dependence of resistivity (plotted in log-log scale) for CoPc, F_{16}CuPc and F_{16}CuPc/CoPc heterojunction films. (b) Plot of reduced activation energy W as a functions of temperature.

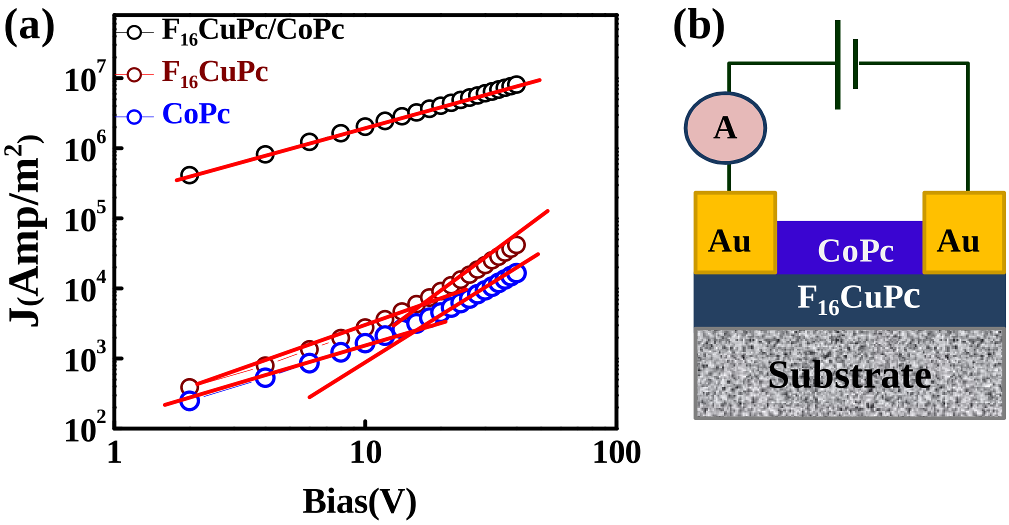

Figure 4.5 (a) Room temperature *J-V* characteristics of F_{16}CuPc(20nm)/CoPc (20nm) heterojunction films along with CoPc and FePc films (b) Schematic representation of circuit diagram for *J-V* measurement.

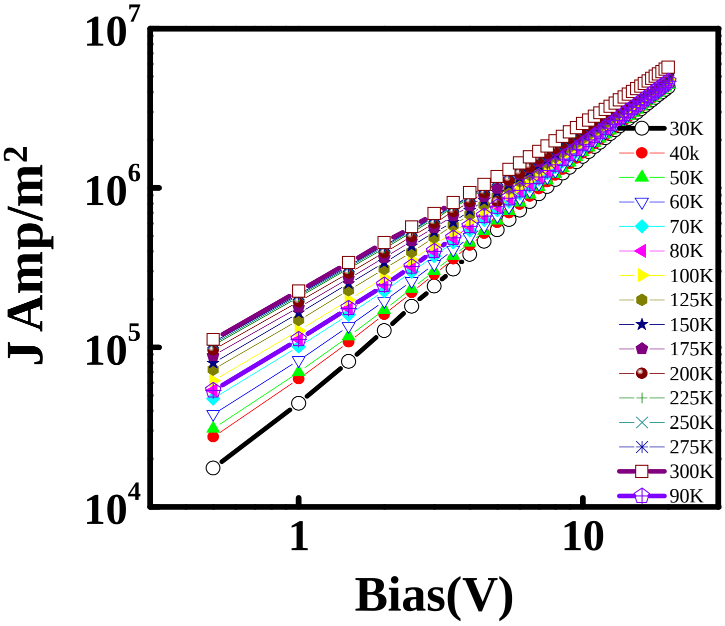

Figure 4.6 Temperature dependent *J-V* characteristics of F_{16}CuPc(20nm)/CoPc(20nm) heterojunction films.

Room temperature *J-V* characteristics of CoPc/F_{16}CuPc heterojunction films, CoPc and FePc films of 20 nm are shown in Fig 4.5 (a). The schematics of circuit diagram for *J-V* measurement of heterojunction films is shown in Fig. 4.5 (b). At a particular bias (for example 10 volts) the *J* value for heterojunction films are three order of magnitude higher as compared to individual CoPc and F_{16}CuPc films, indicates a charge carrier accumulation at heterojunction interfaces. Further, to understand charge transport properties of the heterojunction films, the *J-V* characteristics were also measured as a function of temperature and results are shown in Fig. 4.6. Heterojunction films show linear *J-V* characteristics i.e. an ohmic conduction in the entire bias (0- 20V) and temperature range of 30K-300K. As we have discussed that Ohmic conduction in molecular semiconductors occurs if the thermally generated carriers exceed that of the injected carriers from the electrode given by eq. (3.1). In order to estimate the charge carrier concentration n_0 for heterojunction films, it is reasonable to assume an average mobility value of ~ 5 cm^2/Vs (as we have calculated for F_{16}CuPc films in Chapter 3). From the linear slope of *J-V* data for heterojunction, we estimate the n_0 as 6.4×10^{17} cm^{-3}, i.e. nearly three orders of magnitude higher compared to individual films. It indicates that for heterojunction there is an accumulation of charge carriers at the interface. Due to this accumulation of charges Ohmic to SCLC transition were not observed in case of heterojunction films.

4.3.3 Kelvin probe study

Heterojunction films were further characterized using scanning Kelvin probe microscopy (SKPM) technique, which measures the surface potential. For the surface potential measurements, films should be prepared on the conducting substrate. In the present study we have chosen conducting indium tin oxide (ITO) coated glass as a substrate for deposition of heterojunction films. In ITO coated glass substrate metal-phthalocyanine molecules preferably stacks in the *edge-on* configuration (similar to the $LaAlO_3$ substrate), therefore surface potential will have similar value as for the films prepared on $LaAlO_3$ substrate [180]. It may be noted that surface potential is highly sensitive to the molecular orientation as it has been reported for phthalocyanine molecules surface potential shifts by 1 eV when the molecular orientation changes from face on to edge on configuration [173]. For understanding the properties of heterojunction interface, we first deposited the 20 nm thick $F_{16}CuPc$ layer on ITO substrate, on the top of this CoPc films (of various thicknesses starting from 0 nm to 20 nm) were deposited by masking half of the $F_{16}CuPc$ surface. The schematic of the grown structure is shown in Fig. 4.7 (a). It may be noted that when the coverage of CoPc layer is ≥ 1nm, features from $F_{16}CuPc$ are fully suppressed. For each thickness of CoPc (on top of $F_{16}CuPc$ layer) we have measured the surface potential of heterojunction films. One of the results of surface potential topography in 2D and 3D for 3 nm thick CoPc film on top of $F_{16}CuPc$ layer is shown in Fig. 4.7 (b) and (c) respectively. The CoPc thickness dependence of surface potential for heterojunction films is summarized in Fig. 4.8, from this it can be seen that with an increasing thickness of CoPc the surface potential falls (from the surface potential value ~ 5700 meV of $F_{16}CuPc$) and after ~8 nm of CoPc thickness achieve a constant value of 5160 meV i.e. surface potential for CoPc. Similarly to understand the interface property on $F_{16}CuPc$ side of heterojunction, we first deposited the 20 nm thick CoPc layer on $LaAlO_3$ substrate, on the top of this we deposited $F_{16}CuPc$ films of various thicknesses starting from 0 nm to 20 nm. The results of surface potential measurement can be seen in the inset of Fig. 4.8 , which show that increasing thickness of $F_{16}CuPc$ the surface potential increases (from the surface potential value of CoPc) and after ~ 10 nm thickness achieve the constant value of surface potential for F_{16}CuPc. Both of these results indicates that molecular levels of both materials exhibits a progressive shift upon deposition and becomes nearly constant after 10 nm thickness. This reflects the band bending of energy levels of both semiconductors at the interface. The initial rapid decrease / increase of surface potential at length scale of ~ 2 nm on each side of the interface indicates the presence of an interface dipole layer . The band bending width (i.e. the thickness where the CoPc or F_{16}CuPc surface potential attains the bulk value) for both CoPc and F_{16}CuPc layers are around 10 nm. The band bending magnitude is obtained from the difference of surface potential value of first starting signal of CoPc and the CoPc bulk surface potential. Based on the Kelvin probe surface potential data, the energy band diagram for the F_{16}CuPc /CoPc heterojunction is shown in Fig. 4.9. The magnitude of interface dipole (Δ) is obtained by taking surface potential difference of CoPc and F_{16}CuPc bulk and band bending into account. The estimated interface dipole value ~ 0.16 eV matches very well with the literature reported value obtained using photoemission technique [170, 172]. The enhanced conductivity of the heterojunction can be explained using Fig. 4.9. The energy level diagram of CoPc and F_{16}CuPc is shown in Fig. 4.9 (a). When CoPc and F_{16}CuPc comes in contact, since surface potential of CoPc (~5.16 eV) is lower than that of F_{16}CuPc (~5.73 eV), therefore CoPc serves as donor while F_{16}CuPc becomes an acceptor. As a result CoPc layer near the interface becomes hole rich and F_{16}CuPc layer becomes electron rich i.e. there is an accumulation of charge carrier at the interface as shown in Fig. 4.10. The total charge density in the accumulation region can be estimated from following equation [161]:

$$N = \frac{2\varepsilon V_D}{eW^2} \tag{4.1}$$

where e is elementary charge, ε is permittivity of organic semiconductor, k is the Boltzmann constant, W is the width of accumulation region and V_D is the built in potential. By taking W ~ 20 nm, ε ~ 2.43 x10^{-11} F/m, V_D as 0.568 eV (i.e. the difference in surface potential values of CoPc and F_{16}CuPc), the estimated value of N was found to be ~ 2.1 x 10^{17} cm^{-3}. Nearly same value of N and n_0 (as obtained from charge transport measurement) indicates that all the charge carrier injected due to formation of interface are free due to high crystalline nature of heterojunctions films.

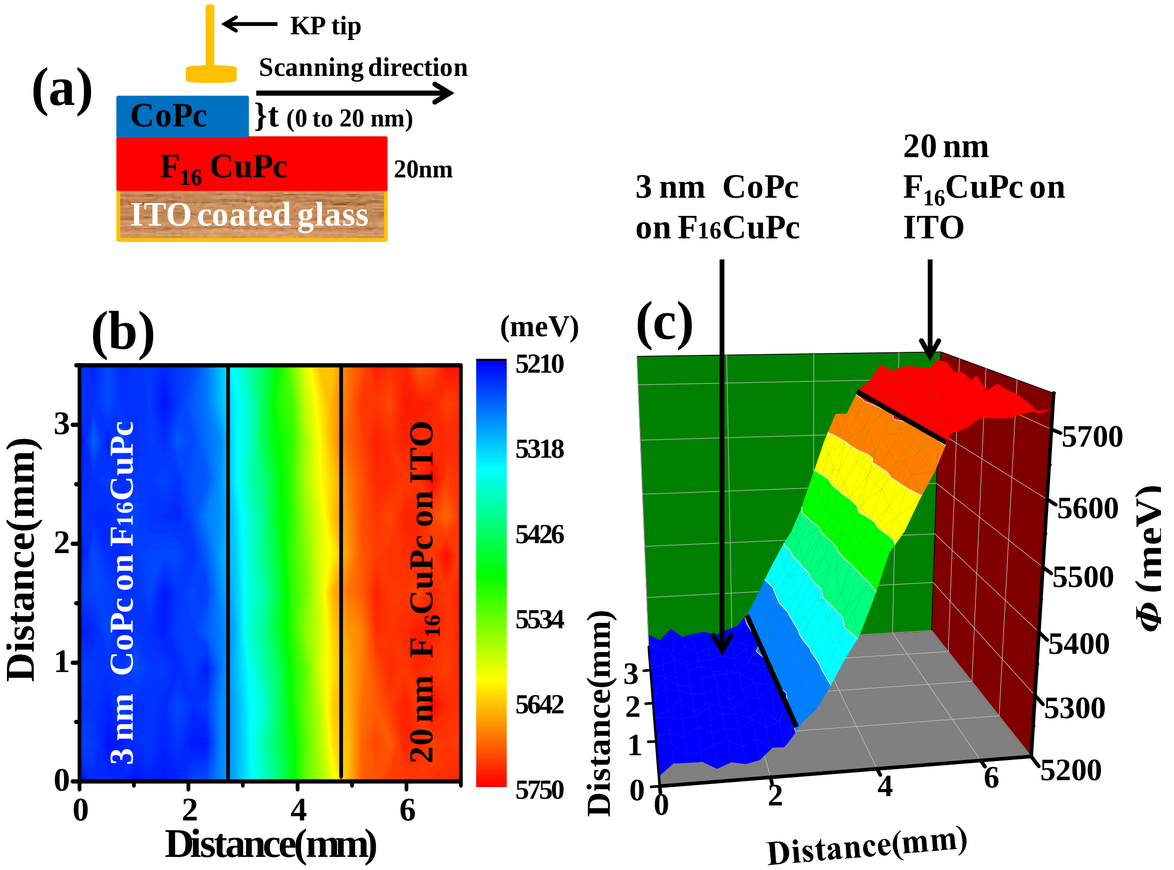

Figure 4.7 (a) Schematic of F_{16}CuPc/CoPc heterojunction films used for surface potential measurements.(b) 2D and (c) 3D image of typical surface potential of F_{16}CuPc(20 nm)/ CoPc(3 nm) heterojunction films.

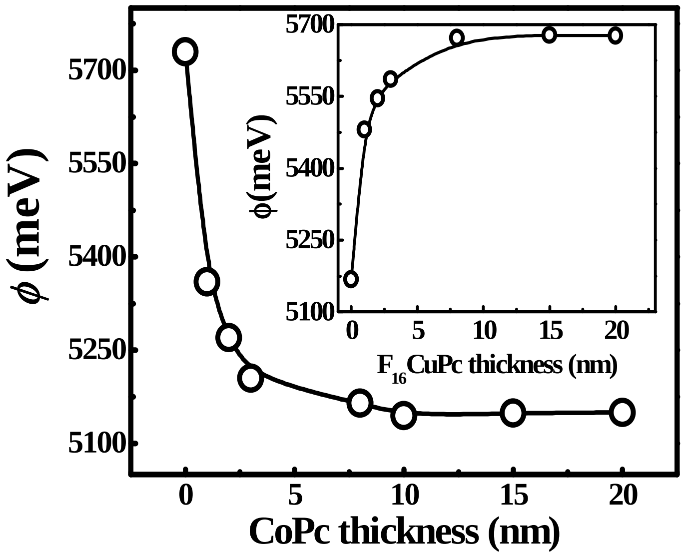

Figure 4.8 Plot of surface potential (ϕ) as a function of CoPc thickness for F_{16}CuPc/CoPc heterojunction films. Inset shows the plot of ϕ as a function of F_{16}CuPc thickness for F_{16}CuPc/CoPc heterojunction films.

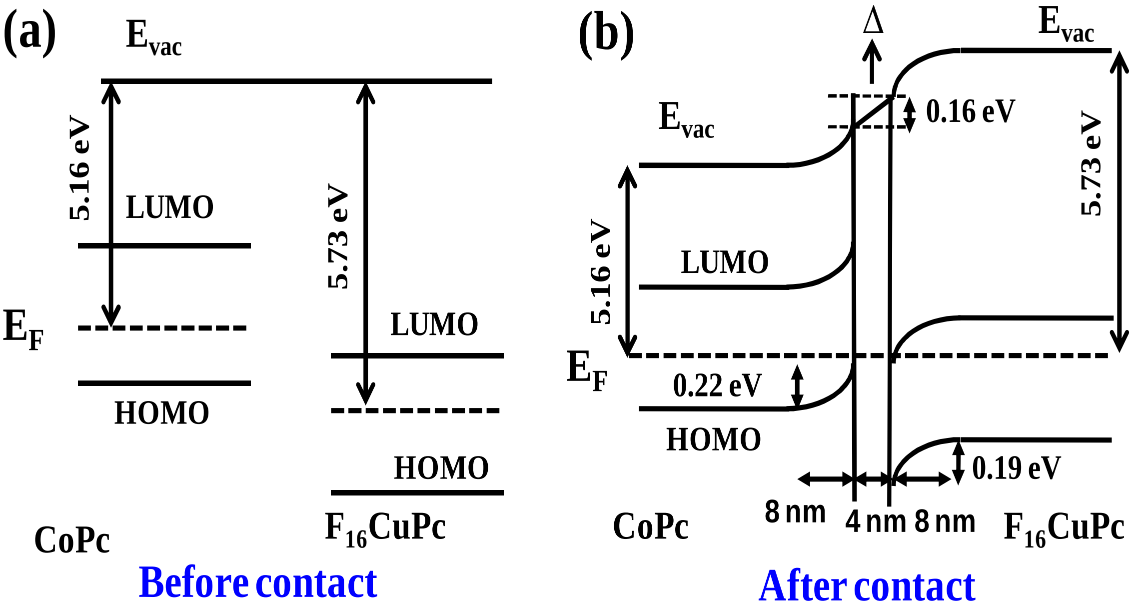

Figure 4.9 Schematic of energy level diagram of CoPc and F_{16}CuPc before (a) and after (b) contact.

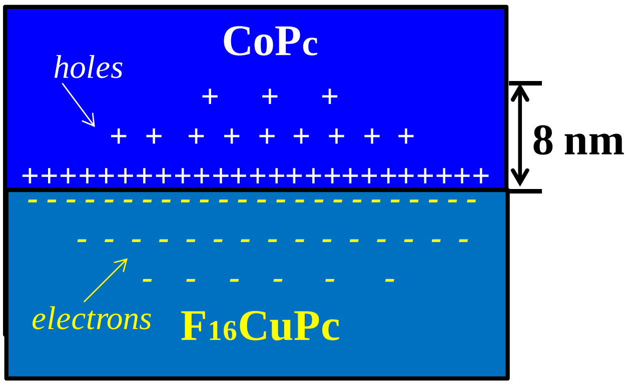

Figure 4.10 The charge carrier accumulation at the F_{16}CuPc/CoPc heterojunction interface.

4.3.4 Reverse rectification behaviour of F_{16}CuPc/CoPc heterojunction

The *I-V* characteristic of F_{16}CuPc (150nm)/CoPc(150nm) heterojunction in out of plane geometry is shown in Fig 4.11. The schematics of circuit diagram for out of plane geometry is shown inset of Fig. 4.11. In can be seen unlike the inorganic *p-n* junction diode, a reverse rectification (i.e. current flow in reverse bias) is observed for F_{16}CuPc (150nm)/CoPc(150nm) heterojunction with rectification ratio 22. Since the interface of Au/CoPc and F_{16}CuPc/Au has a good ohmic contact, the *I-V* curve indicates the characteristics of F_{16}CuPc/CoPc heterojunction.

This reverse rectification can also be explained by energy level diagram shown in Fig. 4.9 (b). As we have discussed above holes are accumulated in the *p*-type CoPc and electrons are accumulated in the *n*-type F_{16}CuPc, which led to upward band and downward band bending in HOMO and LUMO of CoPc and F_{16}CuPc respectively. F_{16}CuPc/CoPc heterojunction thus produces a built in electrical field, self bias, from *p*-type to *n*-type at the interface. This accumulation of charge carrier is quite different from inorganic *p-n* junctions where the space charge region is composed of immobile, negative and positive ions in *p*-type and *n*-type semiconductors, respectively. As a result, the built in electrical field is from *n*-

type to *p*-type in case of inorganic *p*-*n* heterojunction. Under forward bias condition, the potential barrier at F_{16}CuPc/CoPc heterojunction is enhanced, because the direction of the applied field is same as that of built-in field. So current through the junction is limited. When reverse bias is applied to the F_{16}CuPc/CoPc heterojunction, the potential barrier at the junction is weakened, since the direction of the applied field is same as that of built-in field. So current can flow through the junction. Therefore F_{16}CuPc/CoPc heterojunction has small current in forward bias and large current in reverse bias.

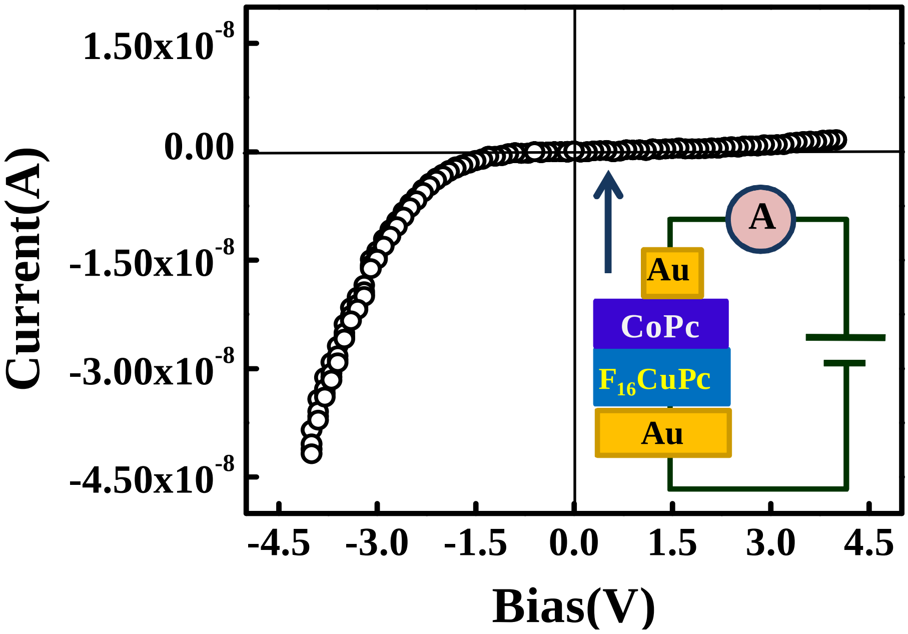

Figure 4.11 *I-V* characteristics of F_{16}CuPc (150 nm)/CoPc (150 nm) heterojunction. Inset show the schematics of the circuit diagram for *I-V* measurement (out of plane geometry).

4.4 CoPc (*p*-type)/FePc (*p*-type) heterojunction

As we have discussed in Chapter 2 binuclear (Co-Fe)Pc is formed, if we deposit the CoPc and FePc mixture with weight ratio 1:1. These binuclear films exhibited very high value of mobility. In order to investigate, it have the same properties as (Co-Fe)Pc binuclear films, we have deposited CoPc/FePc on $LaAlO_3$ substrate using molecular beam ebitaxy. The growth temperature and deposition rate were, respectively, 200°C and 2Å /s.

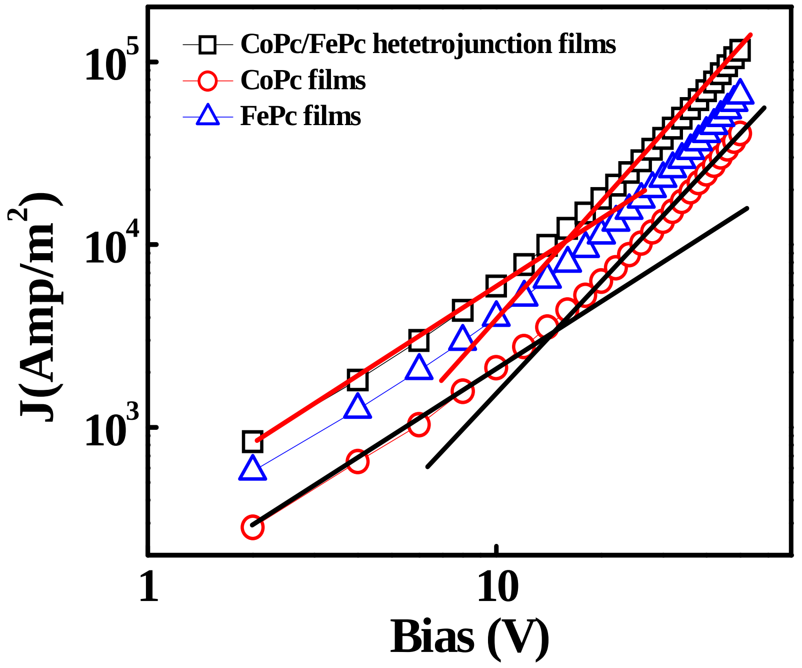

Figure 4.12 Room temperature *J-V* characteristics of CoPc, FePc and CoPc(20nm)/FePc(20nm) heterojunction films.

The *J-V* characteristics on CoPc(20nm)/FePc(20nm), CoPc (20nm) and FePc (20nm) films are shown in Fig. 4.12. The *J-V* characteristics of CoPc(20nm)/FePc(20nm) heterojunction films are identical to the individual CoPc and FePc layer, indicates no charge carrier accumulations at the interfaces. Therefore the temperatures dependent *J-V* characterises of CoPc(20nm)/FePc(20nm) were not measured for further analysis. The measured value of work function of 20 nm FePc films is ~ 5.1 eV, which is identical to the work function of CoPc films of 20 nm prepared under identical condition, therefore no charge transfer occurs at the CoPc/FePc heterojunction interface.

4.5 Conclusions

The *p-n* heterojunction comprising of *p*-type CoPc (20nm) and *n*-type F_{16}CuPc (20nm) heterojunctions showed ohmic conductance with three orders of magnitude higher conductivity as compare to individual CoPc or F_{16}CuPc layer. The higher conductivity F_{16}CuPc/CoPc heterojunction is due to the charge carrier accumulation at the interface, which is confirmed by Kelvin probe study. The thickness of charge carrier accumulation layer at the interface was estimated to be ~20 nm. Interestingly these heterojunction films exhibited reverse rectification behavior i.e. conducts current only in reverse bias. On the other hand, CoPc/FePc (*p-p* type) heterojunction films do not exhibited any charge transfer at the interface. Therefore their electrical properties are identical to the individual layers.

CHAPTER-5

GAS SENSING USING MONONUCLEAR AND BINUCLEAR PHTHALOCYANINE FILMS

5.1 Introduction

Concerns for clean environment require strict regulations on toxic gas emission from industries and automobiles. In order to enforce these regulations, there is a need for more sensitive gas-sensing devices that are able to detect toxic gases in the parts-per-billion range [181]. For instance, Cl_2 gas is widely used in various useful processes, such as, water purification, bleaching of pulp in paper mills, treatment of sewage effluents and as insecticides. Cl_2 is notoriously toxic gas, which can be lethal at low doses. The toxic limit of Cl_2 for eight hours time weighted average is 0.5 ppm [2]. This requires development of sensors that can detect Cl_2 in ppb level. In recent years, many results were reported on Cl_2 sensing, and Table 5.1 summarizes several materials used for chemiresistive (i.e. a change in conductance on gas exposure) Cl_2 detection. From Table 5.1, it can be seen that there are only few materials such as bisporphyrin, cobalt phthalocyanine (CoPc), and $Zn_2In_2O_5$-$MgIn_2O_4$, which can sense the ppb level of Cl_2 gas. The working temperature of these devices is very high i.e. in the range of 180-300°C. It can also be seen from the table 5.1, the materials such as polypyrrole-ZnO nanocomposite, SnO_2 with Sb doping and fluorinated ethylene propylene (FEP)/polyanniline, which can detects the Cl_2 gas at room temperature but at ppm level. Therefore there is a need of material which can detect the ppb level of Cl_2 gas at room temperature. Apart from this, for a practical commercial gas sensing application one requires: (i) large area and cost effective methods of films making (ii) low temperature of operation hence low cost of instrumentation and as at low temperature of operation no structural reorganization of the films takes place, therefore the sensing characteristics will be reproducible for prolonged operations.

In this chapter we discuss the room temperature Cl_2 gas sensing of drop caste CuPcTs films. In addition, as we have discussed in chapter 3 that binuclear phthalocyanine films have very high mobility compare to mononuclear phthalocyanine. Cl_2 gas sensing of high mobility binuclear (Co-Fe)Pc with a comparison to mononuclear phthalocyanine, will also be discussed.

Table 5.1

Different materials used for chemiresistive detection of chlorine.

Materials used	**Working temperature (°C)**	**Detection limit (in ppm)**	**Ref.**
Polypyrrole-ZnO	25	1	[182]
SnO_2 with Sb doping	25	3	[183]
FEP/polyanniline	25	100	[184]
Cu-phthalocyanine	170	0.18	[185]
Co-phthalocyanine	180	0.005	[31]
Bisporphyrin	180	0.01	[186]
Mg-Phthalocyanine	200	0.18	[187]
WO_3/$FeNbO_4$	230	2	[188]
$CdIn_2O_4$	250	0.2	[189]
$CdSnO_3$	250	0.1	[190]
CuO-$CdIn_2S_4$	250	400	[191]
In_2O_3	250	0.5	[192]

In_2O_3-Fe_2O_3	250	0.2	[193]
$NiFe_2O_4$	250	1000	[194]
SnInO	300	3	[195]
$Zn_2In_2O_5$-$MgIn_2O_4$	300	0.01	[196]
WO_3	300	1	[197]
ZnO	400	300	[193]

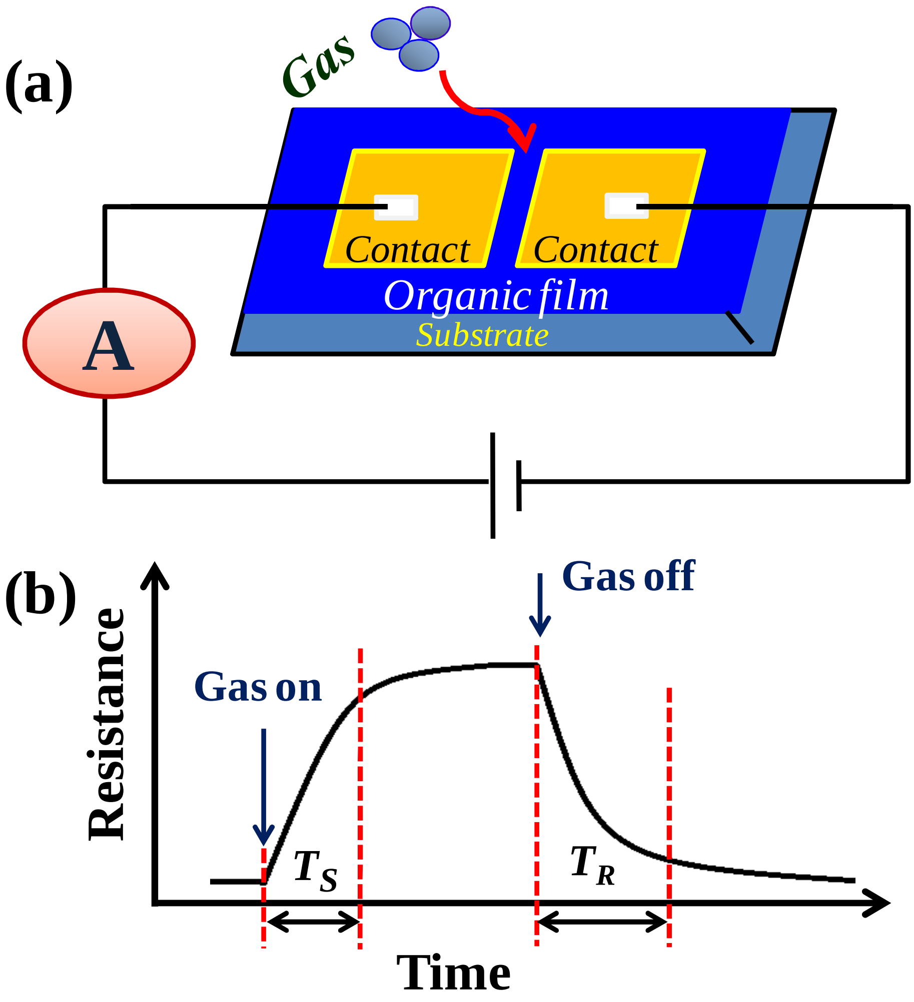

Figure 5.1 (a) Schematics configuration (b) Response curve of chemiresistive gas sensor.

5.2 Chemiresistive gas sensors and its characteristics parameters

A chemiresistive sensor essentially is a “resistor” whose electric resistance is very sensitive to the chemical environment. In the simplest form of a chemiresistor, a semiconductor material is deposited between a pair of electrodes on an insulating substrate. The gaseous species act as either electron donor or electron acceptor and therefore change the device conductivity. In our case we have deposited phthalocyanine and used gold electrode, as shown in Fig 5.1(a). A change in electrical resistance of the device is measured as a function of time for known amount of exposed gas. The response curve is represented by variation in resistance of sensors with time on exposure and withdrawal of analyzing of gas as shown in Fig. 5.1 (b).

A chemiresistive sensor is characterized by following five parameters: (i) sensitivity, (ii) response time, (iii) recovery time, (iv) selectivity and (v) long term stability. The sensitivity (S) of a sensor can be defined by many ways, including (a) A ratio of resistance in air to that in gas i.e. $S = R_{\mathrm{air}}/R_{\mathrm{gas}}$, (b) $S\,(\%) = 100 \times (R_{\mathrm{air}} - R_{\mathrm{gas}})/R_{\mathrm{air}}$. A positive value of S implies film resistance decreases on gas exposure and vice versa or (c) $S = \{(C_{\mathrm{g}}-C_0)/C_0\} \times 100$, where C_{g} and C_0 are the conductance in gas and air respectively [181]. The response time (T_S) is the time interval over which conductance attains a fixed percentage (usually 90%) of final value when the sensor is exposed to full-scale concentration of the gas. Recovery time (T_R) is the time interval over which sensor conductance reduces to 10% of the saturation value when the sensor is exposed to full-scale concentration of the gas and then placed in the clean air. A good sensor should have a small response and recovery times so that sensor can be used over and over again. Moreover, the sensor should be selective to a particular gas only and sensor should not degrade on continuous operations for long durations.

5.3 Cl_2 Gas sensing properties of mononuclear phthalocyanine films

5.3.1 MBE grown FePc and CoPc films

In this section we present the Cl_2 gas sensing properties of FePc and CoPc films grown on (0001) Al_2O_3 substrate. In Fig. 5.2 (a), a plot of sensitiviy ($S = C_g / C_0$) as function of operating temperature is shown for FePc and CoPc fims (at 30 ppb of Cl_2 gas exposure). FePc and CoPc films shows a measurable conductance change only after 100°C. It cen be seen that *S* shows it maximum value around 170ºC and this behaviour is in agreement with the reported literature for phathlocaynine films [9, 31, 101]. In this case all films shows an enhancement in conuctance on exposure to Cl_2 gas as expected for a p-type semiconductor. The conductance versus time curves (at 170°C) for different doses of Cl_2 gas for FePc and CoPc films are shown in Fig. 5.2 (b) and Fig. 5.2 (c) respectively. From these data's, it may be noted that even though the chamber is leak tight, the conductance does not saturate on exposure to Cl_2 gas, it could be due to the following reason: there are two competing phenomena here, one is the reaction of Cl_2 gas with the films, which result in response and second is the replacement of adsorbed gas molecule by the surrounding oxygen, which results in the recovery. Due to faster kinetics of both the processes saturation cannot be achieved in these samples. As seen from Fig. 5.2 (b), for pure FePc film the change in conductance (from base conductance value) increases on exposure of Cl_2 gas in the range of 10-500 ppb. For concentration > 500 ppb the conductance change decreases in magnitude and finally films does not sense the Cl_2 gas. In a similar manner CoPc films shows best gas sensing characteristics in the concentration range of 10 – 5000 ppb only, as shown in Fig. 5.2 (c). In the Cl_2 gas sensing mechanism the central metal atom play an important role [198]. The chemical binding of Cl_2 molecule with the phthalocyanines metal atom is also supported by theoretical work where it has been shown that oxidizing gases strongly chemisorbs to the central metal atom of MPcs and physisorbs to all non metal sites [199].

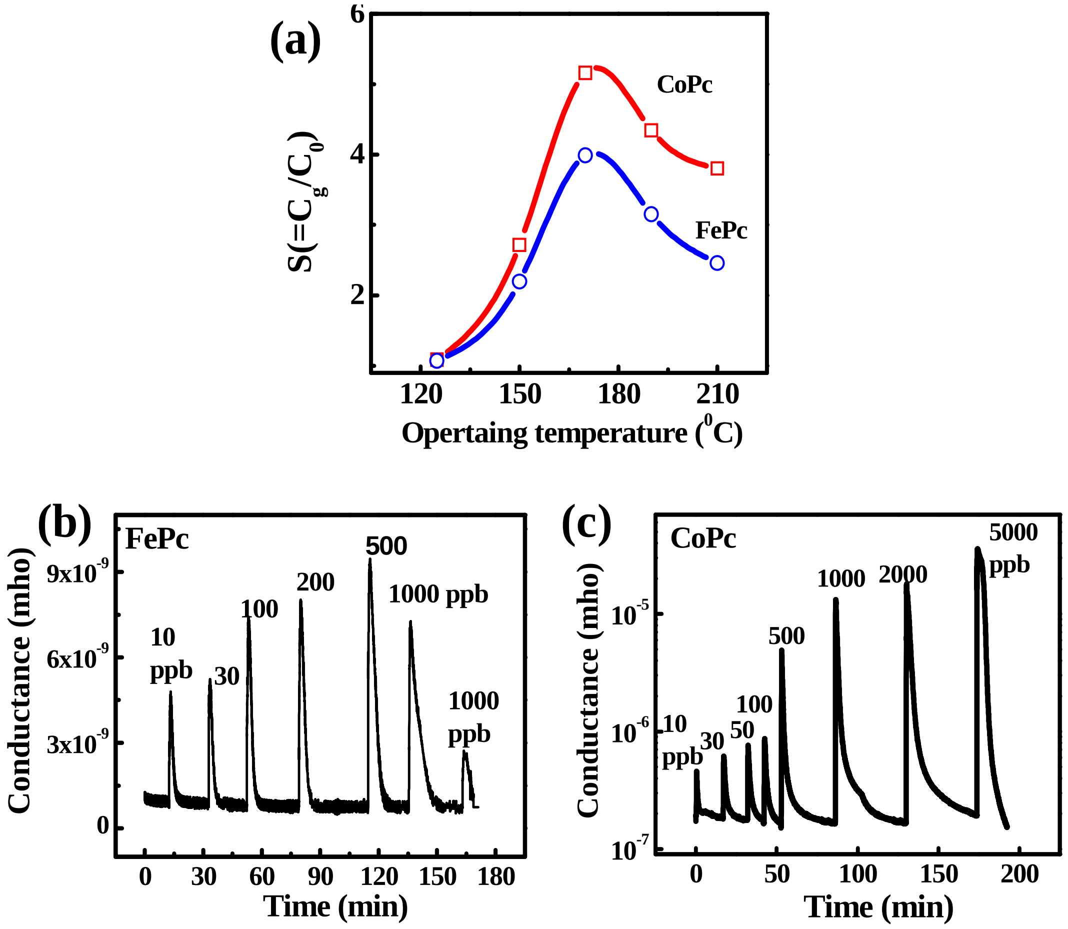

Figure 5.2(a) Temperature dependence of the sensitivity *S* (at 30 ppb of Cl_2 exposure) for FePc and CoPc films (b) Time dependence of the conductance (at 170°C) of the FePc films for different doses of Cl_2 gas (c) Time dependence of the conductance (at 170°C) of the FePc films for different doses of Cl_2 gas

5.3.2 Drop casted CuPcTs films

In this section we will discuss the room temperature Cl_2 gas sensing characteristics of CuPcTs films of nominal thickness ~1 μm were prepared on quartz substrates using drop casting method.

5.3.2.1 Response curve

Typical response curves recorded at room temperature for different Cl_2 concentrations are shown in Fig. 5.3. It may be noted that Cl_2 exposure up to 2000 ppb, resulted in a highly reproducible response curves, with a very fast response time (~ 4 s) and a full recovery in ~ 10 min. It suggest that CuPcTs films can be used as chemical sensor in the gas exposure range of 5-2000 ppb, however for gas concentration > 2000 ppb, the degradation of films limits their sensing application**.**

5.3.2.2 Linearity and reproducibility

The variation of $S = \{(C_g - C_0)/C_0\} \times 100$ as a function of Cl_2 concentration is shown in Fig. 5.4 (a). At 5ppb, 20ppb and 50ppb of Cl_2 concentrations, the sensitivity values are 65%, 79% and 89% respectively. It is seen that for Cl_2 concentration in the 5-2000 ppb range, S increases linearly between 65 and 625 %. However, for Cl_2 doses >2000 ppb, not only the S value decreases, the full recovery also never completes. To test the reproducibility of the response curve, we have recorded the response curve of the CuPcTs films for a repeated Cl_2 exposure of 100 ppb for many times, the data shown in Fig. 5.4 (b) is for five times exposure. The nearly same value of conductance on every time exposure of the films shows that the response curves are highly reproducible.

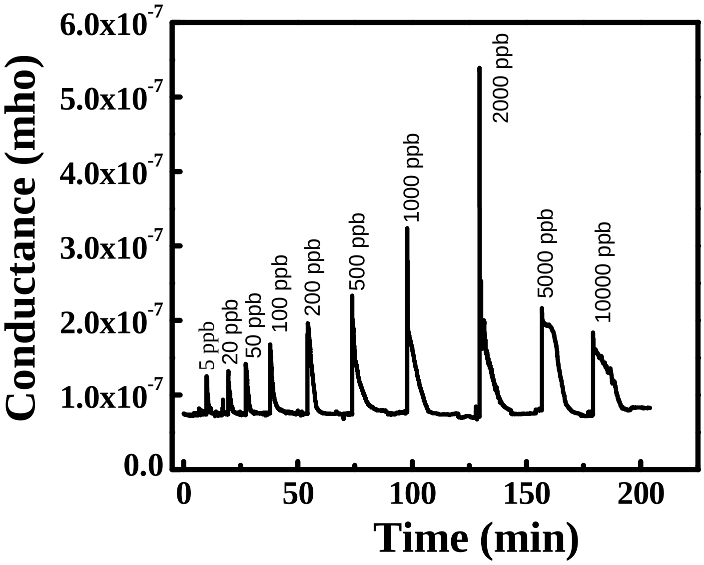

Figure 5.3 Response curves of CuPcTs recorded after exposing to different concentration of Cl_2 gas.

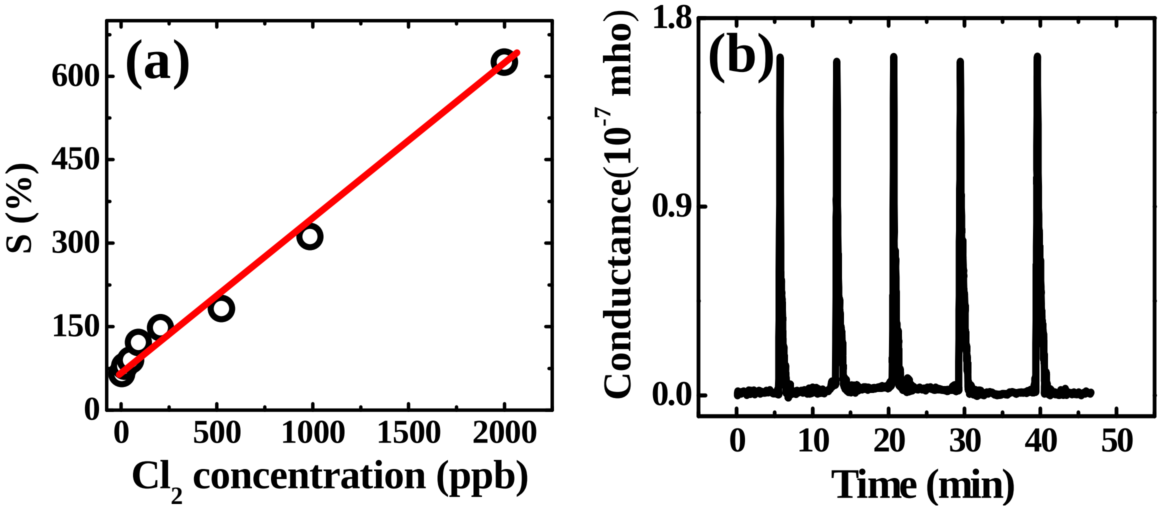

Figure 5.4 (a) Variation of sensitivity (*S*) as a function of Cl_2 gas concentration, which shows linear dependence (b) The response of the curve of the CuPcTs films for a repeated exposure of 100 ppb of Cl_2 gas.

5.3.2.3 Selectivity

To test selectivity of CuPcTs film, response curves (change in conductance of the film as a function of time) were recorded at 500 ppb concentration of different gases i.e. Cl_2,

H_2S, NH_3, CH_4, CO and NO. The histogram showing the sensitivity for different gases is shown in Fig. 5.5. It may be noted from the histogram that films are highly selective to the Cl_2, and the sensitivity value is ~184 %. For all other gases, the sensitivity was < 0.1 %.

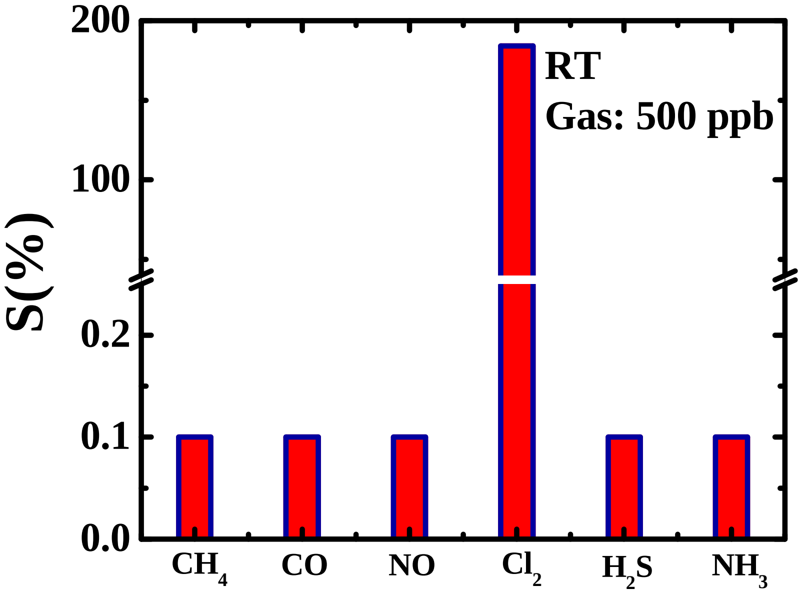

Figure 5.5 Selective histogram of CuPcTs films towards 500 ppb of different gases at room temperature.

5.3.2.4 Explanation of reversible and irreversible response

(a) Reversible response

First we explain why the response is reversible at ≤ 2000 ppb Cl_2 concentrations and irreversible at higher concentrations. CuPcTs films are intrinsically insulators and turn semiconductors only when they are exposed to atmosphere. This is because oxygen from ambient chemisorbs at the film surface. The presence of adsorbed oxygen (O_2^-), corresponding to the binding energy at 533 eV was confirmed by the XPS analysis, as shown in Fig.5.6. Once the films is exposed to the low concentration of Cl_2 gas, it replaces the adsorbed oxygen (as being more electronegative than oxygen) as well as get adsorbed at other free sites on the films surface, and pick up the electron from there. As a result the conductance rises, but later this adsorbed Cl_2 is replaced by the atmospheric oxygen due to its abundance in the surrounding and results in the lowering of conductance. This reversible response is a prerequisite for chemiresistive sensors.

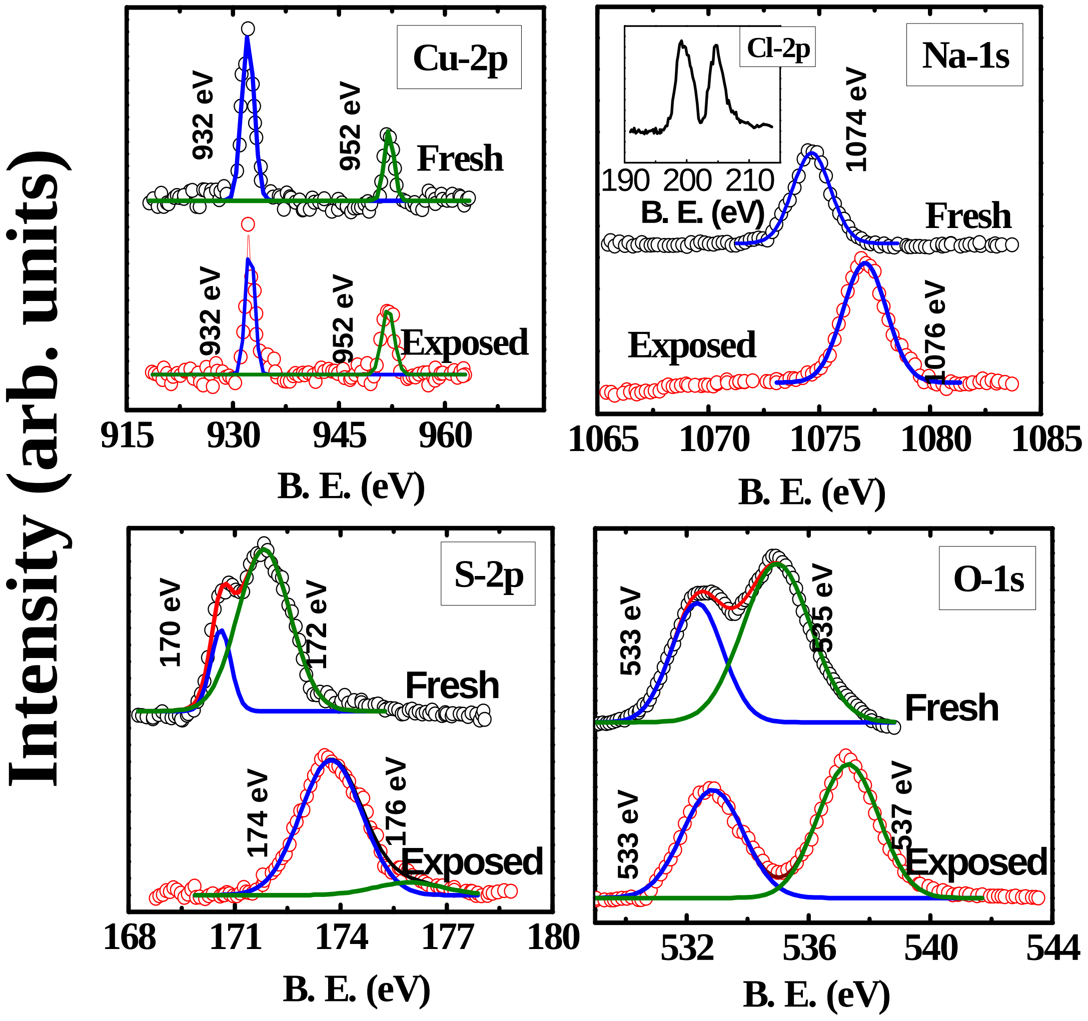

Figure 5.6 Cu-2p, Na-1s, S-2p and O-1s XPS spectrum recorded for fresh and 10 ppm Cl_2 exposed CuPcTs films. Inset of Na-1s spectra shows the presence of Cl-2p peak in the exposed films.

(b) Irreversible response

The irreversible response of the CuPcTs films at higher Cl_2 concentrations (>2000ppb) indicates oxidation of the CuPcTs molecules. Since oxidation implies formation of a chemical bond, therefore energy and the presence of other species are required to reverse this process. Otherwise the process will be irreversible, as observed in the present case. In order to confirm the oxidation of CuPcTs, XPS and FTIR spectra were recorded for the freshly prepared films and after their exposure to a high dose (10 ppm) of Cl_2. The obtained XPS results are presented in Fig. 5.6. First we look at Cu-2p XPS spectrum, as in metal phthalocyanine it is the preferable site for gas adsorption [198] . The peak at 932 eV and 952 eV corresponds to the Cu-$2p_{3/2}$ and Cu-$2p_{1/2}$ respectively. As seen there is no change in the spectrum after gas exposure, so it rules out the possibility of gas reaction at copper sites, which are the most prominent reaction sites for CuPc materials.

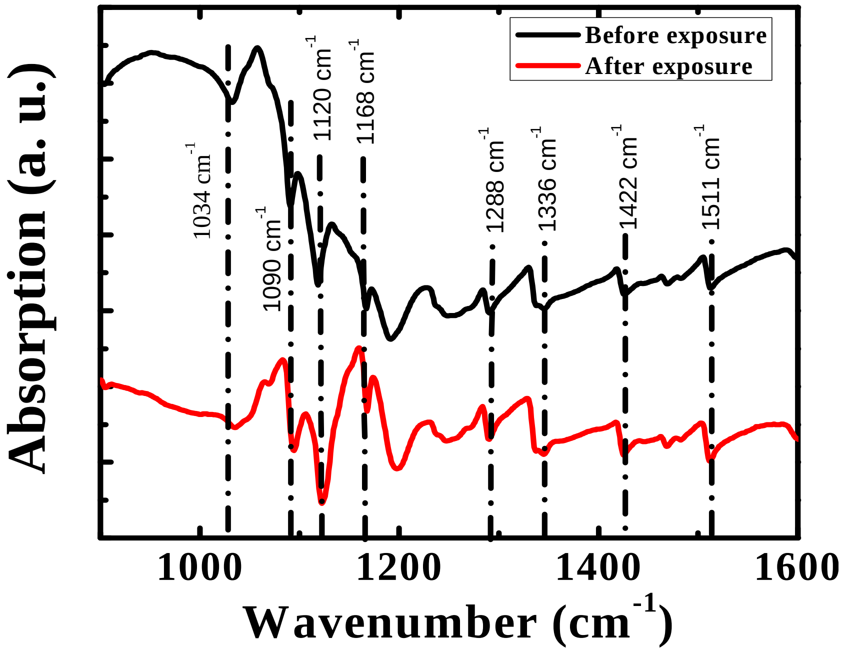

Figure 5.7 FTIR spectra data recorded for fresh and 10 ppm Cl_2 exposed CuPcTs films**.**

The major changes in the XPS spectrum occurs at sulphonated group site. The core level O-1s XPS spectrum of fresh CuPcTs films indicates presence of oxygen in two different chemical states. The peaks at 533 eV and 535 eV correspond to correspond to chemisorbed oxygen at films surface and oxygen present in the sulphonated group, respectively [78]. However, for Cl_2 exposed film, there is a large shift in the O peak at 535 eV i.e. related to S / Na atoms, indicating possibility of Cl_2 at oxygen sites of sulphonated group. This can possibly happen if the Cl_2 molecules get attached to O and form an oxychloride compound. The reaction will also lead to increase in the binding energies of S-2p and Na-1s peaks, as seen in Fig. 5.6. The presence of Cl-2p peak (shown in the inset of Na-1s XPS data) at 199 eV and 205 eV in exposed films verifies the existence of physisorbed and chemisorbed chlorine respectively. This information is further supported by the FTIR data presented in Fig. 5.7. For fresh film the noticeable FTIR peaks are: 1034 cm^{-1} (SO_3 symmetric stretching bond), 1090 cm^{-1} (C-N stretching bond), 1120 and 1168 cm^{-1} (C-H in plane banding vibration), 1288 cm^{-1} (SO3 asymmetric stretching bond) and 1336 cm^{-1}, 1422 cm^{-1} , 1511 cm^{-1} (characteristic of C-N stretching) [200]. However, after Cl_2 exposure, the intensity of the peak at 1034 cm^{-1} (SO_3 stretching bond) becomes significantly lower. All other peak do not show any shift or intensity change after Cl_2 exposure. The intensity of any FTIR peak is related to the dipole-moment. The lowering of intensity indicates the lowering of the dipole-moment of SO_3 group. This result can be explained by Cl_2 attacks on the oxygen sites of SO_3 group, which pick up some charge from it and results in lowering of dipole-moment.

Therefore XPS and FTIR result indicates that for higher concentration, the response becomes irreversible, which is found to be due to the chemical bond formation between Cl_2 and SO_3Na group of CuPcTs films.

5.3.2.5 Elovich isotherms for reversible response

In reactions involving chemical adsorption of gases on a solid surface without desorption of the products, the adsorption rate decreases with time due to an increase in surface coverage [201-203]. One of the most useful models for describing such activated chemical adsorption is the Elovich equation, which is given by

$$\frac{d\theta}{dt} = a\exp(-b\theta) \tag{5.1}$$

where θ is the amount of gas adsorbed at time t and a, b are constants. In the Elovich equation, constant a is regarded as the initial adsorption rate because $\frac{d\theta}{dt}$ approaches a when θ approaches 0 and it depends on the activation energy. Constant b is related to a measure of the extent to which the surface has been screened by the potential barrier for successive adsorption. Given that $\theta = \theta_t$ at time equals t and $\theta_t = 0$ at t =0, the integrated form of Eq. 5.1 is

$$\theta_t = \left(\frac{1}{b}\right)\ln\left(ab\right) + \left(\frac{1}{b}\right)\ln\left[t + \left(\frac{1}{ab}\right)\right] \tag{5.2}$$

In the present case, we assume that the change in the conductance (ΔC) is proportional to the amount of adsorbed Cl_2 molecules θ. The Elovich isotherm describes adsorption phenomena occurring on surfaces, which are energetically heterogenous or on surfaces where the adsorption process induces an energetic heterogeneity [201, 203]. The CuPcTs films contain many adsorption sites and Cl_2 adsorption leads to a charge-transfer between film and Cl_2. However, this process is limited by a ‘potential barrier’ formed from the dipole layer created by the redistribution of charge between the Cl_2 molecule and the CuPcTs film. The increase of this potential barrier with successive adsorption events provides an adsorption induced surface heterogeneity. The adsorbate–adsorbate interactions are known to make the heat of adsorption and desorption dependent on the coverage [201]. This makes adsorption rate to decreases exponentially with time due to an increase in surface coverage**.** As shown in Fig. 5.8 (a), the plots of ΔC vs ln t, which are derived from Fig. 5.3, are linear, indicating that the interaction obeys the Elovich equation. From the slopes, values of b are calculated for different Cl_2 concentration. As shown in the 5.8 (b), log b – log $[Cl_2]$ plot is linear in nature. Therefore, Cl_2 concentration apart from the sensitivity plot, as shown in Fig. 5.8 (b), can also be determined from b that is derived from the response rate $\Delta C/dt$.

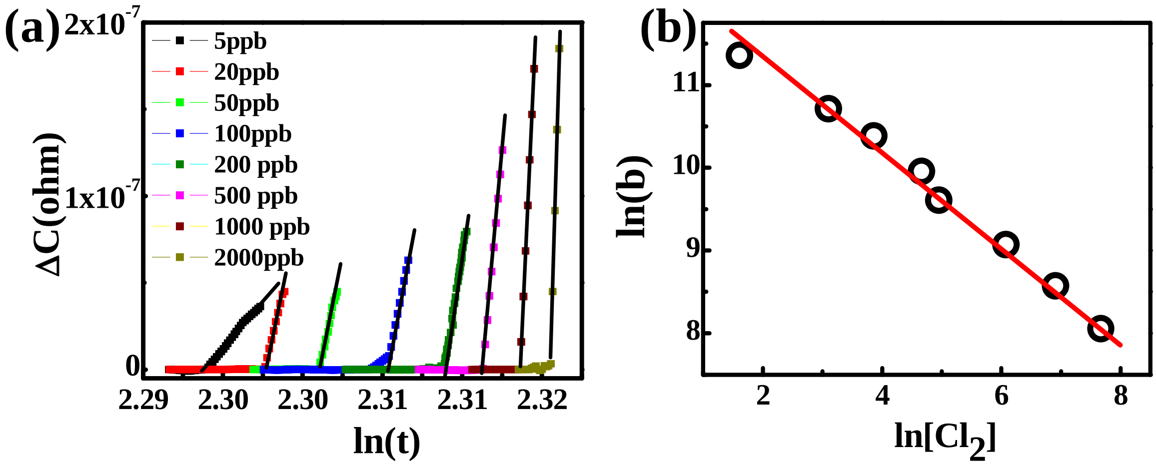

Figure 5.8 (a) Change in conductance (ΔC) as a function of ln(t), which was derived from the response curves in Fig. 5.3. Straight-line fit of data is in accordance with Elovich equation and the slope of linear fits yields parameter b. (b) Linear correlation between ln b and ln $[Cl_2]$.

5.4 Cl_2 gas sensing properties of binuclear (Co-Fe)Pc films

In Chapter 3 we have shown that very high value μ of in binuclear (Co-Fe)Pc films (prepared on (0001) Al_2O_3 substrate) as compare to FePc and CoPc films. Now we discuss the influence of high μ of binuclear films on its gas sensing characteristics. A plot of sensitiviy ($S = C_g / C_0$) as function of operating temperature for binuclear (Co-Fe)Pc fims along with CoPc and FePc films (at 30 ppb of Cl_2 gas exposure) is shown in Fig. 5.9 (a) and the value of S is higher as compare to FePc and CoPc films in all temperature range 120 to 210 °C. The conductance versus time curves (at 170°C) is shown for different doses of Cl_2 gas for binuclear films the results are shown in Fig. 5.9 (a). It is interesting to note that binuclear films can detect even 5 ppb of Cl_2 gas (10 ppb in case FePc and CoPc films) , and the reversible gas sensing characteristics has been obtained in the concentration range of 5 – 500 ppb. In order to compare the gas sensing characteristics of all films, response curve i.e. $S = \{(C_g - C_0)/C_0\} \times 100$ has been plotted, as shown in Fig. 5.10 (a)) as a function of time for a particular exposure of 500 ppb of Cl_2 gas. It can be seen that response of binuclear films is about 16 and 13 times higher than that of FePc and CoPc films respectively. For all films the response time (i.e. time required to reach 90% of the saturation conductance) is nearly same as ~ 10 sec, however the recovery time is highest (~18 min) for composite films. In Fig. 5.10 (b), we have plotted the S for all films at gas concentration of 500 ppb. It can be seen that the binuclear (Co-Fe)Pc films films shows highest value of S. The sensitivity of any materials depends on following factors: (i) numbers of available sites for the gas interaction. (ii) charge carriers released after gas interaction should easily move to the collecting electrode. Due to relatively rough surface of the CoPc and FePc films although the numbers of available sites for gas - material interaction can be more as compared to binuclear films but comparatively poor structural order reduces the sensitivity of these films. Inset of Fig. 5.10 (b) shows the sensitivity of binuclear (Co-Fe)Pc films for various oxidizing gases, it reveals that these films are highly sensitive to Cl_2 gas.

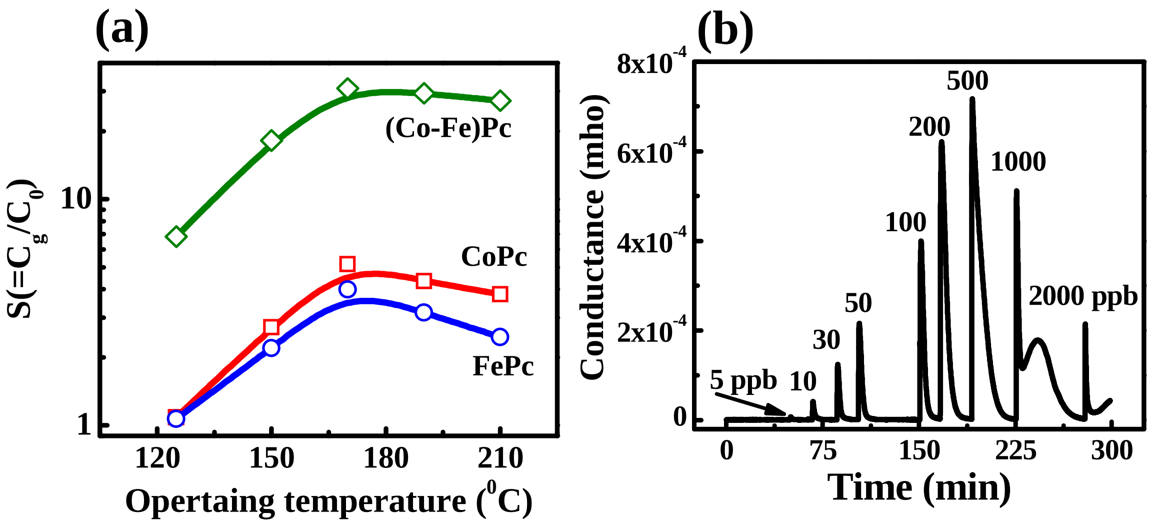

Figure 5.9 (a) Temperature dependence of the sensitivity *S* (at 30 ppb of Cl_2 exposure) for binuclear films (b) Time dependence of the conductance (at 170°C) of the binuclear films for different doses of Cl_2 gas.

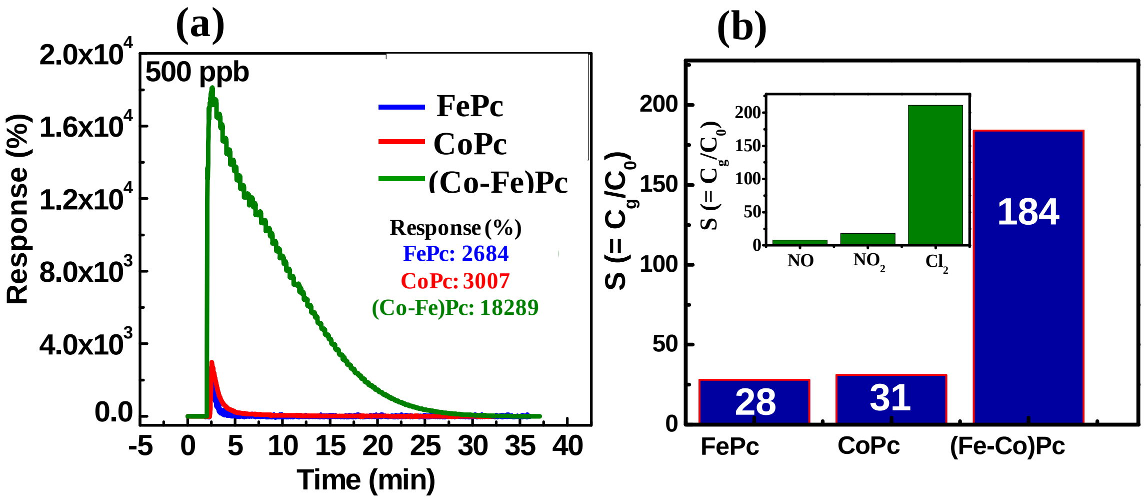

Figure 5.10 (a) Comparison of the response for FePc, CoPc and binuclear (Co-Fe)Pc films at 500 ppb for Cl_2 exposure (b) Comparison of Sensitivity for all films at 500 ppb of Cl_2 gas exposure. Inset bar chart showing the sensitivity of the binuclear films for various oxidizing gases.

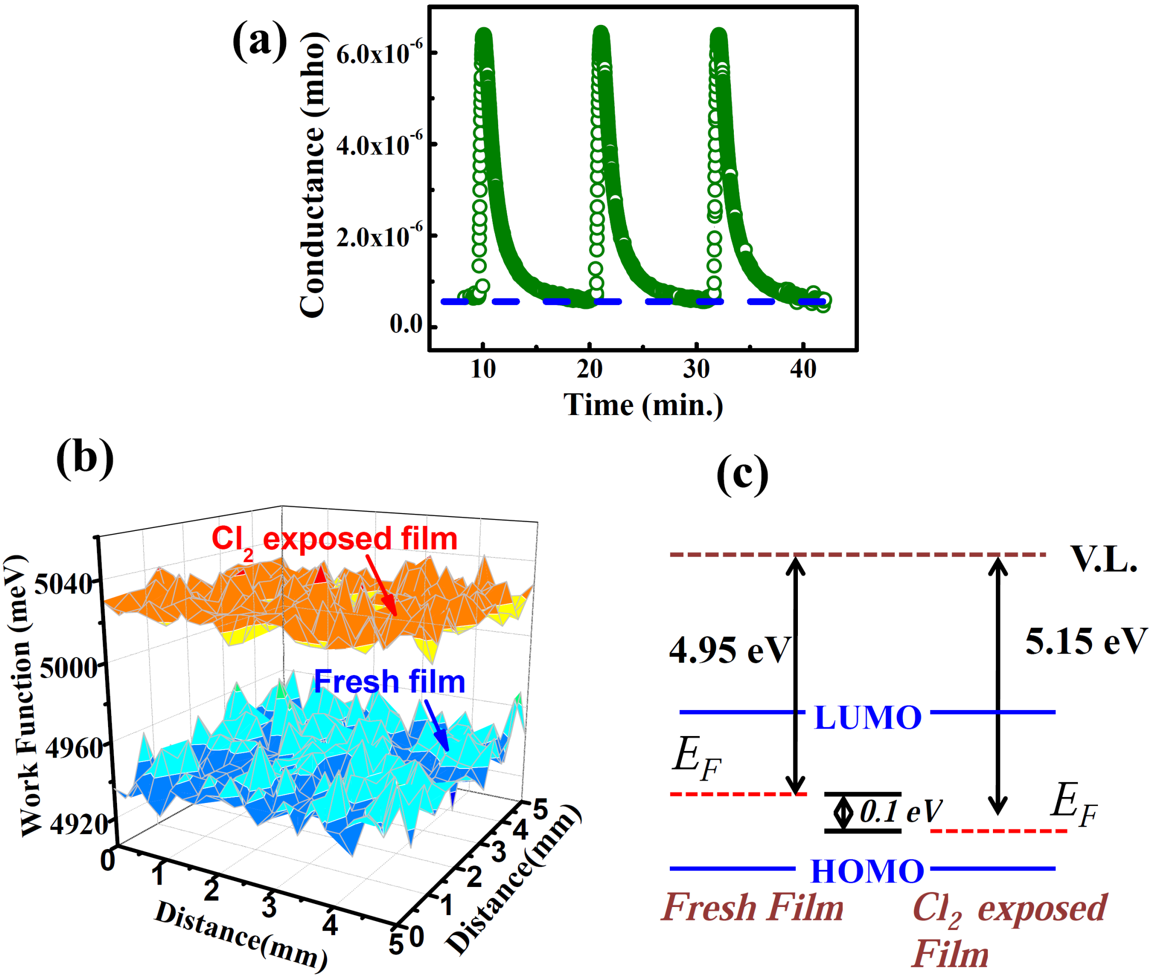

Figure 5.11 (a) Demonstration of the reproducibility (at 5ppb of Cl_2) and base conductance drift for binuclear (Co-Fe)Pc films. (b) Work function imaging of the fresh and Cl_2 exposed binuclear (Co-Fe)Pc films and (c) Shift in Fermi level after the exposure of Cl_2 gas.

The demonstration of the reproducibility (at 500 ppb of Cl_2) and base conductance drift for binuclear films is shown in Fig. 5.11 (a). It reveals that sensing characteristics are highly reproducible without any drift of base conductance. The effect of Cl_2 exposure on binuclear films is also reflected in the work function value. Fig. 5.11 (b) shows the three dimensional view of work function imaging for fresh and Cl_2 exposed binuclear films. It is seen that work function of fresh binuclear films is enhanced by 0.1 eV after Cl_2 exposure. The increase in work function value after gas exposure is expected as binuclear molecule is *p*-type in nature and an increase in carrier concentration on exposure will push fermi level towards the LUMO level as shown in Fig. 5.11 (c). In case of FePc and CoPc films, work function also enhanced by 0.1 eV, after the exposure of Cl_2 gas. This indicates equal numbers of charge carrier are producing after the interaction of Cl_2 gas, but due to high mobility, binuclear films exhibited highest sensitivity.

5.5 Conclusions

The gas sensing characteristics of CuPcTs, CoPc, FePc and (Co-Fe)Pc films has been investigated. CuPcTs films exhibited room temperature ppb level Cl_2 gas sensitivity. Selectivity, repeatability, stability and linearity (sensitivity vs concentration) in the range 5 ppb to 2000 ppb are investigated. The chemical adsorption process of Cl_2 on CuPcTs has been analyzed using Elovich equation, which provides an alternative way of qualifying Cl_2 concentration from response rate of sensor.

The Cl_2 gas sensing properties of FePc and CoPc films were investigated. The highest sensitivity was obtained at 170°C. It was found that CoPc and FePc films can detect 10 ppb of Cl_2 gas.

Due to the high mobility of (Co-Fe)Pc films, they exhibited enhanced response for Cl_2 gas, which is about 16 and 13 times higher than that of FePc and CoPc films. Interestingly, it was found that (Co-Fe)Pc films can detect even 5ppb of Cl_2 gas.

CHAPTER-6

SUMMARY AND CONCLUSIONS

Thin films of mononuclear phthalocyanine (FePc, CoPc and $F_{16}CuPc$) and binuclear phthalocyanine (Co-Fe)Pc were deposited by MBE with a perfect control over growth parameters such as deposition rate, substrate temperature and film thickness on different substrate i.e. (0001) Al_2O_3 , (001) $LaAlO_3$, (100) $SrTiO_3$ quartz and ITO. The growth temperature and deposition rate were respectively, 200°C and 2Å/s. Binuclear (Co-Fe)Pc films were found to grown only on (0001) Al_2O_3 substrates at 200°C if deposited using the CoPc/FePc mixture in 1:1 (w/w) ratio. Thin films of CuPcTs were also prepared using drop casting method. In addition all grown films were characterized by various techniques such as, SEM, AFM, GIXRD, UV-Vis, FTIR, Kelvin probe and Raman Spectroscopy. Formation of binuclear (Co-Fe)Pc was confirmed by MALDI mass spectroscopy. The charge transport properties of grown films were investigated by measuring the temperature dependent *J-V* characteristics as well as resistivity in the temperature range 300-25 K. Also, the suitability of the grown films was examined for their possible application as chemiresistive gas sensors.

In addition *p-n* heterojunction comprising of *p*-type (CoPc) and *n*-type ($F_{16}CuPc$) as well as *p*-type (CoPc) and *p*-type (FePc) were fabricated using MBE. The charge transport properties of these films were also investigated.

The major conclusions are already presented at the end of each chapter. Here we make a summary of the main results obtained during the thesis work.

1. It has been demonstrated that mononuclear FePc, CoPc and binuclear (Co-Fe)Pc films grow with molecules *face-on* stacking on (0001) Al_2O_3 substrate due to the interaction between molecule and of Al terminated surface. AFM and GIXRD studies revealed that (Co-Fe)Pc phthalocyanine films have better structural ordering and hence smooth morphology as compared to the mononuclear films. This is attributed to the additional dipole moment of binuclear (Co-Fe)Pc molecules, which results better *face-on* stacking as compare to the mononuclear CoPc and FePc films.
2. Due to the better structure ordering the binuclear (Co-Fe)Pc films exhibited μ ~110 cm^2/Vs, while in case of CoPc and FePc films mobility were found to be 5.3 and 1.1 cm^2/Vs.
3. The temperature dependence of resistivity of binuclear (Co-Fe)Pc films exhibited metallic behavior in the temperature range 300K-25K which is the manifestation of the improved ordering also. The *J-V* characteristics of binuclear (Co-Fe)Pc films exhibited trap-free SCLC in the temperature range 300K to 25K. For CoPc and FePc films the temperature dependent resistivity showed that, these films are in the critical regime of metal–insulator transition. The *J-V* characteristics of mononuclear films exhibited SCLC with exponential distribution of traps at low temperature.
4. The temperature dependent *J-V* characteristics of FePc films have also been investigated at very high bias *i.e.* in the bias range of ± 200 V. In the temperature

range of 300 K–30 K, the charge transport is governed by bulk-limited processes with a bias dependent crossover from ohmic ($J \sim V$) to exponentially distributed shallow trap mediated space-charge-limited conduction ($J \sim V^{\alpha}$, $\alpha \geq 2$) to space charge limited conduction with field enhanced mobility ($ln\ \mu \sim E^{1/2}$). However, at temperatures < 100 K, the charge transport is governed by electrode-limited process, which undergo a bias dependent transition from Schottky ($ln\ J \sim V^{1/2}$) to multistep-tunnelling (MUST).

5. In the case of CoPc films grown on (100) $SrTiO_3$ substrate, it has been demonstrated that the molecule stack in *edge-on* configuration. The temperature dependence of resistivity exhibited semiconductor to like transition at ~110K. XRD measurement revealed that this transition is due to in-plane compressive strains induced by structural phase transition (from cubic-to tetragonal ~ 110K) of $SrTiO_3$ substrate reduce the intermolecular distance.
6. Charge conduction in FePc films under high electrical field has been investigated. A bias dependent transition from ohmic to space-charge limited conduction to space charge limited conduction with field enhanced mobility is observed. At temperatures <100 K, by analyzing the low bias (< 100 V) data, which is governed by Schottky–barrier limited conduction. However at higher bias multistep tunnelling was observed in the FePc films.
7. Structure and morphology of water soluble phthalocyanine (CuPcTs) films prepared by drop casting method were found to be independent of substrate, and have usually amorphous character. We demonstrated that below 280K these films do not transport any current.

8. The gas sensing characteristics of CuPcTs, CoPc, FePc and (Co-Fe)Pc films has been investigated. CuPcTs films exhibited room temperature ppb level Cl_2 gas sensitivity. Selectivity, repeatability, stability and linearity (sensitivity vs concentration) in the range 5 ppb to 2000 ppb are investigated. The chemical adsorption process of Cl_2 on CuPcTs has been analyzed using Elovich equation, which provides an alternative way of qualifying Cl_2 concentration from response rate of sensor.The Cl_2 gas sensing properties of FePc and CoPc films were investigated. The highest sensitivity was obtained at 170°C. It was found that CoPc and FePc films can detect 10 ppb of Cl_2 gas.Due to the high mobility of (Co-Fe)Pc films, they exhibited enhanced response for Cl_2 gas, which is about 16 and 13 times higher than that of FePc and CoPc films. Interestingly, it was found that (Co-Fe)Pc films can detect even 5ppb of Cl_2 gas.
9. The *p*-*n* heterojunction comprising of *p*-type CoPc (20nm) and *n*-type F_{16}CuPc (20nm) heterojunctions showed ohmic conductance with three order of magnitude higher conductivity as compare to individual CoPc or F_{16}CuPc layer. The higher conductivity F_{16}CuPc(20nm)/CoPc(20nm) heterojunction is due to the charge carrier accumulation at the interface, which is confirmed by Kelvin probe study. The thickness of charge carrier accumulation layer at the interface was estimated to be ~20 nm. Interestingly these heterojunction films exhibited reverse rectification behavior i.e. conducts current only in reverse bias. On the other hand, CoPc(20nm)/FePc(20nm) (*p*-*p* type) heterojunction films do not exhibited any charge transfer at the interface. Therefore their electrical properties are identical to the individual layers.

Future Plan

In the present thesis work, we have obtained higher ordered CoPc, FePc as well as binuclear (Co-Fe)Pc films with record mobility 110 cm^2/Vs. In addition we have fabricated *p-n* heterojunction with high conducting interface. These samples can be used for further investigated some of the possible examples are as follows:

1. Other metal phthalocyanines such as NiPc, CuPc, AgPc and ZnPc can be explored.
2. The magnetic properties of ordered binuclear films, along with the CoPc and FePc films can be investigated. In binuclear films, due to the interaction of two phthalocynine rings one can expect improved magnetic ordering. In addition high mobility binuclear films can be used for fabrication of field effect transistor.
3. The sensing properties of $F_{16}CuPc/CoPc$ can be explored.

Bibliography

[1] F Gutmann, LE Lyons, H Keyzer, Organic semiconductors: R.E. Krieger Pub. Co.; 1983.

[2] N Karl, Charge carrier transport in organic semiconductors, Synthetic Metals, 133–134(2003) 649-57.

[3] S Samanta, A Singh, A Kumar, AK Debnath, DK Aswal, SK Gupta, et al., Improved charge conduction in cobalt-phthalocyanine thin films grown along 36.8[degree] boundary of SrTiO[sub 3] bicrystals, Applied Physics Letters, 98(2011) 143301-3.

[4] HY Choi, SH Kim, J Jang, Self-Organized Organic Thin-Film Transistors on Plastic, Advanced Materials, 16(2004) 732-6.

[5] CD Dimitrakopoulos, PRL Malenfant, Organic Thin Film Transistors for Large Area Electronics, Advanced Materials, 14(2002) 99-117.

[6] J Park, S Lee, HH Lee, High-mobility polymer thin-film transistors fabricated by solvent-assisted drop-casting, Organic Electronics, 7(2006) 256-60.

[7] H Sirringhaus, Device Physics of Solution-Processed Organic Field-Effect Transistors, Advanced Materials, 17(2005) 2411-25.

[8] DK Aswal, S Lenfant, D Guerin, JV Yakhmi, D Vuillaume, Self assembled monolayers on silicon for molecular electronics, Analytica Chimica Acta, 568(2006) 84-108.

[9] DK Aswal, JV Yakhmi, Molecular and Organic Electronics Devices: Nova Science Pub Incorporated; 2010.

[10] C Joachim, JK Gimzewski, A Aviram, Electronics using hybrid-molecular and mono-molecular devices, Nature, 408(2000) 541-8.

[11] SP Koiry, DK Aswal, AK Chauhan, V Saxena, SK Nayak, SK Gupta, et al., Electrical bistability in electrografted 5-(4-undecenyloxyphenyl)-10,15,20-triphenylporphyrin monolayer on Si, Chemical Physics Letters, 453(2008) 68-72.

[12] SP Koiry, P Jha, DK Aswal, SK Nayak, C Majumdar, S Chattopadhyay, et al., Diodes based on bilayers comprising of tetraphenyl porphyrin derivative and fullerene for hybrid nanoelectronics, Chemical Physics Letters, 485(2010) 137-41.

[13] DJ Wold, CD Frisbie, Formation of Metal−Molecule−Metal Tunnel Junctions: Microcontacts to Alkanethiol Monolayers with a Conducting AFM Tip, Journal of the American Chemical Society, 122(2000) 2970-1.

[14] CK Chiang, CR Fincher, Jr., YW Park, AJ Heeger, H Shirakawa, EJ Louis, et al., Electrical Conductivity in Doped Polyacetylene, Physical Review Letters, 39(1977) 1098-101.

[15] L-L Chua, J Zaumseil, J-F Chang, ECW Ou, PKH Ho, H Sirringhaus, et al., General observation of n-type field-effect behaviour in organic semiconductors, Nature, 434(2005) 194-9.

[16] RJ Kline, MD McGehee, EN Kadnikova, J Liu, JMJ Fréchet, Controlling the Field-Effect Mobility of Regioregular Polythiophene by Changing the Molecular Weight, Advanced Materials, 15(2003) 1519-22.

[17] V Podzorov, SE Sysoev, E Loginova, VM Pudalov, ME Gershenson, Single-crystal organic field effect transistors with the hole mobility ~ 8 cm^2/V s, Applied Physics Letters, 83(2003) 3504-6.

[18] Y Zhang, JR Petta, S Ambily, Y Shen, DC Ralph, GG Malliaras, 30 nm Channel Length Pentacene Transistors, Advanced Materials, 15(2003) 1632-5.

[19] M Mas-Torrent, C Rovira, Role of Molecular Order and Solid-State Structure in Organic Field-Effect Transistors, Chemical Reviews, 111(2011) 4833-56.

[20] SR Forrest, The path to ubiquitous and low-cost organic electronic appliances on plastic, Nature, 428(2004) 911-8.

[21] N Karl, J Marktanner, Structural Order and Photoelectric Properties of Organic Thin Films, Molecular Crystals and Liquid Crystals Science and Technology Section A Molecular Crystals and Liquid Crystals, 315(1998) 163-8.

[22] W Warta, R Stehle, N Karl, Ultrapure, high mobility organic photoconductors, Applied Physics A: Materials Science & Processing, 36(1985) 163-70.

[23] Y Gok, SZ Yildiz, The synthesis and characterization of new copper(ii) phthalocyanines containing four 20-member tetraaza-dioxa macrocyclic moieties, Journal of Coordination Chemistry, 36(1995) 175-81.

[24] CE Dent, RP Linstead, AR Lowe, 217. Phthalocyanines. Part VI. The structure of the phthalocyanines, Journal of the Chemical Society (Resumed), (1934) 1033-9.

[25] CC Leznoff, ABP Lever, Phthalocyanines: properties and applications: VCH; 1996.

[26] M-S Liao, S Scheiner, Electronic structure and bonding in metal phthalocyanines, Metal=Fe, Co, Ni, Cu, Zn, Mg, The Journal of Chemical Physics, 114(2001) 9780-91.

[27] Z Bao, AJ Lovinger, J Brown, New Air-Stable n-Channel Organic Thin Film Transistors, Journal of the American Chemical Society, 120(1998) 207-8.

[28] B Crone, A Dodabalapur, YY Lin, RW Filas, Z Bao, A LaDuca, et al., Large-scale complementary integrated circuits based on organic transistors, Nature, 403(2000) 521-3.

[29] YY Lin, A Dodabalapur, R Sarpeshkar, Z Bao, W Li, K Baldwin, et al., Organic complementary ring oscillators, Applied Physics Letters, 74(1999) 2714-6.

[30] M Bouvet, Phthalocyanine-based field-effect transistors as gas sensors, Analytical and Bioanalytical Chemistry, 384(2006) 366-73.

[31] AK Debnath, S Samanta, A Singh, DK Aswal, SK Gupta, JV Yakhmi, Parts-per-billion level chlorine sensors with fast kinetics using ultrathin cobalt phthalocyanine films, Chemical Physics Letters, 480(2009) 185-8.

[32] M Feng, W Shi-Rong, L Xiang-Gao, Y Dong-Hang, Improved Performance of Fluorinated Copper Phthalocyanine Thin Film Transistors Using Para-hexaphenyl as the Inducing Layer, Chinese Physics Letters, 28(2011) 118501.

[33] T Higuchi, T Murayama, E Itoh, K Miyairi, Electrical properties of phthalocyanine based field effect transistors prepared on various gate oxides, Thin Solid Films, 499(2006) 374-9.

[34] F Yakuphanoglu, M Caglar, Y Caglar, S Ilican, Improved mobility of the copper phthalocyanine thin-film transistor, Synthetic Metals, 160(2010) 1520-3.

[35] H Yanagi, H Kataura, Y Ueda, Improved photovoltaic properties for Au/AlPcCl/n-Si solar cells with morphology-controlled AlPcCl deposition, Journal of Applied Physics, 75(1994) 568-76.

[36] CJ Brown, Crystal structure of [small beta]-copper phthalocyanine, Journal of the Chemical Society A: Inorganic, Physical, Theoretical, (1968) 2488-93.

[37] RD Gould, Structure and electrical conduction properties of phthalocyanine thin films, Coordination Chemistry Reviews, 156(1996) 237-74.

[38] N Uyeda, M Ashida, E Suito, Orientation Overgrowth of Condensed Polycyclic Aromatic Compounds Vacuum-Evaporated onto Cleaved Face of Mica, Journal of Applied Physics, 36(1965) 1453-60.

[39] S M. Bayliss, S Heutz, G Rumbles, T S. Jones, Thin film properties and surface morphology of metal free phthalocyanine films grown by organic molecular beam deposition, Physical Chemistry Chemical Physics, 1(1999) 3673-6.

[40] M Ashida, N Uyeda, E Suito, Unit Cell Metastable-form Constants of Various Phthalocyanines, Bulletin of the Chemical Society of Japan, 39(1966) 2616-24.

[41] JM Robertson, 136. An X-ray study of the structure of the phthalocyanines. Part I. The metal-free, nickel, copper, and platinum compounds, Journal of the Chemical Society (Resumed), (1935) 615-21.

[42] Josep Oriol Osso Torne thesis, Growth, Structure, and Optical Properties of Highly Ordered Organic Thin Films of Phthalocyanine and Diindenoperylene: Universitat Autònoma de Barcelona. Departament de Física; 2004.

[43] M Ashida, N Uyeda, E Suito, Thermal transformation of vacuum-condensed thin films of copper-phthalocyanine, Journal of Crystal Growth, 8(1971) 45-56.

[44] GA Williams, BN Figgis, R Mason, SA Mason, PE Fielding, Structure of phthalocyaninatocobalt(II) at 4.3 K: a neutron-diffraction study, Journal of the Chemical Society, Dalton Transactions, (1980) 1688-92.

[45] Keizo Kato, Naoki Watanabe, Shigenobu Katagiri, Kazunari Shinbo, Futao Kaneko, Jason Locklin, et al., Electrical Properties and Gas Response in Alternate Layer-by-Layer Films of Copper Phthalocyanine Dyes, Japanese Journal of Applied Physics, 43(2004).

[46] G Chaidogiannos, F Petraki, N Glezos, S Kennou, S Nešpůrek, Soluble substituted phthalocyanines for OFET applications, Materials Science and Engineering: B, 152(2008) 105-8.

[47] S Paul, M Joseph, Polypyrrole functionalized with FePcTSA for NO2 sensor application, Sensors and Actuators B: Chemical, 140(2009) 439-44.

[48] AY Tolbin, LG Tomilova, Subphthalocyanines and their analogues: methods for the synthesis and structure modification, Russian Chemical Reviews, 80(2011) 531.

[49] W Liu, MR Hempstead, WA Nevin, M Melnik, ABP Lever, CC Leznoff, Disproportionation, electrochemistry, and electronic coupling involving mononuclear and binuclear cobalt phthalocyanine derivatives, Journal of the Chemical Society, Dalton Transactions, (1987) 2511-8.

[50] YJ Zhang, LS Li, J Jin, S Jiang, Y Zhao, TJ Li, et al., Organized Langmuir−Blodgett Monolayers and Multilayers Based on Semiamphiphilic Binuclear Phthalocyanine: Structural and Photovoltaic Characteristics, Langmuir, 15(1999) 2183-7.

[51] YJ Zhang, Y Li, Q Liu, J Jin, B Ding, Y Song, et al., Molecular rectifying behaviors of a planar binuclear phthalocyanine studied by scanning tunnelling microscopy, Synthetic Metals, 128(2002) 43-6.

[52] CC Leznoff, H Lam, SM Marcuccio, WA Nevin, P Janda, N Kobayashi, et al., A planar binuclear phthalocyanine and its dicobalt derivatives, Journal of the Chemical Society, Chemical Communications, (1987) 699-701.

[53] L Liu, L-P Guo, X-J Bo, J Bai, X-J Cui, Electrochemical sensors based on binuclear cobalt phthalocyanine/surfactant/ordered mesoporous carbon composite electrode, Analytica Chimica Acta, 673(2010) 88-94.

[54] R Ruiz, D Choudhary, B Nickel, T Toccoli, K-C Chang, AC Mayer, et al., Pentacene Thin Film Growth, Chemistry of Materials, 16(2004) 4497-508.

[55] F Schreiber, Organic molecular beam deposition: Growth studies beyond the first monolayer, physica status solidi (a), 201(2004) 1037-54.

[56] SR Forrest, Ultrathin Organic Films Grown by Organic Molecular Beam Deposition and Related Techniques, Chemical Reviews, 97(1997) 1793-896.

[57] M Hara, H Sasabe, A Yamada, AF Garito, Epitaxial Growth of Organic Thin Films by Organic Molecular Beam Epitaxy, Japanese Journal of Applied Physics, 28(1989) 306-8.

[58] A Koma, Van der Waals epitaxy—a new epitaxial growth method for a highly lattice-mismatched system, Thin Solid Films, 216(1992) 72-6.

[59] A Koma, Molecular beam epitaxial growth of organic thin films, Progress in Crystal Growth and Characterization of Materials, 30(1995) 129-52.

[60] E Umbach, M Sokolowski, R Fink, Substrate-interaction, long-range order, and epitaxy of large organic adsorbates, Applied Physics A: Materials Science & Processing, 63(1996) 565-76.

[61] A Yamashita, T Hayashi, Organic molecular beam deposition of metallophthalocyanines for opto-electronics applications, Advanced Materials, 8(1996) 791-9.

[62] H Wang, F Zhu, J Yang, Y Geng, D Yan, Weak Epitaxy Growth Affording High-Mobility Thin Films of Disk-Like Organic Semiconductors, Advanced Materials, 19(2007) 2168-71.

[63] T Wang, D Ebeling, J Yang, C Du, L Chi, H Fuchs, et al., Weak Epitaxy Growth of Copper Hexadecafluorophthalocyanine ($F_{16}CuPc$) on p-Sexiphenyl Monolayer Film, The Journal of Physical Chemistry B, 113(2009) 2333-7.

[64] X Qiao, L Huang, J Zhang, H Tian, Y Geng, D Yan, Weak Epitaxy Growth of Phthalocyanine on Inducing Layers of Fluorinated 5,5″-Bis(biphenyl-4-yl)-2,2′:5′,2″-terthiophene, The Journal of Physical Chemistry B, 116(2012) 1812-8.

[65] H Wang, D Song, J Yang, B Yu, Y Geng, D Yan, High mobility vanadyl-phthalocyanine polycrystalline films for organic field-effect transistors, Applied Physics Letters, 90(2007) 253510-3.

[66] AK Debnath, S Samanta, A Singh, DK Aswal, SK Gupta, JV Yakhmi, et al., Growth of iron phthalocyanine nanoweb and nanobrush using molecular beam epitaxy, Physica E: Low-dimensional Systems and Nanostructures, 41(2008) 154-63.

[67] S Samanta, DK Aswal, A Singh, AK Debnath, MS Kumar, Y Hayakawa, et al., Bias and temperature dependent charge transport in high mobility cobalt-phthalocyanine thin films, Applied Physics Letters, 96(2010) 013305-3.

[68] MC Petty, Molecular Electronics: From Principles to Practice: John Wiley & Sons; 2008.

[69] K Seshan, Handbook of Thin-Film Deposition Processes and Techniques: Principles, Methods, Equipment and Applications: Noyes Publications/William Andrew Pub.; 2001.

[70] Instruction Manual, Multiview 4000SPM/AFM, Nanonics Imaging Pvt. Ltd, Israel.

[71] I Horcas, R Fernandez, JM Gomez-Rodriguez, J Colchero, J Gomez-Herrero, AM Baro, WSXM: A software for scanning probe microscopy and a tool for nanotechnology, Review of Scientific Instruments, 78(2007) 013705-8.

[72] PJ Goodhew, FJ Humphreys, R Beanland, Electron Microscopy and Analysis: Taylor & Francis; 2001.

[73] IM Watt, The Principles and Practice of Electron Microscopy: Cambridge University Press; 1997.

[74] S Zhang, L Li, A Kumar, Materials characterization techniques: CRC Press; 2009.

[75] DP Woodruff, TA Delchar, Modern Techniques of Surface Science: Cambridge University Press; 1994.

[76] D Briggs, P Seah, Practical surface analysis: by auger and x-ray photo-electron spectroscopy: Wiley; 1983.

[77] JW John F. Watts, An Introduction to Surface Analysis by XPS and AES: John Wiley and Sons; 2003.

[78] JF Moulder, J Chastain, Handbook of X-ray Photoelectron Spectroscopy: A Reference Book of Standard Spectra for Identification and Interpretation of XPS Data: Physical Electronics; 1995.

[79] W Kemp, Organic spectroscopy: Macmillan; 1987.

[80] DA Skoog, FJ Holler, SR Crouch, Principles of Instrumental Analysis: Thomson Brooks/Cole; 2007.

[81] P Larkin, Infrared and Raman Spectroscopy; Principles and Spectral Interpretation: Elsevier; 2011.

[82] B Schrader, Infrared and Raman Spectroscopy: John Wiley & Sons; 2008.

[83] L Kelvin, V. Contact electricity of metals, Philosophical Magazine Series 5, 46(1898) 82-120.

[84] A Subramanyam, Kelvin Probe For Surface Engineering : Fund And Design: Ane Books Pvt Ltd; 2010.

[85] WA Zisman, A new method of measuring contact potential differences in metals, Review of Scientific Instruments, 3(1932) 367-70.

[86] BD Cullity, Elements of X Ray Diffraction: BiblioBazaar; 2011.

[87] M.F. Toney, T.C. Haung, S. Brennan, Zophia Rek, X-ray depth profiling of iron oxide thin films, Journal of Materials Research, 3(1988) 351-6.

[88] E. Barrena, J.O. Osso, F. Schreiber, M. Garriga, M.I. Alonso, H. Dosch, Self-organization of phthalocyanines on Al_2O_3 ((1120) in aligned and ordered films., Journal of Materials Research, 19(2004) 2061-7

[89] K Dreisewerd, The Desorption Process in MALDI, Chemical Reviews, 103(2003) 395-426.

[90] F Frank, On Miller-Bravais indices and four-dimensional vectors, Acta Crystallographica, 18(1965) 862-6.

[91] A Kirfel, K Eichhorn, Accurate structure analysis with synchrotron radiation. The electron density in Al_2O_3 and Cu_2O, Acta Crystallographica Section A, 46(1990) 271-84.

[92] J Ahn, JW Rabalais, Composition and structure of the $Al_2O_3\{0001\}$-(1 × 1) surface, Surface Science, 388(1997) 121-31.

[93] PJ Eng, TP Trainor, GE Brown Jr., GA Waychunas, M Newville, SR Sutton, et al., Structure of the Hydrated α-Al_2O_3 (0001) Surface, Science, 288(2000) 1029-33.

[94] SD Wang, X Dong, CS Lee, ST Lee, Orderly Growth of Copper Phthalocyanine on Highly Oriented Pyrolytic Graphite (HOPG) at High Substrate Temperatures, The Journal of Physical Chemistry B, 108(2004) 1529-32.

[95] SA Chambers, T Droubay, DR Jennison, TR Mattsson, Laminar Growth of Ultrathin Metal Films on Metal Oxides: Co on Hydroxylated α-Al_2O_3(0001), Science, 297(2002) 827-31.

[96] A Singh, S Samanta, A Kumar, AK Debnath, DK Aswal, SK Gupta, et al., Role of structural disorder in charge transport properties of cobalt phthalocyanine thin films grown by molecular-beam epitaxy, Organic Electronics, 11(2010) 1835-43.

[97] R Seoudi, GS El-Bahy, ZA El Sayed, Ultraviolet and visible spectroscopic studies of phthalocyanine and its complexes thin films, Optical Materials, 29(2006) 304-12.

[98] D Schlettwein, K Hesse, H Tada, S Mashiko, U Storm, J Binder, Ordered Growth of Substituted Phthalocyanine Thin Films: Hexadecafluorophthalocyaninatozinc on Alkali Halide (100) and Microstructured Si Surfaces, Chemistry of Materials, 12(2000) 989-95.

[99] SA Hayward, EKH Salje, Cubic-tetragonal phase transition in SrTiO3 revisited: Landau theory and transition mechanism, Phase Transitions, 68(1999) 501-22.

[100] S Geller, VB Bala, Crystallographic studies of perovskite-like compounds. II. Rare earth alluminates, Acta Crystallographica, 9(1956) 1019-25.

[101] J Zhang, H Wang, X Yan, J Wang, J Shi, D Yan, Phthalocyanine Composites as High-Mobility Semiconductors for Organic Thin-Film Transistors, Advanced Materials, 17(2005) 1191-3.

[102] DR Tackley, G Dent, W Ewen Smith, Phthalocyanines: structure and vibrations, Physical Chemistry Chemical Physics, 3(2001) 1419-26.

[103] DR Tackley, G Dent, W Ewen Smith, IR and Raman assignments for zinc phthalocyanine from DFT calculations, Physical Chemistry Chemical Physics, 2(2000) 3949-55.

[104] J Jiang, O Bekaroglu, Y Bian, Functional Phthalocyanine Molecular Materials: Springer; 2010.

[105] ES Dodsworth, ABP Lever, P Seymour, CC Leznoff, Intramolecular coupling in metal-free binuclear phthalocyanines, The Journal of Physical Chemistry, 89(1985) 5698-705.

[106] NF Mott, RW Gurney, Electronic processes in ionic crystals: Dover Publications; 1964.

[107] SC Jain, V Kumar, Conducting Organic Materials and Devices: Elsevier/Academic Press; 2007.

[108] S Nešpůrek, O Zmeškal, J Sworakowski, Space-charge-limited currents in organic films: Some open problems, Thin Solid Films, 516(2008) 8949-62.

[109] KC Kao, W Hwang, Electrical Transport in Solids: With Particular Reference to Organic Semiconductors: Pergamon Press; 1981.

[110] MA Lampert, P Mark, Current injection in solids: Academic Press; 1970.

[111] MA Lampert, Simplified Theory of Space-Charge-Limited Currents in an Insulator with Traps, Physical Review, 103(1956) 1648-56.

[112] S Nešpurek, EA Silinsh, Space-charge-limited current theory for molecular crystals with gaussian distribution of local trapping states, physica status solidi (a), 34(1976) 747-59.

[113] S NeŠpůrek, P Smejtek, Space-charge limited currents in insulators with the Gaussian distribution of traps, Czechoslovak Journal of Physics, 22(1972) 160-75.

[114] BH Hamadani, Electronic charge injection and transport in organic field-effect transistors: RICE UNIVERSITY; 2007.

[115] A Miller, E Abrahams, Impurity Conduction at Low Concentrations, Physical Review, 120(1960) 745-55.

[116] WD Gill, Drift mobilities in amorphous charge-transfer complexes of trinitrofluorenone and poly-n-vinylcarbazole, Journal of Applied Physics, 43(1972) 5033-40.

[117] JG Simmons, Conduction in thin dielectric films, Journal of Physics D: Applied Physics, 4(1971) 613.

[118] WR Salaneck, Conjugated Polymer and Molecular Interfaces: Science and Technology for Photonic and Optoelectronic Applications: Marcel Dekker; 2002.

[119] F So, Organic Electronics: Materials, Processing, Devices and Applications: CRC Press; 2010.

[120] H Ishii, N Hayashi, E Ito, Y Washizu, K Sugi, Y Kimura, et al., Kelvin probe study of band bending at organic semiconductor/metal interfaces: examination of Fermi level alignment, physica status solidi (a), 201(2004) 1075-94.

[121] H Ishii, K Sugiyama, E Ito, K Seki, Energy Level Alignment and Interfacial Electronic Structures at Organic/Metal and Organic/Organic Interfaces, Advanced Materials, 11(1999) 605-25.

[122] M Knupfer, H Peisert, Electronic properties of interfaces between model organic semiconductors and metals, physica status solidi (a), 201(2004) 1055-74.

[123] H Vázquez, YJ Dappe, J Ortega, F Flores, A unified model for metal/organic interfaces: IDIS, ‘pillow’ effect and molecular permanent dipoles, Applied Surface Science, 254(2007) 378-82.

[124] JG Simmons, Electric Tunnel Effect between Dissimilar Electrodes Separated by a Thin Insulating Film, Journal of Applied Physics, 34(1963) 2581-90.

[125] RH Fowler, L Nordheim, Electron Emission in Intense Electric Fields, Proceedings of the Royal Society of London Series A, 119(1928) 173-81.

[126] AS Dhoot, GM Wang, D Moses, AJ Heeger, Voltage-Induced Metal-Insulator Transition in Polythiophene Field-Effect Transistors, Physical Review Letters, 96(2006) 246403.

[127] M Raikh, X Wei, Current-Voltage Characteristics of Polymer Light-Emitting Diode at Low Voltages, Molecular Crystals and Liquid Crystals Science and Technology Section A Molecular Crystals and Liquid Crystals, 256(1994) 563-9.

[128] JH Wei, YL Gao, XR Wang, Inverse square-root field dependence of conductivity in organic field-effect transistors, Applied Physics Letters, 94(2009) 073301-3.

[129] CR Crowell, The Richardson constant for thermionic emission in Schottky barrier diodes, Solid-State Electronics, 8(1965) 395-9.

[130] JG Simmons, Transition from Electrode-Limited to Bulk-Limited Conduction Processes in Metal-Insulator-Metal Systems, Physical Review, 166(1968) 912-20.

[131] BS Barkhalov, YA Vidadi, Properties of Al(copper phthalocyanine)Ag diode structures with Schottky barriers, Thin Solid Films, 40(1977) L5-L8.

[132] F-R Fan, LR Faulkner, Photovoltaic effects of metalfree and zinc phthalocyanines. I. Dark electrical properties of rectifying cells, The Journal of Chemical Physics, 69(1978) 3334-40.

[133] C Hamann, C Tantzscher, Electrical properties of organic/inorganic thin film sandwiches, Thin Solid Films, 36(1976) 81-4.

[134] AK Hassan, RD Gould, The electrical properties of copper phthalocyanine thin films using indium electrodes, Journal of Physics D: Applied Physics, 22(1989) 1162.

[135] AK Hassan, RD Gould, Asymmetric electrical conductivity in oxygen-doped thin films of copper phthalocyanine, using gold and aluminium electrodes, International Journal of Electronics, 69(1990) 11-7.

[136] TS Shafai, RD Gould, Observations of Schottky and Poole-Frenkel emission in lead phthalocyanine thin films using aluminium injecting electrodes, International Journal of Electronics, 73(1992) 307-13.

[137] TS Shafai, RD Gould, Electrical characteristics of lead phthalocyanine thin films using aluminium Schottky barriers and gold ohmic contacts, International Journal of Electronics, 73(1992) 1043-5.

[138] T Matsushima, H Sasabe, C Adachi, Carrier injection and transport characteristics of copper phthalocyanine thin films under low to extremely high current densities, Applied Physics Letters, 88(2006) 033508-3.

[139] K Xiao, Y Liu, G Yu, D Zhu, Influence of the substrate temperature during deposition on film characteristics of copper phthalocyanine and field-effect transistor properties, Applied Physics A: Materials Science & Processing, 77(2003) 367-70.

[140] A Sussman, Space-Charge-Limited Currents in Copper Phthalocyanine Thin Films, Journal of Applied Physics, 38(1967) 2738-48.

[141] RD Gould, Dependence of the mobility and trap concentration in evaporated copper phthalocyanine thin films on background pressure and evaporation rate, Journal of Physics D: Applied Physics, 19(1986) 1785.

[142] RD Gould, RIR Blyth, Conductivity and Absorption Measurements in Nickel Phthalocyanine Thin Films, physica status solidi (a), 120(1990) K57-K61.

[143] C Hamann, On the trap distribution in thin films of copper phthalocyanine, physica status solidi (b), 26(1968) 311-8.

[144] GM Delacote, JP Fillard, FJ Marco, Electron injection in thin films of copper phtalocyanine, Solid State Communications, 2(1964) 373-6.

[145] V Coropceanu, J Cornil, DA da Silva Filho, Y Olivier, R Silbey, J-L Brédas, Charge Transport in Organic Semiconductors, Chemical Reviews, 107(2007) 926-52.

[146] S Samanta, A Singh, AK Debnath, DK Aswal, SK Gupta, JV Yakhmi, et al., Oxygen induced hysteretic current-voltage characteristics of iron-phthalocyanine thin films, Journal of Applied Physics, 104(2008) 073717-6.

[147] AM Saleh, AO Abu-Hilal, RD Gould, Investigation of electrical properties (ac and dc) of organic zinc phthalocyanine, ZnPc, semiconductor thin films, Current Applied Physics, 3(2003) 345-50.

[148] Q Xianfeng, C Jiangshan, M Dongge, Trap-free space-charge-limited electron transport in amorphous tin(IV) phthalocyanine dichloride thin film, Journal of Physics D: Applied Physics, 43(2010) 215402.

[149] PWM Blom, MJM de Jong, MG van Munster, Electric-field and temperature dependence of the hole mobility in poly(p-phenylene vinylene), Physical Review B, 55(1997) R656-R9.

[150] YZ Wu, CR Zhang, DJ Zhang, Determination of carrier mobility in disordered organics from current-voltage characteristics, Applied Physics Letters, 95(2009) 033508-3.

[151] N. F. Mott, Metal–Insulator Transition 2nd ed. (Talor-Francis, London,1990) and references therein.

[152] T. A. Skotheim, R.L. Elsenbaumer, JR Reynolds, Handbook of Conducting Polymers, 2nd ed., Marcel Dekker Inc., New York 1998.

[153] CO Yoon, R M, D Moses, AJ Heeger, Transport near the metal-insulator transition: Polypyrrole doped with PF_6, Physical Review B, 49(1994) 10851-63.

[154] L Cao, E Sozontov, J Zegenhagen, Cubic to Tetragonal Phase Transition of SrTiO3 under Epitaxial Stress: An X-Ray Backscattering Study, physica status solidi (a), 181(2000) 387-404.

[155] WM Lu, X Wang, ZQ Liu, S Dhar, A Annadi, K Gopinadhan, et al., Metal-insulator transition at a depleted $LaAlO_3$/SrTiO3 interface: Evidence for charge transfer induced by SrTiO3 phase transitions, Applied Physics Letters, 99(2011) 172103-3.

[156] VK Vlasko-Vlasov, YK Lin, DJ Miller, U Welp, GW Crabtree, VI Nikitenko, Direct Magneto-Optical Observation of a Structural Phase Transition in Thin Films of Manganites, Physical Review Letters, 84(2000) 2239-42.

[157] NF Mott, WD Twose, The theory of impurity conduction, Advances in Physics, 10(1961) 107-63.

[158] R Temirov, S Soubatch, A Luican, FS Tautz, Free-electron-like dispersion in an organic monolayer film on a metal substrate, Nature, 444(2006) 350-3.

[159] M Ahlskog, M Reghu, AJ Heeger, T Noguchi, T Ohnishi, Electronic transport in the metallic state of oriented poly(p-phenylenevinylene), Physical Review B, 53(1996) 15529-37.

[160] L Li, Q Tang, H Li, W Hu, X Yang, Z Shuai, et al., Organic thin-film transistors of phthalocyanines, Pure and Applied Chemistry, 80(2008) 2231-40.

[161] BG Streetman, SK Banerjee, Solid State Electronic Devices: Pearson Prentice-Hall; 2009.

[162] BC Nandu, NC Andrew, C Isabelle, JC Michael, GC Markys, EM Craig, et al., High-mobility solution-processed copper phthalocyanine-based organic field-effect transistors, Science and Technology of Advanced Materials, 12(2011) 025001.

[163] R Zeis, T Siegrist, C Kloc, Single-crystal field-effect transistors based on copper phthalocyanine, Applied Physics Letters, 86(2005) 022103-3.

[164] P Peumans, SR Forrest, Very-high-efficiency double-heterostructure copper phthalocyanine/C[sub 60] photovoltaic cells, Applied Physics Letters, 79(2001) 126-8.

[165] SS Sun, NS Sariciftci, Organic Photovoltaics: Mechanism, Materials, And Devices: Taylor & Francis; 2005.

[166] CW Tang, Two-layer organic photovoltaic cell, Applied Physics Letters, 48(1986) 183-5.

[167] CW Tang, SA VanSlyke, Organic electroluminescent diodes, Applied Physics Letters, 51(1987) 913-5.

[168] H Wang, Y Donghang, Organic heterostructures in organic field-effect transistors, NPG Asia Mater, 2(2010) 69-78.

[169] H Alves, AS Molinari, H Xie, AF Morpurgo, Metallic conduction at organic charge-transfer interfaces, Nat Mater, 7(2008) 574-80.

[170] D Yan, H Wang, B Du, Introduction to Organic Semiconductor Heterojunctions: John Wiley & Sons; 2010.

[171] K Harada, AG Werner, M Pfeiffer, CJ Bloom, CM Elliott, K Leo, Organic Homojunction Diodes with a High Built-in Potential: Interpretation of the Current-Voltage

Characteristics by a Generalized Einstein Relation, Physical Review Letters, 94(2005) 036601.

[172] KM Lau, JX Tang, HY Sun, CS Lee, ST Lee, D Yan, Interfacial electronic structure of copper phthalocyanine and copper hexadecafluorophthalocyanine studied by photoemission, Applied Physics Letters, 88(2006) 173513-3.

[173] W Chen, S Chen, H Huang, DC Qi, XY Gao, ATS Wee, Molecular orientation dependent interfacial dipole at the F_{16}CuPc/CuPc organic heterojunction interface, Applied Physics Letters, 92(2008) 063308-3.

[174] W Chen, DC Qi, YL Huang, H Huang, YZ Wang, S Chen, et al., Molecular Orientation Dependent Energy Level Alignment at Organic−Organic Heterojunction Interfaces, The Journal of Physical Chemistry C, 113(2009) 12832-9.

[175] H Yamane, Y Yabuuchi, H Fukagawa, S Kera, KK Okudaira, N Ueno, Does the molecular orientation induce an electric dipole in Cu-phthalocyanine thin films?, Journal of Applied Physics, 99(2006) 093705-5.

[176] J Wang, H Wang, X Yan, H Huang, D Yan, Organic heterojunction and its application for double channel field-effect transistors, Applied Physics Letters, 87(2005) 093507-3.

[177] JL Yang, S Schumann, TS Jones, Morphology and Structure Transitions of Copper Hexadecafluorophthalocyanine (F16CuPc) Thin Films, The Journal of Physical Chemistry C, 114(2009) 1057-63.

[178] J Yang, D Yan, Weak epitaxy growth of organic semiconductor thin films, Chemical Society Reviews, 38(2009) 2634-45.

[179] F Zhu, J Yang, D Song, C Li, D Yan, Single-crystal-like organic heterojunction with 40 nm thick charge accumulation layers, Applied Physics Letters, 94(2009) 143305-3.

[180] T Kambayashi, H Ohta, H Hoshi, M Hirano, H Hosono, H Takezoe, et al., Epitaxial Growth of a Copper-phthalocyanine on a Transparent Conductive Substrate with an Atomically Flat Surface, Crystal Growth & Design, 5(2004) 143-6.

[181] DK Aswal, SK Gupta, Science And Technology Of Chemiresistor Gas Sensors: Nova Science Publishers; 2007.

[182] A Joshi, DK Aswal, SK Gupta, JV Yakhmi, SA Gangal, ZnO-nanowires modified polypyrrole films as highly selective and sensitive chlorine sensors, Applied Physics Letters, 94(2009) 103115-3.

[183] A Chaparadza, SB Rananavare, Room temperature Cl_2 sensing using thick nanoporous films of Sb-doped SnO_2, Nanotechnology, 19(2008) 245501.

[184] S Jain, AB Samui, M Patri, VR Hande, SV Bhoraskar, FEP/polyaniline based multilayered chlorine sensor, Sensors and Actuators B: Chemical, 106(2005) 609-13.

[185] T Miyata, S Kawaguchi, M Ishii, T Minami, High sensitivity chlorine gas sensors using Cu–phthalocyanine thin films, Thin Solid Films, 425(2003) 255-9.

[186] K Garg, A Singh, AK Debnath, SK Nayak, S Chattopadhyay, DK Aswal, et al., Bis-porphyrin films as ppb level chemiresistive sensors, Chemical Physics Letters, 488(2010) 27-31.

[187] T Miyata, T Minami, Chlorine gas sensors with high sensitivity using Mg-phthalocyanine thin films, Applied Surface Science, 244(2005) 563-7.

[188] DR Patil, LA Patil, Room temperature chlorine gas sensing using surface modified ZnO thick film resistors, Sensors and Actuators B: Chemical, 123(2007) 546-53.

[189] DH Dawson, DE Williams, Gas-sensitive resistors: surface interaction of chlorine with semiconducting oxides, Journal of Materials Chemistry, 6(1996) 409-14.

[190] C Xiangfeng, C Zhiming, High sensitivity chlorine gas sensors using CdSnO3 thick film prepared by co-precipitation method, Sensors and Actuators B: Chemical, 98(2004) 215-7.

[191] MD Mahanubhav, LA Patil, Studies on gas sensing performance of CuO-modified CdIn2O4 thick film resistors, Sensors and Actuators B: Chemical, 128(2007) 186-92.

[192] J Tamaki, J Niimi, S Ogura, S Konishi, Effect of micro-gap electrode on sensing properties to dilute chlorine gas of indium oxide thin film microsensors, Sensors and Actuators B: Chemical, 117(2006) 353-8.

[193] J Tamaki, C Naruo, Y Yamamoto, M Matsuoka, Sensing properties to dilute chlorine gas of indium oxide based thin film sensors prepared by electron beam evaporation, Sensors and Actuators B: Chemical, 83(2002) 190-4.

[194] CV Gopal Reddy, SV Manorama, VJ Rao, Semiconducting gas sensor for chlorine based on inverse spinel nickel ferrite, Sensors and Actuators B: Chemical, 55(1999) 90-5.

[195] C Xiangfeng, High sensitivity chlorine gas sensors using $CdIn_2O_4$ thick film prepared by co-precipitation method, Materials Research Bulletin, 38(2003) 1705-11.

[196] T Miyata, T Hikosaka, T Minami, High sensitivity chlorine gas sensors using multicomponent transparent conducting oxide thin films, Sensors and Actuators B: Chemical, 69(2000) 16-21.

[197] F Bender, C Kim, T Mlsna, JF Vetelino, Characterization of a WO_3 thin film chlorine sensor, Sensors and Actuators B: Chemical, 77(2001) 281-6.

[198] FI Bohrer, A Sharoni, C Colesniuc, J Park, IK Schuller, AC Kummel, et al., Gas Sensing Mechanism in Chemiresistive Cobalt and Metal-Free Phthalocyanine Thin Films, Journal of the American Chemical Society, 129(2007) 5640-6.

[199] NL Tran, AC Kummel, A density functional theory study on the binding of NO onto FePc films, The Journal of Chemical Physics, 127(2007) 214701-7.

[200] P Bertoncello, M Peruffo, An investigation on the self-aggregation properties of sulfonated copper(II) phthalocyanine (CuTsPc) thin films, Colloids and Surfaces A: Physicochemical and Engineering Aspects, 321(2008) 106-12.

[201] RI Masel, Principles of Adsorption and Reaction on Solid Surfaces: Wiley; 1996.

[202] R Tongpool, S Yoriya, Kinetics of nitrogen dioxide exposure in lead phthalocyanine sensors, Thin Solid Films, 477(2005) 148-52.

[203] EF Vansant, P Voort, KC Vrancken, Characterization and Chemical Modification of the Silica Surface: Elsevier; 1995.